Topological Aspects of 1-Dimensional Closed & Open Quantum Systems

Kevin Kavanagh

M.Sc.

Thesis presented for the degree of

Doctor of Philosophy

to the

Maynooth University

Department of Theoretical Physics

October 2022

Head of Department

Dr. J. K. Slingerland

Deputy Head of Department

Dr. Jiří Vala

Research Advisors

Dr. Graham Kells & Dr. J. K. Slingerland

To my family

Contents

1 Introduction **1**

1.1 Structure . . . 3

2 Changing Formalisms **7**

2.1 Language of Spins . . . 7

2.2 Creation & Annihilation Operators . . . 9

2.3 Open Systems & Third Quantization . . . 10

2.3.1 Operators are to Superoperators as States are to Operators . . 11

2.3.2 Closed system dynamics . . . 12

2.3.3 Open system dynamics . . . 14

3 Tensor Network Basics **17**

3.1 Diagrams & Notation . . . 18

3.2 Matrix Product States . . . 19

3.3 Density Matrix Renormalisation Group . . . 24

3.3.1 Creating MPS & MPO for Simulation . . . 26

4 Majorana Based Topological Memories **31**

4.1 Majorana Zero Modes . . . 32

4.2 Topological Aspect of Majorana Fermions . . . 37

4.3 Topological Quantum Order . . . 40

4.3.1 An Argument for No Phase Error . . . 41

4.3.2 Time-Dependent Perturbations . . . 45

4.3.3 TQO Inheritance . . . 46

4.4 An Interacting Majorana Topological Memory . . . 47

4.4.1 Numerical Verification . . . 50

4.5 Spectral Correlations: Green's Functions . . . 51

4.5.1 Extension to Fermionic & Multi-particle Operators . . . 53

5 Quantum Exclusion Process **57**

5.1 Model and methods . . . 59

5.1.1 Review of TASEP . . . 59

5.1.2 Combining the TXY & TASEP Models . . . 61

5.1.3 TXY-TASEP Superoperator 64
5.2 Non-Equilibrium Steady State 65
5.2.1 Obtaining NESS from DMRG 66
5.2.2 NESS as a Perturbation of the Maximally Mixed State 71
5.3 Effect of Hamiltonian Processes on Lattice Currents 74
5.3.1 Continuity Equation: Currents, Sources and Sinks 75
5.3.2 Steady State Current 77
5.3.3 Quantum Effect on the Steady State Current 78
5.3.4 Role of the Quantum Phase Transition 78

6 Liouvillian Gap of Dissipative Quantum Systems 83
6.1 The Liouvillian Gap 85
6.1.1 Emergence of a Liouvillian Gap from XY Anisotropy and Bulk Dissipation 85
6.1.2 MPS obtained $\mathcal{E}_{\text{gap}}$ versus $\mathcal{E}_1^{(2)}$ 87
6.1.3 Analysis of the $s = 2$ Spectrum 88
6.1.4 Relaxation Rate Compared to Related Models 88
6.2 Kernel Projection for the Liouvillian Gap 89
6.2.1 Model 89
6.2.2 Setup of Kernel Projection Method 91
6.3 Kernel Projection Method for Dephasing 94
6.3.1 Weak quantum limit - Projection to the $\mathbb{L}$ kernel 95
6.3.2 Strong quantum limit - Projection to the $\mathbb{H}$ kernel 96
6.3.3 Gap Analysis 98
6.4 Further Models of Dissipation 99
6.4.1 Symmetric Simple Exclusion Process 99
6.4.2 Totally asymmetric simple exclusion process 100
6.5 Block Perturbation Theory 102
6.6 The Meaning of Even and Odd Sector Gaps 105
6.7 Spectrum of the Odd Sectors 106

7 Conclusion 109

A Numerical MPS Methods: A Further Use Case 113
A.1 Model 114
A.2 Lattice Implementation of DSF 115
A.3 Comparison against Green's Function Methods 116
A.4 XX Dynamical Structure Factor 118
A.5 Chiral Dynamical Structure Factor 118

B Canonical Basis 121

C TASEP & Its Quantum Embedding **123**
C.1 Exclusion Process 123
C.2 TASEP Embedded in a Quantum Spin Chain 130

D Performing the Gap Integral **135**
D.1 Change of Variables 136
D.2 Gap Integral as a Contour Integral 138

Bibliography **143**

Declaration

I declare that this thesis has not been submitted in whole, or in part, to this or any other university for any other degree and is, except where otherwise stated, the original work of the author.

Kevin Kavanagh, 16 February 2023

Acknowledgements

It is difficult to believe that I will be submitting my thesis in a day. Over these past years, these final steps have felt at times out of reach and at others frighteningly close. While momentarily difficult to imagine, it is certainly impossible to conceive of arriving at this point without all of the people along the way who brought me here and helped me in some way.

Firstly, I must thank my supervisor Graham for providing me with this enormous opportunity to pursue a PhD. His unending support, understanding and patience is above anything that I could have expected before I began. You have always been able to guide me through problems, both large and small. Ultimately I could not have asked for a better supervisor. I hope you will believe me when I say that I could not have done this without the support and guidance that you so readily provided.

I must thank Graham for also bringing together Shane and Luuk to complete our research group. Shane has been a friend and a mentor for this entire endeavour. He has helped me to make sense when I was not making any. He has always been able to find the question that got to the heart of anything that was troubling us. All I'm saying is that you are an excellent physicist, a devoted colleague and a great friend. Luuk, I am glad to have had you to share the burden of the PhD with, especially in the early days when we were both finding our feet. You gave me a valuable perspective on the work we did together. I could not have asked for a better group to work with and hope that we can continue to work together into the future.

I have to acknowledge that I have had the good fortune to have another supervisor, Joost. His ideas and perspectives during our work together have been invaluable. Ever since my first time at Maynooth he has taught me an incalculable amount and been enthusiastic to help me at any time. Without his support I would have never thought I could have started a PhD, much less so reach this point. There are many more people at Maynooth that have made an impact on me over the years. From the very beginning all of my other lecturers there: Paul, Jonivar, Charles, Jiří, Brian and Prof. Heffernan. More recently all of the staff and other students: Suzie, Monica, Peter, Alex, Babatunde, John, Aonghus, Darragh, Goran and Stephen. A special thanks to Paul and Stephen for all of the help and inspiration you gave me from the first time I arrived at Maynooth so many years ago.

From DIAS I must thank Eucharia, George, Werner, Marianne, Tony, Denjoe,

Dion, Leron, Takaki, Mahul, Ronan, Mary, Helena, Grace, Pauline, Colette and Michelle for making Burlington Road a great place to work over the years. More recently also thanks to Venus, Giandomenico, Neetu, Saki, Elo, Jasmine and Giorgio for making these last few stressful months more enjoyable. I hope you will all enjoy DIAS as much as I have and improve the institute with your contributions. To all of the people in other universities around Ireland that have inspired me and shared part of this experience, especially Emma and Jonas, I thank you. I cannot forget my friends and colleagues from Utrecht that I have worked with and have motivated me to pursue a PhD.

A few immensely important people have not yet appeared. Ian, it feels as though you have been there since before the beginning. I place a lot of value in the times we worked together. You helped to pull together our paper with fresh insights when we were unsure and helped me in other projects without hesitation. More so, I cherish the time we spent together, all of that time in retrospect was a joyous reprieve that made the difficult periods of this PhD much easier. I hope you and Niamh flourish wherever you end up next. Domenico I could almost say the same to you, you welcomed me on my return to Dublin like an old friend. Your advice, especially for writing this thesis, has been essential. Your depth of knowledge at times was astounding and gave me a greater appreciation of the work we did. I hope that I can be even half as passionate and helpful as you have been.

Aaron. You have been with me since the very beginning, all the way back to when you first tried to talk to me in Maynooth. I am immensely grateful for that day. Since then, we have followed each other almost every step of the way to this point. I want to say that I am indebted to you in an uncountable number of ways. I cannot dream of a better person to have endured all of the tough times with and to have savoured all of the sweet moments with. You have made me in the process a better physicist and more importantly a better person. I only hope that our paths continue to cross as we move forward.

Many thanks remain for my oldest friends who made my return to Dublin years ago feel like I never left. Ailbhe, Luke, Jack, Eoin and Stephen you all kept Dublin feeling like home. To my friends further afield: Damjan, Efi and Pieter. Without your encouragement and friendship I may have completely lost confidence in being able to finish this thesis. Your unwavering support stabilised me when I wavered. You hosted me when I needed time away. When we were isolated by lockdowns and by distance you all kept in touch to make those times feel less solitary.

Finally, I thank my family. My parents Pat and Carol, who ensured a future for me that they may not have imagined before it began but stuck with me the entire time. It is difficult to put into words the amount of gratitude I have for all that you have done for me, that has allowed me to even believe that this was possible. To my brothers Brian and Alan who gave support even when they did not understand

what I was doing, thank you both. To Michelle, without you I would not be in this position. Certainly, I would not be the person I am today without your love and support. Thanks to Justin for always offering support when I needed it. Sam and Cody, you have been a source of joy these past few years and I am grateful I could be here during this time to see you grow up. Many more thanks are deserved for the rest of my family: Nicola, Leanne, Demi, Khloe, Josh, Reece, Erin and Lorcan. Thanks to all of you for being there one way or another over the years.

I suspect that all of these names have not captured the full collection of people that are in my life, or who have passed through it, who contributed to my journey here. It may be unlikely that I can know every person that has influenced me all along the way, but nonetheless I thank you all.

Abstract

We consider the p-wave superconductor in one spatial dimension from two perspectives. Firstly as a closed system and secondly as an open system.

As a closed system, we analyse the p-wave superconductor as a candidate platform which can host Majorana bound states. In particular, we consider how interaction driven errors could spoil the encoding of protected qubit states constructed from these bound states. We present a generic analysis of how the property of topological quantum order (TQO) suppresses an interaction driven dephasing process. We use this to quantify the extent of correlation between spectral densities from different topological sectors. Our key result, verified numerically for the p-wave superconductor, is that despite mismatched bulk spectra the TQO property ensures that interaction driven phase errors are suppressed up to a time which scales with system length.

As an open system, we bring the model into contact with various environments. We do so to understand the interplay of quantum and classical transport phenomena. Our key result in this case is that there is, in general, a strong dependence on the superconductor pairing and the boundary dissipation rates in the final non-equilibrium steady states. Further, we demonstrate that under weak dissipation topological properties of the closed system manifest themselves in a key aspect of the open quantum system dynamics, the Liouvillian gap. We find that this indicator of relaxation time retains information of these properties robustly for a number of dissipative processes.

Chapter 1

Introduction

The foundation of this thesis is the study of one dimensional many-body quantum systems. We will be particularly interested in the topological aspects of models which share a common core. That core is the one dimensional p-wave superconductor, and in this thesis, we consider it from two principal perspectives. Firstly, as a closed system, we investigate its feasibility as a topological quantum memory when particle interactions are introduced for a time-dependent system. Secondly, as an open system, we explore how its inherent quantum effects impact stochastic/classical transport processes and the survival of its closed system features to various environments. These models, taken from either view, provide a rich platform upon which we can study diverse aspects of condensed matter physics in a relatively simple setting.

As a closed, non-interacting system the p-wave superconductor has been proposed as a topological platform which supports unpaired Majorana zero modes (MZM) at its boundaries [Kit01]. These zero energy modes can be used to encode a qubit, the quantum analogue of a classical bit of information [NC00], into the ground state of the system. Since two such MZM constitute a single fermionic degree of freedom that costs zero energy to occupy, their presence necessitates a degenerate ground state. A qubit encoded via this degenerate ground state is tolerant against local noise processes [Kit03] due to the non-local configuration of the constituent MZM. Furthermore, the zero energy Majorana modes are isolated energetically from non-Majorana excitations by a finite energy gap.

The p-wave superconductor is one example of topological states of matter [Pac12; Sta16] which have come to represent a promising direction in the attainment of quantum computation. More precisely the p-wave superconductor in 1-dimension belongs to a class of symmetry protected topological (SPT) models. This is due to the topological features relying on the presence of symmetries to be manifest. While these models do not have inherent bulk topological features they may have non-trivial boundary states. These non-trivial boundary states are those that may prove useful in the pursuit of topological quantum computation.

The importance of platforms based on topological states of matter stems from

their potential to circumvent the inherent fragility of quantum information and the compounded errors associated with logic gate imperfections [Con+19]. While there has been a vast proliferation of proposed quantum computation platforms since the field's inception [Den+02; Nay+08; Ali+11; SD12; SL13; ST13], utilising topological states of matter remains an encouraging route to obtaining fault-tolerant quantum computation [Kit03; BHM10].

However, these statements are true only in the case of zero temperature, without difficult to simulate electron density-density interactions. In a real implementation, interactions and undesired excitations are inevitable. There, it is conceivable that the resultant energy spectrum in interacting regimes can allow for a dynamically generated error process that is undetectable. In this thesis, we will show how the property of topological quantum order (TQO) [WN90; Wen90; HW05; Zen+19], is robust enough to protect against such interaction-driven error processes - and then use this analysis to make strong statements about how robust the topological degeneracy is above the gap.

To demonstrate this claim we utilise a number of techniques, some of which are especially relevant (unique) to one spatial dimension. For example, on a mathematical level we produce a proof against the destructive error processes that can arise in an interacting p-wave superconductor hosting MZM. This proof rests on the result that local observables on the states that make up the qubit space are equal, up to exponentially small corrections in the spatial separation of the Majorana, and that the disturbances introduced to such an interacting system can still only propagate at some finite speed [Con+19; Coo+21b]. We then produce numerical verification of this same fact using tensor network methods [Orú19] which were originally born out of the study of one dimensional many-body quantum systems. Specifically, we leverage a time-evolution technique based on matrix product states (MPS), and operators (MPO), called the time dependent variation principle (TDVP) [Hae+11; Pae+19] to calculate Green's functions of local operators, which then allows us to make concrete verifiable statements about the low energy spectrum. In particular, we demonstrate that errors are indeed systematically suppressed up to a time that scales with the system size. Crucially, these errors are symptomatic of local operators becoming non-local under time evolution, rather than interaction-driven error processes for systems with TQO.

The second strand of this thesis focuses on how quantum effects can influence classical or stochastic transport phenomena [Sti01]. To address this issue we examine models of one dimensional transport that combine quantum and classical processes, investigating the salient features of this amalgamation. We are particularly interested in the effect that quantum processes can have on the eventual steady states and associated relaxation rates [BP02]. Our main result is that while simple kinetic terms (e.g coherent hopping) in the quantum Hamiltonian have negligible

effects generally [TWV12], once superconductor pairing is present the behaviour of the combined system is radically altered [Kav+22a]. Specifically, we find that pair-creation and annihilation will result in a finite relaxation rate for all system sizes, and thus superconductivity will generally drive the system rapidly to its eventual steady state. Perhaps more intriguing is the fact that, when the quantum processes are relatively strong with respect to the classical processes, the steady state relaxation rate has an explicit dependence on the topological nature of the Hamiltonian. These effects can enhance steady-state currents, and we provide a unique way of understanding these issues via continuity equations with sources.

To arrive at these results we employ a variety of approaches. To treat classical and quantum processes on the same footing we make use of Kraus operators [NC00] and open quantum system methods, the dynamics of which are encoded via a Lindblad master equation; also referred to as the Gorini-Kossakowski-Sudarshan-Lindblad (GKSL) master equation [GKS76; Lin76]. Further, to extract the steady states and relaxation rates of the systems studied we use variants of MPS and time dependent tensor network methods adapted to the open system contextz. Throughout this analysis, we also employ a method called third (or operator) quantisation [Pro08] - making particular use of what is called the canonical representation [Kel15a; Kel15b] to investigate the problem. The latter allows us to focus our efforts on specific relevant sectors, and we present here techniques to numerically and analytically calculate the relaxation rates in a variety of regimes.

1.1 Structure

The structure of the thesis is as follows.

To begin we will describe some of the different formalisms that are employed throughout the thesis to describe the systems of interest, this discussion comprises Chapter 2. We describe the generic p-wave superconductor and how it is related to the Heisenberg spin model by application of the Jordan-Wigner transformation [JW28]. We end this chapter with an overview of the third quantisation framework.

Next, in Chapter 3 we give an overview of the tensor network techniques that are common to the numerical methods employed in the remaining chapters. The key techniques included are matrix product states (MPS), the construction of matrix product operators (MPO) from a Hamiltonian as an example and time evolution using density matrix renormalisation group (DMRG).

Chapter 4 then introduces the notion of Majorana zero modes in more concrete terms and the notion of topology in this setting. Following this, we provide the full analysis of topological protection of a Majorana-based qubit against a dynamically generated phase error process. This is achieved by leveraging the property of topo-

logical quantum order to produce a proof against such an error process. Later, we provide numerical verification and Green's function analysis. This numerical verification relies on a couple of tensor network techniques that are summarised in the prior chapter. The main tools we need here are MPS and DMRG. Specific to this topic we also apply Green's function techniques to demonstrate the key aspect of the TQO property. Specifically, TQO implies that the expectation values of local observables, on the degenerate ground state space, are equal up to an exponentially small correction that depends on the spatial separation between the Majorana. By probing the Green's functions of local observables we can analyse this statement quantitatively, and then leverage the result to infer implications for the many-body spectrum.

Afterwards, with a good understanding of the features of the p-wave superconductor model, we introduce the totally asymmetric simple exclusion process (TASEP) at the beginning Chapter 5. The main focus of the remainder of this chapter is the properties of the steady state of the full TXY-TASEP model, in particular making a comparative study against the classical steady-states of TASEP that are already well understood. The TXY-TASEP model is a combination of the transverse XY (TXY) Hamiltonian, i.e. the p-wave model expressed as a spin chain, subject to dissipation in the form of a classical stochastic hopping process, the TASEP model. Crucially, we observe a striking dependence on the superconductor pairing in the character of the final steady states. We end this chapter with a study of the effects of pair creation/annihilation on the steady-state current and, in particular, if current can be enhanced by superconductor pairing.

Note that the technical details of combining the p-wave superconductor and the TASEP model are reserved for Appendix C. The principal notion therein is to express both models in spin language such that they can be viewed as components of a Lindblad master equation. The result is a p-wave superconductor (expressed as the transverse XY model) that has been opened up to an environment, modelled by the TASEP. By noticing this it becomes rather direct to trade TASEP for other dissipative processes.

Finally, Chapter 6 begins with a preliminary discussion on the Liouvillian gap, the quantity that determines the relaxation rate. With this in mind, we provide numerical evidence of the topological fingerprints that can be observed in the behaviour of this gap for the TXY-TASEP model. To make this observation concrete, we consider simpler models, exploiting the Lindbladian setting to exchange TASEP for other dissipative processes such as the Symmetric Simple Exclusion Process (SSEP) and on-site dephasing.

In our analysis, we show how perturbing the kernel of the dissipator, where the steady state resides, by the quantum processes allows one to produce an effective, integrable XXZ spin chain. Further, this quantitatively explains why *any* supercon-

ductivity in the Hamiltonian produces an open, constant (in system size) relaxation gap as the excitation gap of the effective XXZ model corresponds to the relaxation gap in this case. Importantly we also elucidate another approach, where we project onto the kernel of the Hamiltonian commutator, and treat the dissipative terms perturbatively. This method is what allows us to extract the precise form of the relaxation gap when coherent effects are more dominant. It is in determining this form that we are able to make the direct connection to the topological nature of the relaxation gap. We then conclude by outlining how the methodology can be applied to the TXY-TASEP - although the results, in this case, do not work out as cleanly.

Throughout both Ch. 5 and Ch. 6 we take a particular perspective on the study of open quantum systems; namely, third quantisation. The technique rests upon a transformation of operators and states used in the open quantum system framework. In practice, this means that the entire Lindblad master equation becomes a single operator (the Liouvillian) acting on a vectorised form of the density matrix. We also take a particular convenient basis of Majorana operators called the canonical representation to assist in these calculations.

Chapter 4 is based on the results of:

Dynamical phase error in interacting topological quantum memories [Coo+21a]
L. Coopmans, S. Dooley, I. Jubb, K. Kavanagh, and G. Kells
Phys. Rev. Research **3**, 033105 (2021)

Chapter 5 and Chapter 6 are based on the results of:

Effects of quantum pair creation and annihilation on a classical exclusion process: the transverse XY model with TASEP [Kav+22a]
K. Kavanagh, S. Dooley, J. K. Slingerland, G. Kells
New J. Phys. **24** 023024 (2022)

Topological fingerprints in pairing-induced Liouvillian gaps [Kav+22b]
K. Kavanagh, J. K. Slingerland, S. Dooley, G. Kells
In preparation (2023)

Additional work that was completed in the duration of this PhD, but does not appear in this thesis is contained in:

Entanglement entropy with Lifshitz fermions [HKV21]
D. Hartmann, K. Kavanagh, and S. Vandoren
SciPost Phys. **11**, 031 (2021)

Chapter 2

Changing Formalisms

The purpose of this chapter is to allow the reader to familiarise themselves with a few complementary modes of expressing and formulating quantum mechanical systems. Each mode is relevant primarily to one strand of this thesis. Section 2.1, "Language of Spins", is relevant to the implementation of numerical implementations throughout and in particular to those results appearing in Ch. 4 and in App. A. In the former case the model in question, a p-wave superconductor or Kitaev chain [Kit01] with and without interactions, is expressed in fermionic operators but the numerical simulations use the equivalent spin formulation. In the latter case (App. A) we show a model that is explicitly expressed in the language of spins. The fermionic formulation in Section 2.2 briefly summarises the mapping between a Hamiltonian expressed in the spin language described and explicit fermionic creation and annihilation operators that are used in Ch. 4. In Section 2.3 we describe a perspective employed to consider systems where it becomes necessary to work with linear operators acting on other operators. These operators are promoted to the role of superoperator in a framework commonly referred to as third quantization [Pro08]. Often such considerations arise when one leaves the realm of closed quantum systems to explore open quantum systems. We use this framework extensively in Ch. 5 and Ch. 6. It is useful to note that the translation between these three formulations gives entirely equivalent descriptions. We utilise them to leverage their individual strengths where appropriate, whether for numerical gain or to extract structure that is otherwise not immediately apparent.

2.1 Language of Spins

Much of the work contained in this thesis can be and has been verified by numerical simulation. These methods include exact diagonalization (for sufficiently small systems) and tensor network methods (primarily MPS and DMRG approaches, described in Ch. 3). These methods are most readily implemented where the physical

system in question can be expressed as a system of spin-$\frac{1}{2}$ particles[1]. The paradigmatic model in this setting is the Heisenberg spin chain. A Hamiltonian for a Heisenberg spin chain is

$$\hat{H} = \sum_{\alpha\in\{x,y,z\}} \sum_{j=1}^{N} J_\alpha \hat{\sigma}_j^\alpha \hat{\sigma}_{j+1}^\alpha + h_\alpha \hat{\sigma}_j^\alpha, \tag{2.1}$$

where $\hat{\sigma}_j^\alpha$, for $\alpha \in \{x, y, z\}$, are Pauli matrices situated at lattice site j. In this case the spin operators appear as nearest neighbours, J_α are the nearest neighbour coupling strengths and h_α are external magnetic fields. The Pauli matrices satisfy the (anti-)commutation relations:

$$\{\hat{\sigma}_j^\alpha, \hat{\sigma}_k^\beta\} = 2\delta_{jk}\delta^{\alpha\beta}\mathbb{1}, \tag{2.2}$$

$$[\hat{\sigma}_j^\alpha, \hat{\sigma}_k^\beta] = 2i\delta_{jk}\varepsilon^{\alpha\beta\gamma}\hat{\sigma}_k^\gamma, \tag{2.3}$$

where $\varepsilon^{\alpha\beta\gamma}$ is the completely anti-symmetric Levi-Čivita symbol and δ_{jk} is the Kronecker delta.

Throughout this thesis we investigate various special cases of this Hamiltonian. These special cases are tabulated in Table 2.1, by listing which couplings are relevant *i.e.* non-zero. The acronym "TXY" refers to the transverse XY model, obtained by setting J_z, h_x, h_y, identically to zero and keeping $J_x \neq J_y$. This particular model can be obtained by a Jordan-Wigner transformation of the Kitaev p-wave superconductor model, which is the focus of Ch. 4.

In the case of the "Open TXY" model the dissipative component of the model is also expressible in the language of spins, though for that case the dissipation does not enter as a piece of the Hamiltonian but rather it appears via operators, which model a system's coupling to an external environment, that comprise the dissipator of a master equation. This master equation is called the Lindblad equation [GKS76; Lin76] and is discussed further in Section 2.3. Nonetheless, by utilising the language of spins we are able to combine the two models on the same footing.

Often, in the work that follows we translate the model at hand to a spin formulation to leverage the numerical benefit of using tensor network methods. Although, in several instances we begin with a fermionic description and return to that description for analytic results at times. The relevant numerical methods utilised are summarised in Ch. 3.

[1] In the case of the tensor network methods used we can readily and with ease generalise the method to higher spins.

Parameters	TXY/Kitaev	Open TXY	XXZ with fields
$J_{x/y}$	$\neq 0$	$\neq 0$	$\neq 0$
J_z	$\neq 0$ & 0	0	0
$h_{x/y}$	0	0	$h_x \neq 0$, $h_y = 0$
h_z	$\neq 0$	$\neq 0$	$\neq 0$
Reference	Chapter 4	Chapter 5 & 6	Appendix A

Table 2.1: This table collects the particular cases of the generic Hamiltonian (2.1) that appear in this thesis with the common name(s) attributed to them and the place they appear in the text. The acronym TXY is used in place of the transverse XY spin model. Open refers to the presence of a dissipative process coupling to an envrionment.

2.2 Creation & Annihilation Operators

Another familiar path to describing quantum mechanical systems is their second quantized form. In this context, we describe the system by a Hamiltonian comprised of particle creation/annihilation operators. One such example would be a tight binding model of the form

$$\hat{H} = -\sum_{j=1}^{N} \left(w_j \hat{c}_j^\dagger \hat{c}_{j+1} - \Delta_j \hat{c}_j^\dagger \hat{c}_{j+1}^\dagger + h.c. \right) - \sum_{j=1}^{N} \mu_j \left(\hat{c}_j^\dagger \hat{c}_j - \frac{1}{2} \right), \tag{2.4}$$

where w_j is the particle hopping strength, Δ_j is the local pair creation/annihilation strength and μ_j is the local particle density. The term appearing as "$h.c.$" simply stands in place of the Hermitian conjugates of the previous terms. The creation and annihilation operators, $c^{(\dagger)}$, making this Hamiltonian satisfy the fermionic anti-commutation relations given by:

$$\{\hat{c}_i, \hat{c}_j^\dagger\} = \delta_{ij}, \tag{2.5}$$

$$\{\hat{c}_i, \hat{c}_j\} = \{\hat{c}_i^\dagger, \hat{c}_j^\dagger\} = 0. \tag{2.6}$$

A particularly useful feature of this Hamiltonian is that it can be readily transformed via Jordan-Wigner [JW28] back to a transverse XY spin model. This transformation is utilised in the process to obtain the numerical results presented in Ch. 4, Ch. 5 and Ch. 6. Though in the latter cases this translation serves as a starting point from which one can then employ the concepts described in the next section.

It is worth elucidating how we can translate this toy model to a special case of the aforementioned Heisenberg Hamiltonian (2.1). We will implement a Jordan-Wigner transformation by identifying the creation/annihilation operators with the products of Pauli matrices that exactly reproduce the canonical anti-commutation relations

for fermion operators, (2.5). The identification necessary is

$$\hat{c}_j^\dagger \equiv \frac{1}{2}\left(\prod_{k=1}^{j-1}\hat{\sigma}_k^z\right)(\hat{\sigma}_j^x + i\hat{\sigma}_j^y), \quad \hat{c}_j \equiv \frac{1}{2}\left(\prod_{k=1}^{j-1}\hat{\sigma}_k^z\right)(\hat{\sigma}_j^x - i\hat{\sigma}_j^y), \tag{2.7}$$

where, as before, $\hat{\sigma}_j^\alpha$ are Pauli matrices at a particular lattice site indexed by j. One can readily verify that by imposing the relations between the Pauli matrices we recover the required anti-commutation relations for the fermion operators. Thus, one can confirm that, by this definition, $\hat{c}_j^{(\dagger)}$ are indeed fermion creation/annihilation operators corresponding to spinless fermion particles. Inserting these identifications into the Hamiltonian (2.4) will yield

$$\hat{H} \to \frac{1}{2}\sum_{j=1}^{N}(w+\Delta)\hat{\sigma}_j^x\hat{\sigma}_{j+1}^x + (w-\Delta)\hat{\sigma}_j^y\hat{\sigma}_{j+1}^y + \mu\sum_{j=1}^{N}\hat{\sigma}_j^z, \tag{2.8}$$

up to a trivial term $N\mu\mathbb{1}$. Given this form of the Hamiltonian, the following identifications are apparent to realise the equivalence:

$$\mu \to 2h^z,\ w \pm \Delta \to J_{x/y}, \tag{2.9}$$

thereby recovering the spin model.

2.3 Open Systems & Third Quantization

Until this point what we have mentioned pertains to closed systems, i.e. those that are considered in isolation. However, we wish to eventually capture the physics of a system that is open to some kind of outside influence. In our context, we will be examining a system of fermions as just described which has additional dissipative processes included. Rather than a Hamiltonian operator dictating the state of the system and its evolution, an open system needs additional structure.

Third quantization for our purposes is introduced to handle operators which act on operators in a manner that allows them to be treated as we would treat operators that act on vectors. This arises when we begin to study open systems described via a Lindblad master equation in Ch. 5 and Ch. 6. There, rather than a state vector, the state of a system is described by a density matrix. Then the action of the Hamiltonian, for example, on the density matrix is essentially a operator acting on another operator. Ultimately, for numerical simulation we would prefer to deal with matrices encoded as matrix product operators (the Hamiltonian) acting on matrix product states (the density matrix). To achieve this we need to use the conceptual core of third quantization which is the Choi-Jamiołkowski isomorphism [Jam72; Cho75]. The remainder of this chapter summarises our use of this isomorphism.

2.3.1 Operators are to Superoperators as States are to Operators

To begin we clarify some of the terminology that has been used up to this point when we have referred to states and operators of a quantum system. We then introduce a less common concept of the superoperator. Firstly, states of finite-dimensional quantum systems are represented as elements of a complex Hilbert space, $|\Psi\rangle \in \mathbb{C}^d$. Given an orthonormal basis $\{|i\rangle\}_{i=1}^d$ for the Hilbert space, a state can be written as

$$|\Psi\rangle = \sum_{i=i}^{d} \psi_i |i\rangle = \begin{pmatrix} \psi_1 \\ \vdots \\ \psi_d \end{pmatrix} \in \mathbb{C}^d, \tag{2.10}$$

where $\psi_i = \langle i|\psi\rangle$ are the complex amplitudes.

Next, operators are linear maps, usually written explicitly in their matrix representation, that take states to states[2],

$$\hat{A} : \mathbb{C}^d \to \mathbb{C}^d, \qquad \hat{A}|\psi\rangle = |\psi'\rangle\,. \tag{2.11}$$

Given a basis $\{|i\rangle\}$, a linear operator can also be written as

$$\hat{A} = \sum_{i,j=1}^{d} a_{ij} |i\rangle \otimes \langle j| = \begin{pmatrix} a_{11} & \dots & a_{1d} \\ \vdots & & \vdots \\ a_{d1} & \dots & a_{dd} \end{pmatrix} \in \mathbb{C}^{d\times d}. \tag{2.12}$$

The set of linear operators form a d^2-dimensional complex Hilbert space where we use the Hilbert-Schmidt inner product between operators as given by $\langle \hat{A}, \hat{B}\rangle = \mathrm{Tr}\left(\hat{A}^\dagger \hat{B}\right)$. In this finite dimensional space this is identical to the Frobenius inner product on two matrices.

The *Choi-Jamiołkowski isomorphism* [Jam72; Cho75] is a way of vectorizing the matrix that represents an operator $\hat{A}$. Given a basis $\{|i\rangle\}$, the isomorphism is the mapping

$$|i\rangle \otimes \langle j| \xrightarrow{\text{iso}} |i\rangle \otimes |j\rangle = |\, ij\rangle\!\rangle, \tag{2.13}$$

where we use the "double ket", $|\,\cdot\rangle\!\rangle$ notation to denote an object after the mapping. Applied to the operator $\hat{A}$, the isomorphism effectively flattens the $d \times d$ matrix into

[2]The hat over a symbol indicates that it is a linear operator.

a vector of length d^2, which we denote as $|\hat{A}\rangle\!\rangle$,

$$\hat{A} \xrightarrow{\text{Choi}} |\hat{A}\rangle\!\rangle = \sum_{i,j=1}^{d} a_{ij} |i\rangle \otimes |j\rangle = \begin{pmatrix} a_{11} \\ \vdots \\ a_{1d} \\ \vdots \\ a_{d1} \\ \vdots \\ a_{dd} \end{pmatrix} \in \mathbb{C}^{d^2}. \tag{2.14}$$

Note that, after the Choi isomorphism, the inner product on the operator space becomes the usual vector inner product in $\mathbb{C}^{d^2}$

$$\langle \hat{A}, \hat{B} \rangle = \mathrm{Tr}\left(\hat{A}^\dagger \hat{B}\right) \xrightarrow{\text{Choi}} \langle\!\langle \hat{A} | \hat{B} \rangle\!\rangle. \tag{2.15}$$

Note that the vectorization satisfies further useful identities such as

$$|\hat{A}\hat{B}\hat{C}\rangle\!\rangle = (\hat{C}^T \otimes \hat{A}) |\hat{B}\rangle\!\rangle, \tag{2.16}$$

see [Šaf18] for further detail.

Superoperators are linear maps $\hat{\hat{\mathcal{O}}}$ that take operators to operators[3]. If the operators are vectorized then the superoperator is represented by a $d^2 \times d^2$ complex matrix:

$$\hat{\hat{\mathcal{O}}} : \mathbb{C}^{d^2} \to \mathbb{C}^{d^2}, \qquad \hat{\hat{\mathcal{O}}} |\hat{A}\rangle\!\rangle = |\hat{A}'\rangle\!\rangle, \tag{2.17}$$

or, more explicitly, given a vectorized orthonormal basis $\{|n\rangle\!\rangle\}_{n=1}^{d^2}$ for the operator space:

$$\hat{\hat{\mathcal{O}}} = \sum_{m,n=1}^{d^2} o_{n,m} |n\rangle\!\rangle \otimes \langle\!\langle m| = \begin{pmatrix} o_{1,1} & \dots & o_{1,d^2} \\ \vdots & & \vdots \\ o_{d^2,1} & \dots & o_{d^2,d^2} \end{pmatrix} \in \mathbb{C}^{d^2 \times d^2}. \tag{2.18}$$

2.3.2 Closed system dynamics

A closed quantum system in a pure quantum state evolves by the Schrödinger equation [Sch26]

$$\frac{d}{dt} |\Psi\rangle = -\frac{i}{\hbar} \hat{H} |\Psi\rangle, \tag{2.19}$$

where $\hat{H}$ is the Hamiltonian. For a finite dimensional system, we interpret the right hand side as a matrix multiplication applied to the state vector. However, a closed quantum system in a mixed state evolves via the (Liouville-)von Neumann

[3]The double hat above a symbol indicates that it is a superoperator, in other words a linear operator on operators.

equation [BP02]

$$\frac{d}{dt}\hat{\rho} = -\frac{i}{\hbar}[\hat{H}, \hat{\rho}], \tag{2.20}$$

where the state of the system is encoded by the density matrix $\hat{\rho}$. The commutator on the right hand side is a combination of matrix multiplication applied to $\hat{\rho}$ from the left and from the right.

Yet, since the commutator is a linear function of the density operator $\hat{\rho}$ it is possible to represent the equation of motion as a single matrix multiplication from the left which acts upon the vectorized density vector, $|\hat{\rho}\rangle\!\rangle$, such that

$$\frac{d}{dt}|\hat{\rho}\rangle\!\rangle = -\frac{i}{\hbar}\hat{\hat{\mathcal{H}}}|\hat{\rho}\rangle\!\rangle. \tag{2.21}$$

Notice the similarity to the pure state evolution here, suggesting that if we can obtain this form we can use all of the tools available to us to analyse closed systems. How then do we convert the Liouville-von Neumann equation (2.20)? We start by choosing an orthonormal basis $\{|i\rangle\}_{i=1}^{d}$ for the state space. Once this is in place, we can work out an expression for the superoperator $\hat{\hat{\mathcal{H}}}$ in terms of the Hamiltonian $\hat{H}$. Start by writing $\hat{\rho}$ and $\hat{H}$ in that basis as:

$$\hat{\rho} = \sum_{i,j=1}^{d} \rho_{ij} |i\rangle \otimes \langle j| , \qquad \hat{H} = \sum_{k,l=1}^{d} H_{kl} |k\rangle \otimes \langle l| . \tag{2.22}$$

Then, substituting into the right hand side of Eq. 2.20 we obtain

$$\begin{aligned} -\frac{i}{\hbar}[\hat{H}, \hat{\rho}] &= -\frac{i}{\hbar}\sum_{i,j,k} H_{ki}\rho_{ij} |k\rangle \otimes \langle j| + \frac{i}{\hbar}\sum_{i,j,l} H_{jl}\rho_{ij} |i\rangle \otimes \langle l| \\ &\xrightarrow{\text{Choi}} -\frac{i}{\hbar}\sum_{i,j,k} H_{ki}\rho_{ij} |k\rangle \otimes |j\rangle + \frac{i}{\hbar}\sum_{i,j,l} H_{jl}\rho_{ij} |i\rangle \otimes |l\rangle \\ &= -\frac{i}{\hbar}\left(\hat{H} \otimes \hat{\mathbb{1}} - \hat{\mathbb{1}} \otimes \hat{H}^T\right)|\hat{\rho}\rangle\!\rangle. \end{aligned} \tag{2.23}$$

The equality in the last line is most easily verified by working backwards from the last line to the previous line. For example,

$$\begin{aligned} \left[\hat{H} \otimes \hat{\mathbb{1}}\right]|\hat{\rho}\rangle\!\rangle &= \left[\left(\sum_{k,l=1}^{d} H_{kl} |k\rangle \langle l|\right) \otimes \left(\sum_{j=1}^{d} |j\rangle \langle j|\right)\right]\left(\sum_{i,j=1}^{d} \rho_{ij} |i\rangle \otimes |j\rangle\right), \\ &= \sum_{i,j,k} H_{ki}\rho_{ij} |k\rangle \otimes |j\rangle , \end{aligned} \tag{2.24}$$

and similarly for $\left[\hat{\mathbb{1}} \otimes \hat{H}^T\right]|\hat{\rho}\rangle\!\rangle$. Thus, the superoperator is represented by the Hermitian matrix

$$\hat{\hat{\mathcal{H}}} = \hat{H} \otimes \hat{\mathbb{1}} - \hat{\mathbb{1}} \otimes \hat{H}^T. \tag{2.25}$$

2.3.3 Open system dynamics

So far, we have brought pure and mixed quantum state time evolution into a superoperator form. However, in both cases we have only considered evolution of a closed system. Once we wish to introduce any type of dissipation or environmental interaction the situation necessitates a different evolution equation. The result is an evolution equation that is in fact the most general way of mapping density matrices to density matrices [BP02]. In particular, will be using the master equation in Lindblad form (for detail on obtaining this see, e.g., Ref. [Sch07])

$$\frac{d}{dt}\hat{\rho} = -\frac{i}{\hbar}[\hat{H},\hat{\rho}] + \sum_{\mu}\left(2\hat{L}_{\mu}\hat{\rho}\hat{L}_{\mu}^{\dagger} - \hat{L}_{\mu}^{\dagger}\hat{L}_{\mu}\hat{\rho} - \hat{\rho}\hat{L}_{\mu}^{\dagger}\hat{L}_{\mu}\right), \tag{2.26}$$

where the operators $\hat{L}_{\mu}$ are called Lindblad operators. Again, since the right hand side is linear in the density operator $\hat{\rho}$, it must be possible to write the master equation as

$$\frac{d}{dt}|\hat{\rho}\rangle\!\rangle = \left(\frac{-i}{\hbar}\hat{\hat{\mathcal{H}}} + \hat{\hat{\mathcal{L}}}\right)|\hat{\rho}\rangle\!\rangle, \tag{2.27}$$

where, in the previous section we have already worked out the superoperator $\hat{\hat{\mathcal{H}}}$ for the Hamiltonian part. What is the Lindblad part $\hat{\hat{\mathcal{L}}}$ in terms of the Lindblad operators? Writing $L_{\mu} = \sum_{k,l=1}^{d} l_{kl}^{(\mu)} |k\rangle \otimes \langle l|$ and their combination appearing in the sum of Eq. 2.26 as $\hat{\hat{\mathcal{L}}}_{\mu}$ we find

$$\begin{aligned}
\hat{\hat{\mathcal{L}}}_{\mu} &= \sum_{ijkl}\left(2l_{ki}^{(\mu)}l_{lj}^{(\mu)*}\rho_{ij}\,|k\rangle\otimes\langle l| - l_{ki}^{(\mu)}l_{kl}^{(\mu)*}\rho_{ij}\,|l\rangle\otimes\langle j| - l_{kl}^{(\mu)}l_{kj}^{(\mu)*}\rho_{ij}\,|i\rangle\otimes\langle l|\right) \\
&\xrightarrow{\text{Choi}} \sum_{ijkl}\left(2l_{ki}^{(\mu)}l_{lj}^{(\mu)*}\rho_{ij}\,|k\rangle\otimes|l\rangle - l_{ki}^{(\mu)}l_{kl}^{(\mu)*}\rho_{ij}\,|l\rangle\otimes|j\rangle - l_{kl}^{(\mu)}l_{kj}^{(\mu)*}\rho_{ij}\,|i\rangle\otimes|l\rangle\right) \\
&= \left(2\hat{L}_{\mu}\otimes\hat{L}_{\mu}^{*} - \hat{L}_{\mu}^{\dagger}\hat{L}_{\mu}\otimes\hat{\mathbb{1}} - \hat{\mathbb{1}}\otimes\hat{L}_{\mu}^{T}\hat{L}_{\mu}^{*}\right)|\hat{\rho}\rangle\!\rangle.
\end{aligned} \tag{2.28}$$

Again, the equality in the last line is most easily proved by working backwards from the last line to the previous line and taking care of the bookkeeping of indices. For example,

$$\begin{aligned}
\left[\hat{L}_{\mu}\otimes\hat{L}_{\mu}^{*}\right]|\hat{\rho}\rangle\!\rangle &= \left[\left(\sum_{k,k'=1}^{d} l_{kk'}^{(\mu)}\,|k\rangle\langle k'|\right)\otimes\left(\sum_{l,l'=1}^{d} l_{ll'}^{(\mu)*}\,|l\rangle\langle l'|\right)\right]\left(\sum_{i,j=1}^{d}\rho_{ij}\,|i\rangle\otimes|j\rangle\right) \\
&= \sum_{i,j,k,l} l_{ki}^{(\mu)}l_{lj}^{(\mu)*}\rho_{ij}\,|k\rangle\otimes|l\rangle\,,
\end{aligned} \tag{2.29}$$

and similarly for $\left[\hat{L}_{\mu}^{\dagger}\hat{L}_{\mu}\otimes\hat{\mathbb{1}}\right]|\hat{\rho}\rangle\!\rangle$ and $\left[\hat{\mathbb{1}}\otimes\hat{L}_{\mu}^{T}\hat{L}_{\mu}^{*}\right]|\hat{\rho}\rangle\!\rangle$. So we see that the Lindblad superoperator is the matrix

$$\hat{\hat{\mathcal{L}}} = \sum_{\mu}\left(2\hat{L}_{\mu}\otimes\hat{L}_{\mu}^{*} - \hat{L}_{\mu}^{\dagger}\hat{L}_{\mu}\otimes\hat{\mathbb{1}} - \hat{\mathbb{1}}\otimes\hat{L}_{\mu}^{T}\hat{L}_{\mu}^{*}\right). \tag{2.30}$$

Adding this resultant matrix to that obtained from the commutator superoperator yields the complete Liouvillian superoperator. Critically, we can often treat this in a similar manner to a closed system Hamiltonian. However, a price must be paid as generically this Liouvillian in matrix form will correspond to a non-Hermitian matrix. Moreover, it is a much larger object of size $4^N \times 4^N$ rather than $2^N \times 2^N$ in the case of a closed system Hamiltonian defined on the same number of sites. Nonetheless, for numerical simulation we can encode the Liouvillian superoperator as a matrix product operator (MPO) so that we are able to leverage the methods (e.g. DMRG) that employ MPO. These tensor network concepts are summarised next in Ch. 3.

Chapter 3

Tensor Network Basics

In this chapter we describe some key ideas behind the topic of tensor networks. We begin with the notation and diagrams used to represent such networks. Afterwards we give an overview on matrix product states (MPS) and the density matrix renormalisation group (DMRG) which underpin the majority of the numerical methods that will appear in later chapters.

Usually one traces the beginning of tensor network methods back to the work White [Whi92] where the DMRG method was first described. However, the core concept of an MPS is older and can be seen in the prior work of Derrida [DDM92] (or [Nis] for a comprehensive history). Both origins are of great relevance to this thesis as the DMRG concept and the numerical methods that arose in the intervening years are present throughout. Moreover, not only the tensor network ideas but also one of the models that presented matrix products ansätze (namely TASEP) appears in Ch. 5 and Ch. 6.

We focus on the methods most relevant to our studies which are those produced for 1-dimensional systems. A great deal of work has been produced in the intervening years since the work of White et. al. for various applications [Vid04; Vid08; Has07; VMC08; Vid09; Eve11; EV11; Swi12a; Swi12b; Orú14; EV14; EV15; Bao+15; Wen+16; Cze+16; FV17; Eve17; Pae+19]. However, the fundamental motivation throughout these works is to overcome the difficulty in simulating many-body systems. Specifically, to circumvent the exponential scaling of many-body quantum systems. In this setting, the number of states in the Hilbert space for a system of N particles with 2 internal degrees of freedom, N spins for example, the total Hilbert space contains 2^N states. Quickly this becomes much too large a number to simulate on a typical computer and if one wishes to perform time evolution or examine systems with more internal degrees of freedom a computational bottleneck rapidly approaches. Tensor networks can, in many cases, alleviate such a bottleneck.

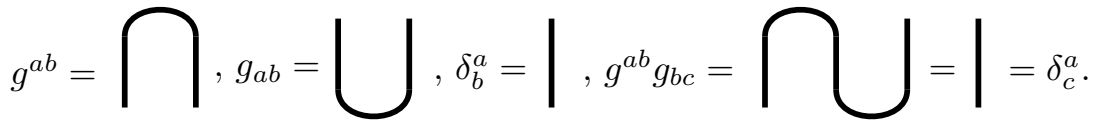

Figure 3.1: A simple graphical calculus diagram showing basic relations between indices and contractions for some metric.

3.1 Diagrams & Notation

Before describing a particular tensor network it is first useful to understand the notation and nomenclature used. The diagrammatic forms of tensor networks are represented using the graphical tensor notation of Penrose [**penrose07**]. This diagrammatic notation is useful when the mathematical expressions used in physics become cumbersome. At first this may seem to be a further abstraction but we will see that for large expressions, which need extensive book-keeping of indices, the diagrams can help conceptualise the manipulations made on the underlying objects.

Starting with a simple example we can look at some common objects that appear in physics. Consider, for example, a metric tensor, g_{ab}. This is far from unwieldy to work with but nonetheless we can replace it by a very simple diagram. We keep track of the indices of the tensor by lines (or legs) that are attached to the body of the tensor diagram. There is no universal consensus on how to draw the body of a tensor so we can choose some shape or line to represent the tensor itself with some labelling if necessary. Upper and lower indices appear as "legs" and "arms" emanating from the tensor in this thesis and in a large portion of the literature. The total number of these uncontracted, or free, limbs is called the "rank" of the tensor network. Consider now the contraction of two metric tensors which produce a Kronecker delta

$$\sum_b g^{ab} g_{bc} = \delta^a_c. \tag{3.1}$$

Using Penrose's graphical tensor notation, we can dispense with the summation (as with Einstein summation convention) and replace the metrics with the lines shown in Fig. 3.1. Additionally since there are no loops the combination of the metrics in graphical notation is explicitly equivalent to a vertical line which is used to denote a Kronecker delta. The joining and deformation of lines in graphical notation becomes analogous to contracting indices (or multiplying tensors) and forming equalities between expressions with multiple such contractions and their simplifications.

While this may not yet seem worthwhile the real benefit is seen from more complicated products of tensors with several repeated indices. For example, say we have a rank (1,1) tensor (matrix) which we wish to contract with a vector. Usually we may write this as, say, $\Gamma^\alpha_\beta v_\alpha$, whereas the graphical form can be drawn as Fig. 3.2. Usually of course we discard a great deal of the labelling seen in the figure.

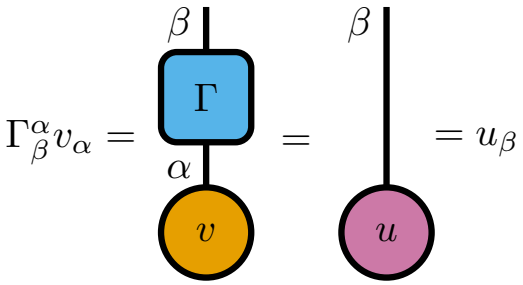

Figure 3.2: (Left-to-right) A matrix-vector multiplication with explicit indices and the graphical form with corresponding indices displayed, usually left implicit in the diagram. The resultant vector in graphical and standard notation.

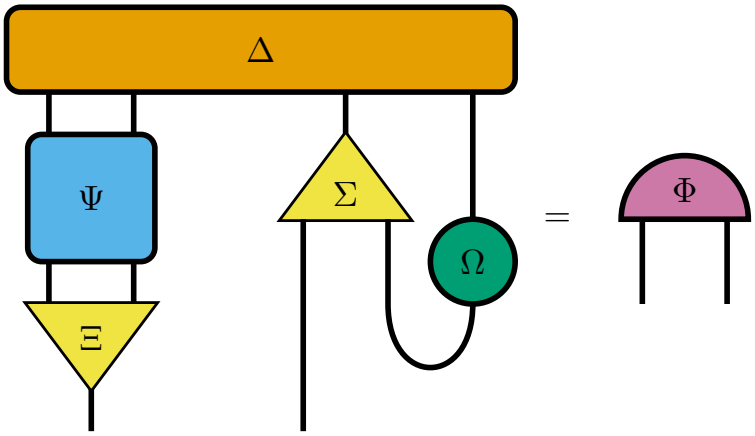

Figure 3.3: An example of contracting an arbitrary set of tensors. In graphical notation it is clear at a glance that the result should have two remaining upper indices in standard notation, corresponding to the two free legs of the diagram.

We can dream up more complicated products and find their graphical representation quite readily and vice-versa. Take for instance,

$$\Delta^{\alpha\beta\gamma\rho}\Psi^{ab}_{\alpha\beta}\Sigma^{cd}_{\gamma}\Xi^{e}_{ab}\Omega_{d\rho} = \Phi^{ce}, \tag{3.2}$$

shown diagrammatically in Fig. 3.3.

Simplifying the LHS of this expression is already not obvious at a glance with only five tensors. If we have 10 or 20 tensors it will become unwieldy to manage the indices as we will see shortly for matrix product state. So instead this expression can be drawn as shown in Fig. 3.3. After contracting the repeated indices we can see immediately from the figure that in the end we have a rank (2,0) tensor without need for examining all of the indices to verify which are summed or not summed.

3.2 Matrix Product States

The most ubiquitous tensor network is the matrix product state (MPS). The motivation in constructing such an object comes from the problem of simulating many-body quantum systems alluded to earlier. Consider how one canonically defines a generic

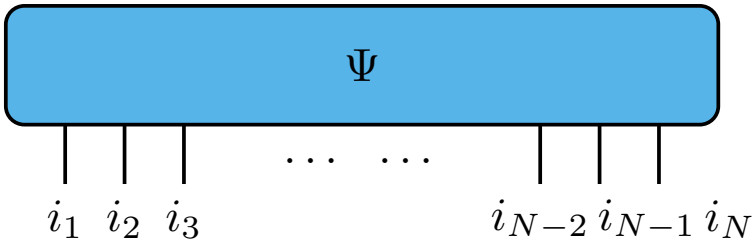

Figure 3.4: The tensor schematic for a state $\Psi^{i_1 \ldots i_N}$ before being split into an MPS.

quantum state. In particular, suppose we want to determine some properties of an N-site spin chain. If we are only concerned for the moment with the spin then we can write the state as

$$|\Psi\rangle = \sum_{i_1 \ldots i_N} \psi^{i_1 \ldots i_N} |i_1 \ldots i_N\rangle \,, \tag{3.3}$$

where the summation variables run over all the possible spin configurations. Figure 3.4 gives the relevant part of this description in diagrammatic form. Once the basis is known, e.g. spin-$\frac{1}{2}$ ($\{|\uparrow\rangle, |\downarrow\rangle\}$) or equivalently the computational basis ($\{|0\rangle, |1\rangle\}$), the actual information of the state is contained in the N-index tensor $\psi^{i_1 \ldots i_N}$.

However, even if there are only two spin states then the number of variables in the ψ-tensor is 2^N. So for even quite small systems, say a one dimensional wire with $N = 50$, we can have 10^{15} variables to worry about. Quickly then numerical simulation becomes intractable. Circumventing this exponential scaling is one of the benefits of utilising an MPS representation. From what we know so far we can have a zoo of tensor networks which may contract into an $(N, 0)$ rank tensor[1]. While we note that a matrix product is not a unique representation [Per+07] for a one dimensional quantum state it is nonetheless useful for most of the systems we examine in this thesis.

Given a quantum state with the generic representation given above an MPS of this state is the tensor network decomposition of the single $(N, 0)$ rank ψ-tensor into N rank 3 tensors. Depending on the system boundary conditions the end tensors may be of lower rank. Taking the generic state described, we would like to do is to decompose the $\psi^{i_1 \ldots i_N}$ tensor into a network of N simpler objects. Figure 3.5 shows the graphical form of the MPS representation of $|\Psi\rangle$ for the case of $N = 8$ with closed boundary conditions.

Notice that in the same way that the ψ tensor has N free legs so too does the MPS state, where each free leg corresponds to a state vector index for the relevant

[1]To connect with the TN diagrams, the rank of a tensor enumerates the number of "legs"/"arms" that a tensor has in its diagram and the number of free limbs in a tensor network is the rank of that network corresponding to the number of free, uncontracted indices in the total expression.

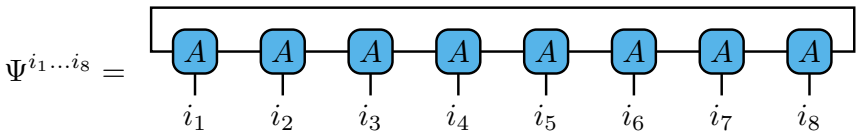

Figure 3.5: The tensor schematic for a state $\Psi^{i_1 \ldots i_8}$ after being split into an MPS. In this case for only 8 sites.

lattice site. In all detail, the mathematical expression for this MPS is

$$|\Psi\rangle = \sum_{\alpha_0 \ldots \alpha_{N+1}=1}^{D} \sum_{i_1 \ldots i_N=1}^{d} A_{\alpha_1}^{i_1 \alpha_0} A_{\alpha_2}^{i_2 \alpha_1} \ldots A_{\alpha_N}^{i_{N-1} \alpha_{N-1}} A_{\alpha_0}^{i_N \alpha_N} |i_1 i_2 \ldots i_N\rangle \,, \tag{3.4}$$

usually the summation will be left implicit. Given the number of tensors and indices required to fully express a matrix product in this manner, the diagrammatic expressions for tensor network objects are generally preferred. We note that while we have labelled the constituent tensors here (Eq. 3.4) with A implying that they are all the same this is not generically the case. This may indeed be the case for translationally invariant systems but at least, for example, MPS with open boundary conditions break this as the end tensors must be of different rank to those in the bulk of the state [McC07; Sch11]. We can see this if we break the summation over α_0, as this would leave an additional free index for the first and last A tensors. This in principle would make these distinct tensors to this in the remainder of the state. Moreover, a non-homogeneous state would automatically require a collection of distinct constituent tensors to construct its MPS representation.

Ignoring the free indices (i_k) the remaining indices are contracted in the same way as a matrix product, hence the name. These contracted indices are known as *bonds* and while the physical indices, i_k, run over the on-site degrees of freedom, the bond indices, α_k, do not. The number of variables these bonds run over is known as the *bond dimension*. Considering $A_{\alpha_{k+1}}^{0\,\alpha_k}$ for example, these $\{\alpha_k, \alpha_{k+1}\}$ correspond to the dimensions of the A^0 matrix. We denote the bond dimension using D. We can achieve an exact representation for any such quantum state if we do not impose a restriction on the size of D [Per+07; Orú14]. Indeed, any state expressible as (3.3) is captured by such a MPS representation if D is unrestricted.

The computational gain in using this representation is to restrict the bond dimension and thus discard unnecessary information. This is done by focusing on a class of states for which the bond dimension is effectively "small" [2]. In fact it was discovered that ground states and states at low-energy or of low entanglement fall into a such a class of states with "small" bond dimension. How then does one know what the bond dimension should or can be? We can get an understanding from the

[2]The meaning of small here is not precise, it effectively means that the bond dimension will not scale exponentially in number of sites or can be restricted to allow for efficient yet accurate simulations.

construction of an MPS from a generic state. An iterated singular value decomposition process is performed on an $(N, 0)$ rank tensor N times, leaving one with an MPS.

The usual prescription begins by performing a singular value decomposition between the first index of the large tensor and the remaining $N-1$ indices. This process is iterated until we are left with N constituent tensors corresponding to each physical index/site (i_k). The matrices which we obtain by this method will be of dimension $D \times D$ and unitary.

To be explicit, suppose we would like to split an N-site system into two pieces. So the full Hilbert space, $\mathcal{H}$, of the system is split into two subspaces, $\mathcal{H}_A \otimes \mathcal{H}_B$. The dimension of these subspaces is then d^m and d^{N-m} respectively where d is the physical dimension. If we propose that the Hilbert spaces have orthonormal bases $|i\rangle, |j\rangle$ respectively then a state of the system may be expressed as

$$|\Psi\rangle = \sum_{i,j} \Psi^{ij} |i\rangle |j\rangle . \tag{3.5}$$

The singular value decomposition of the matrix Ψ is given by

$$\Psi = UsV^\dagger, \tag{3.6}$$

where U and V are unitary matrices of dimensions $m \times m$ and $(N-m) \times (N-m)$ respectively. The matrix s then is a diagonal matrix of dimension $m \times (N-m)$. All the entries of s are non-negative real numbers, where $s_{11} \geq s_{22} \geq \cdots \geq s_{mm}$. They are the singular values of Ψ. Replacing Ψ in the original expression we have

$$|\Psi\rangle = \sum_{i,j} \sum_{k} U_{ik} s_{kk} V^*_{kj} |i\rangle |j\rangle = \sum_{k} s_{kk} |a_k\rangle |b_k\rangle , \tag{3.7}$$

where $|a_k\rangle$ and $|b_k\rangle$ are the transformed bases according to

$$|a_k\rangle = \sum_{i}^{m} U_{ik} |i\rangle , \ |b_k\rangle = \sum_{j}^{N-m} V^*_{kj} |j\rangle . \tag{3.8}$$

The second form in the transformed bases is known as the Schmidt decomposition. Pictorially, we can see the procedure in Fig. 3.6 for the case of $N = 4$. One should understand here which legs correspond to which indices. The i index corresponds to the left most leg in the diagram. The j index corresponds to the remaining 3 legs which in the procedure are grouped together as one index j running over the concatenated set of i_2, i_3, i_4. The k index corresponds to the bond between U, s and $V^\dagger$.

To understand, consider the Schmidt decomposition as a superposition of many states in which each term is comprised of a product of a basis state of A and a basis state of B weighted by a value s_{kk}. From the distribution of the values of s_{kk} we

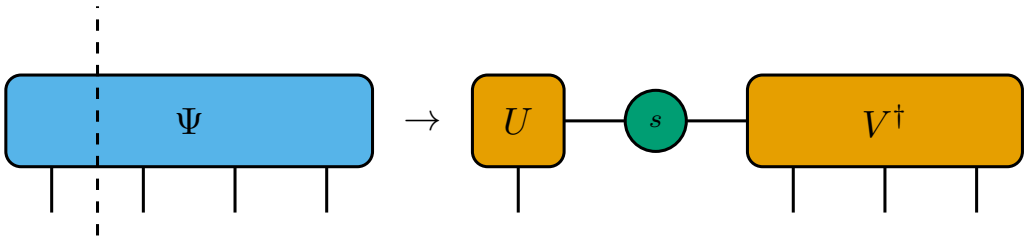

Figure 3.6: Schematic representation of the first step in the single value decomposition (SVD) procedure to obtain an MPS from a state tensor.

can gain some insight into the amount of entanglement between the two systems [3]. Suppose that there is one singular value $s_{11} = 1$, evidently this will correspond to a product state $|a_1\rangle |b_1\rangle$. On the other hand if all the singular values are equal, $s_{kk} = 1/\sqrt{m}\ \forall\ k$, then we have a maximally mixed state, an equal superposition of all basis states.

It is known that for the class of states we are interested in, low energy and low entanglement states, the size of these singular values typically decays rapidly for a value of k much less than m [Per+07]. In fact for large matrices many of the singular values will in fact be zero, particularly for the types of states which are of interest to us. This leads one to conclude that a great deal of these singular values can be discarded. If the singular values are identically zero or vanishingly small after a certain k then most or all of the pertinent information about the state will be retained. As such we restrict the sum to run up to D with the intention of removing the zero or vanishingly small singular values

$$|\Psi\rangle \to |\tilde{\Psi}\rangle = \sum_{k=1}^{D \ll m} s_{kk} |a_k\rangle |b_k\rangle . \tag{3.9}$$

In the case of MPS the number of values which are kept is the bond dimension. So in fact the number of variables is reduced from d^N to $poly(D, N)$. It must be stressed that this D is chosen to be small enough to provide an efficient encoding of the state but not so small as to render it an inaccurate representation. For an exact faithful representation the bond dimension would be exponential in N. This decomposition is a central component of the DMRG method. In essence what is happening when the bond dimension is restricted is that we are restricting ourselves to a subspace of the Hilbert space which contains the states that are of interest to us, namely ground states of local gapped Hamiltonians. In comparison to the full Hilbert space of such a Hamiltonian, the subspace containing these states will in fact require a bond dimension which is not exponential in N but rather may be constant or at least some well controlled polynomial in N. The appropriate value

[3] The entanglement we refer to here and throughout is the von Neumann entropy as defined by $\mathcal{S}_A \equiv -\mathrm{Tr}(\rho_A \log(\rho_A))$, where ρ_A is the reduced density matrix on a subsystem A. Equivalently this entropy can be defined directly from the singular values as $\mathcal{S}_A \equiv -\sum_k (|s|^2_{kk} \log(|s|^2_{kk}))$.

then of the bond dimension will depend on the states which we aim to represent and the accuracy required to faithfully represent them. By construction an MPS state supports local correlations, that is correlations which decay exponentially, and lead to saturated entropy bounds at large scales. This is due to the nature of the MPS being comprised of nearest neighbour interactions, which can be seen from the structure of the network.

Another point of interest is that this prescription of splitting a state tensor with multiple indices into several tensors each located at an individual site is also applied to operators. These are matrix product operators. This is another key ingredient in the DMRG method. In that context a local Hamiltonian may be decomposed as a sum of nearest neighbour terms. Its action then on the state is equivalent to a contraction of the MPS with the MPO. We will describe this further next as we discuss a few of the aspect of the DMRG method.

3.3 Density Matrix Renormalisation Group

In this thesis the most widely used instance of a tensor network method is the density matrix renormalisation group approach to access a system's ground state and time-evolution methods built upon the DMRG paradigm.

As already stated the basic concept of an MPS being used to represent a quantum state is precisely that, a representation. However, the numerical efficacy of the representation hinges upon the approximation made within the procedure via SVD to decompose a quantum state into a product of relatively smaller component objects. An exact representation of a state is predicated on having an unrestricted bond dimension, D. However, by the argument of the previous section the SVD procedure captures the vast majority of the salient features of relevant low-energy states. This procedure in its original implementation by White [Whi92], now known under the name density matrix renormalisation group (DMRG), restricts the bond dimension via a bound on entanglement. The bound $D' \leq D$ restricts the number of singular values kept in the SVD, which as mentioned a large proportion of which are zero for the types of states that are relevant i.e. ground-states, low-energy and low-entanglement states. For these classes of states an MPS is a highly efficient representation. We can quantify the accuracy of this representation by the truncation error

$$|| \, |\Psi\rangle - |\Psi'\rangle \, || = 2 \sum_{i=1}^{N} (\epsilon_i(D) - \epsilon_i(D')), \tag{3.10}$$

where $\epsilon_i(s)$ is the sum of the s largest singular values from the SVD at site i. This can be seen as a downside indeed that there is a "baked in" error in the representation of states. Nonetheless, one can view this as a quantifier of accuracy to be controlled in numerical simulations. It should be stressed that for certain states, indeed the

vast majority relevant to this thesis, that this truncation error will be kept at a very low value. Equally, one should remain cognisant of the fact that in time-evolution methods that entanglement grows and bond dimensions of time-evolved states should reflect this in order to capture accurately the dynamics of a system. Some further instances where the bond dimension must necessarily grow are, as mentioned, highly entangled states and states near phase transitions.

Staying away from these problematic classes of states we can gain a great deal from codifying states and Hamiltonians as MPS and matrix product operators (MPO) respectively. Once a Hamiltonian is constructed as an MPO, which is readily and efficiently done when the component operators are typical "local" operators, the ground-state can be found by the DMRG method efficiently for far larger system sizes than are accessible by typical exact diagonalisation (ED) approaches. For example, at various points in this thesis we leverage MPS methods to access systems of sizes around 100 sites or more for systems wherein ED methods would breakdown at the scale of 12-15 sites. The variational method to determine the ground-state from a given Hamiltonian MPO is given is great detail in [Sch11]. The core idea is a repeated application of tensor contraction of the MPO with an initial state, which may be a random MPS of fixed bond dimension, which is then subsequently returned to the form of an MPS. At each step the updates on the MPS are determined by the choices which minimize the energy driving the algorithm towards the ground-state. The algorithm itself is explained in great detail in [Sch05; Sch11]. A schematic of the basic conceptual procedure appears in Fig. 3.7. Further detail on DMRG and other tensor network methods (e.g. PEPS, MERA) appears in [BC17].

As alluded to previously, time evolution can become complicated due to entanglement growth. As such the truncated bond dimension must necessarily grow with respect to time to maintain a fixed truncation error which in turn increases computational costs. Nonetheless these errors and costs can be controlled and ultimately the procedure remains conceptually simple. Say one has already obtained the ground-state $|\psi_0\rangle$ in MPS form:

- Next, the MPO representing the exponentiation of the Hamiltonian is applied to $|\psi_0\rangle$ and contracted. This constitutes a single time step, dt, such that $|\psi_0(0)\rangle \rightarrow |\psi_0(dt)\rangle$.

- After contraction another SVD is performed on $|\psi_0(dt)\rangle$. This is where the bond dimension can be adjusted "on-the-fly".

- Reiterate the prior steps.

Indeed, a lot of technical details are skimmed over in this short description but these are the basic steps. This method is reliant on the Trotterization of the

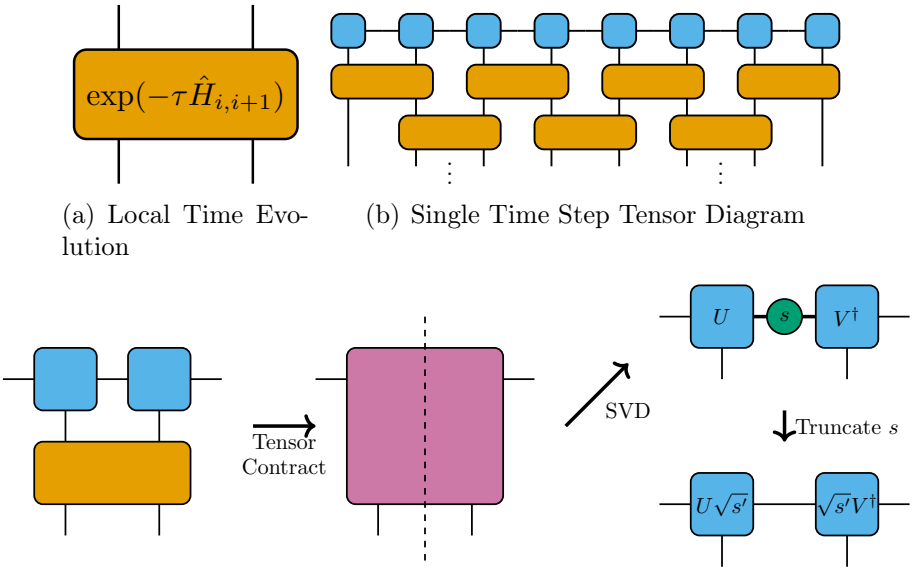

(a) Local Time Evolution

(b) Single Time Step Tensor Diagram

(c) Tensor Contraction and Truncation

Figure 3.7: Tensor diagram of the MPS time evolution procedure. (a) The exponentiated local time evolution operator as an MPO. (b) A single time step dt for an 8-site MPS. (c) The combined contraction and truncation step for each of the operators appearing in (b).

imaginary-time evolution operator by which we mean

$$e^{-\tau \hat{H}} \approx \prod_{i=1}^{N/2} e^{-\tau \hat{h}_i} \prod_{i=1}^{N/2} e^{-\tau \hat{h}_{i+1}} + \mathcal{O}(\tau^2). \tag{3.11}$$

We provide a tensor diagram schematic of this process in Fig. 3.7. Given the local Hamiltonian term, $\hat{H}_{i,i+1}$, (Fig. 3.7(a)) contract these terms across the full initial state, see Fig. 3.7(b). The individual contractions and bond dimension truncation step is contained in Fig. 3.7(c). To achieve the full update procedure in a single shot, one must convert the entire Trotterized time evolution into a single-layer MPO as can be demonstrated schematically in Fig. 3.8.

3.3.1 Creating MPS & MPO for Simulation

As a final note we will describe how to set up an initial state as an MPS or a Hamiltonian as an MPO for numerical simulation. In principle as described one can generate the MPO associated with a Hamiltonian by creating the full matrix representation of the total operator and use successive SVD transformations to obtain the MPO representation at a desired accuracy determined by the number of singular values retained. This is often presented as the approach to take but only in principle. In practice, we can directly translate a local Hamiltonian to its MPO formulation without any intermediate manipulations.

The apparent obstacle is to take a sum of (k-local) operators to a product of on-site operators. For example to take the generic Heisenberg Hamiltonian (Eq. 2.1)

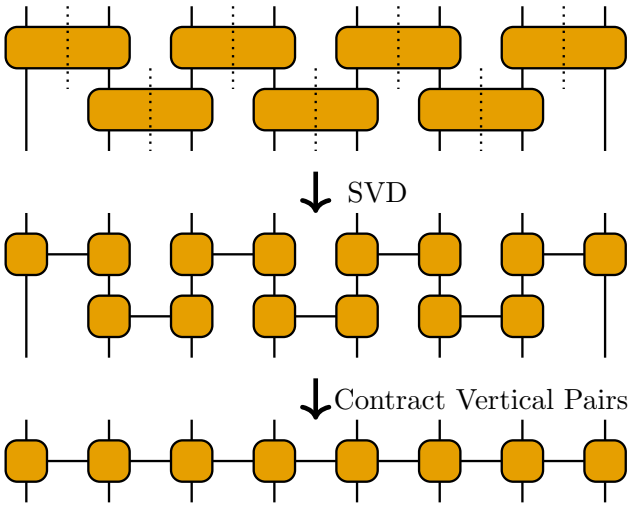

Figure 3.8: Schematic procedure to convert a Trotterized time evolution single step into a single layer MPO. The nearest neighbour evolution operator is first split via SVD, then the resultant tensors are contracted in their vertical pairs to create the on-site single layer MPO.

into a form that is explicitly a matrix product. More specifically we need a operator valued matrix M which encodes the terms of the 2-local Hamiltonian terms in this example. The solution is easier than it seems if one considers the expansion of the terms in the Hamiltonian sum. Consider the expanded form of $\sum_{j=1}^{N} J_x \hat{\sigma}_j^x \hat{\sigma}_{j+1}^x$, which when written explicitly is

$$\begin{aligned} \sum_{j=1}^{N} J_x \hat{\sigma}_j^x \hat{\sigma}_{j+1}^x = J_x \hat{\sigma}_1^x \otimes \hat{\sigma}_2^x \otimes \mathbb{I} \otimes \mathbb{I} \otimes \dots \\ + \mathbb{I} \otimes J_x \hat{\sigma}_2^x \otimes \hat{\sigma}_3^x \otimes \mathbb{I} \otimes \dots \end{aligned} \tag{3.12}$$

We want to find the matrices M the entries of which are operators such that $\hat{H} = \hat{O}_{\text{MPO}} = \prod_i M^{[i]}$, where this product is the contraction of the bond indices of the $M^{[i]}$ or a matrix multiplication on the bond indices. All we need to consider is an arbitrary operator string as appears in the expansion above, e.g. $\mathbb{I} \otimes \cdots \otimes \mathbb{I} \otimes \hat{O}_i \otimes \hat{O}_{i+1} \otimes \cdots \otimes \mathbb{I}$, and the allowed combinations of the constituent operators, $\hat{O}_i \otimes \hat{O}_{i+1}$. In the generic Hamiltonian there are 7 distinct operators that can appear in an operator string, $\{\mathbb{I}, \hat{\sigma}_i^x \hat{\sigma}_{i+1}^x, \hat{\sigma}_i^y \hat{\sigma}_{i+1}^y, \hat{\sigma}_i^z \hat{\sigma}_{i+1}^z, \hat{\sigma}_i^x, \hat{\sigma}_i^y, \hat{\sigma}_i^z\}$, with their associated coefficients. We can encode these using 5 operator string states. Examining an arbitrary operator string starting from the right, when we encounter a magnetic field term, say $h_x \hat{\sigma}_i^x$, we know that all operators to the left of this must be $\mathbb{I}$. This goes for all such field operators. For the nearest neighbour terms, e.g. $J_z \hat{\sigma}_i^z \hat{\sigma}_{i+1}^z$, we first encounter $\hat{\sigma}_{i+1}^z$ from the right which leads us to conclude that a $J_z \hat{\sigma}_i^z$ immediately appears next in the operator product. In effect we describe these transitions as transitions between string states. We can thus enumerate the string states as follows, reading them from right to left:

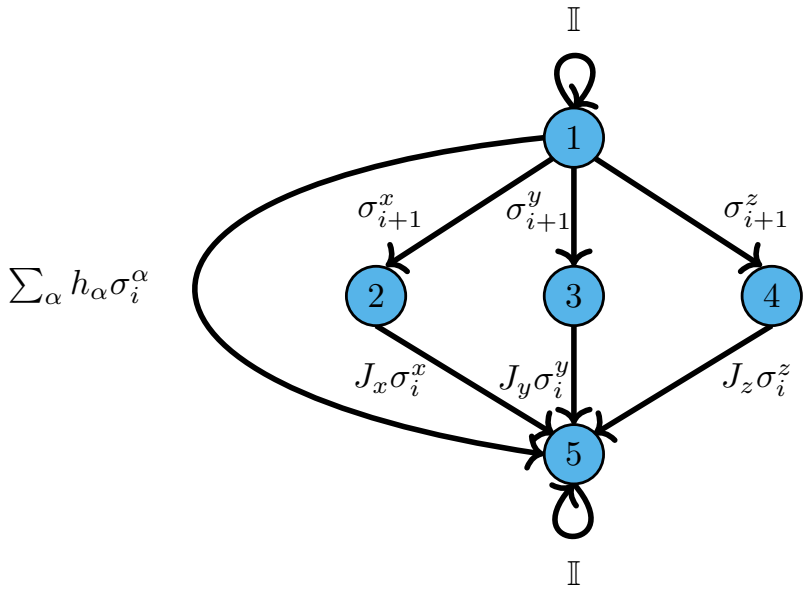

Figure 3.9: Depiction of the finite state automata (FSA) to encode the MPO operator valued matrix $M^{[i]}$ for the generic Heisenberg spin Hamiltonian (2.1). String states are the numbered vertices, as enumerated in the text, and the appropriate operators label the edges describing the string state transitions.

1. Only $\mathbb{I}$ to left,
2. One $\hat{\sigma}_{i+1}^x$ to immediate left,
3. One $\hat{\sigma}_{i+1}^y$ to immediate left,
4. One $\hat{\sigma}_{i+1}^z$ to immediate left,
5. Either one of $J_\alpha \hat{\sigma}_i^\alpha$ or only $\sum_\alpha h_\alpha \hat{\sigma}_i^\alpha$ to left.

The transitions between these states are then given by the relevant operators, we visualise this using a schematic inspired by finite state automata in Fig. 3.9.

From this diagram it becomes much easier to construct the matrix $M^{[i]}$ which, using these rules, is given by

$$M^{[1]} = \begin{pmatrix} \sum_\alpha h_\alpha \sigma^\alpha & J_y\sigma^y & J_x\sigma^x & J_z\sigma^z & \mathbb{I} \end{pmatrix}, \tag{3.13}$$

$$M^{[i]} = \begin{pmatrix} \mathbb{I} & 0 & 0 & 0 & 0 \\ \sigma^x & 0 & 0 & 0 & 0 \\ \sigma^y & 0 & 0 & 0 & 0 \\ \sigma^z & 0 & 0 & 0 & 0 \\ \sum_\alpha h_\alpha \sigma^\alpha & J_y\sigma^y & J_x\sigma^x & J_z\sigma^z & \mathbb{I} \end{pmatrix}, \tag{3.14}$$

$$M^{[N]} = \begin{pmatrix} \mathbb{I} & \sigma^x & \sigma^y & \sigma^z & \sum_\alpha h_\alpha \sigma^\alpha \end{pmatrix}^T, \tag{3.15}$$

where we have also included the first and last site boundary operator valued vectors to complete the Hamiltonian sum. We note that we can proceed in the same manner for next-nearest neighbour interaction terms and increasingly long-range interactions. The FSA diagram requires intermediate states to "fill in" the space between the k-local operators and this leads to a more filled operator valued matrix but nonetheless the process follows similarly. For further detail on these constructions for MPO and more examples we refer to Ref. [McC07; CB08; Sch11].

In Appendix A we show a particular application that utilises exactly this MPO construction to prepare the model for simulation. This XXZ spin model with external fields has Green's functions that are difficult to compute by hand yet are readily accessed with these numerical methods. In particular, we can probe mixed spin-spin correlation functions and their Fourier transformations all within the framework we have described in this chapter.

Chapter 4

Majorana Based Topological Memories

In this chapter we will isolate a particular, often overlooked, issue that can arise in the pursuit to realise topological quantum computing platforms derived from the use of Majorana Zero Modes (MZM). Generically, topological schemes to protect and manipulate quantum information are based on fractional excitations called anyons. Majorana zero modes are a simple example of such excitations. In these approaches information is stored in anyon pairs and, by moving them apart, one can encode this information in a non-local way [Kit01; Den+02; Kit03; Kit06; Nay+08; ST13]. This is the key feature that allows topological memories to be robust against local noise and decoherence processes.

In these topological platforms the computational space is a degenerate ground state manifold that emerges when these quasi-particle excitations are far apart (see Fig. 4.1). The degeneracy of this subspace is fundamentally important because it protects against quantum memory corruption in the form of unwanted qubit rotations, which arise via the accumulation of relative dynamical phases. If present such a process could lead to an undetectable error. Other errors, such as bit-flip error, have been studied in a similar context to that of this chapter previously [Con+19], as such we focus on the dynamical phase error process in particular. This feature of the ground state manifold arises from a more general property, sometimes called Topological Quantum Order (TQO) [WN90; Wen90; HW05; BHM10; Zen+19]. Among other things, TQO implies that, for states within this manifold, the expectation values of local observables are equal up to some exponentially small correction that depends on the spatial separation between anyons.

However, in this pursuit we will first give a short description of Majorana zero modes in Section 4.1. In particular, we show how unpaired Majorana arise beginning with the Ising model transformed into a model of (Majorana) fermions for particular Hamiltonian parameters. Further, here we demonstrate the degeneracy of the model's ground state, an essential feature of the p-wave superconductor model. In

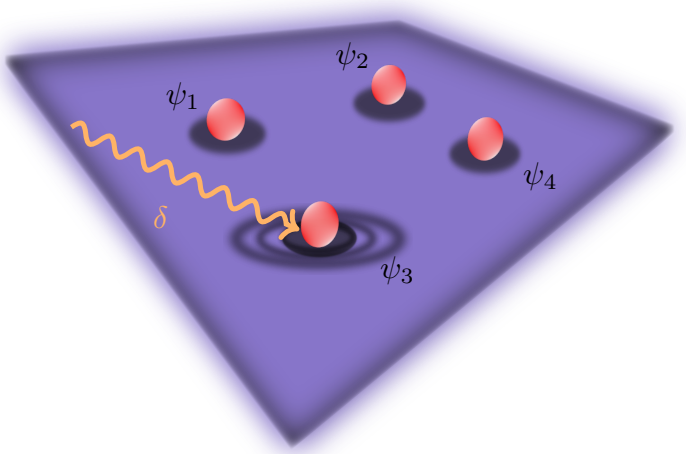

Figure 4.1: Schematic view of a 2D topological memory consisting of 4 anyons, generically labelled by ψ_i. Information is stored non-locally, and any local excitation, denoted here by δ, occurring near one anyon must propagate through the system for an error to occur.

Section 4.2 we elaborate on the topological aspect of the model and its phase transition. After these preliminaries, in Section 4.3 we present the error process that we are interested in and the property of topological quantum order that protects against it. In addition, we include here two notes on time-*dependent* perturbations and inheritance of the TQO property between related models. The final Section 4.4 covers our numerical verification of the TQO protection for the p-wave interacting superconductor model.

4.1 Majorana Zero Modes

A natural starting point in the quest to produce a quantum computing platform is to ask how one encodes the most basic unit of quantum information, the qubit. We will not give an account of all extant approaches to achieving this goal and will focus on that approach which is relevant to this chapter alone. The core ideas necessary to understand how Majorana excitations translate to encoding qubits begins with a simple spin model that we can build upon and bring close to a realisable physical platform.

As a first step consider the one dimensional Ising model [Isi25] on N lattice sites. One can view this as an instance of the generic Hamiltonian described in Chapter 2

with many of the couplings set to zero so that we have a Hamiltonian of the form

$$H = -J \sum_{j=1}^{N-1} \hat{\sigma}_j^z \hat{\sigma}_{j+1}^z - h_x \sum_{j=1}^{N} \hat{\sigma}_j^x, \tag{4.1}$$

where $\hat{\sigma}_j^a$ are the same Pauli matrices as previously described in Ch. 2, $J > 0$ is the nearest neighbour coupling strength and $h_x > 0$ is an external magnetic field in the x-direction. This model is known to have a quantum phase transition (QPT) [Sac11] at zero temperature. The point of the QPT is where the coupling matches the field strength, i.e. $J = h_x$. For larger coupling strength the model exhibits an ordered phase and for larger magnetic field a disordered phase. To be more precise, consider the ground state for the case of $J \neq 0$, $h_x = 0$. There, the groundstate is doubly degenerate and takes the form of either the all up ($|\bar{\uparrow}\rangle$) or all down ($|\bar{\downarrow}\rangle$) spin state. In the other case of $J = 0$, $h_x \neq 0$ the groundstate is unique and corresponds to the state where all spins are aligned with the external magnetic field, in the $\hat{x}$-direction. The total magnetization defined as the expectation value of the sum of local $\hat{\sigma}_j^z$ operators serves as the order parameter in this case where it is zero in the disordered phase and non-zero in the ordered phase.

At this point we begin to bring this model towards one that can be seen as a model of fermions in which we can define the aforementioned Majorana zero modes. By using the same Jordan-Wigner transformation as in Eq. 2.7 one can produce a similar fermionic Hamiltonian as in Ch. 2. Performing the calculation yields

$$H = -J \sum_{j=1}^{N-1} \left(\hat{c}_j^\dagger \hat{c}_{j+1} + \hat{c}_{j+1}^\dagger \hat{c}_j + \hat{c}_{j+1} \hat{c}_j + \hat{c}_j^\dagger \hat{c}_{j+1}^\dagger \right) + 2h_x \sum_{j=1}^{N} \hat{c}_j^\dagger \hat{c}_{j+1} - N h_x \mathbb{I}. \tag{4.2}$$

Recall that Majorana fermions can be formally defined via self adjoint operators that abide by the usual fermionic (anti-)commutation relations (2.5) [Maj08]. These we define from the fermionic operators c_j as

$$\gamma_{2j} \equiv \hat{c}_j + \hat{c}_j^\dagger, \quad \gamma_{2j-1} \equiv -i \left(\hat{c}_j - \hat{c}_j^\dagger \right), \tag{4.3}$$

giving the inverse relations

$$\hat{c}_j^\dagger = \frac{1}{2} \left(\gamma_{2j-1} - i\gamma_{2j} \right), \; \hat{c}_j = \frac{1}{2} \left(\gamma_{2j-1} + i\gamma_{2j} \right). \tag{4.4}$$

We can see that these relations produce manifestly self-adjoint γ operators. It is directly checked using the fermionic commutation relations that the γ operators inherit the fermionic relations, using directly (4.3), so that the following are true

$$\{\gamma_{2m}, \gamma_{2n}\} = \delta_{mn} = \{\gamma_{2m-1}, \gamma_{2n-1}\}, \quad \{\gamma_{2m}, \gamma_{2n-1}\} = 0. \tag{4.5}$$

Implicit in this definition of the Majorana operators is the notion that they constitute two "half"-fermions since a single c_j fermion operator is "split" into a superposition of two constituent Majorana fermions. The odd/even labelled Majorana can be considered as the real/imaginary components of a typical fermion. Regardless of interpretation, a single lattice site j is effectively split into an odd and even labelled site in the γ operators. This is the key viewpoint to realise a Majorana based qubit. If the Majorana modes corresponding to γ_{2j} and γ_{2j-1} can be spatially separated then errors arising from local error processes should in effect be prevented. We will make this point concrete as we continue.

The result of defining these Majorana fermions allows one to express the Hamiltonian of the Ising model as

$$H = -iJ \sum_{j=1}^{N-1} \gamma_{2j}\gamma_{2j+1} + ih_x \sum_{j=1}^{N} \gamma_{2j-1}\gamma_{2j}, \tag{4.6}$$

by inserting the definitions directly and keeping note that the γ operators square to the identity.

At this point it is prudent to consider the symmetries of the system we have described. In the spin picture we have a manifest spin-flip symmetry, meaning that the parity operator which flips all spins given by

$$\mathcal{P} = \prod_{j=1}^{N} \hat{\sigma}_j^x, \tag{4.7}$$

leaves the Ising Hamiltonian (4.1) invariant. Written in γ operators via Jordan-Wigner and the definitions of γ yields

$$\mathcal{P} = \prod_{j=1}^{N} i\gamma_{2j-1}\gamma_{2j}. \tag{4.8}$$

How do we interpret this operator then? In the spin picture this corresponded to the symmetry of spin flipping at all sites. In the fermionic setting this corresponds to the fermion parity. In other words, rather than spin parity we find the fermion number parity i.e. whether there is an odd or even number of fermionic excitations in the system. This splits the Hamiltonian spectrum into two distinct parity sectors designated the odd/even sectors. This is made manifest by inspecting the fermion Hamiltonian (4.2), one can see that while the $\hat{c}_j\hat{c}_{j+1}$ and $\hat{c}_j^\dagger\hat{c}_{j+1}^\dagger$ break fermion number conservation they only do so in steps of 2 so that the parity of the fermion number remains fixed at all times. Only operators with an odd number of fermion operators in total will break this parity. For the majority of condensed matter systems of interest such odd-fermion operators are not present to maintain fermionic parity, as is the case here.

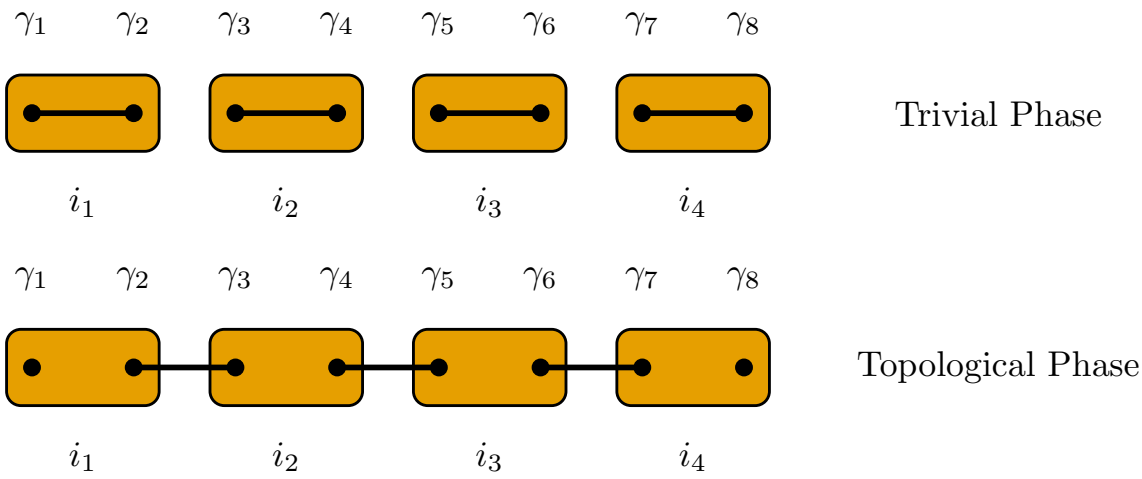

Figure 4.2: Observe in the upper schematic for $J = 0$ the model is fully dimerized, hence topologically trivial. In the lower schematic for $h_x = 0$ the two end Majorana become uncoupled from the rest of the lattice, referred to as the topological phase.

Returning now to the Majorana Hamiltonian (4.6) we can examine the limiting cases of the couplings to see how the QPT of the Ising model relates to Majorana zero modes. Recall that in the extreme case of $J \neq 0$, $h_x = 0$ that the spin model gave a doubly degenerate groundstate. In the Majorana representation this corresponds to inter-site couplings linked but intra-site couplings set to zero which leaves γ_1 and γ_N uncoupled from the bulk of the lattice. Since these together comprise a single fermionic excitation we can see that by construction we have obtained a non-local degree of freedom across the lattice. In this spirit this is deemed the topological phase of the model. In contrast, the other case of $J = 0$, $h_x \neq 0$ produces a fully dimerized system which has a unique ground state and hence is the topologically trivial phase of the model. Schematically this can be seen in Fig. 4.2. Notice how, in effect, the end Majorana, denoted γ_1 and γ_8, have become uncoupled from the remainder of the lattice.

More strictly speaking these are described as strong zero modes and characterize the topological order of the system. Away from this exact limit the MZM should more precisely be referred to as Majorana bound states as, for finite size systems, there can be some overlap of the Majorana and strictly speaking they are not zero modes. By definition strong zero modes are those operators which commute with the Hamiltonian in the thermodynamic limit, written formally as ψ such that

$$[H, \psi] = 0 + \mathcal{O}(e^{-\frac{L}{\xi}}), \tag{4.9}$$

where $L = N\varepsilon$, ε being the lattice spacing, and $\xi \in \mathbb{R}^+$ a constant length scale, i.e. the correlation length of the system. However, for the finite size system that we study in Sec. 4.3 & Sec. 4.4 the system is sufficiently large to consider the above commutator as, for all practical purposes, equal to zero.

In addition, the zero mode can be defined via its mapping under the parity

operator, $\mathcal{P}$. The defining relation requires that

$$\mathcal{P}\psi = -\psi\mathcal{P}, \tag{4.10}$$

meaning that the zero mode maps a state in one parity sector to a state with opposite parity. It is also required for existence that the zero mode operator has a well defined normalization in the thermodynamic limit but this is automatically true for MZMs since $\gamma^\dagger\gamma = 1$ by definition. If such a zero mode is present in a model then this implies that the model has a degenerate spectrum. Given what we have stated up to now, we can see immediately that, given a state $|\phi\rangle$ with energy e_ϕ, the expression

$$H\psi\,|\phi\rangle = \psi H\,|\phi\rangle = \psi e_\phi\,|\phi\rangle\,, \tag{4.11}$$

indicates the degeneracy since by definition of ψ the two states $|\phi\rangle$ and $\psi\,|\phi\rangle$ are of opposite parity. If this zero mode is localised/confined to a lattice boundary it is referred to as an edge zero mode and can, in principle, be used to store information in the context of topological quantum computation.

Using what we have learned up to this point we again consider the Ising model in the Majorana language. Consider the topologically non-trivial Hamiltonian, where $h_x = 0$,

$$H = -iJ\sum_{j=1}^{N-1}\gamma_{2j}\gamma_{2j+1}. \tag{4.12}$$

By inspection one can see that neither γ_1 nor γ_{2N} are included in the sum so it is trivial to verify that these two boundary Majorana commute with the Hamiltonian. Their relation to the parity operator, $\mathcal{P}$, is also directly checked confirming their status as zero modes and specifically edge zero modes. While this example is the extreme case these zero modes exist for $h_x \neq 0$ so long as $J > h_x$ i.e. within the topological non-trivial regime. In this regime one can construct boundary zero modes systematically [Fen16; Pel+20].

Why then do we refer to these two regimes as topological and topologically trivial having previously deemed them ordered and disordered phases for the Ising model? In brief we stress that while the Ising and Kitaev models are formally equivalent, as they can be mapped into one another by Jordan-Wigner transformation, the models are physically inequivalent [GST14]. The phase transition in the Ising model is precipitated by breaking spin reflection symmetry spontaneously whereas the Kitaev model transition is associated to the occupancy of the fermionic mode constructed from Majorana zero modes. These zero modes themselves are characteristic of a symmetry protected topological (SPT) phase. Furthermore, consider the differences between the degenerate ground states in each model. On the one hand, for the Ising model the two ground states would require a local spin flip at every site to obtain the all up state, $|\bar{\uparrow}\rangle$, from the all down state $|\bar{\downarrow}\rangle$. On the other hand, for the Kitaev

model the degenerate ground states are those that only differ by the occupancy of the Dirac fermionic zero mode that is constructed from the two boundary MZM, γ_1, γ_8. These ground states only differ by the occupancy of this *global* fermion mode. Furthermore, the topological phase transition is associated by a change in a discrete topological invariant which we demonstrate in the following section.

4.2 Topological Aspect of Majorana Fermions

We now examine a slight generalization of the model in the previous section which brings us closer to the model used for the remainder of this chapter. This is a toy model for a spinless p-wave superconductor on an N-site lattice in one dimension. Moreover, we make more concrete sense of the topological notions of the prior and ensuing discussions. The model itself is usually referred to as the Kitaev model [Kit01] with the Hamiltonian

$$H = -\sum_{j=1}^{N-1} \left(w\hat{c}_j^\dagger \hat{c}_{j+1} + \Delta \hat{c}_j \hat{c}_{j+1} + h.c. \right) - \sum_{j=1}^{N} \mu(\hat{c}_j^\dagger \hat{c}_{j+1} - \frac{1}{2}). \tag{4.13}$$

For the moment all the parameters are uniform across the lattice, this is for convenience and spatial dependence will be introduced at a later point. For now, similar to before, $w > 0$ represents the kinetic term and μ the chemical potential. Finally, Δ represents superconducting pairing. In principle this is complex valued, we can make this explicit but for our purposes we take a real valued Δ as the complex phase can be removed by a global phase rotation [ST13]. In addition, a potential profile and interactions can be introduced to bring the model into a more physically realistic form but we leave this for later, see Sec. 4.4.

In a similar fashion to the fermion form of the Ising model this model has a phase transition at $\mu = \pm 2w$ which is of the same character as the transition in the Ising model. In fact, it is clear that the Kitaev model reduces to the Ising model of the previous section (4.2) via the identification: $\mu = -2h_x$, $w = J$ and $\Delta = J$. To determine the topological characteristics of this model we first Fourier transform the bulk Hamiltonian and examine the spectrum of the result. The Fourier transformation of the creation/annihilation operators used is

$$\hat{c}_j = \frac{1}{\sqrt{N}} \sum_{k=-N/2}^{N/2} \hat{c}_k e^{-ikj}, \; \hat{c}_j^\dagger = \frac{1}{\sqrt{N}} \sum_{k=-N/2}^{N/2} \hat{c}_k^\dagger e^{ikj}. \tag{4.14}$$

Performing this transformation, one obtains

$$H = -\sum_k (\mu + 2w\cos k) \left(\hat{c}_k^\dagger \hat{c}_k + \hat{c}_{-k}^\dagger \hat{c}_{-k} \right) + 2i\Delta \sin k \left(\hat{c}_k \hat{c}_{-k} + \hat{c}_k^\dagger \hat{c}_{-k}^\dagger \right) + N\mu. \tag{4.15}$$

This is readily arranged into the form

$$H = \sum_k C_k^\dagger H_k C_k + \frac{1}{2} N\mu\mathbb{I}, \tag{4.16}$$

where $C_k \equiv \left(\hat{c}_k \hat{c}_{-k}^\dagger\right)^T$. Decomposing the 2×2 matrix H_k in a basis of Pauli matrices yields

$$H_k = d_z(k)\sigma^z + d_y(k)\sigma^y, \tag{4.17}$$

where $d_z(k) = -\mu - 2w\cos k$ and $d_y(k) = 2\Delta \sin k$. The single particle energies can be extracted by diagonalising this 2×2 matrix or equivalently performing a Bogoliubov transformation on C_k, denoted generically as $\tilde{C}_k = \mathcal{U}C_k$, which in the process defines the quasiparticle excitations of the system, $\tilde{C}_k$. It is easily checked that $\tilde{c}$ and $\tilde{c}^\dagger$ satisfy the usual fermionic anticommutation relations. Moreover, this brings H_k into the form

$$\varepsilon_k \sigma^z = \mathcal{U}^\dagger H_k \mathcal{U}, \tag{4.18}$$

where ε_k are the single particle energies and are given by

$$\varepsilon_k = \pm\sqrt{(\mu + 2w\cos k)^2 + 4\Delta^2 \sin^2 k}. \tag{4.19}$$

These single (quasi-)particle energies then sum over allowable k-values to determine the many body energy spectrum. The energy gap between the conduction and valence bands is thus determined via ε_k. In Fig. 4.3 this gap and its closure is shown for a selection of parameter values. One can see that the closure of the gap coincides with the phase transition that manifests the Majorana zero modes in the Kitaev model namely when $|\mu| \to 2w$. In this way one can see that the two phases are separated by this gap closure. In particular the two regimes cannot be connected continuously without closing the gap. The topological regime is that where $\mu \in \{-2w, 2w\}$ and the trivial regime is where μ is outside this range of values. One can understand this trivial regime from the fact that the vacuum, $\mu \to -\infty$, and fully occupied band, $\mu \to \infty$, are adiabatically connected.

Notice, further, that the location of the gap closure shifts from $k = 0$ to $k = \pm\pi$. This can be readily understood by checking where the single particle energy (4.19) vanishes for each regime. The dispersion component will vanish at the Fermi wavevector, $\pm k_F$, determined by

$$k_F = \arccos\left(\frac{\mu}{-2w}\right). \tag{4.20}$$

Similarly, the pairing term, $2\Delta\sin(k)$, only vanishes at $k_F = 0, \pm\pi$. The corresponding values, then, of $\mu/-2w$ are where this fraction is equal to ± 1; which is precisely where $\mu = \pm 2w$. Thus, the spectrum becomes gapless for $\mu = -2w$ at $k_F = 0$ and

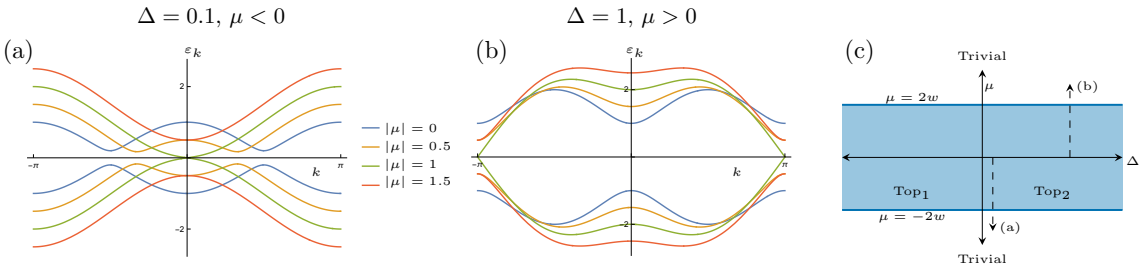

Figure 4.3: Here we show the single particle energies for several regimes, at $w = 0.5$. (a) For $\Delta = 0.1$ and $\mu < 0$ we can see the gap open for all μ values except where $|\mu| = 2w$. (b) Similarly, for $\Delta = 1$ and $\mu > 0$ the same can be seen with the gap closing only at $\mu = 2w = 1$. Away from this point the open gap is larger than the prior example corresponding to a larger value of Δ. Further we can see that the point that the gap closes moves from $k = 0$ to $k = \pm\pi$ coinciding with the change in sign of μ. (c) A schematic of the phase diagram of the model, where the blue band indicates the topological region(s), and labelling for the parameters used in (a) & (b).

similarly, for $\mu = 2w$ at $k_F = \pm\pi$ as we can observe from Fig. 4.3.

Additionally, Fig. 4.4 shows the curve created by plotting the vector $d(k) = (d_y(k), d_z(k))$. Here we can make a concrete statement regarding the topology of the system. Each of the plotted loops can be characterized by their winding number about the origin as k runs through $[-\pi, \pi]$ or along the first Brillouin zone. In particular one finds that for $|\mu| > 2w$ there is a winding number of 0, for $|\mu| < 2w$ a winding number of 1 and at the transition $|\mu| = 2w$ the winding is undetermined [Sta16]. This is the topological invariant that we have been building towards. The discrete jump from 0 to 1 and vice-versa is accompanied by the appearance and disappearance of the Majorana zero modes that we have described. This topological invariant is known as the Chern number [Sta16].

As for the Ising model example we can write this model in terms of Majorana operators using the same definitions (4.4) as then. This produces a similar Majorana Hamiltonian as before

$$H = \frac{i}{2}\sum_{j=1}^{N-1}(w-\Delta)\,\gamma_{2j}\gamma_{2j+1} - \frac{i}{2}\sum_{j=1}^{N-1}(w+\Delta)\,\gamma_{2j}\gamma_{2j+1} - \frac{i\mu}{2}\sum_{j=1}^{N}\gamma_{2j-1}\gamma_{2j} - N\mu\mathbb{I}. \tag{4.21}$$

This Hamiltonian then has a very similar limit where exact Majorana zero modes reside at the end points. This parameter configuration is $\mu = 0$ and $w = \Delta$ which produces

$$H = -iw\sum_{j=1}^{N-1}\gamma_{2j}\gamma_{2j+1}, \tag{4.22}$$

which clearly as before does not include the end Majorana. Away from this special point the Majorana zero modes are not so straightforward to write down but nonetheless are present in the system as long as the gap remains open. The simi-

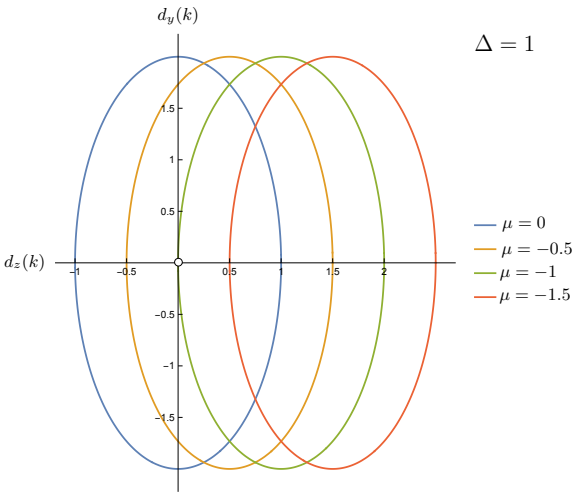

Figure 4.4: Here we plot the vector components $d_y(k)$ and $d_z(k)$ to show that when $\mu = 2w$ the loop inscribed by the vectors touches the origin. When the origin is enclosed by the loop the winding number is the $|\nu| = 1$. The sign of the winding number depends on the sign of Δ, in this case $+1$.

larities continue as in the Ising model example whereby the fermion parity operator commutes with this Hamiltonian so that fermion number is conserved modulo 2.

At this point we note that despite this being a "toy model" of a superconducting wire there are numerous proposals for producing effective models which qualitatively match this Kitaev model [AKL18; BH13]. Moreover, given that the two Majorana constitute a single fermionic degree of freedom, one can propose concretely a lattice model as we have done here of 4 Majorana on a superconducting wire which are encoded in a system with a 4-fold ground state degeneracy. In this way one can take this system as a building block of a topologically protected quantum memory. Given the 4-fold degeneracy, the occupancy of these degrees of freedom can be separated by their fermion parity into two 2-fold degenerate subspaces which comprise a candidate platform for encoding a single qubit of information. The natural question which then arises is how well protected from errors is this candidate platform? The answer to this is the objective of the remainder of this chapter wherein we examine an error process which has been overlooked to a degree. We provide an argument and verification for the topological protection of such a system in the following.

4.3 Topological Quantum Order

The error process that we specifically address here which can corrupt the quantum memory with undesirable qubit rotations is dynamical *phase error*. This can occur when the quantum state partially leaves the ground state manifold and returns later with a dynamically altered phase. This type of error could arise on a mean-field level if there are causally connected perturbations near different anyons [Con+19]. In this scenario the distance between anyons plays an important role in delaying/reducing

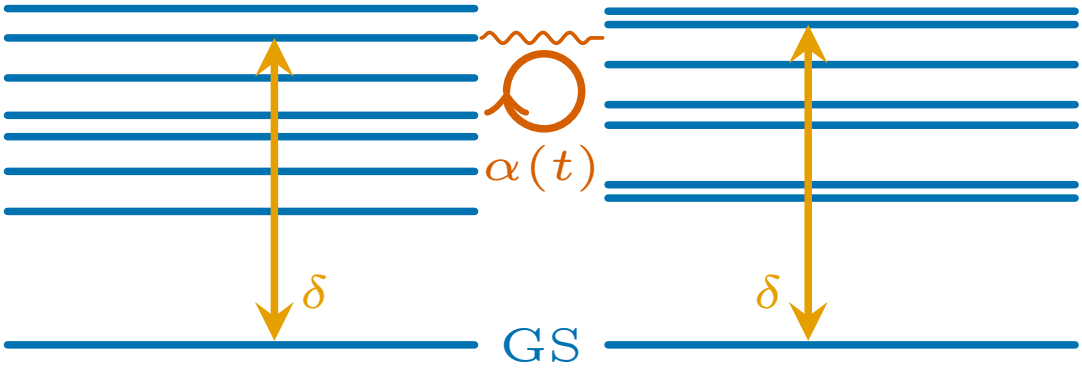

Figure 4.5: Slight energy mismatches between higher energy states (indicated by the curved line) in topological sectors open up an apparent relative phase error, $\alpha(t)$, when a local process, δ, couples the protected ground states with the excited states.

the onset of this type of secondary error process. In interacting systems however, a different scenario for phase error still exists because the aforementioned ground state degeneracy does not necessarily extend to a degeneracy in bulk eigenstates. One could then reasonably worry about processes whereby a single localised perturbation creates, and then at a later time, returns an excitation that has accumulated some relative dynamical phase from its time spent in the energy mismatched bulk.

In the remaining sections we show that, despite a mismatched bulk spectrum schematically shown in Fig. 4.5, TQO guarantees that such interaction driven phase errors are suppressed up to a time that scales with system size, in Sec. 4.3.1. A consequence of this suppression is that, although the bulk spectra from distinct topological sectors differ, there is necessarily a high degree of correlation between spectral densities. This correlation can be intuitively quantified by considering appropriate Green's functions involving the ground state manifold.

We demonstrate these general results, that hold for any system with TQO, using a concrete example in Sec. 4.4. Namely, a Majorana based topological memory based on interacting p-wave superconducting wires [FK08; LSD10; ORO10; CST11; Ali+11], as shown schematically in Fig. 4.7, and provide a simple path to establishing the TQO condition for this type of system. We back up our key claims using a MPS approach known as the time-dependent variational principle (TDVP) [Hae+11; Pae+19] which allows us to: (1) show that, even in regimes where interactions and time-dependent perturbations are relatively strong, there is no phase error other than what one would expect from mean-field like effects, and (2) directly calculate spectral densities in each topological sector and give a quantitative demonstration on the degree of correlation that must exist between them, see Sec. 4.5.

4.3.1 An Argument for No Phase Error

Now we establish the core argument against a potentially fatal undetectable error. We present the argument in generic terms before linking to a more concrete model.

As such, consider some gapped local Hamiltonian H with anyonic quasi-particles. By local Hamiltonian we mean a sum of Hermitian operators that are each only non-trivial on several neighbouring sites. Take the Hamiltonians of the previous sections as examples. Generically, we express this as

$$H = \sum_x H_x, \tag{4.23}$$

where x can be two nearest neighbour lattice sites, for example.

For simplicity, we assume there are two ground states, $|e\rangle$ and $|o\rangle$, corresponding to (e)ven and (o)dd parity respectively. This is the case for the Majorana examples used throughout this chapter. It is straightforward to generalise the argument to a higher dimensional ground state manifold. Crucially, we assume that for large enough system diameter L, there is a length L^* that scales in some way with L (this length must satisfy $L^* \geq cL$ for some constant $c > 0$), for which the ground states satisfy the topological quantum order (TQO) property:

Definition 4.1. For every local operator, O, supported in a region of diameter at most L^*, we have

$$\langle e| O |e\rangle = \langle o| O |o\rangle + \mathcal{O}(e^{-L/\xi}), \tag{4.24}$$

for some constant $\xi > 0$. That is, local operators cannot be used to distinguish the two sectors, up to exponential corrections in L.

From the TQO property one can see that the ground states are degenerate, up to exponential corrections in the system length L [BHM10; BH11]. That is, $\langle a| H |a\rangle$ is approximately the same for either parity sector labelled by $a = e, o$. Note that, H is a sum of a polynomial (in L) number of k-local terms, H_x. TQO implies that $\langle a|H_x|a\rangle$ is sector independent up to $\mathcal{O}(e^{-L/\xi})$, which dominates the polynomial in L in the sum $\langle a|H|a\rangle = \sum_x \langle a|H_x|a\rangle$.

Although TQO makes no *direct* claims on the behaviour of states above the gap that separates the ground state manifold from the bulk excited states, it can be used however to *derive* certain properties see e.g. [BHM10]. In what follows we show how TQO bounds the dynamically driven phase error, and how this results in a large number of constraints on the bulk spectrum.

We consider two instantaneous local perturbations of the system, separated by a time t. The unitary evolution operator in this case is

$$U(t) = e^{i\delta'} e^{-iHt} e^{-i\delta} , \tag{4.25}$$

where δ and δ' are local Hermitian operators (possibly at different locations) that do not mix the even and odd sectors. By a *phase error* we mean that $\langle a| U(t) |a\rangle$ is different for the even and odd sectors. We can expand in the energy eigenstates,

$|a,n\rangle$, to get

$$\langle a|\, U(t)\, |a\rangle = \sum_n e^{-iE_{a,n}t}\, \langle a|\, e^{i\delta'}\, |a,n\rangle\, \langle a,n|\, e^{-i\delta}\, |a\rangle\,, \tag{4.26}$$

where $E_{a,n}$ is the energy of the n^{th} eigenstate in the a-sector. For special cases, where there is a degeneracy between the two sectors for all bulk energies, i.e. $E_{e,n} = E_{o,n}$, and where the overlaps $\langle a,n|\, e^{-i\delta}\, |a\rangle$ are sector independent, there is no phase error. Neither condition necessarily holds for an interacting system. Nevertheless, one can make the following argument for the suppression of phase error.

First, we write

$$\langle a|\, U(t)\, |a\rangle = e^{-iE_0 t}\, \langle a|\, e^{i\delta'} O(t)\, |a\rangle\,, \tag{4.27}$$

where we have defined $O(t) \equiv e^{-iHt} e^{-i\delta} e^{iHt}$, and we have used $e^{-iHt}\, |a\rangle = e^{-iE_0 t}\, |a\rangle$ where, by the approximate ground state degeneracy, E_0 is exponentially close between the sectors. From the Lieb-Robinson bounds [LR72], i.e. the theoretical limits on the speed of information propagation in a non-relativistic quantum system, we note that we can approximate $O(t)$ by an operator $\tilde{O}(t)$, supported in a region of size $\sim v|t|$ about δ, up to corrections of order $\mathcal{O}(e^{-(L-v|t|)/\xi})$. Our argument involves several exponential error terms; each with its own rate constant ξ. To avoid ambiguity, we take ξ to be the smallest such constant such that each error estimate is valid. Here, v is the Lieb-Robinson speed of propagation for H. We can then pick some $T^* \sim L^*/v$, such that the maximum size of $\tilde{O}(t)$ over the range of times $|t| < T^*$ is at most L^*, and such that $\tilde{O}(t)$ approximates $O(t)$ to order $\mathcal{O}(e^{-L/\xi})$. This TQO region and operator growth is shown schematically in Fig. 4.6. There are two cases to consider: cx

1. If δ' is contained in an L^* sized region about δ for sufficiently large L, then, for all times $|t| < T^*$, $e^{i\delta'}\tilde{O}(t)$ is contained in a region of size at most L^*. TQO then implies that $\langle a|\, e^{i\delta'}\tilde{O}(t)\, |a\rangle$ is sector independent to order $\mathcal{O}(e^{-L/\xi})$. Putting everything together, for times $|t| < T^* \sim L^*/v$ we find that $\langle a|\, U(t)\, |a\rangle$ is approximately equal between the sectors, up to exponential corrections in L. In this situation we say there is *no phase error*.

2. If δ' is not contained in an L^* sized region about δ, then the separation between δ and δ' must be growing with L. The fact that the system is gapped means that $\langle a|\, e^{i\delta'}\tilde{O}(t)\, |a\rangle \approx \langle a|\, e^{i\delta'}\, |a\rangle\, \langle a|\, \tilde{O}(t)\, |a\rangle$, up to an exponential correction in the operator separation [Has04; HK06], and hence a correction of order $\mathcal{O}(e^{-L/\xi})$. For $|t| < T^*$ the TQO condition implies that $\langle a|\, \tilde{O}(t)\, |a\rangle$ is sector independent up to exponential corrections, and hence $\langle a|\, e^{i\delta'}\tilde{O}(t)\, |a\rangle$ is too. That is, we again have exponentially vanishing phase error for times $|t| < T^*$.

Note that the exact time, T^*, for which no phase error arises, depends upon the specific system, the specific perturbations, and their separation. The preceding

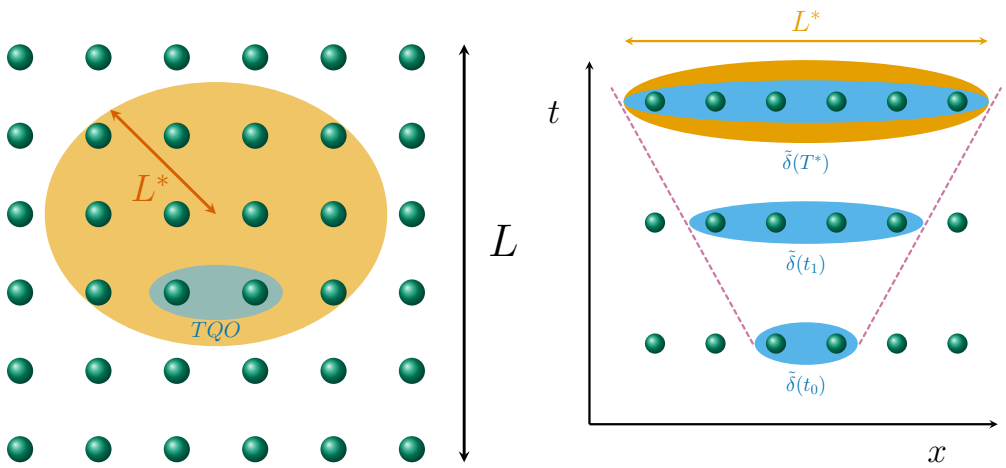

(a) System TQO Schematic (b) Operator Growth in Time

Figure 4.6: (a) A schematic showing the a tightly localised area of the system wherein the TQO property is satisfied. This is within a larger area defined by the characteristic length T^*. (b) Using the same colouring we illustrate growth of a 2-local operator, in this instance, up to a characteristic time T^* after which the TQO property is manifestly broken. Starting from an initial operator, $\tilde{\delta}(t_0)$, evolving through time the region where the operator acts grows past the point that it acts across the full L^* region. However, since the characteristic time and length is proportional to the system length L one can, in principle, expand the system size in consideration to allow for a longer time T^* or length L^*.

argument should be understood as heuristic justification that T^* scales as L^*/v, and hence as L/v. We address the more general scenario of time-dependent perturbations, and we make similar arguments for the suppression of phase error in Sec. 4.3.2.

The suppression of phase error implies a large number of constraints on the bulk spectra in the following way. From (4.26) we can write the amplitude of the phase error, denoted here by $\alpha(t)$, as

$$\begin{aligned}\alpha(t) &= \langle e| U(t) |e\rangle - \langle o| U(t) |o\rangle , \\ &= \sum_{n>0} \lambda_{e,n,\delta\delta'} e^{-iE_{e,n}t} - \lambda_{o,n,\delta\delta'} e^{-iE_{o,n}t} + \mathcal{O}(e^{-L/\xi}),\end{aligned} \tag{4.28}$$

where $\lambda_{a,n,\delta\delta'} = \langle a| e^{i\delta'} |a,n\rangle \langle a,n| e^{-i\delta} |a\rangle$, and the sum runs from $n > 0$ as the ground state contribution is contained in the exponential correction on the far RHS. Above we showed that $|\alpha(t)|$ is exponentially suppressed. This then implies that the magnitude of difference between the even and the odd sums (for $n > 0$) on the RHS is also exponentially suppressed in L. Crucially, this is also the case for many pairs of local operators, δ and δ', though the exact form of the suppression may differ in each case. One can then consider this constraint between the even and odd sums for *all* such pairs, resulting in a substantial number of constraints on the bulk spectra. The effect of this on the bulk splittings is illustrated for a specific model in Sec. 4.4.

4.3.2 Time-Dependent Perturbations

In the previous argument we used a time-independent perturbation, δ. However, the argument extends also to time-dependent perturbations, $\delta(t)$, the details of which we now summarise. Consider such a time-dependent local perturbation $\delta(t)$. The time-ordered unitary evolution operator is then

$$U(t) = T\{e^{-i\int_0^t dt' H+\delta(t')}\}\ . \tag{4.29}$$

To show there is no phase error we need to show that $\langle a|\, U(t)\, |a\rangle$ is approximately sector independent. As $U(t)$ is not a local operator we cannot immediately use the TQO condition. However, we can turn it into a local operator times a non-local operator that acts trivially on the system eigenstates

$$U(t) = e^{-iHt} \times T\{e^{-i\int_0^t dt' \tilde{\delta}(t')}\}, \tag{4.30}$$

where $\tilde{\delta}(t) \equiv e^{iHt}\delta(t)e^{-iHt}$, which essentially follows from the interaction picture.

From the Lieb-Robinson bounds, we can approximate $\tilde{\delta}(t)$, and hence the time-ordered unitary involving $\tilde{\delta}(t)$, by an operator supported in a region of size $\sim v|t|$, up to corrections of order $\mathcal{O}(e^{-(L-v|t|)/\xi})$. Thus, we have

$$\begin{aligned} \langle a|\, U(t)\, |a\rangle &= \langle a|\, e^{-iHt} \times T\{e^{-i\int_0^t dt' \tilde{\delta}(t')}\}\, |a\rangle\ , \\ &= e^{-iE_0 t}\, \langle a|\, T\{e^{-i\int_0^t dt' \tilde{\delta}(t')}\}\, |a\rangle\ , \end{aligned} \tag{4.31}$$

where E_0 is the same in both sectors up to corrections of order $\mathcal{O}(e^{-L/\xi})$. For $|t| < T^* \sim L^*/v$, we make an error of order $\mathcal{O}(e^{-L/\xi})$ by approximating the time-ordered unitary in a region of size L^*. In doing so we can then use TQO to argue that the expectation value on the last line is sector independent to order $\mathcal{O}(e^{-L/\xi})$, and hence $\langle a|\, U(t)\, |a\rangle$ is too, i.e. no phase error.

If we now include a second time-dependent perturbation $\delta'(t)$, separated from $\delta(t)$ such that $[\tilde{\delta}(t), \tilde{\delta}'(t)] \approx 0$ up to exponential corrections in the separation between $\delta(t)$ and $\delta'(t)$, then the unitary $U(t)$ approximately factorises as

$$U(t) \approx e^{-iHt} \times T\{e^{-i\int_0^t dt' \tilde{\delta}(t')}\} \times T\{e^{-i\int_0^t dt' \tilde{\delta}'(t')}\}. \tag{4.32}$$

It is straightforward to apply the gap argument from the previous sections to show that this will also not incur a phase error for $|t| < T^* \sim L^*/v$. This means that we can avoid the error process by having a sufficiently large system such that this time is large enough.

4.3.3 TQO Inheritance

A critical point must be made before we attend to the example in the next section. The example therein does not in fact satisfy *exact* topological quantum order. Nevertheless, we are able to apply the arguments in [HW05] to show how the interacting Majorana wire, H, inherits *approximate* TQO (4.24) from some simpler system, denoted here by H', with *exact* TQO. That is, the expectation values of any sufficiently local operator in the even and odd ground states of H' are *exactly* equal. For H to inherit TQO from H' we require the two Hamiltonians to be quasi-adiabatically connected via a local process that does not close the gap. By quasi-adiabatically we mean that we require that any deviation from a precisely adiabatic process is at most exponentially suppressed with respect to the system size.

There are several choices for H' that satisfy these requirements. For particular parameters, H_0 (the non-interacting wire) has exact TQO for any operator of size at most $L-1$ [Kit01], and one can tune from H_0 to H by locally tuning the interaction strength and the other system parameters in a way that does not close the gap.

A more useful choice for H', due to its proximity to H in parameter space, is a partially interacting wire where density-density interactions are present in the entire system expect for a small local region. Specifically, we tune the couplings on one side of the wire (say the right) to what we refer to as the *special local* Kitaev limit, denoted by H_K, where $\Delta_{L-1} = w$, $\mu_L = 0$ and $u_{L-1} = 0$ (recall that the L'th site refers to the last site of the left wire). In this limit there are interactions throughout all of the wire except the last two sites, which allows a fully decoupled Majorana to sit on the right hand edge, and thus guarantees a precise even-odd degeneracy for all many-body states [Kel15a]. In the same way, H_K is guaranteed to satisfy the exact TQO condition for operators of size at most $L_K^* = L-1$, i.e. the entire length of the wire except a single site. The fact that our fully interacting system of interest, H, differs from H_K on a single site, means that it is relatively easy to quasi-adiabatically connect the two. This manifests in the approximate TQO condition of H as a smaller exponential error than would arise from a longer quasi-adiabatic path to H.

Taking $H' = H_K$, we now follow [HW05] to derive approximate TQO for H. Denoting the ground states of H_K as $|a\rangle_K$ (for $a = e, o$), we have the exact TQO condition: ${}_K\langle e| O |e\rangle_K = {}_K\langle o| O |o\rangle_K$ for every local operator O supported in a region of size at most $L_K^* = L-1$. We consider a 1-parameter family of Hamiltonians $H(t)$, where $H(0) = H$ and $H(\tau) = H_K$, where τ is the time we tune for. In [HW05] they define a unitary operator, denoted here by V, that quasi-adiabatically transitions between H and H_K. We only consider cases for which $H(t)$ remains gapped throughout the tuning process [MN18]. Since this is a local process, $H(t)$ is always a sum of local terms.

Following [HW05], we consider some local observable O. We then form O_l, which

only acts on sites within a distance l from the support of O. Specifically, O_l is the partial trace (up to some constant) of $VOV^\dagger$ over all sites more than a distance l from the support of O. One can then show that,

$$\langle a|\, O\, |a\rangle = {}_K\langle a|\, Q^\dagger O_l Q\, |a\rangle_K + \mathcal{O}(e^{-l/\xi}), \tag{4.33}$$

where ξ is some constant, and Q is a unitary operator acting only within the ground state manifold.

To use the exact TQO of the local H_K limit in the RHS above, we require O_l to be supported in a region of size at most $L_K^* = L - 1$. If the length of O is d_O, then the length of O_l is $d_O + 2l$, which is less than or equal to L_K^* if $l \leq 1/2(L - 1 - d_O)$. To connect up with Eq. 4.24, we further assume that $d_O \leq L^*$, where L^* is some length satisfying $cL \leq L^* < L$, for some constant $c > 0$. At worst we then have $l \sim L$, and hence the error above is order $\mathcal{O}(e^{-L/\xi})$, for some (possibly different) constant ξ.

Finally, given the exact TQO of the special local Kitaev limit, and the fact that Q only acts within the ground state manifold, we find that the expectation value, ${}_K\langle a|\, Q^\dagger O_l Q\, |a\rangle_K$, is the same for both sectors. For the fully interacting Majorana system, H, this implies that $\langle a|\, O\, |a\rangle$ is the same for both sectors, up to $\mathcal{O}(e^{-L/\xi})$ for operators O of size at most L^*. This is the previously stated approximate TQO condition of Eq. 4.24.

While the above argument concerned the special local Kitaev limit and a locally connected H, it is clearly applicable to any pair of locally connected (gapped) systems where one is known to satisfy an exact TQO condition. This is of course also true more generally for higher dimensional ground state manifolds satisfying the same condition.

4.4 An Interacting Majorana Topological Memory

To demonstrate the result of the arguments presented in Sec. 4.3, we model a simple topological memory consisting of two one-dimensional p-wave superconducting wires separated by a potential barrier, as shown in Fig. 4.7. The $2L$-site (L sites each for the left and right wires) lattice Hamiltonian [Kit01] for this is given by

$$\begin{aligned} H_0 = &- \sum_{x=1}^{2L} [\mu_x - V_x](c_x^\dagger c_x - 1/2) \\ &- \sum_{x=1}^{2L} (w\, c_x^\dagger c_{x+1} + h.c) + \sum_{x=1}^{2L} (\Delta_x c_x^\dagger c_{x+1}^\dagger + h.c.), \end{aligned} \tag{4.34}$$

where Δ_x is the superconducting gap, μ_x is the on-site chemical potential, V_x is the potential profile, w is the hopping parameter and the $c_x^{(\dagger)}$ represent fermion

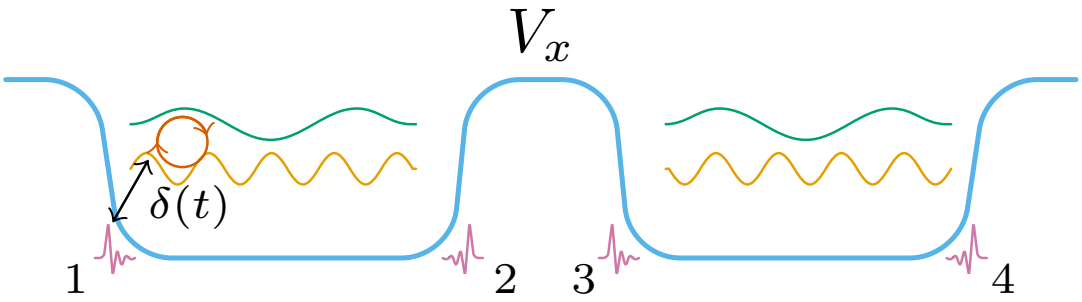

Figure 4.7: As a concrete model we consider a symmetry-protected topological quantum memory consisting of two p-wave superconducting wires separated by a potential barrier, V_x. In this setup 4 Majorana zero-modes occur at the domain boundaries, as indicated by the purple lines numbered 1-4 at the bottom. Local fluctuating noise can be realized, for example, by oscillating the left domain boundary by some $\delta(t)$ perturbation, or as a quasi-particle tunneling into the system.

(creation) annihilation operators. To simulate the two-wire setup of the Majorana based topological memory we utilise the potential profile:

$$V_x = V_{\text{outer}}[f(x_1 - x) + f(x - x_4)] + V_{\text{inner}}[f(x - x_2) - f_3(x - x_3)], \tag{4.35}$$

where x_i, for $i = 1, 2, 3, 4$, encodes the lattice site positions of 4 domain walls, and $f(x) = (1+\exp(-x/\sigma))^{-1}$ is a Sigmoid function, which allows for the implementation of Sec. 4.3.3. We also choose the separating potential, and separation $|x_2 - x_3|$, to be large enough so as to render both wires fully disconnected. Note that any time-dependent noise protocols only influence the left wire, and we assume that all low energy bulk excitations occur only in the left wire.

In Fig. 4.8 and 4.9 we oscillate the walls of the left wire. This is implemented by replacing $x_{1,2}$ with a time-dependent function $x_{1,2}(t) = (v_{\max}/\omega)\sin\omega t$, with a velocity $v_{\max}$ and frequency ω that does not break (super-)adiabaticity [KRO13; SS13; Con+19; Coo+21b]. This is the time-dependent perturbation relevant to the arguments presented thus far.

Interactions are modelled using a nearest-neighbour density-density term

$$H_{\text{int}} = \sum_{x=1}^{2L-1} u_x c_x^\dagger c_x c_{x+1}^\dagger c_{x+1}, \tag{4.36}$$

where u_x is the interaction strength. The fully interacting Hamiltonian of interest is $H = H_0 + H_{\text{int}}$. This model can be effectively realized in proximity coupled systems [FK08; LSD10; ORO10; CST11; Ali+11; ST13] which are backed up with extensive experimental evidence [Mou+12; Den+12; Das+12; Fin+13; Chu+13; Alb+16; Den+16; Nad+14; Rub+15; Paw+16; For+19; Ren+19]. For discussions on different types of noise that can occur in these systems see [RL12; BWT12; RBS12; KH13; YF14; Ng15; PD15; Hu+15; Ipp+16; Bro+16; AKL18; Kna+18; Zha+19; KRO13; SS13; Con+19; Coo+21b], these error processes include qubit-

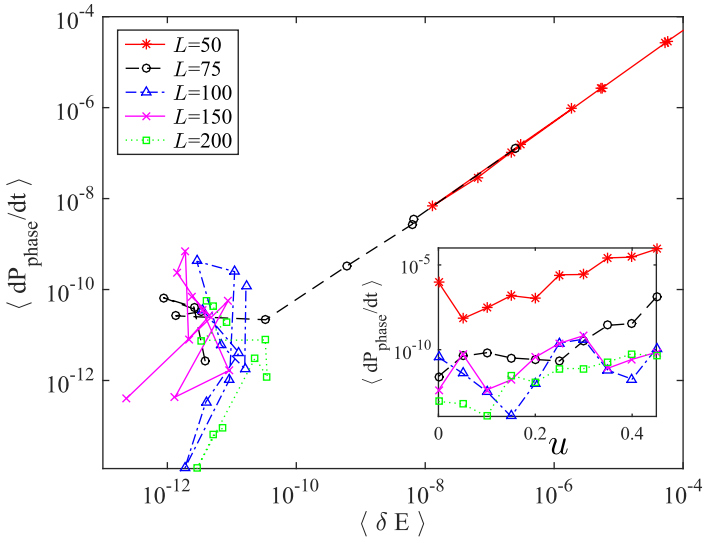

Figure 4.8: Time-averaged rate of phase error as a function of interaction driven ground state splitting. The TDVP-MPS methodology can pick up an interaction driven phase rotation (error) resulting from finite-size ground state splitting of order $\langle \delta E \rangle \sim 10^{-10}$. For system sizes where no appreciable splitting occurs we do not detect any systematic phase rotation. Inset: same data as in the main figure plotted against interaction strength (in units of w). In these simulations we oscillated the left boundary wall (4.35) with frequency $\omega = 1$ and maximum velocity $v_{\max} = 0.1$. The time-averaging was done over an $\mathcal{O}(1)$ multiple of the oscillation period. We also set uniform parameters $\mu = -1.5$ and $\Delta = 0.7$.

loss from non-adiabatic movement of the confining potential, bit-flip and phase flip errors though not the dynamical interaction driven phase error discussed herex.

The non-interacting Hamiltonian, H_0, gives rise to four Majorana zero energy modes Γ_j [Kit01], localised at the domain walls between topological ($\mu_x + V_x \leq 2w$) and non-topological regions encoded by V_x. These Majorana modes can be paired into two Dirac fermionic zero-modes $\hat{\beta}_0^{\mathtt{L/R}} = \frac{1}{\sqrt{2}}(\Gamma_{1/3} + i\Gamma_{2/4})$, one for the left ($\mathtt{L}$) and one for the right wire ($\mathtt{R}$) [1]. From the 4-fold degeneracy associated with these zero-modes we can, without loss of generality, define the topologically protected ground states from the even-parity sector (states with an even number of excitations) as:

$$|00\{0\}\rangle = |0\rangle_{\mathtt{L}} |0\rangle_{\mathtt{R}} |\{0\}\rangle\,, \quad |11\{0\}\rangle = |1\rangle_{\mathtt{L}} |1\rangle_{\mathtt{R}} |\{0\}\rangle\,, \tag{4.37}$$

in which $|\{0\}\rangle = |0\rangle^{\otimes L-2}$ corresponds to the ground state of the bulk modes and $|0\rangle_\alpha, |1\rangle_\alpha$ are the respective unoccupied and occupied Dirac zero-mode for the $\alpha = \mathtt{L/R}$ wire. In discussions, one can effectively forget about the right wire, its purpose is to keep the system in the even-parity sector overall. Henceforth, any mention of even and odd sectors, and wires, in the remainder of the chapter refers to the left wire only.

When local interactions are present ($u_x \neq 0$) we can no longer label many-body

[1] This definition is much the same as in Eq. 4.4, though tailored for this particular example.

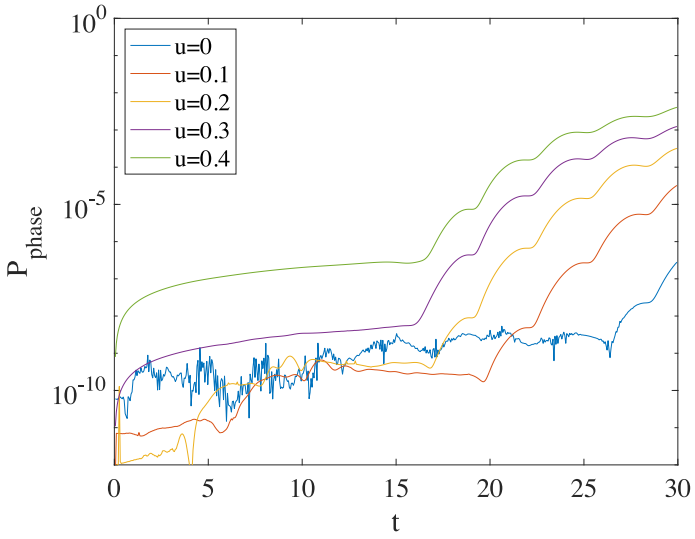

Figure 4.9: Phase error for two oscillating walls. In this simulation we set uniform parameters $w = 1$, $\Delta = 0.8$, $\mu = -1.2$, $L = 70$, $dt = \pi/60$ and a bond dimension of $D = 50$. Both walls were oscillated with frequency $\omega = 1$ and maximum velocity $v_{\max} = 0.1$.

eigenstates of H in terms of their quasi-particle occupation numbers. Nonetheless, as we have shown in Sec. 4.3.3, the system inherits approximate TQO, in part because the topological *ground state* degeneracy holds (up to exponential corrections in the length of the system). Crucially, these conditions hold so long as the interactions do not close the excitation gap [MN18]. On the other hand, the same degeneracy between the excited states can be broken by interactions when the spectrum contains overlapping quasi-particle bands [Kel15a; Mor+17; KMM18; Pel+20], leaving open the possibility for phase errors to be returned to the ground state without the need for quasi-particle propagation. The results presented here are focused solely upon the dynamically generated phase errors that can occur because of bulk spectrum mismatches in an interacting system. However, based on our arguments thus far this mechanism must be suppressed because H has TQO and we numerically confirm this below.

4.4.1 Numerical Verification

We present numerical results for the more general case of a time-dependent perturbation. Specifically, we simulate an oscillating perturbation $\delta(t)$ on the left boundary of the Majorana wire. The phase error itself is quantified by

$$P_{\text{phase}}(t) \equiv \frac{1}{4} |\langle e| U(t) |e\rangle - \langle o| U(t) |o\rangle|^2, \tag{4.38}$$

where $P_{\text{phase}}(t) = 0$ corresponds to no phase error.

Our numerical results are obtained using TVDP-MPS simulations [Hae+11; Pae+19],

also summarised in Ch. 3. In Fig. 4.8, we examine the time-averaged rate of phase error as a function of the the time-averaged energy difference, $\langle \delta E \rangle$, between the approximately degenerate ground states for finite size systems. The ground state energy splitting is time-averaged since the spectrum varies in time due to the time-dependent perturbation. The results clearly show that the numerical methodology is capable of detecting phase error in the dynamics once the ground state splitting is of order $\langle \delta E \rangle \sim 10^{-10}$. When the system is large enough, such that interactions do not make a detectable change to $\langle \delta E \rangle$, we do not see any systematic increase in the phase error.

We also consider the case of a second oscillating perturbation $\delta'(t)$ at the right boundary of the wire. Fig. 4.9 shows that in this case, after a time $T^* \sim L/v$ there is a sudden increase in phase error. This is well understood on a mean field level: excitations originating at one wall return to the ground state space at the other wall, generating a σ^z error in the ground state space (see, e.g., [SS13; Con+19]). Pertinently, before T^* we see no evidence of any other systematic phase error, other than that which can be attributed to the small detectable splitting in the ground state manifold.

To provide some context to the results for the phase error, we present additional numerical TDVP-MPS simulation results for our interacting topological memory. In particular we show numerical results for the qubit-loss error (infidelity) as defined by

$$P_{\text{loss}}(t) \equiv 1 - |\langle e| U(t) |e\rangle|^2 - |\langle o| U(t) |o\rangle|^2. \tag{4.39}$$

In Fig. 4.10 we show the response of the system to a single oscillating boundary across a range of frequencies from the almost adiabatic regime, $\omega \ll E_{\text{gap}}$, up to frequencies far in excess of the topological gap. The results resemble the expected local density of states in the wire, in a given parity sector. We see that repulsive interactions lower the peak resonant frequency (in agreement with an expected reduction to the band edge). We also see that the topological memory degrades slightly across all frequencies. This is somewhat different from what is observed in non-interacting studies, where a lower bulk gap from, say, a reduced p-wave pairing or a lower wire electron density, can result in an improved robustness to high-frequency perturbations, see Fig. 2 (b) of [Con+19] and compare against Fig. 4.10.

4.5 Spectral Correlations: Green's Functions

It is important to note the deviations observed in phase error after T^* are not really driven by the phase error accumulated in the bulk states, but are symptomatic of the fact that the dynamics will eventually turn local operators into non-local ones. However, the fact that we cannot observe phase error before T^*, for all initially local perturbations, implies that the even-odd excited energy spectra in the interacting

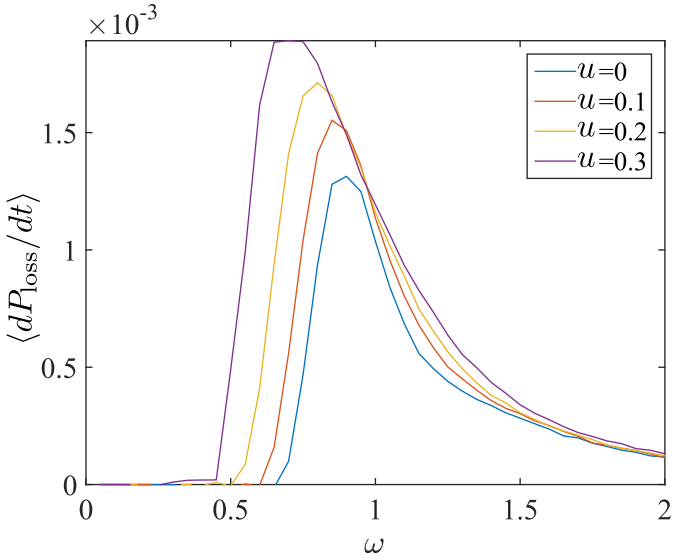

Figure 4.10: Averaged rate of qubit-loss versus frequency of the left boundary wall for 4 different interaction strengths. The frequency covers a wide regime from slow almost adiabatic oscillations, $\omega \ll E_{\text{gap}}$, to high (non-adiabatic) frequencies $\omega \gg E_{\text{gap}}$. The resonance peak shifts to lower frequencies with increasing interaction strength, corresponding to an expected reduction in the gap. Moreover across all frequencies the rate of qubit-loss increases with interaction strength. For this plot we set $L = 50$, $v_{\max} = 0.1$, $w = 1$, $\mu = -1$ and $\Delta = 0.5$.

model are related to a unique aspect of systems with TQO. This is most clearly demonstrated by Fourier transforming the system's Green's functions. These spectral correlation functions are interesting in their own right as tools to probe the properties of a model and demonstrate the power of time evolved tensor network techniques. We provide an appendix (App. A) that demonstrates another application of the techniques used in this section.

Consider, for example, taking

$$e^{i\delta'} = 2c^\dagger_{x'}c_{x'} - \mathbb{1},\ e^{-i\delta} = 2c^\dagger_x c_x - \mathbb{1}, \tag{4.40}$$

in $U(t)$ in (4.25) and define the Green's function for the a-sector as

$$G^a(x, x', t) \equiv e^{iE_0 t}\langle a|U(t)|a\rangle\ , \tag{4.41}$$

which depends on the operator positions, x and x', and the time t. For convenience, we fix $x = 1$ (the left boundary of the wire) or $x = L/2$ (the middle of the wire) in what follows, and consider G^a as a function of (x', t) only.

No phase error implies that the difference, $D_{eo} \equiv G^e - G^o$, is exponentially suppressed for times $|t| < T^*$, and hence so is the integral of D_{eo} over $[-T^*, T^*]$. One can then verify that this implies that the Fourier transform, $\mathcal{F}[D_{eo}](k, \omega)$, is exponentially suppressed when convolved with the Fourier transform, $\mathcal{F}[\Theta]$, of some cut-off or box function, e.g. $\Theta(t) \sim 1$ for $|t| < T^*$ and ~ 0 otherwise. In other words,

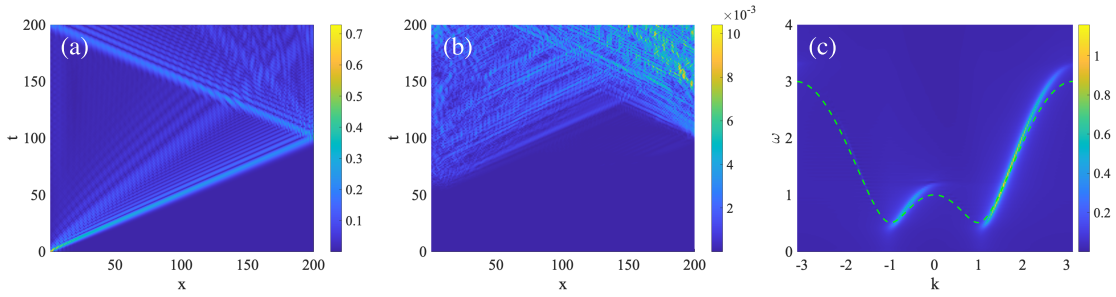

Figure 4.11: The single particle Green's functions (a) $|G^e(1,x,t)|$ and (b) the difference between sectors $|D_{eo}| = |G^e(1,x,t) - G^o(1,x,t)|$, which shows that the two correlators are the same up to exponentially small corrections for a time T^*. (c) Introducing a cut-off in time, $\Theta(t) = e^{-.03|t|}$, leads to spectral density $\mathcal{F}[\Theta \times G^a](k,\omega)$ that is weighted around positive group velocities. The dashed line shows the free single particle dispersion for comparison. The resolution of $\mathcal{F}[\Theta \times G^e]$ is set by $1/L$ for momenta and $1/T^* \sim v/L$ for frequency. At this resolution there are only exponentially small differences between $\mathcal{F}[\Theta \times G^e]$ and $\mathcal{F}[\Theta \times G^o]$.

while the spectral functions, $\mathcal{F}[G^a](k,\omega)$, differ between sectors, these differences are washed out by smearing, or convolving, with $\mathcal{F}[\Theta]$. For a box function, with cut-off T^*, $\mathcal{F}[\Theta]$ has the form of a sinc function with width $\sim 1/T^*$, and hence a convolution with $\mathcal{F}[\Theta]$ acts to smear $\mathcal{F}[G^a](k,\omega)$ by this width in the ω direction. It is important to note that this is not a perturbative statement.

4.5.1 Extension to Fermionic & Multi-particle Operators

The analytical arguments above rest heavily on the Lieb-Robinson bounds, which are formulated as commutation relations between local operators. Fermionic operators such as c_x are non-local, as they can be seen as strings of local operators through the Jordan-Wigner representation. Even powers of such fermionic operators, on the other hand, are local. Our analytical results, therefore, only pertain to the latter, and hence can only address time-dependent changes within parity preserving Hamiltonians.

Despite this, in Fig. 4.11 we illustrate the Green's functions and their FT's for fermionic operators

$$e^{i\delta'} = c^\dagger_{x'} + c_{x'}, \; e^{-i\delta} = c^\dagger_1 + c_1 \tag{4.42}$$

in $U(t)$ in (4.25) and define the Green's functions as before. The resulting resolution in reciprocal space $[k \times \omega]$ is of the order $[1/L \times v/L]$. One can estimate from Fig. 4.9 that the Lieb-Robinson speed $v \propto u$, and hence, while increased interactions imply a coarser grained energy correlation between sectors, making the system larger allows us to systematically improve this bound. The numerical results, in particular the cancellations of even and odd Green's functions up to a time T^* (Fig. 4.11 (b)), indicate that it may be possible to extend the analytical argument to fermionic perturbations. The work in [NSY18; HK06] likely offers a good starting point for

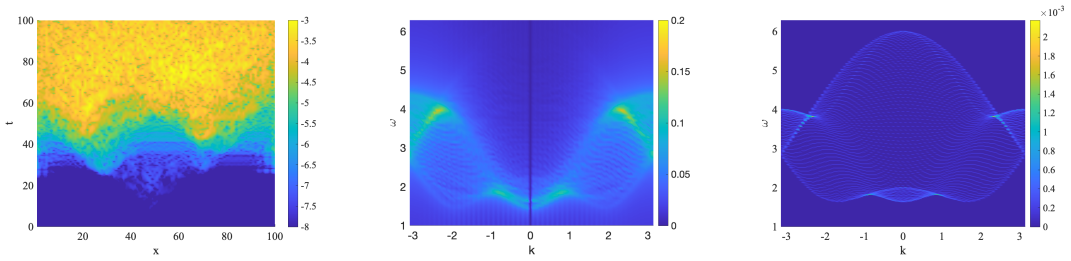

(a) $\log_{10}|G^e(x,t) - G^o(x,t)|$ (b) $\mathcal{F}(\Theta \times G^e)$ (c) 2-particle density

Figure 4.12: (a) The difference $|G^e(x,t) - G^o(x,t)|$ is negligible up to a time $t = T^*$. (b) As a result, $\mathcal{F}(\Theta \times G^e) \approx \mathcal{F}(\Theta \times G^o)$ for a cut-off function $\Theta(t)$ that drops off after T^*. (c) The total momentum resolved 2-particle spectral density of the non-interacting system ($u_x = 0$) for a system size of $L = 100$.

such a generalisation.

For multi-particle Green's functions the situation is similar except that T^* should have a quantity proportional to the spatial extent, l, of the local operators subtracted from it, i.e. $T^* \to T^* - l/v$. For the spatial resolution, although there are now many more states participating in the evolution, we also have many more possible local operators to choose from. As a demonstration, we show some results for the 2-particle spectral densities. We set $e^{i\delta'} = 2c^\dagger_{x'}c_{x'} - \mathbb{1}$ and $e^{-i\delta} = 2c^\dagger_x c_x - \mathbb{1}$ in $U(t)$ in Eq. 4.25 and define the Green's function for the a-sector as in Eq. 4.41. In this case, we fix $x = L/2$ (the middle of the wire) so as to not couple to the zero-modes (which tends to blur our spatial Fourier transform) and then plot $G^e(L/2, x', t)$ and the difference $D_{eo} \equiv G^e(L/2, x', t) - G^o(L/2, x', t)$, which is given in a log scale for clarity. Fig. 4.12(a) shows, up to numerical errors of $\mathcal{O}(10^{-8})$ that D_{eo} is exponentially suppressed for some initial time T^*. Furthermore, this time scales with the system size L.

Fig. 4.12(b) shows the shape of the 2-particle spectral density as a function of the total momentum, after cutting off the Green's function for $t > T^*$. Fig 4.12(b) can be compared against the exact density determined from the single particle solutions of a periodic system, given in Fig. 4.12(c).

The energetic resolution obtained in Fig. 4.12(b) is effectively governed by the Lieb-Robinson velocity and L. However, as we stressed above in the constraints section, we are free to choose from a large number of local operators with which we can generate a much larger set of spectral constraints (Eq. 4.28). For example, we could generate the entire 3-parameter functions $G^a(x, x', t)$ and perform a 2D Fourier transform on the first two spatial components, from which we could obtain a tighter k-space resolution.

Remarks

In this chapter we have examined a process wherein undetectable interaction induced errors could be introduced into a topological quantum memory. However, by leveraging the topological quantum order (TQO) property and, in particular, the inheritance of TQO between adiabatically connected systems we have argued that this property protects against such error processes. This protection persists up to a characteristic time scale which scales with the system size. Thus, in principle, these errors can be circumvented by utilising a sufficiently large system. Additionally, this argument has been verified in detail numerically using time-evolved tensor network and Green's function methods. Primarily, we used the density matrix renormalisation group (DMRG) technique to access the system's groundstate. Subsequently, we employed the time dependent variational principle (TDVP) technique to generate time evolution of the system. The same techniques are applied to access the Green's functions and in some cases examined under Fourier transformation.

Next, rather than considering the p-wave superconductor with interactions, we expose the model to dissipation and examine the effect of combining quantum transport with a stochastic, or classical, transport model.

Chapter 5

Quantum Exclusion Process

A valuable way of understanding a many-body system is to characterise its phase diagram and the associated transitions. This approach is useful across a broad class of systems, from the classical to the quantum realms, at zero-temperature, and both in- and out-of thermal equilibrium. Although typically such domains are clearly separated, there are situations where phase transitions in one such domain can influence the behaviour of another. Indeed, one can investigate the interplay between the different domains if one can put both in the same framework.

A useful framework to address such issues is the Lindblad master equation [GKS76; Lin76], through which one may combine both Hamiltonian and classical stochastic dynamics. This methodology has been used, for example, to explore mixed classical-quantum transport [Pro08; PP08; Eis11; TWV12]. However, despite this success, it is difficult to find systems where an interesting interplay can be maintained between classical/stochastic and quantum phases. For example, for a spin chain with stochastic processes encoded in the Lindblad jump operators only at the boundary spins, the typical steady state behaviour is largely dictated by the quantum properties of the bulk Hamiltonian (see e.g. [Pro08; PP08]). On the other hand, if bulk stochastic processes are also allowed, these typically dominate [Eis11; TWV12] and leaves little to no trace of the quantum phase transition to survive at late times.

In this chapter we discuss a spin chain model where both classical stochastic and quantum phases are simultaneously relevant to a degree that allows for a genuine interplay between them in the late-time properties. The model is a combination of the transverse XY (TXY) Hamiltonian[1], or equivalently the Kitaev chain [Kit01], with a one-way/unidirectional classical stochastic hopping process, modelled by the totally asymmetric simple exclusion process (TASEP). We refer to the combination of these two models as the TXY-TASEP.

The TASEP, considered in isolation, has a phase diagram for its non-equilibrium steady state (NESS) that is determined by the stochastic "hop-on/hop-off" rates at its boundaries. The TXY Hamiltonian undergoes a quantum phase transition in

[1]See also Ch.2 and Ch.4 for more discussion and work related to this model.

its ground state as the transverse magnetic field parameter is increased, assuming a non-zero XY anisotropy parameter Δ, at $\Delta = 0$ the model is critical for any magnetic field value. In fact, this quantum phase transition (QPT) has already been alluded to in Ch. 4 where we described the representative ground state(s) associated with each phase of the model.

When the two models are combined, we find that for zero anisotropy, $\Delta = 0$, the NESS retains many of the properties associated with the classical TASEP and, as such, its behaviour can be essentially controlled via the stochastic boundary rates. Indeed, the steady state in this case is largely indistinct from the TASEP steady state with no additional processes. On the other hand, in the regime associated with the anti-ferromagnetic (topological) phase of the XY model, the steady-state more closely resembles a perturbed infinite temperature state, but where the stochastic boundary rates do still dictate some key properties of the perturbation away from this maximally mixed state.

From the perspective of the TASEP phase diagram (see e.g. [DDM92] and Fig. 5.2), we see that steady states of the low- and high-density phases are far more susceptible to the pair creation/annihilation associated with the XY anisotropy terms, see Fig. 5.8. These low- and high-density steady states as the name suggests are states with respectively few or many occupied lattice sites. This effect is much less pronounced in the maximal current phase, where the tendency of the XY anisotropy to drive the system towards half-filling is complementary to the maximal current micro-states that are themselves half-occupied states.

The TXY-TASEP system does not allow for a direct analytical treatment, as available for related models [GS92; Kim95; GE05; GE06; Pro08; ŽP10; CRS10; CR12; LP14; Žni15; Pro16; BDS15; Zha+19; EP20; ISN21; RE21]. Our results are therefore arrived at by using a combination of numerical methods and approximate approaches. On a numerical level we apply matrix product state (MPS) methods [NCS02; Sch11; Pae+19] to study steady states and their particle currents [TWV12]. Moreover, we use third quantization [Pro08; ŽP10], and exploit the block structure that occurs naturally via the associated canonical Majorana representation [GC12; Kel15a; Kel15b], to make concrete perturbative statements.

An overview of the chapter is as follows: In section 5.1 we introduce key aspects of the transverse XY and TASEP models, providing detail of our main results and the physical picture that emerges. In section 5.2 we detail our main numerical results, focusing in particular on the relationship of the non-equilibrium steady state (NESS) with both the TASEP steady state and the maximally mixed state. In section 5.3 we will describe preliminary examinations on the effects of the anisotropy parameter Δ on the current of the steady state. In particular how a region of the lattice with non-zero Δ can effect the resultant current profile in the steady state from what is known in the classical model. We devote Chapter 6 to analysing the Liouvillian gap

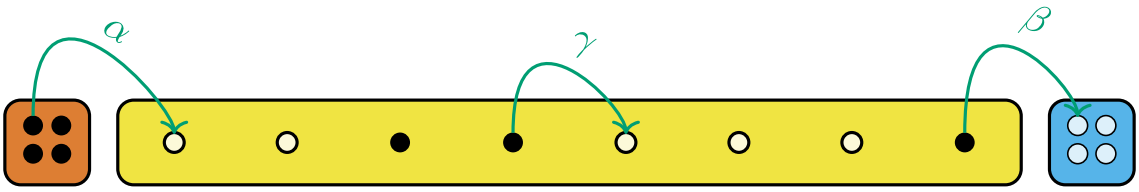

Figure 5.1: In this figure we schematically describe the totally asymmetric exclusion process. The green arrows show processes that are allowed within the TASEP model (with $\gamma = 1$ usually). Additional processes with matching weights in the left direction recovers the SSEP. The orange and blue regions on either side of the lattice (coloured yellow) denote infinite baths of particles and holes respectively and are not explicitly modelled.

of the TXY-TASEP model and related models.

5.1 Model and methods

To begin we briefly review the exclusion process as it is usually classically defined. Details on obtaining the steady state solution for the TASEP via a matrix product ansatz (MPA) solution are reserved for App. C. Therein also, we explain how to promote the dynamics of this model to that of a dissipative process via Kraus operators on diagonal density matrices to provide a compatibility with the dynamics of the transverse XY model. This second model has been described in Ch.2 and analysed in a fermionic context in Ch. 4. We then combine them to create the TXY-TASEP model which is the model of interest in this chapter and part of the next, Ch. 6.

5.1.1 Review of TASEP

The totally asymmetric exclusion process (TASEP) is a paradigmatic model of stochastic transport in one dimension. Schematically, we summarise the processes which constitute this model in Fig. 5.1. One of the important properties of the model is that it admits a MPA solution for its steady state. We provide the full detail on how one obtains this solution in App. C. This ansatz solution captures many of the salient features of the model as the steady state itself is the primary descriptor of the late time behaviour. Moreover, this MPA allows one to determine directly the steady state current which in turn dictates the phase diagram of the model. We can see from examining the current that the model splits into three main phases that are determined by the boundary rates, α and β.

This dependence on the boundary rates is shown in the steady state phase diagram Fig. 5.2 and can be understood intuitively from the processes given in Fig. 5.1. We can see that when γ, the bulk hopping rate, is set to one that any particle in the bulk always moves to the right. This is the set up we maintain throughout for this model. Then if there is an inequality between α and β there will be an inequality

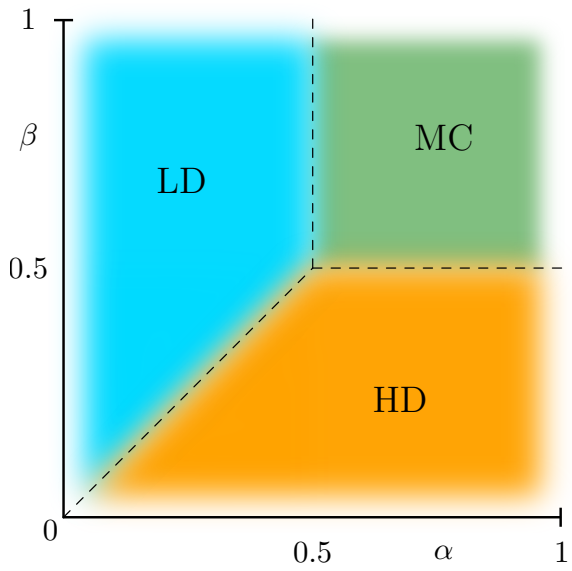

Figure 5.2: The TASEP phase diagram which depends only on the boundary rates α and β. For both rates greater than $\frac{1}{2}$, the steady state is described as being in the maximal current (MC) phase. For $\alpha < \frac{1}{2}$ and $\beta > \alpha$ the steady state is in the low-density (LD) phase. Similarly, for $\beta < \frac{1}{2}$ and $\alpha > \beta$ the steady state is in the high-density (HD) phase.

between the amount of particles entering and leaving the lattice. More particles entering rather than leaving, $\alpha > \beta$, causes the lattice to fill and therefore the steady state becomes a high-density state. Conversely, if the rate of particles leaving is greater than the rate of particles entering, $\alpha < \beta$, this causes a deficit of particles and thus a low-density steady state. The remaining phase is the maximal current phase wherein both boundary rates are greater than $\frac{1}{2}$. In this case the steady states are half filled states. One such state is the alternately occupied/unoccupied state where at every instance of time all particles are allowed to move to the right by one lattice site. Evidently, this is the situation that allows for the largest current to pass though the system by the allowed TASEP processes.

We derive the MPA and the associated currents based on [DDM92; Der+93] in full detail in App. C. At least at the level of the steady states then, we can construct them in a form already amenable to the machinery we have in place for simulating quantum systems. In particular we can compare the MPA states of TASEP against those steady states obtained from our numerical simulation, namely DMRG as described in Ch. 3.

The next step to bring TASEP onto the same footing as the TXY model is to promote the stochastic dynamics to one that is compatible with the dynamics of the TXY model. Usually TASEP is formulated as a discrete time process. However, we can reformulate the entire process within the conceptual framing of a quantum channel via Kraus operators [NC00]. We detail the steps to achieve this outcome in App. C. To summarise, we embed the classical state (or configuration) at a given time, t, onto the diagonal of a density matrix, $\rho(t)$. The dynamics are then encoded

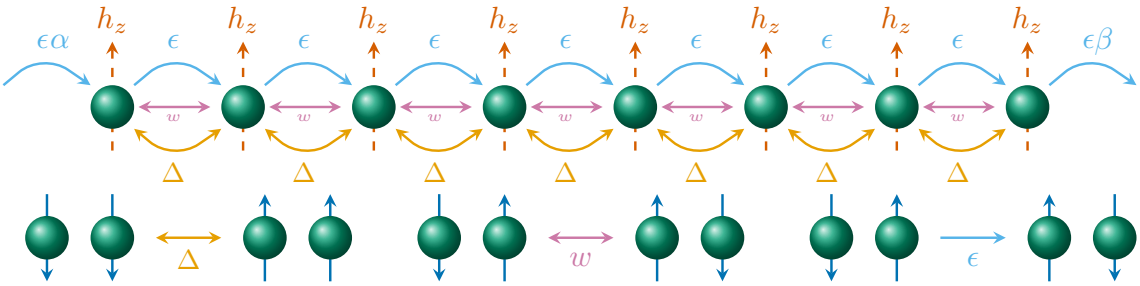

Figure 5.3: Our model is a chain of two-level quantum systems evolving by the combination of the transverse XY Hamiltonian (TXY) and the totally asymmetric simple exclusion process (TASEP). In the lower layer we show explicitly the allowed transitions between nearest neighbour spin configurations with the associated model parameters indicated. In addition we typically set $w = 1$ throughout.

into a set of Kraus operators, $\{K_i^{(j)}\}$, for each lattice site, i, that act as

$$\rho(t + dt) = \sum_i \sum_j \hat{K}_i^{(j)} \rho(t) \hat{K}_i^{(j)\dagger}. \tag{5.1}$$

For the specific forms of these Kraus operators, see App. C. We then recover a continuous time master equation from this in the limit as $dt \to 0$. This master equation has the form

$$\begin{aligned} \frac{d}{dt}\hat{\rho}(t) &= \frac{1}{N+1}\left(\alpha \mathcal{D}[\hat{\sigma}_1^+] + \beta \mathcal{D}[\hat{\sigma}_N^-]\right) \\ &+ \frac{1}{N+1}\left(\gamma \sum_{i=1}^{N-1} \mathcal{D}[\hat{\sigma}_i^- \otimes \hat{\sigma}_{i+1}^+]\right)(\hat{\rho}(t)), \end{aligned} \tag{5.2}$$

where $\mathcal{D}[\hat{\ell}](\hat{\rho}) \equiv \hat{\ell}\hat{\rho}\hat{\ell}^\dagger - \frac{1}{2}\hat{\ell}^\dagger\hat{\ell}\hat{\rho} - \frac{1}{2}\hat{\rho}\hat{\ell}^\dagger\hat{\ell}$. This form of the TASEP dynamics precisely matches the dissipative part of a Lindblad master equation [GKS76; Lin76], see also Ch 2.

5.1.2 Combining the TXY & TASEP Models

Now that we have the classical dynamics expressed as a quantum channel we can add the quantum dynamics to have both the TXY and TASEP models together. As already indicated both are separately well understood as paradigmatic models for transport in one dimensional systems. The XY spin model with a transverse magnetic field can be solved exactly by mapping to a free fermion model with superconducting terms present due to the XY anisotropy. Likewise, the classical TASEP is solvable in the sense that there is an ansatz solution for the NESS [DDM92; Der+93].

We thus incorporate both models into a single Lindblad master equation [GKS76;

Lin76]

$$\begin{aligned} \frac{d\hat{\rho}}{dt} &= -i\lambda\mathbb{H}(\hat{\rho}) + \epsilon\mathbb{L}(\hat{\rho}), \\ &= \mathcal{L}(\hat{\rho}). \end{aligned} \tag{5.3}$$

The TXY model is represented by the following commutator $\mathbb{H}(\rho) = [\hat{H}, \hat{\rho}]$, with overall strength λ and the Hamiltonian

$$\hat{H} = -h_z \sum_{j=1}^{N} \hat{\sigma}_j^z + \sum_{j=1}^{N-1} \left(\frac{1+\Delta}{2} \hat{\sigma}_j^x \hat{\sigma}_{j+1}^x + \frac{1-\Delta}{2} \hat{\sigma}_j^y \hat{\sigma}_{j+1}^y \right). \tag{5.4}$$

Here h_z is the transverse magnetic field and $0 \leq \Delta \leq 1$ the anisotropy parameter. We note that if $\Delta \neq 0$, the TXY-Hamiltonian has a quantum phase transition at $|h_z| = 1$ (see Fig. C.2(a)). The anisotropic terms can be rewritten as $2\Delta(\hat{\sigma}_i^+ \hat{\sigma}_{i+1}^+ + \hat{\sigma}_i^- \hat{\sigma}_{i+1}^-)$, so they can be seen to introduce pair creation/annihilation when Δ is non-zero. We make this statement in the view that, after a Jordan-Wigner transformation, $\hat{H}$ can be rewritten in terms of spinless fermions, which is known as the Kitaev chain [Kit01]. Then the spin model can be reinterpreted as particles hopping on a one dimensional lattice where spin-up corresponds to an occupied state and spin-down to an unoccupied state. This further allows us to leverage our intuition of particles (whether fermions or hard-core bosons) hopping along a lattice in addition to spin excitations.

In the second term of Eq. 5.3 we have the totally asymmetric simple exclusion process (TASEP), with overall strength ϵ and modelled by the Lindblad operator [TWV12]

$$\mathbb{L}(\hat{\rho}) = \alpha\mathcal{D}[\hat{\sigma}_1^+](\hat{\rho}) + \beta\mathcal{D}[\hat{\sigma}_N^-](\hat{\rho}) + \sum_{j=1}^{N-1} \mathcal{D}[\hat{\sigma}_j^- \hat{\sigma}_{j+1}^+](\hat{\rho}), \tag{5.5}$$

where $\mathcal{D}[\hat{\ell}](\hat{\rho}) = \hat{\ell}\hat{\rho}\hat{\ell}^\dagger - \frac{1}{2}\hat{\ell}^\dagger\hat{\ell}\hat{\rho} - \frac{1}{2}\hat{\rho}\hat{\ell}^\dagger\hat{\ell}$. The TASEP has three distinct phases with respect to α and β (see Fig. C.2(b)):

$$\begin{aligned} \text{MC phase:} &\quad \alpha > 1/2 \quad \text{and} \quad \beta > 1/2, \\ \text{LD phase:} &\quad \alpha < 1/2 \quad \text{and} \quad \beta > \alpha, \\ \text{HD phase:} &\quad \beta < 1/2 \quad \text{and} \quad \beta < \alpha. \end{aligned} \tag{5.6}$$

This phase diagram can be deduced from the exact MPA solution for the TASEP steady state, with infinite dimensional matrices [DDM92]. However, the exact solution can also be accurately approximated by a MPS with a relatively small bond dimension [TWV12]. In this way we can generate an efficient matrix product state description of the TASEP steady state in a way that can be further extended to find the steady state $\hat{\rho}_{\text{NESS}}$ of the full Liouvillian $\mathcal{L}$, where an exact MPS or ansatz is

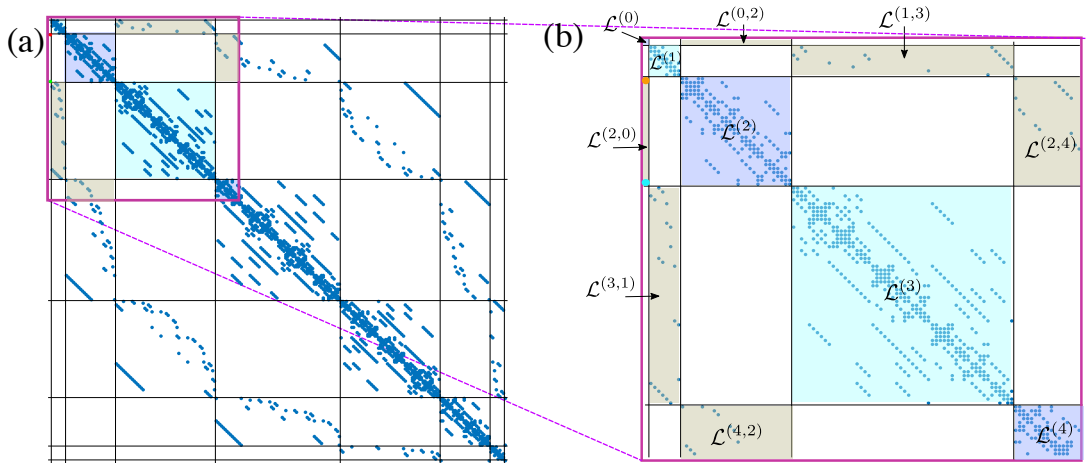

Figure 5.4: (a) The structure of $\mathcal{L}$ in the canonical basis for a system size of $N = 4$. (b) The $s = 0$ block that corresponds to the maximally mixed/thermal state is connected via terms dependent on the bulk and boundary driving to states $|\phi_L\rangle\!\rangle = |\gamma_1\gamma_2\rangle\!\rangle$, $|\phi_R\rangle\!\rangle = |\gamma_{N-1}\gamma_N\rangle\!\rangle$. These elements are highlighted, on the left within the $\mathcal{L}^{(2,0)}$ sub-block, by the upper *orange* dot and lower *cyan* dot, which have respective values $-\epsilon(\beta - 1/2)$ and $\epsilon(\alpha - 1/2)$.

not known. Away from the purely classical model, we can obtain the full NESS by a density matrix renormalisation group (DMRG) implementation modified for open quantum systems [OV08; PŽ09; JNK13].

We note that Eq. 5.5 is part of a continuous-time master equation, while TASEP is often considered as a discrete time stochastic process. Additionally, instead of considering a master equationn, by viewing the TASEP as a discrete time Markov process one can translate the model to a non-Hermitian spin chain for which Bethe anatz methods can be applied to determine analytic results, see e.g. [GS92; Kim95; GE05; GE06]. We note also that our approach is not the only one with the aim to introduce quantum effects into classical exclusion processes. A number of recent works have proposed quantum modified versions of the SSEP [BJ19; BP21] and ASEP [Ber+22] which employ a non-Hermitian Hamiltonian formulation of the exclusion process that introduces noise in the particle hopping amplitudes.

In the remainder of this chapter we present our findings on the steady state and the current associated as obtained from the corresponding TXY-TASEP model's Liouvillian superoperator $\mathcal{L}$, as we vary the model parameters, including the parameter ϵ/λ which controls the relative strength of the quantum TXY model and the classical TASEP in Eq. 5.3. We set $\lambda = 1$ for the remainder of this chapter, essentially allowing λ to define the unit of frequency. We note that the steady state of $\mathcal{L}$ for the isotropic Hamiltonian, with $h_z = \Delta = 0$ and TASEP, has been previously explored by other methods [TWV12]. Also, the case of zero bulk TASEP hopping has been explored in the more general scenario where particles can hop on or off either end of the chain [PP08]. Before getting into the results we must make explicit the superoperator of the model. While the generalities of third quantization

have been summarised in Ch. 2 we make specific the transformations implemented for our results to be obtained.

5.1.3 TXY-TASEP Superoperator

In the following, it will be useful to represent the superoperator $\mathcal{L}$ in Eq. 5.3 as a matrix that acts on a vectorized representation of the quantum state $\hat{\rho}$. The general approach for a superoperator formulation has been covered in Ch. 2. In this instance we also choose a convenient basis of orthonormal operators $\{\Gamma_i\}$ with respect to the Hilbert-Schmidt inner product, i.e., $\langle\langle\Gamma_i|\Gamma_j\rangle\rangle \equiv \mathrm{Tr}\Big(\Gamma_i^\dagger\Gamma_j\Big) = \delta_{ij}$. We choose the so-called canonical Majorana basis [GC12; Kel15a; Kel15b]:

$$\begin{aligned}
\Gamma^{(0)}: &\quad \mathbb{I}/\sqrt{2^N}, \\
\Gamma^{(1)}: &\quad \gamma_1/\sqrt{2^N}, \gamma_2/\sqrt{2^N}, \ldots, \gamma_{2N}/\sqrt{2^N}, \\
\Gamma^{(2)}: &\quad i\gamma_1\gamma_2/\sqrt{2^N}, i\gamma_1\gamma_3/\sqrt{2^N}, \ldots, i\gamma_{2N-1}\gamma_{2N}/\sqrt{2^N}, \\
&\quad \text{etc.}
\end{aligned} \tag{5.7}$$

These Majorana operators are defined from the spin operators as:

$$\gamma_{2n-1} = \left(\prod_{k=1}^{2n-2}\sigma_k^z\right)\sigma_{2n-1}^x,\ \gamma_{2n} = \left(\prod_{k=1}^{2n-1}\sigma_k^z\right)\sigma_{2n}^y, \tag{5.8}$$

for $n = 1, 2, \ldots, N$. This is simply the combination of the Jordan-Wigner transformation shown in Ch. 2 and the definition of a Majorana operator from Sec. 4.1. As shown in Eq. 5.7, an element $\Gamma_a^{(s)}$ of this basis is a product of Majorana operators, where the upper index s is the number of γ's in the product, and a labels the basis elements within each s subspace. The factors of $1/\sqrt{2^N}$ ensure the normalisation $\langle\langle\Gamma_a^{(s)}|\Gamma_b^{(s')}\rangle\rangle = \delta_{ss'}\delta_{ab}$. In this basis the Liouvillian superoperator $\mathcal{L}$ has the matrix elements

$$\mathcal{L}_{ab}^{(s,s')} = \langle\langle\Gamma_a^{(s)}|\mathcal{L}(\Gamma_b^{(s')})\rangle\rangle, \tag{5.9}$$

where the upper indices (s, s') label blocks in the matrix and the lower indices a, b label the matrix elements within the (s, s') block [see Fig. 5.4 (a,b) for an illustration of the matrix structure]. Likewise, the vectorized density operator in this operator basis has the elements $\rho_a^{(s)} = \mathrm{Tr}\Big(\Gamma_a^{(s)}\rho\Big)$.

The superoperator $\mathcal{L}$ has some other interesting features that are worth pointing out. First, we note that it preserves the parity of the label s (i.e., the operator $\mathcal{L}(\Gamma^{(s)})$ is a linear combination of operator basis elements with the same parity as s). This is true provided that the Hamiltonian preserves the parity, which is the situation we have for the TXY Hamiltonian. This is seen clearly in Fig. 5.4(a,b), where $\mathcal{L}^{(s,s')} = 0$ if s and s' have different parity. Also, we highlight the $s = s' = 0$

block [upper-left corner of Fig. 5.4(a,b)], corresponding to the operator basis element $\Gamma^{(0)} = \mathbb{I}/\sqrt{2^N}$. Using the master equation (5.3), it is straighforward to show that this matrix element is always zero $\mathcal{L}^{(0)} = 0$. Similarly, it can be shown that this element is only connected to two others in the $\mathcal{L}^{(2,2)}$ block, via the off-diagonal block $\mathcal{L}^{(2,0)}$ [as illustrated in Fig. 5.4(b)]. The two non zero elements are:

$$\langle\langle 2^{-\frac{N}{2}}\gamma_1\gamma_2|2^{-\frac{N}{2}}I\rangle\rangle = \epsilon(\alpha - 1/2), \tag{5.10}$$

$$\langle\langle 2^{-\frac{N}{2}}\gamma_{2N-1}\gamma_{2N}|2^{-\frac{N}{2}}I\rangle\rangle = -\epsilon(\beta - 1/2), \tag{5.11}$$

which are highlighted in Fig. 5.4. If these two matrix elements are zero (i.e., if $\alpha = \beta = 1/2$ or if $\epsilon = 0$) then the maximally mixed state $\rho \sim \Gamma^{(0)} \sim \mathbb{I}$ is a valid steady state of the Liouvillian. If both matrix elements are non-zero but small then we expect the NESS to be close to the maximally mixed state. This intuition is based partly on the structure produced in our expression of the Liouvillian superoperator (see Fig. 5.4 and Eq. 5.9) and on prior work for a related system which allows for a NESS ansatz [Žni11] with the maximally mixed state as the zeroth order state. We will exploit this feature later in Section 5.2.2 to perturbatively estimate the steady state and later the gap scaling in the small ϵ limit in Section 6.1.

Furthermore, generically speaking, for a Lindblad equation comprised of a Hamiltonian which is quadratic and Lindblad jump operators that are linear in fermion operators one finds that the Liouvillian superoperator admits such a (near-)block diagonal matrix form. As a result, the superoperator can be solved block-by-block. There are cases however where exact treatments of the superoperator are possible despite the underlying Lindblad equation not being entirely quadratic. Asymmetric boundary driving [Pro08; PP08] and quartic stochastic processes [Eis11; Žun14] are two such examples. Although similar approaches cannot be directly applied to TXY-TASEP, we will show that using the canonical representation yields a useful block structure which allows for perturbative estimation of the Liouvillian gap in the weak classical regime in Ch. 6.

5.2 Non-Equilibrium Steady State

The non-equilibrium steady state (NESS) is defined as the state $\hat{\rho}_{\text{NESS}}$ for which $\mathcal{L}(\hat{\rho}_{\text{NESS}}) = 0$. The case for studying the NESS is straightforward: it governs the system's late time behaviour. There are various examples of open quantum spin chains for which the NESS can be calculated exactly through analytical methods. One important class are those for which matrix product ansatz solutions exist for the NESS [Žni10; Žni11; Pro11; KPS13; Pro15]. This includes, for example, the purely classical TASEP ($\lambda = 0$ in our model) for which a matrix product ansatz solution was found by Derrida *et al.* [DDM92]. Other formulations allow one to utilise the methodology from the Bethe Ansatz [GS92; Kim95; GE05; GE06; CRS10; CR12;

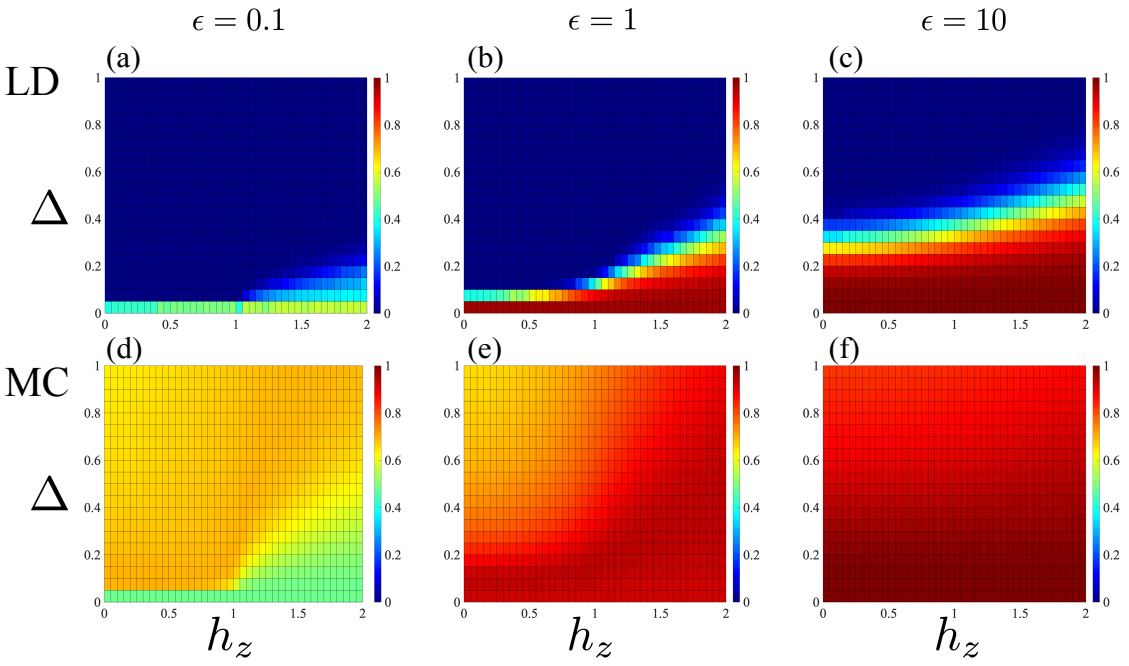

Figure 5.5: These figures contain numerical data for the overlap, as defined in Eq. 5.12, for three cases of $\epsilon = \{0.1, 1, 10\}$ and capturing features of the three TASEP phases. In (a)-(c), for the low density (LD) phase [$\alpha = 0.1$ & $\beta = 0.3$] we observe a strong effect on the overlap with changing Δ, in the high density (HD) phase one can see similar features. In (d)-(f), for the maximal current (MC) phase [$\alpha = 0.7$ & $\beta = 0.9$] we show the relatively weak effect of increasing Δ, note the restricted color range of values for this row of figures. For all figures we have a system size of $N = 50$.

LP14; Pro16; BDS15; Zha+19; EP20; ISN21] or operator quantization [Pro08; PP08; Eis11]. However, these exact analytical methods cannot be applied to the full TXY-TASEP to determine the NESS. Instead, in this section we employ the density matrix renormalisation group (DMRG) algorithm (Sec. 3.3) to numerically determine $\hat{\rho}_{\text{NESS}}$.

5.2.1 Obtaining NESS from DMRG

We begin by comparing $\hat{\rho}_{\text{NESS}}$ to the classical TASEP steady state $\hat{\rho}_{cl}$, defined as the state for which $\mathbb{L}(\hat{\rho}_{cl}) = 0$ (where $\mathbb{L}$ is defined in Eq. 5.5). For given TASEP boundary hopping rates (α, β) we know from the work of Derrida *et al.* [DDM92] how to construct $\hat{\rho}_{cl}$ from its exact matrix product ansatz. However, introducing the Hamiltonian term in Eq. 5.3 generically modifies the steady state so that it is no longer equal to the classical TASEP steady state $\hat{\rho}_{cl}$. For a given (α, β) we quantify the difference between $\hat{\rho}_{\text{NESS}}$ and $\hat{\rho}_{cl}$ with the overlap

$$\mathcal{O}(\hat{\rho}_{\text{NESS}}, \hat{\rho}_{cl}) = \frac{\langle\langle \rho_{\text{NESS}} | \rho_{cl} \rangle\rangle}{\sqrt{\langle\langle \rho_{\text{NESS}} | \rho_{\text{NESS}} \rangle\rangle \langle\langle \rho_{cl} | \rho_{cl} \rangle\rangle}}, \tag{5.12}$$

where $\langle\langle A|B\rangle\rangle = \text{Tr}\left(\hat{A}^\dagger \hat{B}\right)$ is the Hilbert-Schmidt inner product for operators $\hat{A}$ and $\hat{B}$. This overlap takes values in the interval $\mathcal{O} \in [0, 1]$, with $\mathcal{O} = 1$ if $\hat{\rho}_{\text{NESS}} = \hat{\rho}_{cl}$

and $\mathcal{O} = 0$ if the states $\hat{\rho}_{\text{NESS}}$ and $\hat{\rho}_{cl}$ are orthogonal (i.e., $\langle\langle \rho_{\text{NESS}} | \rho_{cl} \rangle\rangle = 0$).

Assuming (α, β) in the LD phase, in Fig. 5.5 [(a)-(c)] we plot the overlap $\mathcal{O}$ as a function of the TXY-model parameters (Δ, h_z), for the three different stochastic strengths $\epsilon = \{0.1, 1, 10\}$. For $\epsilon = 10$ the Liouvillian $\mathcal{L}$ is dominated by the TASEP component of the model. It is not surprising, therefore, that in Fig. 5.5(c) we see large regions in parameter space where $\mathcal{O} \approx 1$. In particular, for small anisotropy Δ we see that $\hat{\rho}_{\text{NESS}}$ and $\hat{\rho}_{cl}$ are very similar. This is consistent with previous work by Temme *et al.* [TWV12], which considered the transport properties for the TXY-TASEP in the special case of zero anisotropy $\Delta = 0$, and found that the isotropic Hamiltonian has little effect. However, even for $\epsilon = 10$ where TASEP dominates, we see in Fig. 5.5(c) that increasing the TXY anisotropy parameter to relatively small values $\Delta \gtrsim 0.5$ can lead to a significant decrease in the overlap $\mathcal{O}$. This suggests that, in the LD phase, the TXY anisotropy Δ plays an important role in driving the NESS away from the TASEP steady state. Similar results are obtained for (α, β) chosen in the HD phase.

When $\epsilon = 0.1$, on the other hand, the TASEP is relatively weak compared to the TXY Hamiltonian in Eq. 5.3. So, intuitively, we may expect the steady state $\hat{\rho}_{\text{NESS}}$ may be very different from $\hat{\rho}_{cl}$. This is borne out in Fig. 5.5(a), where $\mathcal{O} \ll 1$ for most values of (Δ, h_z). However, even in this parameter regime we see a significant overlap $\mathcal{O}$ when $h_z > 1$ and Δ is small, i.e., for parameters in the ferromagnetic phase of the TXY-Hamiltonian. This indicates that the quantum phase transition has an effect the properties of the NESS.

As mentioned above, our numerical results in Fig. 5.5 [(a)-(c)] are plotted for (α, β) in the LD phase, and similar results are obtained in the HD phase. However, the results are quite distinct for (α, β) in the MC phase. In Fig. 5.5 [(d)-(f)] we can see that the overlap does not go to zero as in the LD phase for all (Δ, h_z). While an attempt has been made to highlight the different regions in (Δ, h_z), the overlap is largely similar across the parameter space.

In Fig. 5.6 we plot the overlap $\mathcal{O}$ as a function of system size N, for various choices of β, at fixed $\alpha = 0.7$. We see that the overlap decays much more slowly with system size for $\beta > 0.5$, in the MC phase. Indeed, extrapolating from the $\log_{10}$ inset figure there is a suggestion that for $N \to \infty$ the overlap approaches a constant non-zero value. Unfortunately, as yet we are unable to definitively confirm this expectation[2].

What can we say about $\hat{\rho}_{\text{NESS}}$ when it is driven away from $\hat{\rho}_{cl}$ by the TXY-

[2]We note that we could obtain larger system sizes above $N = 100$ to be more certain of this suspicion however the effective MPS sizes needed are double this number as we are performing the analysis in the doubled superoperator space. This is merely a symptom of the fact that we have exchanged a state vector for a density matrix and further vectorized this density matrix. The Liouvillian superoperator itself is scaling as $4^N \times 4^N$ and as such significantly larger systems would become too computationally intensive.

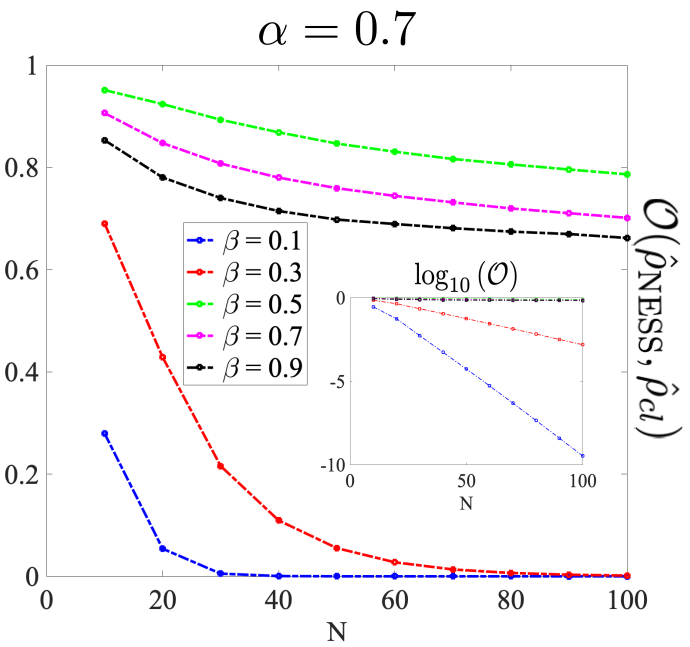

Figure 5.6: In this figure, the overlap is shown against system size, N, showing an exponential decay with system size within the HD phase where $\beta = 0.1$, $\beta = 0.3$, (see inset showing $\log_{10}(\mathcal{O})$). In the MC phase the overlap decays at a slower rate with respect to system size. The remaining parameters are: $\Delta = 0.1, h_z = 0.5$ and $\epsilon = 0.1$.

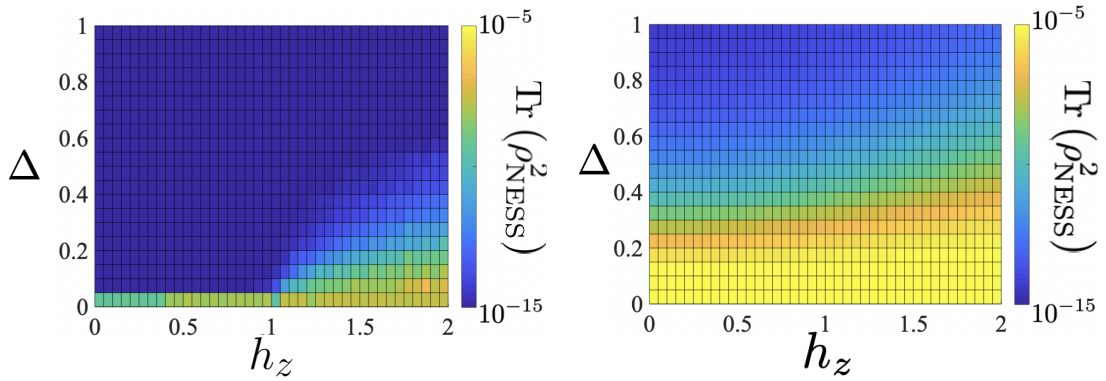

(a) $\epsilon = 0.1$ (b) $\epsilon = 10$

Figure 5.7: At classical rates $(\alpha, \beta) = (0.1, 0.3)$, LD phase, we show the purity/mixedness of the NESS at two relative strengths ϵ representative of the weak/strong classical limits. In (a) $\epsilon = 0.1$, weak classical regime, we can see that increased Δ quickly produces a more mixed state for all h_z though more slowly for $h_z > 1$. In (b) $\epsilon = 10$, strong classical regime, the value of h_z has less relevance yet the effect of increasing Δ remains apparent. $N = 50$ for both figures.

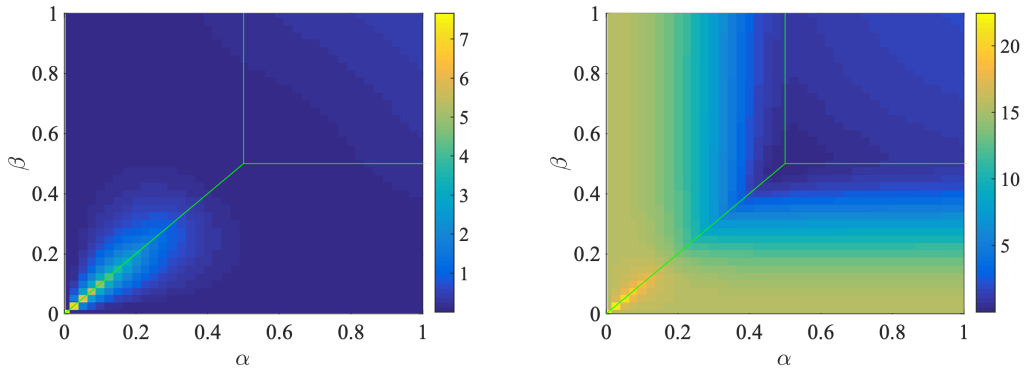

(a) $N = 50$, $\Delta = 0$ (b) $N = 50$, $\Delta = 0.2$

Figure 5.8: The susceptibility of $\hat{\rho}_{cl}$ to dynamics by the Liouvillian $\langle\langle \rho_{cl} \left| \mathcal{L}^\dagger \mathcal{L} \right| \rho_{cl} \rangle\rangle = \lambda^2 \langle\langle \rho_{cl} \left| \mathcal{H}^2 \right| \rho_{cl} \rangle\rangle$. [(a),(b)] The introduction of pairing Δ allows the the classical steady state to couple strongly to the quantum commutator in both low and high density phases.

Hamiltonian? We can gain some insight by studying the mixedness $\mathrm{Tr}(\hat{\rho}^2_{\mathrm{NESS}})$ of the steady state. In Fig. 5.7[(a)-(b)] we plot the mixedness of the steady state $\hat{\rho}_{\mathrm{NESS}}$ of the full Liouvillian in the LD regime. As the parameter ϵ decreases, corresponding to increasing relative strength of the TXY-Hamiltonian, we see that the NESS is driven towards a much more mixed state. Moreover, with decreasing ϵ one can clearly resolve signatures of the phase transition of the TXY-model at $h_z = 1$ and $\Delta > 0$, see Fig. 5.7 (a).

We have shown then that increasing the TXY anisotropy can drive the NESS away from the classical TASEP steady state, for (α, β) in the LD/HD phase. To better understand this, we examine the overlap

$$\langle\langle \rho_{cl} | \mathcal{L}^\dagger \mathcal{L} | \rho_{cl} \rangle\rangle = \left| \frac{d}{dt} | \rho_{cl} \rangle\rangle \right|^2, \tag{5.13}$$

which quantifies the susceptibility of the TASEP steady state $\hat{\rho}_{cl}$ to dynamics of the full Liouvillian. Since $\mathbb{L}|\rho_{cl}\rangle\rangle = 0$ we observe that

$$\langle\langle \rho_{cl} | \mathcal{L}^\dagger \mathcal{L} | \rho_{cl} \rangle\rangle = \lambda^2 \langle\langle \rho_{cl} | \mathcal{H}^2 | \rho_{cl} \rangle\rangle, \tag{5.14}$$

so that the susceptibility depends only on the Hamiltonian part of the Liouvillian[3].

In Fig. 5.8 (a) we see that the isotropic Hamiltonian $\Delta = 0$ has a relatively small effect on the classical steady state. However, for $\Delta > 0$, Fig. 5.8 (b) shows that $\hat{\rho}_{cl}$ responds very strongly to the TXY-Hamiltonian in the LD and HD phases, although not in the MC phase. This is reinforced by Fig. 5.9, which shows the susceptibility scales linearly with system size N in the HD phase, but sub-linearly in the MC phase.

[3]This is not a particularly deep statement but a result of $\mathbb{L}|\rho_{cl}\rangle = 0$, since ρ_{cl} is the steady state of the TASEP.

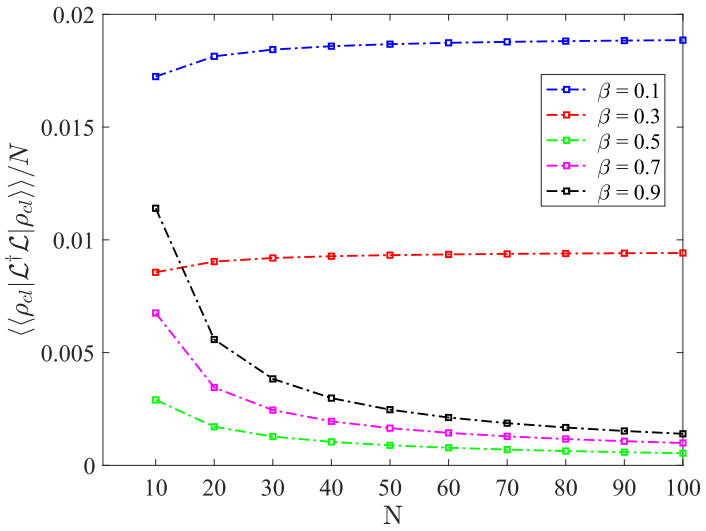

Figure 5.9: The susceptibility of $\hat{\rho}_{cl}$ to dynamics by the Liouvillian $\langle\langle\rho_{cl}\,|\mathcal{L}^\dagger\mathcal{L}|\,\rho_{cl}\rangle\rangle = \lambda^2\langle\langle\rho_{cl}\,|\mathcal{H}^2|\,\rho_{cl}\rangle\rangle$. The strength of this coupling scales linearly with the system size in the low and high density phases (upper two lines). We emphasis this by plotting the susceptibility divided by N so that the upper lines remain largely constant and the lower lines decrease. All data in this figure was plotted with $w = 1$, $h_z = 0.5$ and $\epsilon = 0.1$.

One can infer the reasons for the strong response of $\hat{\rho}_{cl}$ in this case by considering the steady state configuration [DDM92; Raj+97; ERS99; NCS02] in those classical phases. In the low density phase, as the name suggests, there are many empty sites. Rewriting the anisotropic terms of the Hamiltonian in Eq. 5.4 as

$$\Delta(\hat{\sigma}_i^x\hat{\sigma}_{i+1}^x - \hat{\sigma}_i^y\hat{\sigma}_{i+1}^y) = 2\Delta(\hat{\sigma}_i^+\hat{\sigma}_{i+1}^+ + \hat{\sigma}_i^-\hat{\sigma}_{i+1}^-), \tag{5.15}$$

the operator $\hat{\sigma}_i^+\hat{\sigma}_{i+1}^+$ associated with the anisotropy can be applied successfully to the state at many locations on the chain. Similarly, in the high density phase there are many occupied sites and the pair annihilation operator, $\hat{\sigma}_i^-\hat{\sigma}_{i+1}^-$, can be applied often without annihilating the state. However, in the maximal current phase the steady state is largely comprised of half-filled configurations which will not couple as strongly to the anisotropic terms.

Another interesting property of the steady state ρ_{NESS} is the "energy" expectation value $\langle E\rangle = \text{Tr}\,\rho_{\text{NESS}}H$ which gives an indication of which Hamiltonian eigenstates take part in the steady state. In Fig. 5.10 we show how the expectation value changes relative to the full eigen-spectrum of the system Hamiltonian. In the LD and HD regimes the expectation value drifts towards the extrema of the many body Hamiltonian spectrum, provided the Hamiltonian is tuned to the paramagnetic region. This occurs due to the energetic importance of either filled or empty sites (up or down spins) in this quantum phase. On the other hand, in the ferromagnetic regimes, the energy of the steady state coincides with the centre of the many-body spectrum backing up the idea that here the system favours something close to the

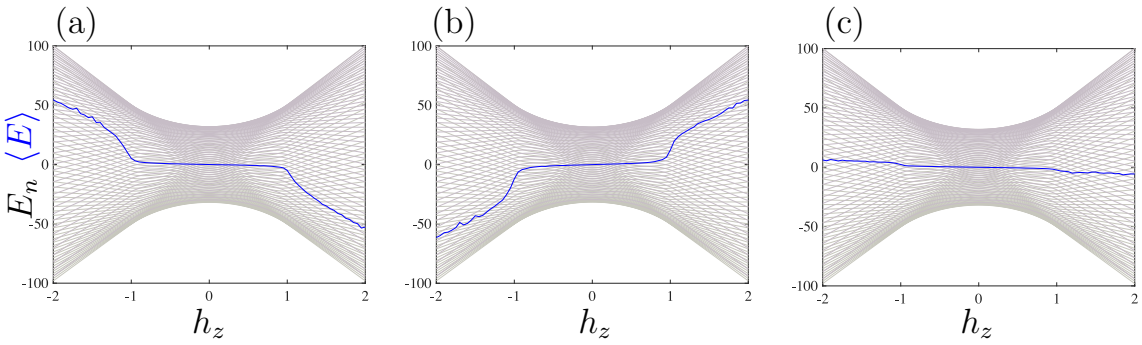

Figure 5.10: The energy expectation values of $\langle E \rangle = \mathrm{Tr}\,\rho_{\mathrm{NESS}} H$ together with the many-body eigen-spectrum, E_n of H, where only band edges are shown. (a) $\alpha = 0.1$, $\beta = 0.3$, $\Delta = 0.1$, (b) $\alpha = 0.3$, $\beta = 0.1$, $\Delta = 0.05$, (c) $\alpha = 0.7$, $\beta = 0.9$, $\Delta = 0.1$. In all figures, $\epsilon = 0.1$ and $N = 50$. In the paramagnetic regimes $|h_z| > 1$ the classical densities determined by the boundary rates result in steady states with a clear low/high energy imbalance [(a) and (b)]. This imbalance is suppressed in the ferromagnetic regime $|h_z| < 1$ and also throughout the maximal current phase (c)

maximally mixed state. In the maximal current phase, this behaviour dominates for all values of the transverse field.

5.2.2 NESS as a Perturbation of the Maximally Mixed State

We have mentioned at various points up until now how the TXY model drives ρ_{cl} towards $\mathbb{I}$, the maximally mixed state. We now formalise this notion by providing an understanding on the NESS as a perturbation on this maximally mixed state. The perturbation theory utilised here for non-Hermitian systems is based on [SW72; LPK14; LPK16]. As a starting point, one defines a "bare" unperturbed Liouvillian $\mathcal{L}_0$ with eigenvalues $\mathcal{E}_n$ and left and right eigenvectors $\langle\langle \tilde{v}_n |$ and $| v_n \rangle\rangle$ such that $\langle\langle \tilde{v}_m | \mathcal{L}_0 | v_n \rangle\rangle = \delta_{nm} \mathcal{E}_n$. We write the perturbation as $\mathcal{L}_1$ and an expansion of the steady state as $| \rho \rangle\rangle = \sum_j | \rho_j \rangle\rangle$, the terms of which are produced iteratively according to

$$| \rho_j \rangle\rangle = \mathcal{L}_0^{-1} \mathcal{L}_1 | \rho_{j-1} \rangle\rangle, \tag{5.16}$$

where $\mathcal{L}_0^{-1}$ is the pseudo-inverse defined as

$$\mathcal{L}_0^{-1} = \sum_{\mathcal{E}_n \neq 0} \frac{| v_n \rangle\rangle \langle\langle \tilde{v}_n |}{\mathcal{E}_n}. \tag{5.17}$$

At this point one might expect that $\mathbb{H}$ is chosen as the unperturbed piece of the Liouvillian and subsequently that $\epsilon \mathbb{L}$ becomes the perturbation. However, one can immediately see an obstacle arising from this choice. Given Eq. 5.17, since $\mathbb{H}$ corresponds to the commutator of the Hamiltonian its spectrum is massively degenerate as all eigenvectors of the Hamiltonian yield zero eigenvalue in the commutator. As a result we would be left with a highly degenerate situation that is difficult to deal with.

We propose a way to circumvent this obstacle by exploiting the structure of $\epsilon\mathbb{L}$. We know that once any part of $\mathbb{L}$ is switched on that the system will immediately have a preferred steady state. As such we propose that to proceed we first treat diagonal ($\backslash$) components of the TASEP term $\mathbb{L}$ differently from the off diagonal ($\backslash\backslash$) ones. Namely, we split the total $\mathbb{L}$ as the sum

$$\epsilon\mathbb{L} \to \epsilon_{\backslash}\mathbb{L}_{\backslash} + \epsilon_{\backslash\backslash}\mathbb{L}_{\backslash\backslash}. \tag{5.18}$$

We note here that this expression of the splitting of $\epsilon\mathbb{L}$ is an equality, however we introduce new ϵ variables for the separate components for this calculation. In the end they will be equalized to the original ϵ variable. While artificial this serves to illuminate from which component of the Liouvillian the corrections arise. Our unperturbed system will then consist of the collective diagonal blocks

$$\mathcal{L}_0 = \sum_{s\in even} \mathcal{L}^{(s)} = \sum_{s\in \text{ even}}^{2N} \epsilon_{\backslash}\mathbb{L}_{\backslash}^{(s)} - i\lambda\mathbb{H}^{(s)}, \tag{5.19}$$

and the perturbation as the remaining off diagonal components

$$\begin{aligned}\mathcal{L}_1 = \mathcal{L} - \mathcal{L}_0 &= \sum_{s\in \text{ even}} \mathcal{L}^{(s,s+2)} + \mathcal{L}^{(s+2,s)}, \\ &= \epsilon_{\backslash\backslash} \sum_{s\in \text{ even}} \mathbb{L}^{(s,s+2)} + \mathbb{L}^{(s+2,s)}.\end{aligned} \tag{5.20}$$

The block diagonal form of $\mathcal{L}_0$ means that we can write down its eigen-spectrum block by block. In practice we observe numerically that the real component of $\mathcal{E}_n^{(s)}$ for small $\epsilon_{\backslash}$ grows linearly such that in what follows it will be useful to write this dependence explicitly and expand the complex eigenvalue as

$$\mathcal{E}_n^{(s)} = \epsilon_{\backslash} r_n^{(s)} + iE_n^s. \tag{5.21}$$

Another property of our unperturbed operator is that the pseudo-inverses of the blocks only act locally within each block. This will allow us to simplify some expressions in the following and implies for example that

$$\mathcal{L}_0^{-1} = \sum_{s\in even} [\mathcal{L}^{(s)}]^{-1}. \tag{5.22}$$

Then, with the maximally mixed state as our starting state $|\,\rho_0\rangle\!\rangle = |\,I\rangle\!\rangle$ we can

proceed according to the iterative procedure (5.16):

$$\begin{aligned}
|\,\rho_1\rangle\!\rangle &= -[\mathcal{L}^{(2)}]^{-1}\mathcal{L}^{(2,0)}|\,I\rangle\!\rangle, \\
|\,\rho_2\rangle\!\rangle &= -[\mathcal{L}^{(4)}]^{-1}\mathcal{L}^{(4,2)}|\,\rho_1\rangle\!\rangle, \\
|\,\rho_3\rangle\!\rangle &= -([\mathcal{L}^{(2)}]^{-1}\mathcal{L}^{(2,4)} + [\mathcal{L}^{(6)}]^{-1}\mathcal{L}^{(6,4)})|\,\rho_2\rangle\!\rangle, \\
&\vdots
\end{aligned} \tag{5.23}$$

where only the non-zero $\mathcal{L}^{(s,s')}$ blocks/elements have been kept. Plugging in the dependence on the overall weights we have for the first order expression:

$$\begin{aligned}
|\,\rho_1\rangle\!\rangle &= -\epsilon_{\backslash\backslash}[\mathcal{L}^{(2)}]^{-1}\mathbb{L}^{(2,0)}|\,I\rangle\!\rangle, \\
&= -\epsilon_{\backslash\backslash}\sum_n \frac{|\,v_n^{(2)}\rangle\!\rangle}{\mathcal{E}_n^{(2)}}\langle\!\langle\tilde{v}_n^{(2)}\,|\mathbb{L}^{(2,0)}|\,I\rangle\!\rangle, \\
&= -\epsilon_{\backslash\backslash}\sum_n \frac{\bar{\alpha}\langle\!\langle\tilde{v}_n^{(2)}|\phi_L\rangle\!\rangle - \bar{\beta}\langle\!\langle\tilde{v}_n^{(2)}|\phi_R\rangle\!\rangle}{\epsilon_{\backslash} r_n^{(2)} + iE_n^{(2)}}|\,v_n\rangle\!\rangle,
\end{aligned} \tag{5.24}$$

with

$$\begin{aligned}
&|\,\phi_L\rangle\!\rangle = |\,\gamma_1\gamma_2\rangle\!\rangle,\ |\,\phi_R\rangle\!\rangle = |\,\gamma_{2N-1}\gamma_{2N}\rangle\!\rangle, \\
&\bar{\alpha} = \alpha - \frac{1}{2},\ \bar{\beta} = \beta - \frac{1}{2},
\end{aligned} \tag{5.25}$$

and where on the last line we have also expanded the $s = 2$ block eigenvalues into their real and imaginary components.

Leaving the inner products in the numerator to one side for a moment we can consider which terms are relevant in this first iterative correction by looking at cases for the coefficients in the sum:

$$\frac{-\epsilon_{\backslash\backslash}}{\epsilon_{\backslash} r_n^{(2)} + iE_n^{(2)}} \sim \begin{cases} \frac{-1}{r_n^{(2)}},\ E_n^{(2)} \ll \epsilon_{\backslash} r_n^{(2)}, \\ \frac{i\epsilon_{\backslash}}{E_n^{(2)}}, \text{otherwise.} \end{cases} \tag{5.26}$$

Evidently as we reinstate $\epsilon_{\backslash\backslash} = \epsilon_{\backslash} \to \epsilon$ and approach $\epsilon \to 0$ the second case is irrelevant and only those coefficients with small to negligible imaginary parts contribute to the correction.

What about the terms $\langle\!\langle\tilde{v}_n^{(2)}|\phi_{L/R}\rangle\!\rangle$? An unusual feature of the block-decomposition is that we could in principle have additional $\epsilon_{\backslash}$ dependences occurring through the $|\,\tilde{v}_n^{(2)}\rangle\!\rangle$. However, in practice we see via direct evaluation that, to leading order, these vector elements are independent of ϵ. This means, that in the limit $\epsilon_{\backslash\backslash} = \epsilon_{\backslash} \to 0$ we approach a fixed steady state that is not the infinite temperature state $|\,I\rangle\!\rangle$. Moreover, the magnitude of this deviation from the thermal state is dictated primarily by the scale given by $1/r^{(2)}$ for which the term $1/r_1^{(2)}$ is the largest.

This outcome runs counter to typical perturbative statements where, as the small

parameter tends to zero, we approach the bare un-perturbed state (in this case $|\, I\rangle\!\rangle$). Recall however that, to avoid dealing with the massive degeneracy of the commutator $\mathbb{H}$, we also allowed the small parameter ϵ to enter into the bare Liouvillian. In this iterative construction then, we do not necessarily expect that each successive iteration will result in contributions that scale according to some positive power of ϵ. Indeed, one expects that further iterations would eventually lead to additional corrections in other s-even sectors that, similarly to the explicit first iterative correction above, do not vanish as $\epsilon \to 0$. This argument is not generic as presented as we have simplified some steps given the specifics of the TXY-TASEP model but nonetheless the non-Hermitian perturbation theory is quite general.

5.3 Effect of Hamiltonian Processes on Lattice Currents

Given that the p-wave superconductor and the totally asymmetric exclusion process (TASEP) model quantum and classical transport in one dimension it is reasonable to consider how the particle current of the hybrid TXY-TASEP model differs from either model in isolation. In this section we examine the current found from the NESS of this hybrid model.

Recall that the steady state current of the stochastic model is known (see [Der+93] and App. C). Depending purely on the boundary rates, (α, β), the steady state current is fixed and uniform across the lattice. Here we explore the effect of (partially) introducing the superconductor model on the known steady state currents of TASEP. In Fig. 5.11 we elaborate on the set up we employ to investigate this effect. For a lattice with N sites as before we have the stochastic process (TASEP) acting throughout the lattice. The quantum processes (as the TXY model) are present only in the middle portion. For the numerical simulations we chose this portion to be $N/2$ and subsequently the left/right $N/4$ size sections of the lattice have no quantum process acting. This is easily implemented by allowing λ to vary along the lattice and introducing a step function via this parameter. Based upon our observations of the effect pairing has on the steady states we focus specifically on how Δ affects the currents in the steady state as [TWV12] has demonstrated the effects of purely coherent hopping.

One would expect that the MC phase of TASEP remains largely unchanged. The notional steady state for the MC phase is a half/alternately filled lattice which is largely unaffected by the action of the Δ-pairing terms in the Hamiltonian. As such we expect that the steady state current remains at the maximum value as determined from the TASEP model. In the LD phase the lattice is less than half filled so one would expect the pair creation term from the Hamiltonian to fill empty sites rapidly such that the current gradually approaches a larger value. In the left region,

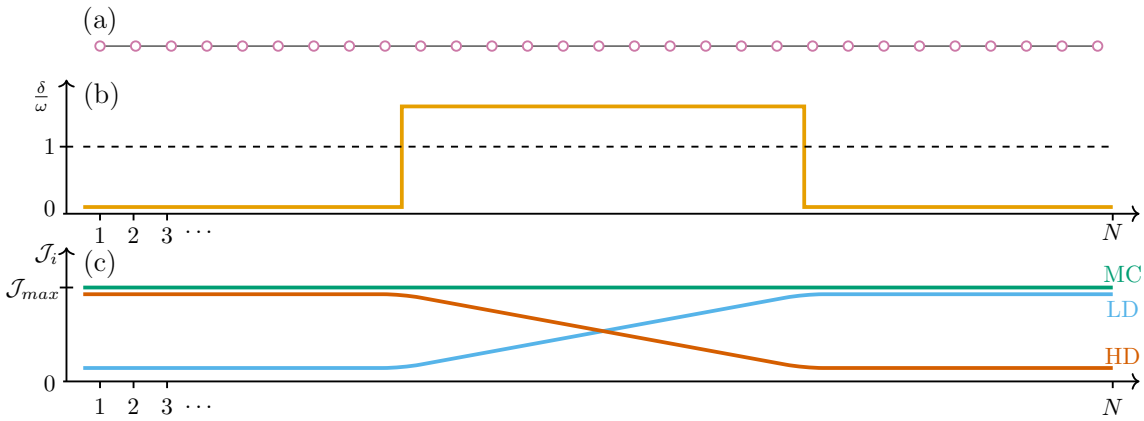

Figure 5.11: (a) The lattice of N sites. (b) The profile of the Hamiltonian parameters. For the numerical results presented in this section this is taken as a step function for convenience. A smooth function can be implemented but for the purpose of this section we take this sharp cut-off. (c) Our expectation of the effect of partial quantum processes.

where pairing terms are absent, the LD configuration will remain largely distinct from the middle region. Mirroring the lattice and exchanging our perspective as holes travelling along a lattice of particles in the opposite direction the very same expectation can be seen for the HD phase. As a result the current profile may appear qualitatively to mirror the LD phase profile about the middle site.

We must stress that what we suggest thus far is based on an intuition developed from the properties of the steady state that are known [Der+93] and the knowledge of the stochastic model that has been presented up to this point. Moreover, recall that in the TASEP we could refer to the local occupations (n_i) and the step-wise update rules to determine the current. The resultant classical current is simply the amount of particle content passing through each link of the lattice. In the hybrid model here we must instead find the equation of motion for the local densities to determine the correct current for a model described by a Lindblad equation.

For the numerical work presented, we have simulated the system by the same tensor network methods as in prior sections and simply set the Hamiltonian parameters to zero in the left and right regions. This allows us to access relatively large system sizes. Our findings indicate that the effects are qualitatively the same for all the sizes we accessed (from 20 up to 100 sites).

5.3.1 Continuity Equation: Currents, Sources and Sinks

First let us define the quantity of the local particle or spin density, denoted for TASEP by n_i,see App. C. We take the expectation value of this quantity with respect to the density matrix to define the local density at any given time i.e.

$$\langle \hat{n}_i \rangle = \langle \hat{\sigma}_i^+ \hat{\sigma}_i^- \rangle = \mathrm{Tr}\big[\hat{\rho}(t)\hat{\sigma}_i^+ \hat{\sigma}_i^-\big], \tag{5.27}$$

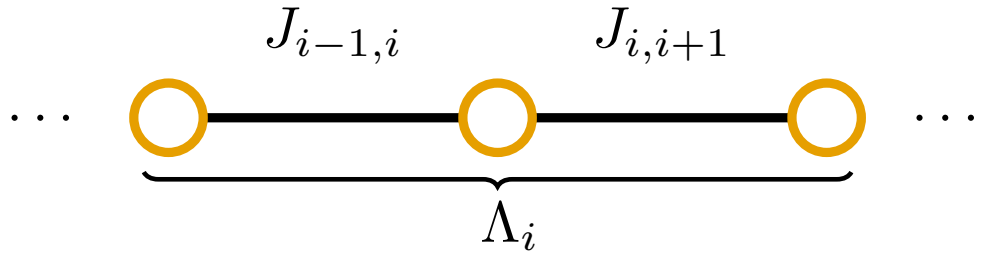

Figure 5.12: The locations of the local terms in the continuity equation relative to a particular site i. See that each source/sink term Λ is contains information from both adjacent sites relative to site i. The J contributions take account of the particle content moving across the adjacent bonds.

which is the probability of finding a particle at site i on the chain. Taking the derivative of this definition and inserting the right hand side of the master equation (5.3) in place of $\frac{d\rho}{dt}$ leads us to the equation of motion for the density

$$\frac{d\langle\hat{n}_i\rangle}{dt} = -i\,\mathrm{Tr}\{\hat{n}_i[\hat{H},\hat{\rho}]\} + \mathrm{Tr}\{\hat{n}_i\mathcal{L}(\hat{\rho})\}. \tag{5.28}$$

After some manipulation this can be written in the form of a continuity equation

$$\frac{d\langle\hat{n}_i\rangle}{dt} = \langle\hat{J}_{i-1,i}\rangle - \langle\hat{J}_{i,i+1}\rangle + \langle\hat{\Lambda}_i\rangle. \tag{5.29}$$

The continuity equation expresses the fact that changes in the particle density at site i are either due to transport of particles across the bond $(i-1,i)$ by the current $\langle\hat{J}_{i-1,1}\rangle$, or across the bond $(i,i+1)$ by the current $\langle\hat{J}_{i,i+1}\rangle$. The final term corresponds to the generation of particles by a source term $\langle\hat{\Lambda}_i\rangle$ which can be positive or negative. We refer to this term as a source when positive and a sink when negative as it acts as a net particle creation or annihilation term respectively. For $1 \leq i \leq N-1$ the particle current operator in Eq. 5.29 is

$$\hat{J}_{i,i+1} = i\lambda\left(\hat{\sigma}_i^+\hat{\sigma}_{i+1}^- - \hat{\sigma}_i^-\hat{\sigma}_{i+1}^+\right) + \gamma\hat{\sigma}_i^+\hat{\sigma}_i^- \cdot \hat{\sigma}_{i+1}^-\hat{\sigma}_{i+1}^+. \tag{5.30}$$

This can be understood as first the contribution to the continuity equation coming from the hopping terms present in the Hamiltonian and secondly a term which is essentially the "*density* $\times$ (1 $-$ *density*)" current of the TASEP written in spin operators. The source/sink operators are given by:

$$\begin{aligned}
\hat{\Lambda}_1 &= 2\alpha\hat{\sigma}_1^-\hat{\sigma}_1^+ + \Delta\hat{\eta}_{1,2}, \\
\hat{\Lambda}_i &= \Delta(\hat{\eta}_{i-1,i} + \hat{\eta}_{i,i+1}), \quad 2 \leq i \leq N-1, \\
\hat{\Lambda}_N &= -2\beta\hat{\sigma}_N^+\hat{\sigma}_N^- + \Delta\hat{\eta}_{N-1,N},
\end{aligned} \tag{5.31}$$

where

$$\hat{\eta}_{i,i+1} \equiv i(\hat{\sigma}_i^+\hat{\sigma}_{i+1}^+ - \hat{\sigma}_i^-\hat{\sigma}_{i+1}^-), \tag{5.32}$$

is the difference between pair-creation and pair-annihilation at the neighbouring sites $(i, i+1)$. We can understand these Λ partly from the intuition we have built from the classical model. The terms with α and β are exactly again those terms that would appear in the classical case from the boundary processes. All the other terms manifestly depend on Δ and stem directly from the pairing terms of the Hamiltonian.

5.3.2 Steady State Current

Now that we have the definitions in place for the model's currents/sources we can consider how they behave for the steady state. The non-equilibrium steady state $\hat{\rho}_{\text{NESS}}$ is defined by the condition that $d\hat{\rho}_{\text{NESS}}/dt = 0$. Since this implies that $d\langle\hat{n}_i\rangle_{\text{NESS}}/dt = 0$ the continuity equation 5.29 gives

$$\langle J_{i,i+1}\rangle_{\text{NESS}} - \langle J_{i-1,i}\rangle_{\text{NESS}} = \langle\hat{\Lambda}_i\rangle_{\text{NESS}}. \tag{5.33}$$

For $\Delta = 0$ we see that

$$\begin{aligned} &\alpha\langle\hat{\sigma}_1^-\hat{\sigma}_1^+\rangle_{\text{NESS}} = \langle J_{1,2}\rangle_{\text{NESS}} = \dots \\ &\dots = \langle J_{N-1,N}\rangle_{\text{NESS}} = \beta\langle\hat{\sigma}_N^+\hat{\sigma}_N^-\rangle_{\text{NESS}}. \end{aligned} \tag{5.34}$$

Thus the current is constant across the chain and is equal to both $\alpha\langle\hat{\sigma}_1^-\hat{\sigma}_1^+\rangle_{\text{NESS}}$ and $\beta\langle\hat{\sigma}_N^+\hat{\sigma}_N^-\rangle_{\text{NESS}}$, which are interpreted as the rate of particles hopping onto and off the chain. This reproduces the result from Temme *et. al.* [TWV12] and, indeed, the classical model that the current has a flat profile across the lattice. In other words, for no Δ, and additionally for the classical model, the current is uniform. However, if $\Delta \neq 0$ we do not expect the current to be constant across the chain, due to particle pair creation/annihilation in the bulk. Summing both sides of Eq. 5.33 over all values of the site index i gives the identity

$$\beta\langle\hat{\sigma}_N^+\hat{\sigma}_N^-\rangle_{\text{NESS}} - \alpha\langle\hat{\sigma}_1^-\hat{\sigma}_1^+\rangle_{\text{NESS}} = \frac{\Delta}{2}\sum_{i=1}^{N-1}\langle\hat{\eta}_{i,i+1}\rangle_{\text{NESS}}. \tag{5.35}$$

This suggests that if the right hand side is positive the current through the chain is enhanced by the particle pair creation/annihilation in the bulk. We note that the Hamiltonian parameters h_z and w do not appear explicitly in Eq. 5.35, but they do appear implicitly in their contribution to the steady state $\hat{\rho}_{\text{NESS}}$.

It was shown in Ref. [Der+93] that for TASEP in the large N limit the current is $\langle\hat{J}\rangle_{\text{NESS}} = 1/4$ in the maximal current phase, $\langle\hat{J}\rangle_{\text{NESS}} = \alpha(1-\alpha)$ in the low-density phase, and $\langle\hat{J}\rangle_{\text{NESS}} = \beta(1-\beta)$ in the high-density phase. In Ref. [TWV12] the authors examined the Hamiltonian for $\Delta = 0$, and found that the coherent contribution to the current decays as system size increases, and appears to vanish

in the $N \to \infty$ limit, and thus in that case the Hamiltonian does not modify the transport properties significantly.

5.3.3 Quantum Effect on the Steady State Current

To illustrate the effect on the steady state current we consider a chain in which the anisotropy parameter Δ_i can vary across the chain, as shown in Fig. 5.11. For the first and last quarters of the chain we have $\Delta_i = 0$ and so, by Eq. 5.34, the current is constant in these regions. In the middle half of the chain, however, we choose $\Delta_i = \Delta > 0$ so that particle pair creation/annihilation can change the current. In Fig. 5.13(a), we see that the effect on the current is small when α and β are chosen to be in the maximal current phase of TASEP, as proposed. However, for α and β in the low-density phase we see that the current is enhanced at the end of the chain as a result of a net particle pair creation in the steady state. Conversely, in the high-density phase there is a net particle pair annihilation, and thus the current is reduced.

The key result here is that the typical current expected from the low- and high-density phases have a strong reaction to the introduction of Δ in the middle portion of the lattice. We observe that the expected current of the low density phase is driven into the corresponding current of the high density phase and vice-versa, Fig. 5.13(a). The stochastic component is largely unaffected up to minor fluctuations, notice the restricted values on plotted in Fig. 5.13(b). We can see the effect of introducing Δ only in the middle of the lattice from the non-zero source terms appearing in the vicinity of the step function (Fig. 5.11), as shown in Fig. 5.13(d). The dominant contribution to the *change* in steady state current stems ultimately from the coherent part Fig. 5.13(c) but note that this does not appear unless there is some non-zero source terms.

5.3.4 Role of the Quantum Phase Transition

The qualitative features of the current change depending on the phase of the quantum model. In particular, within the topological phase ($|\mu| < 2w$ or $h_z < 1$) the current in the low- and high-density phases appear to be most affected as we have argued. These effects are summarised in Fig. 5.14 and for increased Δ in Fig. 5.15. In the (a) panel of each we can see the pronounced increase/decrease in the low-density and high-density phases respectively within the topological phase of the Hamiltonian. In the trivial phase of the Hamiltonian, see (b) panels, the effects on the current change sharply. For (α, β) near the critical line, $\alpha = \beta$, any enhancement or effect on the profile of the current appears to be suppressed. This is in part due to the fact that steady states on the critical line behave in much the same way as those in the MC phase. Moreover, where an effect remains the features of the

$$\Delta = 0.2,\ h_z = 1,\ N = 20$$

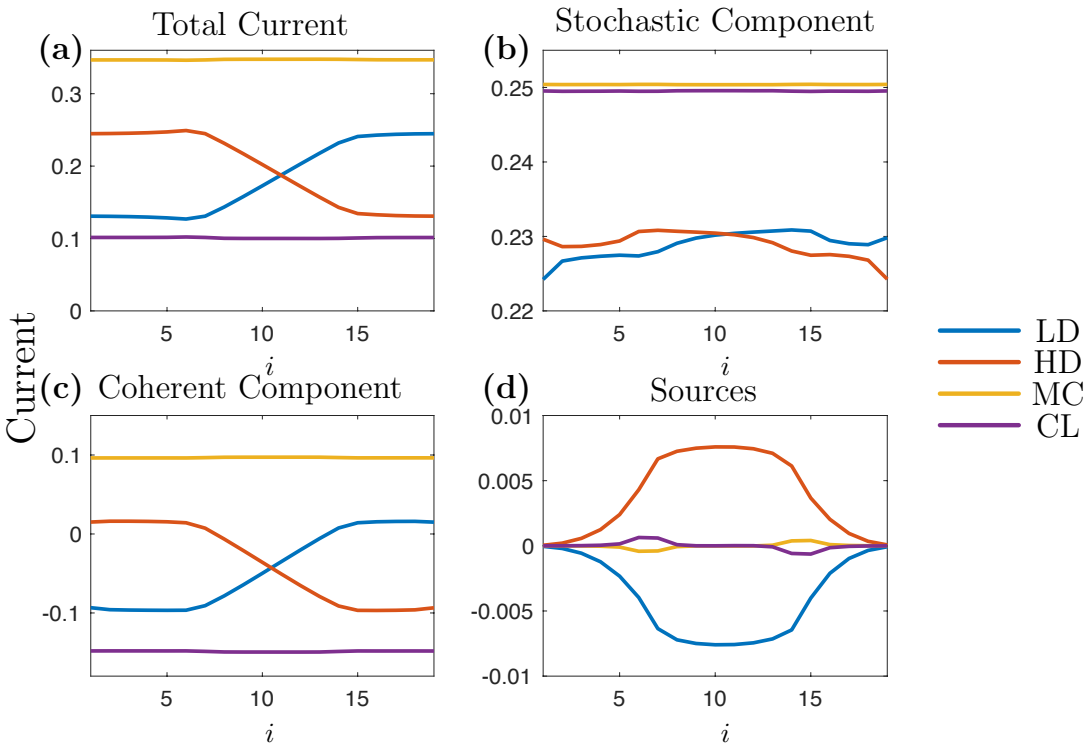

Figure 5.13: Here we present the current profiles of the components of the current as expressed in the continuity equation. (a) The total current for all three TASEP phases and on the critical line (CL), where $\alpha = \beta$. As proposed only the current for (α, β) in the LD/HD phases are significantly changed. It appears that in the middle region the current is increased/decreased to match the corresponding value of the current for (β, α). (b) Changes in the stochastic component of the current. We see that these profiles remain largely flat. For larger system sizes the LD/HD profiles have less variation than in this small case. (c) The coherent component of the current reflects the changes in the total current. (d) The changes to the source terms which follow the step function of the Hamiltonian parameters we impose. For larger system size this profile becomes sharper but nonetheless there is some non-zero effect extending past the boundary of the middle region as the source Λ_i is defined over several sites. In these simulations we set $w = 1, \Delta = 0.2, h_z = 1, N = 20$, further with the particular choices $(\alpha, \beta) = \{(0.2, 0.2), (0.2, 0.7), (0.7, 0.2), (0.7, 0.7)\}$ corresponding to the CL, LD, HD and MC phases respectively. The symmetry of LD/HD plots in (a) is a reflection of the (α, β) values chosen in those regions.

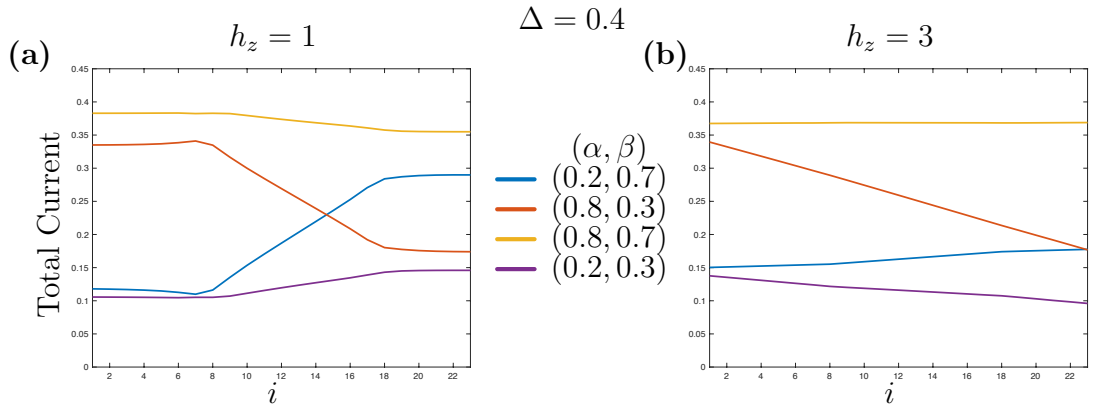

Figure 5.14: We can see the effect of pairing in topological (a) and trivial (b) phases of the quantum model at $\Delta = 0.4$, for each phase of TASEP and near the critical line. (a) In the topological phase, we see a similar variation in the current for the low- and high-density phases. In this case our choice of (α, β), $(0.2, 0.7)$ and $(0.8, 0.3)$ respectively, these curves are no longer symmetric. For the lowest curve, we are deep in the low-density phase and close to the critical line, at $(\alpha, \beta) = (0.2, 0.3)$, thus the effect is less pronounced. Similarly, the effect in the MC phase at $(0.8, 0.7)$ is less pronounced than the effect in the LD/HD phases. (b) In the trivial phase of the quantum model the effect of pairing is distinct from the topological phase. Any effect seen is less pronounced and the steady state comes close to a flat profile unless the parameters (α, β) are chosen *far from the critical line* $\alpha = \beta$.

current profile are altered. We no longer retain flat profiles on the left and right portions of the lattice. Rather, the current follows a straight sloped line which stems almost entirely from the coherent component of the current. The contributions from sources in the trivial regime are orders of magnitude smaller than those from the coherent current. As a consequence pairing effects are broadly suppressed in this phase. In Fig. 5.15 where we have a doubled pairing strength the features are similar. Although increased Δ increases the effects seen, the effect is not particularly sizeable.

It appears that to observe any significant enhancement, or indeed reduction, to the steady state current one must have model parameters which place the system in the topological phase of the quantum model *and* in the low-density or high-density phase of the classical model. In particular, if it is desired for the left and right sides of the system to interpolate between the behaviour of the low- and high-density phases of TASEP.

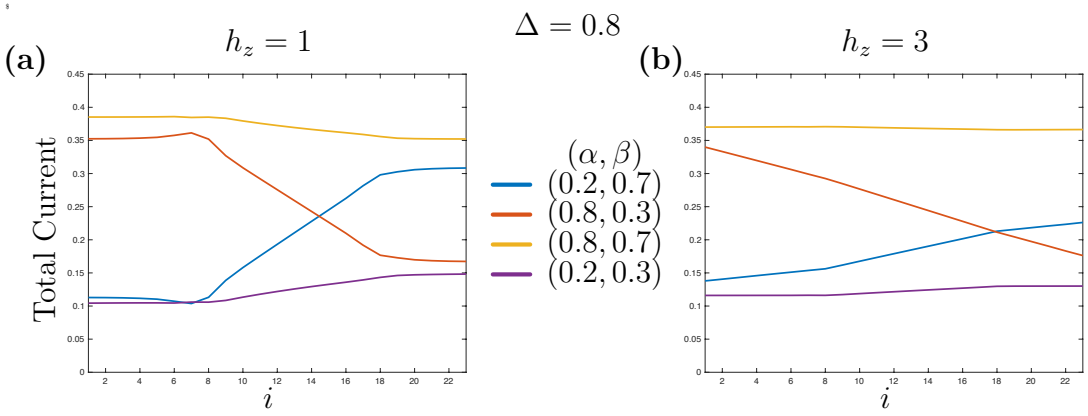

Figure 5.15: We can see the effect of pairing in topological (a) and trivial (b) phases of the quantum at $\Delta = 0.8$, for (α, β) in the LD/HD/MC phases and LD near the critical line of the TASEP. The important point to note here is that the increase of Δ corresponds to an increase in the effect of pairing on the current, albeit the result of a doubled value of Δ is slight in this weak dissipative regime, $\epsilon = 0.1$.

Chapter 6

Liouvillian Gap of Dissipative Quantum Systems

When studying the steady state of the TXY-TASEP model we found that the presence of non-zero XY anisotropy was the key feature of the model that allowed for an interplay between quantum and classical effects to manifest. Together with the bulk stochastic process, we find that this then opens a constant Liouvillian gap that persists even for large system sizes. The precise functional form of the gap depends on the underlying quantum phase and is thus controlled by the bulk topology of the p-wave superconductor band-structure, see Fig. 4.3. This results in gap behaviour that is different in each of the quantum phases of the model. Our key result is that the non-trivial topology of the Kitaev p-wave model model can typically directly affect the behaviour of the Liouvillian gap, and that moreover, the scaling of the gap is related to the presence of superconductor pairing in the quantum model. This survival of quantum features under dissipation is found by exploiting the canonical representation of the Liouvillian superoperator an making projections onto components of the superoperator.

As such we claim that evidence of the underlying quantum phase transition of the Kitaev model remains even under TASEP dissipation but moreover, for a variety of dissipative processes. In essence there is a fingerprint of the quantum phase transition left in the model even under the influence of dissipation. The notion of topological condensed matter in this context is, at its core, the idea that single-particle band-structures can have non-trivial topologies and that these exotic forms can radically influence the way matter behaves. This notion has been around for several decades and has been enormously successful, with direct applications for metrology [WN90; MR91; DFN05; He+17], spintronics [QZ10], and quantum information processing [Kit03; Kit06; Nay+08; CGD11].

The majority of works in this area focus on equilibrium properties of matter, where topology most clearly arises in quantities calculated by integrating over momentum-space parametrizations of the single-particle excitation bands, as in

Ch. 4. Other indicators of topology (e.g. ground state degeneracies [HW05], equivalences between local ground-state correlators [LW06; Coo+21a], bulk-boundary correspondences [KK12; Lee16], tensor network classifications [Bul+17; Cir+17; Jon+21]) can be used beyond the implicitly non-interacting band theory of solids.

The fingerprints of topology are not, however, constrained to the equilibrated realm. Indeed, there has been much evidence of topology in recent years on numerous frontiers such as Floquet systems [Rie+18; Ful+19; RL20; SRM21], non-Hermitian models [Kun+18; EKB19; BBK21], entanglement transitions in weakly measured models [Geb+20; Wan+22; LAB21], along with proposals to engineer topological steady states in open quantum systems [Bar+13; BZD15; SBD16; Iem+16; GBZ16; Bar+20; Ton+20; Wol+20; MD20; AFD21; HSD22]. There are also deep connections to be made between the stability of open quantum systems, the scaling of the Liovillian gap, and the character of steady-state correlators. In this latter context one can formulate topological analogs that hold in an open quantum setting.

This chapter is structured as follows: In section 6.1 we introduce the Liouvillian gap and summarise the observations we have found for the gap in the TXY-TASEP model also studied in the previous chapter. These observations are made within the same third quantized framework utilised previously, found numerically by tensor network simulations. Further, we outline some of the salient features of the gap in this context. Next, in section 6.2 we describe the projection method we employ to demonstrate the immediate opening of a gap from non-zero pairing strengths and to obtain the precise form of the Liouvillian gap. Therein, the methodology described is rather generic. In section 6.3 we provide an illustrative implementation of the method using the TXY model with on-site dephasing. For this choice of dissipation the calculations are direct and exemplify the projection method. Despite its relative simplicity, we show the immediate effect of non-zero pairing strength opening a constant (in system size) gap. In addition, the gap in this model possesses the topological features observed numerically for TXY-TASEP. We end this section with the explicit forms of the Liouvillian gap in the thermodynamic limit. Crucially, in section 6.4 we repeat our analysis for the Hermitian SSEP and TASEP models of dissipation which verifies our numerical observations. These calculations are slightly more involved yet the final form of the Liouvillian gap remains the same as in the illustrative example. The remaining sections (Sec. 6.5, 6.6 & 6.7) expand on the technical aspects and interpretations of the block perturbation theory used in section 6.1 and section 6.2. These technical considerations are particularly pertinent for the TXY-TASEP and similar models which do not possess a Liouvillian superoperator that is exactly block diagonal. Nonetheless, our methodology can be reliably applied to them provided these technical considerations are satisfied.

6.1 The Liouvillian Gap

One can consider the Liouvillian gap as a key indicator of relaxation times towards the NESS [DS00; NCS02; GE06; OV08; PŽ09; Kes+12; JNK13]. Given a Liouvillian superoperator, with matrix representation $\mathcal{L}_{ab}^{(s,s')}$, generically this can be non-Hermitian. As a result this admits a complex eigenspectrum, resulting in a set of complex eigenvalues $\{\mathcal{E}_0, \mathcal{E}_1, \mathcal{E}_2, \dots\}$. Then without loss of generality these can be ordered according to their real parts $0 \geq \mathrm{Re}(\mathcal{E}_0) \geq \mathrm{Re}(\mathcal{E}_1) \geq \dots$. The non-equilibrium steady state corresponds to the eigenvalue with zero real part, $\mathrm{Re}(\mathcal{E}_0) = 0$, that being the one that does not decay in the long time limit. All other eigenvalues corresponds to decaying modes[1]. Then the Liouvillian gap is defined as

$$\mathcal{E}_{gap} \equiv -\mathrm{Re}(\mathcal{E}_1), \tag{6.1}$$

where $\mathcal{E}_1$ is the eigenvalue of $\mathcal{L}$ with non-zero real component closest to zero. For a review of gap behaviour in a variety of related models see [Žni15]. Generically, in such studies a key indicator is how the Liouvillian gap scales as a function of the system size, N, e.g. $\mathcal{E}_{\mathrm{gap}} \sim N^{-z}$ where the exponent z depends on the particular model studied. By finding this relationship, one can understand the relaxation time of the model in question. The relaxation time is usually the inverse of this gap. Thus, a gap that approaches zero in the $N \to \infty$ limit corresponds to a diverging relaxation time.

6.1.1 Emergence of a Liouvillian Gap from XY Anisotropy and Bulk Dissipation

As indicated we utilise a convenient basis for the Liouvillian superoperator (Sec. 5.1.3). Using this, we find that the gap for this system can be obtained via a MPS based approach [OV08; PŽ09; JNK13]. Moreover we find that, in this limit, the full Liovillian gap is closely shadowed by the gap obtained by restricting to the 2-excitation sector only ($s = 2$) - the $\mathcal{E}_n^{(2)}$ gap used in section 5.2.2. Analysing the scaling of $s = 2$ sector we find that it, and therefore the full Liouvillian gap scales as

$$\mathcal{E}_{\mathrm{gap}} \sim f(\Delta, h_z) + \mathcal{O}(N^{-1}), \tag{6.2}$$

where $f(\Delta, h_z)$ is non-zero when $|\Delta| > 0$. We will refer to this function as the "gap function" as it determines the features of the gap in the thermodynamic limit. Indeed extrapolating our numerical results to $N \to \infty$ seems confirms this, see Fig. 6.1. We should note that the gap function depends on more than Δ and h_z but

[1] We are assuming here that there is a unique steady state and hence only one such zero eigenvalue. Generically, this is not necessarily the case but for the models of interest here it will be so.

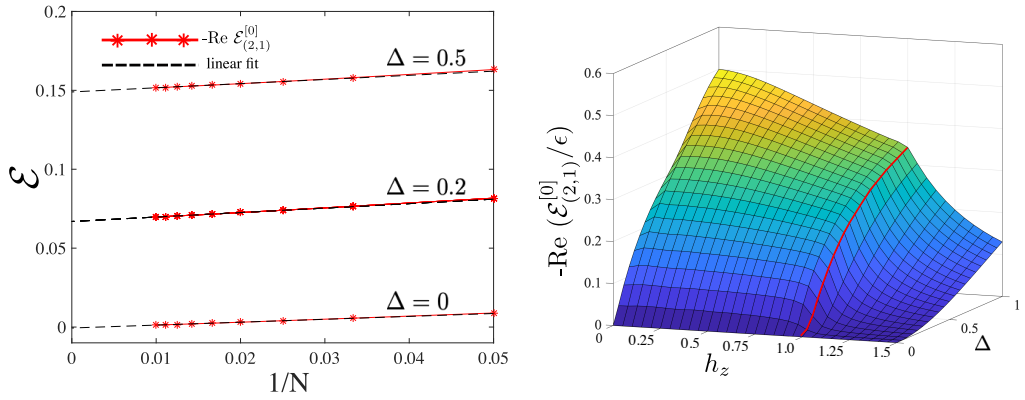

(a) Extrapolated $N \to \infty$ (b) Gap Across Phase Diagram Extrapolated

Figure 6.1: (a) Spectral gap scaling with $\alpha = 0.1$, $\beta = 0.3$, $\epsilon = 0.1$, $h_z = 0.5$. A nonzero Δ introduces a persistent gap in the $N \to \infty$ limit. (b) A scan of the projected $N \to \infty$ limit. The character of the gap changes when one traverses the quantum phase transition at $h_z = 1$ (red line). We note that the quantity plotted in the right figure is precisely $r_1^{(2)}$ of Sec. 5.2.2.

these are the critical variables for describing the functional form. In particular, the gap function does not depend on N in the thermodynamic limit. In this limit, the gap becomes precisely equal to this function.

Crucially, because of the constant gap, even in the thermodynamic limit one can move quickly between these limiting cases by simply tuning the transverse field at fixed Δ. Note that by "quickly" here, we mean that we have a finite relaxation time, independent of the system size but dependent on the model parameters. Systems with a finite gap in this limit are described as *rapidly mixing* and it can be shown that the resultant steady states are robust to local perturbations and uncorrelated at a scale equivalent to the inverse gap size [Žni15; Pou10; NVZ11; KE13; Luc+15; Cub+15]. Our results, obtained by similar methods to prior studies of a dissipative XY model [BİI12; JNK13], suggest that the XY system parameters can be used to quickly engineer and tune specific features into the steady state and as such have the potential to be used as a means of rapid state preparation.

We can identify the non-zero gap as a consequence of combining both an XY anisotropy and bulk dissipation. This is the distinguishing feature of the model as a non-zero gap is present in neither the XX model, i.e. the XY model without anisotropy, with TASEP [TWV12] nor with the symmetric simple exclusion process (SSEP) [Eis11]. Indeed, this feature of the gap is absent in the XY model with only boundary driving [PŽ09] processes. As such, we have determined after some examination that the ultimate requirements for a gap with these specific features are the TXY model as the Hamiltonian and dissipation across the full lattice, i.e. bulk and boundary dissipation. The precise functional form of the gap function $f(\Delta, h_z)$ for different types of dissipation, including TASEP, is found in section 6.2.

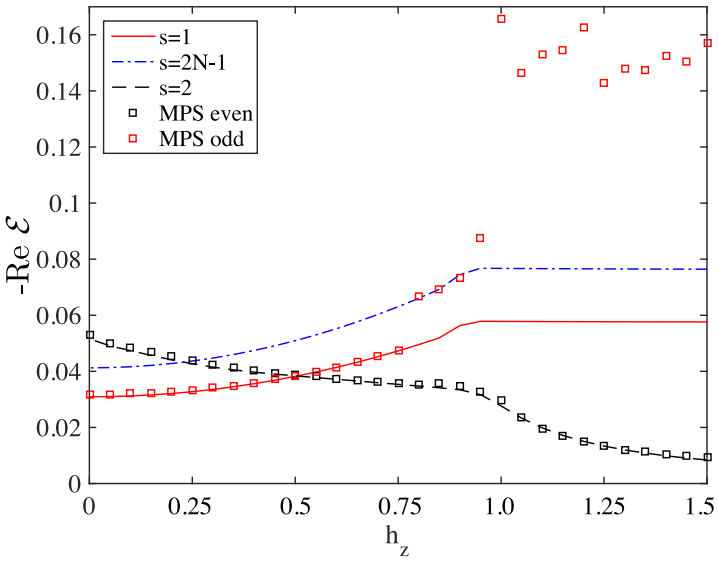

Figure 6.2: Comparison of projection and MPS methods for a line cut at: $\alpha = 0.1$, $\beta = 0.3$, $\Delta = 0.7$, $\epsilon = 0.1$ and $N = 30$. A low bond dimension ($D = 20$ in this case) can be used to estimate gapped low lying states in both sectors by adding a weighted parity operator to $\mathcal{L}$. The even-sector gap can be estimated directly due to the specific form the Liouvillian takes in the canonical basis, which means that one can decouple the $s = 0$ block without affecting any other eigenvalues.

6.1.2 MPS obtained $\mathcal{E}_{\text{gap}}$ versus $\mathcal{E}_1^{(2)}$

Our key claims on the scaling of the gap are based on the assertion that, in the weak dissipation regime, the full Liouvillian gap can be estimated by only solving the $s = 2$ sub-block. Our primary tool here is a MPS calculation where we can effectively project out the steady state from the variational algorithm. Here we exploit the structure that the Liouvillian superoperator takes in the canonical Majorana representation (as in Fig. 5.4), specifically using the fact that the $s = 0$ block is only connected to the $s = 2$ block via a single off-diagonal block, $\mathcal{L}^{(2,0)}$. This allows one to project out the steady state from the MPO that represents the full Liouvillian operator, while leaving all other eigenvalues unaffected.

In Fig. 6.2 we compare the results from $\mathcal{E}_1^{(2)}$ with the eigenvalues obtained from a full MPS treatment of a system of $N = 30$ and see excellent agreement right across the phase diagram. In Sec. 6.5 we also detail a perturbative argument for why these values are so close, using the Rayleigh-Schrödinger non-Hermitian formulation [SW72] of the TXY-TASEP system. A synopsis of this calculation is that in the small ϵ regime, we can consider s-blocks as only being weakly connected to their $(s \pm 2)$-block neighbours. Here the true $\mathcal{E}_{\text{gap}}$ can be expanded as

$$\mathcal{E}_{\text{gap}} = \mathcal{E}_1^{(2)} + \mathcal{E}_1^{(2)\prime} + \mathcal{E}_1^{(2)\prime\prime} + \ldots, \tag{6.3}$$

where $\mathcal{E}_i^{(s)}$ is the i^{th} eigenvalue from the s diagonal block and $\mathcal{E}_i^{(s)\prime}$ and $\mathcal{E}_i^{(s)\prime\prime}$ are the first and second order corrections. We expand on the meaning and calculation

of these corrections in Sec. 6.5. They are found by considering the connectivity of the Liouvillian superoperator's block structure in the canonical basis. Crucially, one finds that the first order correction $\mathcal{E}_1^{(2)\prime}$ is zero and that the second order correction is much smaller than the zeroth order estimate, and typically scales as ϵ^p where $p > 2$, see Sec. 6.5. As such the corrections quickly become vanishingly small.

6.1.3 Analysis of the $s = 2$ Spectrum

In the weak classical limit we can use $\mathcal{E}_1^{(2)}$ now as a proxy for the full gap and more fully analyse the parameter space of the model and assess its scaling as a function of system size, see Fig. 6.1. Our main result is that, in the thermodynamic limit $N \to \infty$, the gap $\mathcal{E}_{\text{gap}} \to f(\Delta, h_z)$ remains open if the anisotropy parameter is non-zero. However the dependence $\mathcal{E}_{\text{gap}}$ has on Δ also relies strongly on the magnetic field parameter, with clear differences occurring between the different quantum phases of the Hamiltonian.

When $\Delta = 0$ we find that $f(0, h_z) = 0$ and thus $\mathcal{E}_{\text{gap}} \sim N^{-1} \xrightarrow{N\to\infty} 0$. This value is completely unaffected by changes in magnetic field h_z, as a result of a Lindblad symmetry present, see e.g. [AJ14]. However, for non zero Δ and when $|h_z| < 1$ (where the underlying Hamiltonian has a topological gap and boundary zero-energy modes, Sec. 4.2) the Liouvillian gap develops linearly with Δ (the superconducting order parameter in the fermionic picture). On the other hand where $|h_z| > 1$, and the system Hamiltonian is non-topological and the gap develops $\propto \Delta^2$. This smaller gap means that perturbations to the thermal state are far more dramatic in this quantum regime, see Sec. 5.2.2. It remains to be seen if this observed behaviour of the gap can be connected in a precise way to the topology of the quantum model or if it is purely symptomatic of the presence of a phase transition. For a discussion on the odd sector blocks $s = 1$ and $s = 2N - 1$ see Sec. 6.6 and Sec. 6.7.

6.1.4 Relaxation Rate Compared to Related Models

The interpretation of the gap as an inverse relaxation time motivates one to consider the scaling of the gap with system size. If one has an inverse relation between the gap and the system size then in the large N limit the system will not relax to the steady state in finite time. As such one often aims to determine the dynamical exponent, z, in the scaling relation $\mathcal{E}_{\text{gap}} \sim N^{-z}$ [Žni15]. If $z = 0$, the longest relaxation times for the dynamics remain finite in the thermodynamic limit, while if $z > 0$ they diverge.

Generically, the dynamical exponent depends on a variety of factors from the model in question. The gap scaling of our model has been found in certain restricted cases where some processes such as bulk dissipation or superconductor pairing are absent. We summarise these known restricted cases in Table 6.1. Notably, we see that the appearance of a constant in system size gap is uncommon for models with

coherent hopping and dissipation modelled by exclusion processes.

$\hat{H}$	$\mathcal{D}$	z	Reference
TXY	Boundary SSEP	$3^{(a)}$	[PP08; Pro08]
None	TASEP	$0, 3/2, 2^{(b)}$	[DS00; NCS02; GE05; GE06]
(T)XY	Boundary Driving	$\geq 1^{(c)}$	[Žni15]
TXY	TASEP, SSEP, dephasing	0	Ch. 6 & [Kav+22b]

Table 6.1: Summary of related restricted cases of the TXY-TASEP model, labelled by the Hamiltonian ($\hat{H}$) and dissipative processes ($\mathcal{D}$) that enter the Lindblad equation. Broadly speaking, coherent hopping models under dissipation which can be obtained by restricting the TXY-TASEP model do not feature finite relaxation rates. It appears that non-zero Δ and dissipation on the full system are required for this feature to manifest. Note: (a) This exponent increases to $z = 5$ for $|h_z| = 1 - \Delta^2$. (b) These exponents correspond to the TASEP phases LD/HD, MC and CL respectively. (c) This has been shown as a generic bound for boundary driven dissipation on the TXY model. The TXY-TASEP model agrees with this bound for $\Delta = 0$, reinforcing the requirement for pairing to be present.

However, the existence of a finite gap for appropriate Hamiltonian parameters places the TXY-TASEP outside of the scope of the results summarised thusfar and indeed also outside the scope of integrable systems results [ZE20; LPP21]. One can draw the conclusion that both bulk and boundary dissipation together with pairing are necessary for a non-vanishing gap in all phases of the TASEP. Furthermore, we show in Sec. 6.3 and Sec. 6.4 that TASEP is not particularly unique in this sense. Additional dissipative processes give rise to the same essential features of the gap, namely dephasing and hermitian SSEP. Though we note that we have not conducted an exhaustive search of dissipative processes.

6.2 Kernel Projection for the Liouvillian Gap

In this section, we reiterate the important aspects of the model, TXY with dissipation, we will use to demonstrate the kernel projection method to obtain the Liouvillian gap. As in the previous chapter we exploit the superoperator representation of the total Liouvillian. As a pedagogical example we take the dissipation to be single site dephasing but include further more involved forms of dissipation such as TASEP which verifies the observations made numerically.

6.2.1 Model

As before we begin this the Lindblad master equation [GKS76; Lin76] in superoperator form. To reiterate, this equation for the evolution of the system's density matrix is comprised of two parts: the Hamiltonian commutator and the dissipator.

In combination we refer to these as the Liouvillian which we write as

$$\frac{d\rho}{dt} = -i\mathbb{H}(\rho) + \epsilon\mathbb{L}(\rho) = \mathcal{L}(\rho). \tag{6.4}$$

Here the commutator $\mathbb{H}(\rho) = [\hat{H}, \rho]$ is with respect to the system Hamiltonian, the transverse XY model:

$$\hat{H} = \frac{\mu}{2}\sum_{j=1}^{N}\sigma_j^z + \frac{1}{2}\sum_{j=1}^{N-1}\left((w+\Delta)\sigma_j^x\sigma_{j+1}^x + (w-\Delta)\sigma_j^y\sigma_{j+1}^y\right). \tag{6.5}$$

From this point we only use notation for parameters matching that of Ch. 4 to keep clear the connection to the topological model. In superoperator form the commutator becomes

$$\mathbb{H}(\rho) \to \mathcal{H}|\rho\rangle\!\rangle = \left(\hat{H}\otimes\mathbb{I} - \mathbb{I}\otimes\hat{H}^T\right)|\rho\rangle\!\rangle, \tag{6.6}$$

where $|\rho\rangle\!\rangle$ is the vectorised density matrix. It can be useful at points to consider the Hamiltonian in its fermionic form, obtained via Jordan-Wigner transformation. The core step here is to use the mapping of Eq.2.7, which yields the fermionic Hamiltonian expressed as

$$\hat{H} = -\mu\sum_{j=1}^{N}(c_j^\dagger c_j - 1/2) + \sum_{j=1}^{N-1}\left(-wc_j^\dagger c_{j+1} + \Delta\ c_j c_{j+1} + h.c.\right). \tag{6.7}$$

We note that if $\Delta \neq 0$, the TXY model has a quantum phase transition at $|\mu| = 2w$. The Hamiltonian is quadratic in fermion operators and therefore can be solved using free fermion solutions $\beta_n^\dagger$ to write

$$\hat{H} = \sum_n E_n(\beta_n^\dagger\beta_n - 1/2). \tag{6.8}$$

We will use this notion of mapping to free fermion solutions later when working with the complete Liouvillian superoperator.

After fixing the Hamiltonian of the Liouvillian (6.4) we note that the dissipator has the superoperator form

$$\mathbb{L}[\ell] = \sum_n \ell_n^*\otimes\ell_n - \frac{1}{2}\mathbb{I}\otimes\ell_n^\dagger\ell_n - \frac{1}{2}\ell_n^T\ell_n^*\otimes\mathbb{I}. \tag{6.9}$$

By using this superoperator form one can see the more clearly the connection to the operators in the canonical basis described in this section. To define each type of dissipation herein, it suffices to define the set of ℓ_n operators. These will be often distinguished by whether they correspond to the bulk or boundary of the underlying lattice. The nature of the Liouvillian gap and the non-equilibrium steady state

can be altered dramatically depending on which are included. We exemplify the methodology with several forms of dissipation that lead to block diagonal Liouvillian matrices. The first, which will exemplify the methodology, is local dephasing appearing next. The others which include exclusion processes appear in short form in Sec. 6.4. These latter dissipative processes produce results for the gap which are not necessarily exact yet provide good approximate descriptions.

6.2.2 Setup of Kernel Projection Method

We now detail the Hamiltonian kernel projection method that allows us to determine a functional form for the Liouvillian gap. First we form a superoperator basis which takes its inspiration from a Majorana fermion operator basis used in the diagonalization of quadratic Hamiltonians. The Majorana fermion operators are defined directly from the spin operators as:

$$\gamma_{2i-1} = -\prod_{k=1}^{i-1} \sigma_k^z \cdot \sigma_i^y, \quad \gamma_{2i} = \prod_{k=1}^{i-1} \sigma_k^z \cdot \sigma_i^x. \tag{6.10}$$

These Majorana operators can be the viewed as a set of operators, $\gamma_{x,y}$, which appear on the opposite upper/lower legs of a $N \times 2$ ladder of sites so that they may be labelled by:

$$\gamma_{x,1} = \gamma_{2i-1}, \quad \gamma_{x,2} = \gamma_{2i}. \tag{6.11}$$

In this way the i index which runs over $2N$ sites in the doubled space is split into the N rungs of the $N \times 2$ ladder. We can implicitly take odd- and even-numbered γ as being on opposite legs of this ladder throughout. The utility of this transformation and relabelling it that any quadratic fermionic Hamiltonian, including Eq. 6.5 under a Jordan-Wigner transformation, can be written as

$$H = i \sum_{ij} A_{ij} \gamma_i \gamma_j. \tag{6.12}$$

In this form, we see that in the (Majorana) canonical basis the commutator of this system $\mathbb{H} = [H, \cdot]$ is block diagonal and moreover, that the eigensystem of the full commutator can be found in a systematic way from the single particle block, which turns out to be the adjacency matrix A [Kel15b].

Building upon this approach, we use an operator basis for the Liouvillian consisting of ordered strings of Majorana operators

$$\Gamma_{\vec{\nu}} = \gamma_1^{\nu_1} \gamma_2^{\nu_2} \dots \gamma_{2N}^{\nu_{2N}}. \tag{6.13}$$

The index ν is a binary label for the elements γ_i that are present in a given operator string. This basis, together with the Hilbert-Schmidt inner product on operators

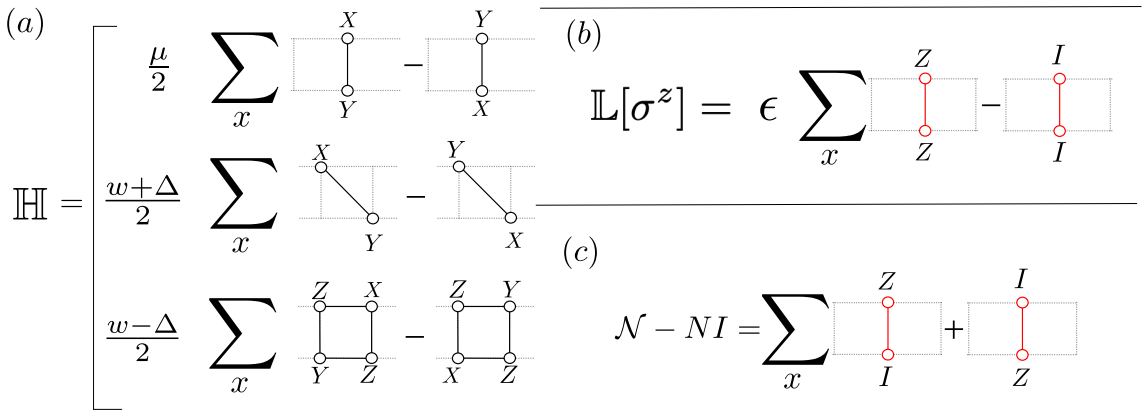

Figure 6.3: (a) The superoperator of the Hamiltonian commutator in the canonical basis. We use the shorthand $A = \sigma^a$. Note that the operator in the transverse XY model basis becomes a sum and combination of other operators in the superoperator ladder basis. For example, σ^z the external field becomes the anti-symmetric combination of X and Y on opposite sides of the ladder as shown in the μ term of (a). Of particular importance in our later analysis of the dephasing terms in Sec. 6.3 is the role played by z-dimers on the rungs of the ladder (b). These correspond to operators consisting of products where both $\gamma_{(x,1)}$ and $\gamma_{(x,2)}$ appear or where they are both absent. (c) Total magnetization term in the canonical basis.

$\langle\langle A|B\rangle\rangle = Tr(A^\dagger B)/2^N$, allows us to write the matrix elements of the total Liouvillian,

$$\mathcal{L}_{\nu,\nu'} = \langle\langle \Gamma_{\vec{\nu}}|\mathcal{L}|\Gamma_{\vec{\nu}'}\rangle\rangle, \tag{6.14}$$

and render the Liouvillian as a sum of spins on a two leg ladder see Figure 6.3.

Before we continue, it is worth to understand how we arrive at Fig. 6.3. As an illustrative example we look at how the σ^z term of the Hamiltonian enters the ladder diagram. Consider, how to express σ^z using the Majorana operators, γ, as defined in Eq. 6.10. We can see readily that

$$\sigma_i^z = -i\gamma_{2i-1}\gamma_{2i} = -i\left(-\prod_{k=1}^{i-1}\sigma_k^z\right)\sigma_i^y\left(\prod_{k=1}^{i-1}\sigma_k^z\right)\sigma_i^x = \sigma_i^z, \tag{6.15}$$

which at this point is trivial. However, taking the γ operators with explicit (x, y) ladder notation (6.11) we have

$$\begin{aligned}\sigma_j^z = -i\gamma_{j,1}\gamma_{j,2} &= -i\left(-\prod_{k=1}^{j-1}\sigma_{k,1}^z\right)\sigma_{j,1}^y\left(\prod_{k=1}^{j-1}\sigma_{k,2}^z\right)\sigma_{j,2}^x \\ &= i\left(\prod_{k=1}^{j-1}\sigma_{k,1}^z\sigma_{k,2}^z\right)\sigma_{j,1}^y\sigma_{j,2}^x.\end{aligned} \tag{6.16}$$

We can see from this why the left portion of the μ term in Fig. 6.3 (a) appears as X-Y. For the right portion, recall that to the right of tensor product we have need the conjugate-transpose of the Hamiltonian. Therefore, the individual terms

are conjugate-transposed which amounts to reversing the order of products of Pauli matrices in this perspective. Then, the second term from the commutator appears as Y-X on opposite sides of the ladder due to the reversed ordering. While this gives some intuition as to why this particular term appears as such on the ladder the explanation is imprecise. For a complete discussion see the Appendix of [Kel15b]. One must take care in translating operators on the original lattice to superoperators on the doubled ladder lattice. In addition, with the introduction of the canonical Majorana basis, there is a rearrangement of basis elements such that the mapping is not quite as direct as we have suggested here. The operator strings that appear above are artefacts of our loose presentation but can be dealt with in a systematic way. The presence of an operator string will ultimately depend on whether we want to use a spin representation of the Γ-Majorana canonical basis or of a Dirac fermion basis. Explicit expressions for the operators that transform the Liouvillian into the canonical Majorana basis appear in App. B. To further understand the subtleties of moving to the superoperator representation see [Pro08].

Some Liouvillian superoperators preserve the number of Majorana in a string, leading one to naturally define a block structure where each block is labelled in terms of the number of Majorana modes present in each state. This is essentially a conservation of the excitation number and is encoded by the operator $\mathcal{N}$ which takes the form of a magnetisation term in the canonical representation, see Figure 6.3(c). We exploit this emergent block structure in the remainder of this paper to determine the Liouvillian gap. While this is not necessarily exact in all cases included in this work; we have found, nonetheless, that this approach is both an effective and close estimate of the true gap. This is in the same spirit as block diagonalising a Hamiltonian matrix representation where an exactly block diagonal matrix is easily exploited but even a close to block diagonal structure can be advantageous.

In the case of the hermitian SSEP [Eis11] this structure occurs exactly, and one can diagonalize the full Liouvillian block by block. This criterion is also met exactly in the case of symmetric boundary driving [PP08] where $\alpha_+ = \alpha_-$ and $\beta_+ = \beta_-$. Indeed, even with a boundary rate asymmetry, one can still write out the full Liouvillian in terms of quadratic fermionic superoperators and thereby determine the steady-state and Liouvillian gap. In the canonical representation, we can understand this as a rendering of the Liouvillian matrix into a lower triangular block form, meaning that the entire spectrum of $\mathcal{L}$ can still be found by solving the blocks individually. Crucially, for the boundary driving problem the higher excitation number block eigenvalues can be understood in terms of eigenvalues of the extremal blocks (e.g. $s = 1$ and $s = 2N - 1$), for further discussion see Ch. 5.

Prosen [Pro08] showed that a convenient way to work in this picture is to define creation and annihilation superoperators, which create the Majorana operator labels

inside the double ket structure. For example

$$\mathsf{G}^\dagger_{x,y}|\, I\rangle\!\rangle = |\, \gamma_{x,y}\rangle\!\rangle. \tag{6.17}$$

Using the canonical representation shown in Fig. 6.3 we can write the full commutator as $\mathbb{H} = \mathbb{H}^R - \mathbb{H}^L$

$$\begin{aligned}\mathbb{H}^S = i\mu \sum_{x=1}^{N} \mathsf{G}^\dagger_{x,1}\mathsf{G}^\dagger_{x,2} + i\frac{1}{2}(w+\Delta)\sum_{x=1}^{N-1} \mathsf{G}^\dagger_{x,1}\mathsf{G}^\dagger_{x+1,2} \\ + i\frac{1}{2}(w-\Delta)\sum_{x=1}^{N-1} \mathsf{G}^\dagger_{x+1,1}\mathsf{G}^\dagger_{x,2},\end{aligned} \tag{6.18}$$

where the operators on the RHS are on the R, L side of the tensor product depending on S. We can also generate eigenvectors of $\mathcal{H}$, using the free-fermion solutions $\beta^\dagger_n = \sum_{i=1}^{2N} W^*_{ni}\gamma_i$ of $\hat{H}$ to make quasi-particle creation superoperators

$$\mathsf{B}_n = \sum_{i=1}^{2N} u_{ni}\mathsf{G}_i, \tag{6.19}$$

such that

$$|\, \beta^\dagger_n\rangle\!\rangle = \mathsf{B}_n|\, I\rangle\!\rangle, \quad |\, \beta_n\rangle\!\rangle = \mathsf{B}^\dagger_n|\, I\rangle\!\rangle, \tag{6.20}$$

are eigenstates of $\mathbb{H}$ with eigenvalue E_n and with support in the single particle block $s = 1$. We can combine operations to make states inside the other blocks. For example,

$$|\, \beta^\dagger_n\beta_m\rangle\!\rangle = \mathsf{B}_n\mathsf{B}^\dagger_m|\, I\rangle\!\rangle, \tag{6.21}$$

has eigenvalue $E_n - E_m$ and is supported in the two quasi-particle block $s = 2$.

6.3 Kernel Projection Method for Dephasing

Up to this point the steps of the kernel projection method have been generic. In this section we use an example to give the reader an understanding of how one would perform the remainder of the calculation. We further split the kernel projection into two parts; one for the case of strong dissipation/weak quantum regime and the case of weak dissipation/strong quantum regime.

The key feature we want to address here is the role that Cooper pair creation and annihilation plays in the steady-state relaxation rate. In cases where the eventual steady-state is a featureless infinite-temperature thermal state, there should be a significant effect that can be argued heuristically: Cooper-pair creation and annihilation will drive the system towards half-filling and the infinite temperature steady-state is naturally dominated by such half-filled states.

To quantify this we choose a system undergoing bulk dephasing, choosing Lind-

blad ℓ operators of the form

$$\ell_x = \sqrt{\epsilon}\sigma_x^z. \tag{6.22}$$

This type of process preserves excitation number symmetry. In the canonical representation (6.14) we can write these terms as

$$\mathbb{L}[\sigma_z] = \epsilon \sum_x (Z_{x,1}Z_{x,2} - \mathbb{I}), \tag{6.23}$$

which we can see commutes with the excitation number symmetry operator shown in Figure 6.3(c). Note in addition that this is the superoperator on the ladder, hence the quadratic Z term coming from either side.

6.3.1 Weak quantum limit - Projection to the $\mathbb{L}$ kernel

In the canonical basis the spin-$|\downarrow\rangle\!\rangle_i$ represents the presence of a Majorana operator as a label in the state $|\gamma_i\rangle\!\rangle$ while spin-$|\uparrow\rangle\!\rangle_i$ represents the absence of such an operator. For dephasing then, we can see that states $|\Gamma\rangle\!\rangle$, where only pairs like $\gamma_{x,1}\gamma_{x,2}$ occur, will sit in the kernel of $\mathbb{L}$. In the weak quantum limit ($1/\epsilon \ll w, |\Delta|, |\mu|$) we can thus consider the commutator $\mathbb{H}$ as a perturbation to this subspace. Setting

$$|\Uparrow\rangle\!\rangle \equiv |\uparrow\uparrow\rangle\!\rangle, \quad |\Downarrow\rangle\!\rangle \equiv |\downarrow\downarrow\rangle\!\rangle, \tag{6.24}$$

and perturbing in this degenerate space we see that on the first order the commutator $\mathcal{H}$ takes us completely out of this space and so $L^{\{1\}} = 0$. On the second order, however, we return to this subspace and can write the resulting effective model as

$$\begin{aligned} L^{\{2\}} = &\frac{w^2 + \Delta^2}{4\epsilon} \sum_i \left(\tau_i^z \tau_{i+1}^z - \mathbb{I}\right) \\ &+ \frac{w^2 - \Delta^2}{4\epsilon} \sum_i \left(\tau_i^x \tau_{i+1}^x + \tau_i^y \tau_{i+1}^y\right) \end{aligned} \tag{6.25}$$

where the τ's are Pauli operators acting on the $|\Uparrow\rangle\!\rangle$ and $|\Downarrow\rangle\!\rangle$ basis. We can understand how these τ operators arise by first considering the terms that could appear at second order in the spin ladder picture. Then we map the operators on the rungs of this resultant ladder in a similar spirit to an effective spin hard-core boson mapping [SDV08]. This amounts to τ appearing from σ as:

$$\begin{aligned} \tau_i^x &\equiv \sigma_{i,1}^x \otimes \sigma_{i,2}^x,\ \tau_i^x \equiv -\sigma_{i,1}^y \otimes \sigma_{i,2}^y, \\ \tau_i^y &\equiv \sigma_{i,1}^x \otimes \sigma_{i,2}^y, \\ \tau_i^z &\equiv \sigma_{i,1}^z \otimes \mathbb{I}_{i,2}, \\ \mathbb{I}_i &\equiv \sigma_{i,1}^z \otimes \sigma_{i,2}^z. \end{aligned} \tag{6.26}$$

The model can be seen to be an XXZ model shifted so that its eigenvalues are

always negative semidefinite, and it can be solved by employing Bethe Ansatz techniques [BdV83]. The no-spin sector has eigenvalue $E_0 = 0$ and corresponds to the effective steady-state. The one spin excitation sector (i.e. the sector with one $\Downarrow$ that sits in the $s = 2$ sector of the full model), has a spectrum

$$E_k = \frac{w^2 - \Delta^2}{\epsilon} \cos(k) - \frac{w^2 + \Delta^2}{\epsilon} \tag{6.27}$$

resulting in a relaxation gap of $-2\Delta^2/\epsilon$ at $k = 0$. The gap is robust as the system length $N \to \infty$ and, as the system maps directly to the XXZ chain, we can also work out the two and higher excitation sectors via the standard Bethe Ansatz approach.

Interestingly the μ (or h_z) parameter does not appear at all on the second order, contributing only at higher orders (4th and above). This means that signatures of the quantum phase transition are essentially washed out in this limit. We will show that this situation changes dramatically in the strong quantum limit, and that the presence of the quantum phase transition is clearly visible in the steady-state relaxation rates.

6.3.2 Strong quantum limit - Projection to the $\mathbb{H}$ kernel

We need to take a different strategy to approach the strong quantum limit ($\epsilon \ll w, |\Delta|, h_z$). To do this, we shall first define, using the free-modes of the Hamiltonian, a set of vectorized operators that lie in the kernel of $\mathcal{H}$. Then, we expand the dephasing term in this basis and show that, for low quasi-particle excitation numbers, this effective Liouvillian permits a direct solution.

It was shown in [Kel15a] that to enumerate states in the kernel of $\mathbb{H}$ one can symmetrically "super-create" terms that have creation and annihilation operators of the same free-fermion modes β, e.g.,

$$\mathsf{K}_n \equiv \mathsf{B}_n \mathsf{B}_n^\dagger - \mathsf{B}_n^\dagger \mathsf{B}_n. \tag{6.28}$$

Operating with a K operator on the identity element (maximally mixed state) gives

$$\mathsf{K_n}|\, I\rangle\!\rangle = |\, K_n\rangle\!\rangle \equiv |\, \beta_n \beta_n^\dagger - \beta_n^\dagger \beta_n\rangle\!\rangle, \tag{6.29}$$

and from here one can span the full kernel of $\mathbb{H}$

$$|\, K_n\rangle\!\rangle,\ |\, K_{n_1}, K_{n_2}\rangle\!\rangle,\ \ldots,\ |\, K_{n_1}, K_{n_2} ..., K_{n_N}\rangle\!\rangle. \tag{6.30}$$

One can then expand the dissipative terms of $\mathbb{L}$ in this basis and use it to make statements about the behaviour of the Liouvillian gap in the weak stochastic limit. In what follows we will be particularly interested in the behaviour of the $s = 2$

particle block

$$\tilde{\mathcal{L}}^{(2)}_{n,m} \equiv \langle\!\langle K_n \,|\mathbb{L}|\, K_m \rangle\!\rangle. \tag{6.31}$$

To work out the functional form for these states we start by assuming a system with periodic boundary conditions, such that, in the Majorana basis, the free fermion modes $\beta^\dagger_k = \sum_r W_{r,k}\gamma_r$ (where $r = (x, y)$) can be expressed as:

$$W_{r,k} = \frac{-e^{ikx}}{\sqrt{2N_x}}(i^y v_k + (-i)^y u_k), \tag{6.32}$$

where

$$u_k = \sqrt{\frac{1}{2} + \frac{\varepsilon_k}{2E_k}}, \quad v_k = -\sqrt{\frac{1}{2} - \frac{\varepsilon_k}{2E_k}} e^{i\arg\Delta_k}, \tag{6.33}$$

and $\varepsilon_k = -\mu - 2t\cos k$, $E_k = \sqrt{\varepsilon_k^2 + |\Delta_k|^2}$, and $\Delta_k = i2\Delta\sin k$. For two particles this gives the state,

$$|\, K_k \rangle\!\rangle = \sum_{r_1,r_2} W_{r_1,r_2,k} |\, \gamma_{r_1}, \gamma_{r_2} \rangle\!\rangle \tag{6.34}$$

with

$$W_{r_1,r_2,k} = \begin{cases} \frac{-i}{NE_k}[(-1)^{y_1}\varepsilon_k \cos k\delta_x - i\Delta_k \sin k\delta_x] \text{ if } y_1 \neq y_2, \\ \frac{i}{N}\sin k\delta_x \qquad\qquad\quad \text{if } y_1 = y_2, \end{cases} \tag{6.35}$$

where $\delta_x \equiv x_1 - x_2$. This expression is purely imaginary if we assume $\Delta \in \mathbb{R}$.

To probe the strong quantum limit we can now project to the 2-particle block to produce the $\tilde{\mathcal{L}}^{(2)}$ using the states $|\, K_k \rangle\!\rangle$ in (6.34). This yields

$$\begin{aligned} \tilde{\mathcal{L}}^{(2)}_{kk'} &= \langle\!\langle K_k \,|\mathbb{L}|\, K_{k'} \rangle\!\rangle, \\ &= \epsilon \sum_{r_1 r_2} W^*_{r_1 r_2 k} W_{r_1 r_2 k'} \langle\!\langle \gamma_{r_1}\gamma_{r_2} \,|\, \sum_x Z_{x,1}Z_{x,2} - \mathbb{I}|\, \gamma_{r_1}\gamma_{r_2} \rangle\!\rangle, \\ &= \epsilon \sum_{r_1 r_2} \frac{1}{N}\frac{\varepsilon_k \varepsilon_{k'}}{E_k E_{k'}} \delta_{x_1 x_2} - \epsilon\delta_{kk'}, \\ \Rightarrow \tilde{\mathcal{L}}^{(2)} &= \frac{\epsilon}{N}\left(|\tilde{\psi}\rangle\langle\tilde{\psi}| - N \right), \end{aligned} \tag{6.36}$$

where we have defined the vector $|\tilde{\psi}\rangle_k \equiv \varepsilon_k/E_k$ with normalised form $|\psi\rangle = J_\psi^{-1}|\tilde{\psi}\rangle$ and $J_\psi^2 = \left\langle \tilde{\psi} \middle| \tilde{\psi} \right\rangle = \sum_k \varepsilon_k^2/E_k^2$. In total, then, by projecting to the 2-excitation kernel $|\, K_k \rangle\!\rangle$ we obtain the sub-matrix

$$\tilde{\mathcal{L}}^{(2)} = \frac{\epsilon}{N} \times \left(J_\psi^2 \,|\psi\rangle\,\langle\psi| - N \right), \tag{6.37}$$

from which we directly read off the principle eigenvalue as,

$$\mathcal{E}_{gap} = -\frac{\epsilon}{N}\sum_k \frac{|\Delta_k|^2}{E_k^2} \xrightarrow{N\to\infty} -\epsilon \int dk \frac{|\Delta_k|^2}{E_k^2}. \tag{6.38}$$

6.3.3 Gap Analysis

Now, writing the expression for the gap (6.38) explicitly we find the following integral form

$$\mathcal{E}_{gap} = -\epsilon \int_{-\pi}^{\pi} dk \frac{|2\Delta \sin(k)|^2}{(\mu + 2w\cos(k))^2 + |2\Delta \sin(k)|^2}. \tag{6.39}$$

To expedite our discussion of the result we leave the details of the evaluation to Appendix D. There, we show how this expression can be evaluated by careful substitution or by considering a contour integral. Remarkably we find that within the topological region ($|\mu| < 2w$), the integral is independent of μ giving

$$\mathcal{E}_{gap} = 4\pi\epsilon \frac{\Delta}{w + \Delta}. \tag{6.40}$$

In the non-topological region ($|\mu| > 2w$) this sharply transitions to

$$\mathcal{E}_{gap} = 4\pi\epsilon \frac{\Delta^2}{w^2 - \Delta^2} \left(\frac{|\mu|}{\sqrt{\mu^2 - 4w^2 + 4\Delta^2}} - 1 \right), \tag{6.41}$$

which decays as $1/\sqrt{|\mu|}$ when $|\mu| \gg 2w$, see Figure 6.4. At the transition, $\mu = 2w$ the integral is not defined.

The constant (with respect to μ) relaxation gap is highly unusual and reminiscent of the behaviour of the topological index or winding number for the XY system, see e.g. [Sta16]. Translating into the spin language it implies that across the entire ferromagnetic region the first-order response of the system is entirely independent of any applied transverse field. Conversely, when the parameters of the Hamiltonian enter the paramagnetic regime, the relaxation gap experiences a sharp drop-off as the field amplitude is made larger. Crucially, neither expression depends on the system length N and therefore means that it is possible to engineer a robust and precisely controlled excitation gap in the thermodynamic limit.

Systems with constant (in length) relaxation gaps are often referred to as rapidly mixing [Pou10; NVZ11; KE13; Luc+15; Cub+15; Žni15]. In the two cases considered, since the jump operators ℓ in all cases are Hermitian, the eventual steady state is the maximally mixed thermal state. This can be seen algebraically, because $[H, \mathbb{I}] = 0$ always and if $\ell = \ell^\dagger$ then $\mathbb{L}(I) = \sum_n \ell^2 - \frac{1}{2}\ell^2 - \frac{1}{2}\ell^2 = 0$. It can also be understood visually from the block structure that $\mathcal{L}$ takes in the canonical basis. If the ℓ are hermitian then the vector $|\, I\rangle\!\rangle$ corresponding to the thermal state is completely disconnected from all other vectors and is thus already an eigenstate with eigenvalue 0. For non-Hermitian jump operators (e.g. the TASEP model of the appendix) the eventual steady-state can be, on a perturbative level, understood as an iteratively dressed thermal state [Kav+22a].

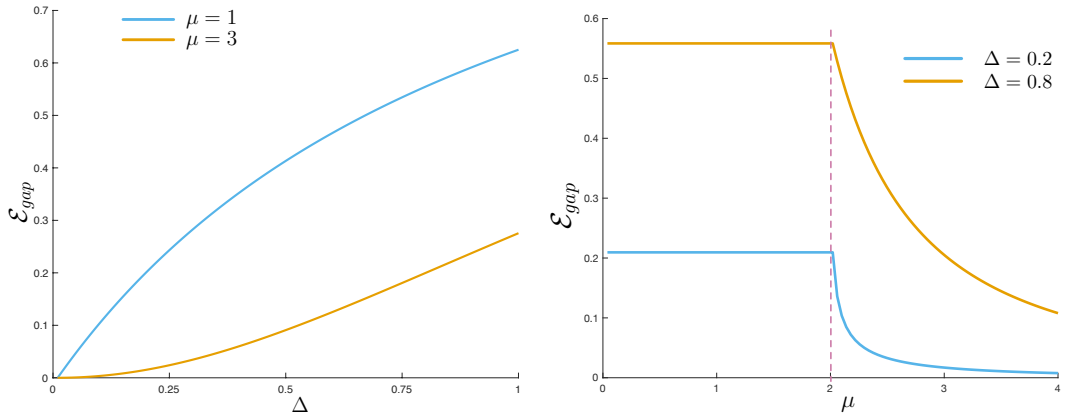

(a) Δ dependent gap at fixed μ (b) μ dependent gap at fixed Δ

Figure 6.4: (a) Plot of the Liouvillian gap with respect to Δ in the topological ($\mu = 1$) and trivial ($\mu = 3$) phases respectively. One can see the difference in the development of the gap from the analytic expressions (6.40 & 6.41) which was observed in our numerics, see e.g. subfigure (b) of Fig. 6.1. (b) The gap plotted against μ at fixed Δ. Here we see the sharp change in behaviour at the phase transition $\mu = 2w$, marked by the dashed line. For both plots we have the coherent hopping $w = 1$.

6.4 Further Models of Dissipation

This section collects the results for the projection method for the symmetric simple exclusion process (SSEP) and totally asymmetric simple exclusion process (TASEP). Both, while being more involved than dephasing, produce a similar Liouvillian gap which admits a topological aspect.

6.4.1 Symmetric Simple Exclusion Process

The same expression also arises in the treatment of stochastic hopping. Consider for example the Hermitian process

$$\begin{aligned} \ell_{2x-1} &= \sqrt{\epsilon}\sigma_x^-\sigma_{x+1}^+ + \sqrt{\epsilon}\sigma_x^+\sigma_{x+1}^-, \\ \ell_{2x} &= \sqrt{\epsilon}\sigma_x^-\sigma_{x+1}^+ - \sqrt{\epsilon}\sigma_x^+\sigma_{x+1}^-, \end{aligned} \tag{6.42}$$

This choice of Hermitian jump operators has the nice property that it preserves what we call excitation number symmetry. When looking at the superoperator matrix representation of the Liouvillian ($\mathbb{L}$) this leads to a hierarchy of blocks that can be solved individually [Eis11].

As in the previous section we project to the 2-particle kernel of the commutator which yields

$$\begin{aligned} \tilde{\mathcal{L}}^{(2)}_{k,k'} &= \langle\langle K_k \,|\mathbb{L}|\, K_{k'}\rangle\rangle, \\ &= \epsilon\frac{4}{N}\cdot\left(\frac{\varepsilon_k\varepsilon_{k'}}{E_kE_{k'}} + \frac{\Delta_k\Delta_{k'}\sin k\sin k'}{E_kE_{k'}}\right). \end{aligned} \tag{6.43}$$

from which we can extract the non trivial eigenvalues exactly from the two level model

$$H_{\text{eff}} = \epsilon \frac{4}{N} \begin{bmatrix} J_\psi^2 & \langle\psi|\phi\rangle \\ \langle\phi|\psi\rangle & J_\phi^2 \end{bmatrix} - 4\epsilon I_2 \tag{6.44}$$

where $|\tilde{\psi}\rangle_k = \varepsilon_k/E_k$ and $|\tilde{\phi}\rangle_k = \sin k \times \Delta_k/E_k$ and $J_\psi^2 = \left\langle \tilde{\psi} \middle| \tilde{\psi} \right\rangle = \sum_k \varepsilon_k^2/E_k^2$, $J_\phi^2 = \left\langle \tilde{\phi} \middle| \tilde{\phi} \right\rangle = \sum_k (\sin k)^2 \Delta_k^2/E_k^2$. A first order estimate of the gap $\mathcal{E}$ is then

$$\mathcal{E} = \frac{4\epsilon}{N} J_\psi^2 - \epsilon = -\frac{4\epsilon}{N} \sum_k \frac{|\Delta_k|^2}{E_k^2}, \tag{6.45}$$

which, as $N \to \infty$, is 4 times the expression given in (6.38). Next, we show how the same expression arises, again on a perturbative level, for the TASEP dissipator that encodes a non-symmetric, non-Hermitian stochastic hopping.

6.4.2 Totally asymmetric simple exclusion process

Temme et. al. [TWV12] considered the totally asymmetric simple exclusion process (TASEP) with coherent hopping (i.e. $\hat{H}|_{\Delta=0}$, the XX model). In the bulk the model consists of $N-1$ stochastic terms,

$$\ell_x = \sqrt{\gamma}\sigma_x^- \sigma_{x+1}^+, \quad \forall x \in \{1, \ldots, N-1\}, \tag{6.46}$$

and two boundary terms which specify particle creation (hop on of spin downs) on the left hand side and particle annihilation (hopping off of spin down) on the right

$$\ell_N = \sqrt{\alpha}\sigma_1^-, \quad \ell_{N+1} = \sqrt{\beta}\sigma_N^+, \tag{6.47}$$

see App. C for a more complete description.

The full Lindblad operator for the TASEP is given diagrammatically in Fig. 6.5. For TASEP we typically assume open boundary conditions for both Hamiltonian and stochastic terms. To produce the precise effective description we could then use single particle fermionic operators from this open boundary scenario. However, to simplify things we instead assume that we can use periodic momentum fermionic creation and annihilation operators to make the zero excitation energy kernel of $\mathcal{H}$. The situation is more complicated here since the superoperator matrix is not block diagonal but using the arguments of [Kav+22a] we note that we can project onto the $s = 2$ block for small ϵ and end up with a situation very similar to (6.42) above

$$\tilde{\mathcal{L}}^{(2)} = \epsilon \frac{N-1}{N^2} \times \left(J_\psi \left|\psi\right\rangle \left\langle\psi\right| + J_\phi \left|\phi\right\rangle \left\langle\phi\right| \right), \tag{6.48}$$

$$- \epsilon \left(1 - \frac{1}{N} + \frac{\alpha+\beta}{N} \right), \tag{6.49}$$

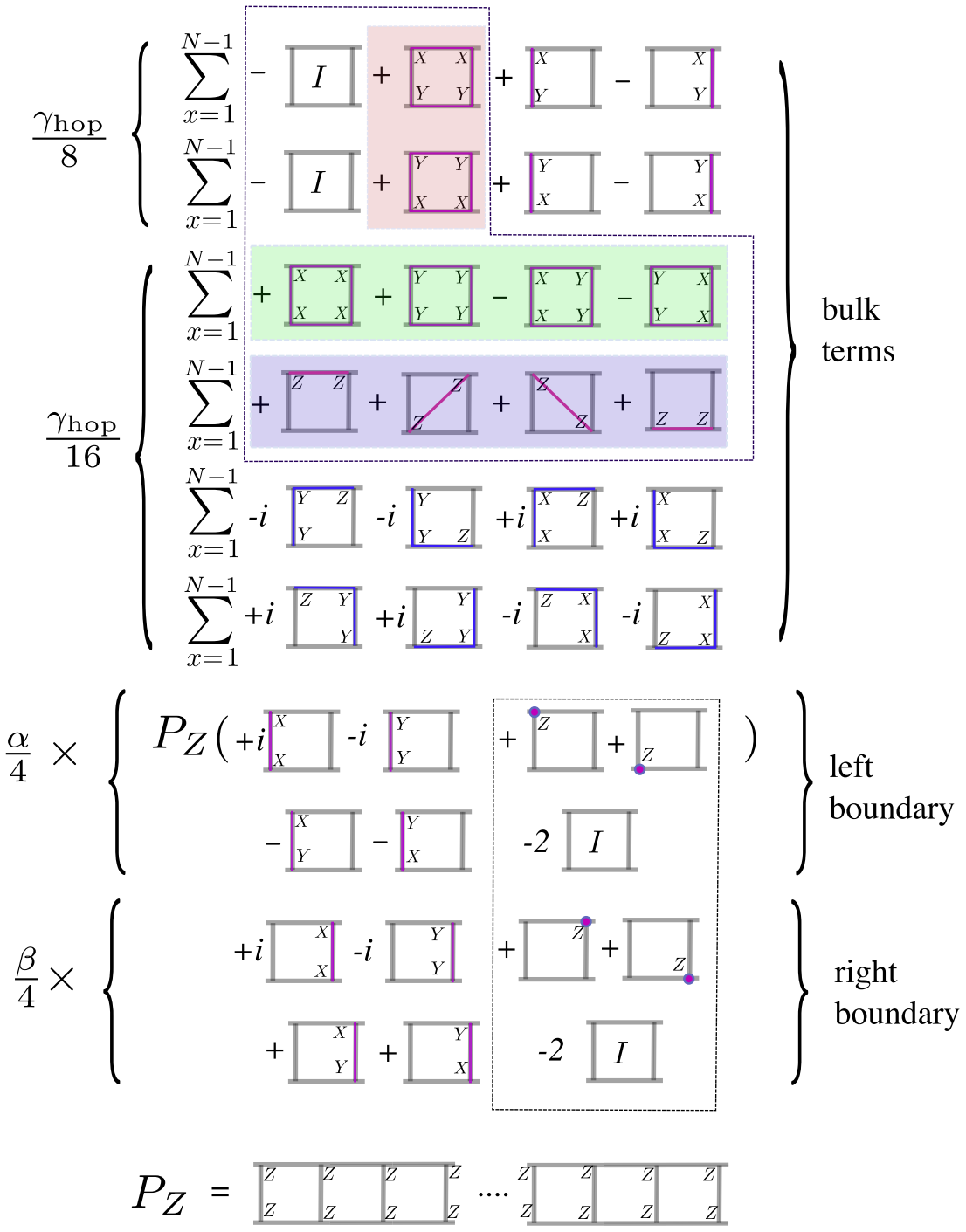

Figure 6.5: Full TASEP Lindblad superoperator in the canonical basis. We use the short hand $X = \sigma^x, Y = \sigma^y, Z = \sigma^z$. Only terms highlighted commute with the excitation number operator $\mathcal{N}$. For the Hermitian SSEP only these highlighted terms appear - albeit multiplied by an overall constant of 4. We have set $\gamma_{\text{hop}} = 1$ throughout this thesis.

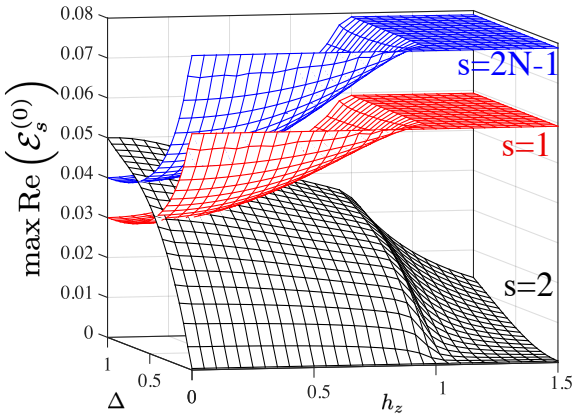

Figure 6.6: Numerically obtained spectral gaps from a number of extremal blocks. One of our main observations is that the complex spectrum near $\mathcal{E} = 0$ is dominated by the states generated from the extremal blocks $\mathcal{L}^{(0)}$, $\mathcal{L}^{(1)}$, $\mathcal{L}^{(2)}$ and $\mathcal{L}^{(2N-1)}$ and that the eigenvalues of these states are well approximated by diagonalizing within each block separately. This can be seen via a non-Hermitian perturbative analysis where the effects of off-diagonal blocks appear only at second order, see Sec. 6.5. In the figure, we give spectral gaps for $s = 1$ (red), $s = 2$ (black) and $s = 2N-1$ (blue) for a system of length $N = 100$, with $\alpha = 0.1$, $\beta = 0.3$, and $\epsilon = 0.1$.

which, using essentially the same analysis as the above, leads to a gap that tends to $\mathcal{E} = -\epsilon f(\Delta, \mu)$ in the $N \to \infty$ limit.

6.5 Block Perturbation Theory

The structure of the Lindblad operator in the canonical basis allows one to see why, in the weak classical limit, one can typically focus on the extremum blocks $s = 0, 1, 2$ and $2N - 1$ to understand the gap scaling. At a numerical level this can be seen in Fig. 6.7 where the blocks corresponding to $s = 1$ and $s = 2$ have the greatest relevance. Starting in the canonical basis, we generalise our previous notation and also label the block matrices according to the excitation number blocks that they connect. For example $\mathcal{L}^{(0,2)}$ is the block-matrix that connects the 0^{th} and 2^{nd} excitation number blocks, whereas, like before, $\mathcal{L}^{(n)}$ labels the n-excitation number diagonal.

We wish to understand how the coupling to other blocks affects the energies of a particular block and so employ a Rayleigh-Schrödinger non-Hermitian formulation problem [SW72], which proceeds very similar to the Hermitian counterpart. We consider the diagonal blocks as our unperturbed system

$$\mathcal{L}_0 = \sum_{s \in even} [\mathcal{L}^{(s)}] = \sum_{s \in \text{ even}}^{2N} \epsilon \backslash \mathbb{L}_{\backslash}^{(s)} - i\lambda \mathbb{H}^{(s)} \tag{6.50}$$

and the perturbation as the off diagonal complement

$$\mathcal{L}_1 = \mathcal{L} - \mathcal{L}_0 = \sum_{s\in \text{ even}} \mathcal{L}^{(s,s+2)} + \mathcal{L}^{(s+2,s)} \tag{6.51}$$

$$= \epsilon_{\backslash\backslash} \sum_{s\in \text{ even}} \mathbb{L}^{(s,s+2)} + \mathbb{L}^{(s+2,s)} \tag{6.52}$$

The left and right eigenvectors $|\,\tilde{v}_i^{(n)}\rangle\!\rangle$ and $|\,v_i^{(n)}\rangle\!\rangle$ are those which diagonalise the diagonal blocks $\mathcal{L}^{(n)}$

$$\langle\!\langle \tilde{v}_i^{(l)} \,|\mathcal{L}^{(n)}|\, v_j^{(m)} \rangle\!\rangle = \mathcal{E}_i^{(n)} \delta_{ij}\delta_{nm}\delta_{ln}, \tag{6.53}$$

Starting with one of the zeroth order states which we obtained by diagonalising one of the diagonal blocks $\mathcal{L}^{(n)}$ we wish to understand how the addition of the off diagonal blocks perturb this eigenvalue:

$$\mathcal{E}_{i,\text{exact}}^{(n)} = \mathcal{E}_i^{(n)} + \mathcal{E}_i^{(n)\prime} + \mathcal{E}_i^{(n)\prime\prime} + ... \tag{6.54}$$

The first order correction $\mathcal{E}_i^{(n)\prime}$ can be easily seen to vanish simply because $\mathcal{L}_1$ does not connect any block to itself

$$\mathcal{E}_i^{(n)\prime} = \langle\!\langle \tilde{v}_i^{(n)} \,|\mathcal{L}_1|\, v_j^{(m)} \rangle\!\rangle = 0. \tag{6.55}$$

The leading correction to the eigenvalue can thus only occur at second order or higher. Generally, the second order correction can be written as

$$\mathcal{E}_i^{(n)\prime\prime} = \sum_{j,m} \frac{\langle\!\langle \tilde{v}_i^{(l)} \,|\mathcal{L}_1|\, v_i^{(n)} \rangle\!\rangle \langle\!\langle \tilde{v}_i^{(l)} \,|\mathcal{L}_1|\, v_i^{(n)} \rangle\!\rangle}{\mathcal{E}_i^{(n)} - \mathcal{E}_j^{(n)}}. \tag{6.56}$$

For the steady state $\left|v^{(0)}\right\rangle$ with $\mathcal{E}^{(0)} = 0$ we see that, because $\mathcal{L}^{(0,2)} = 0$, there can be no higher order corrections to this eigenvalue (as one would expect). In our MPS calculations the same feature can be used to decouple the steady state from the even parity sector and allows us to converge variationally on the first even-parity excited state above the gap.

Our primary focus here is to understand the energy scaling of states from the $s = 2$ excitation-number block on a perturbative level. As $\mathcal{L}^{(0,2)} = 0$ we only have to consider perturbative paths that connect to the $s = 4$ block and thus:

$$\mathcal{E}_i^{(2)\prime\prime} = \sum_{j} \frac{\langle\!\langle \tilde{v}_j^{(2)} \,|\mathcal{L}^{(2,4)}|\, v_j^{(4)} \rangle\!\rangle \langle\!\langle \tilde{v}_j^{(4)} \,|\mathcal{L}^{(4,2)}|\, v_i^{(2)} \rangle\!\rangle}{\mathcal{E}_i^{(2)} - \mathcal{E}_j^{(4)}}. \tag{6.57}$$

The analysis above is fairly conventional. However there is one anomaly in that we have hidden the small parameter ϵ in both the diagonal and off diagonal blocks. Thus, we expect the parameter ϵ to appear in both numerator and denominator of the second order expansion above. For the off-diagonal terms the contribution there

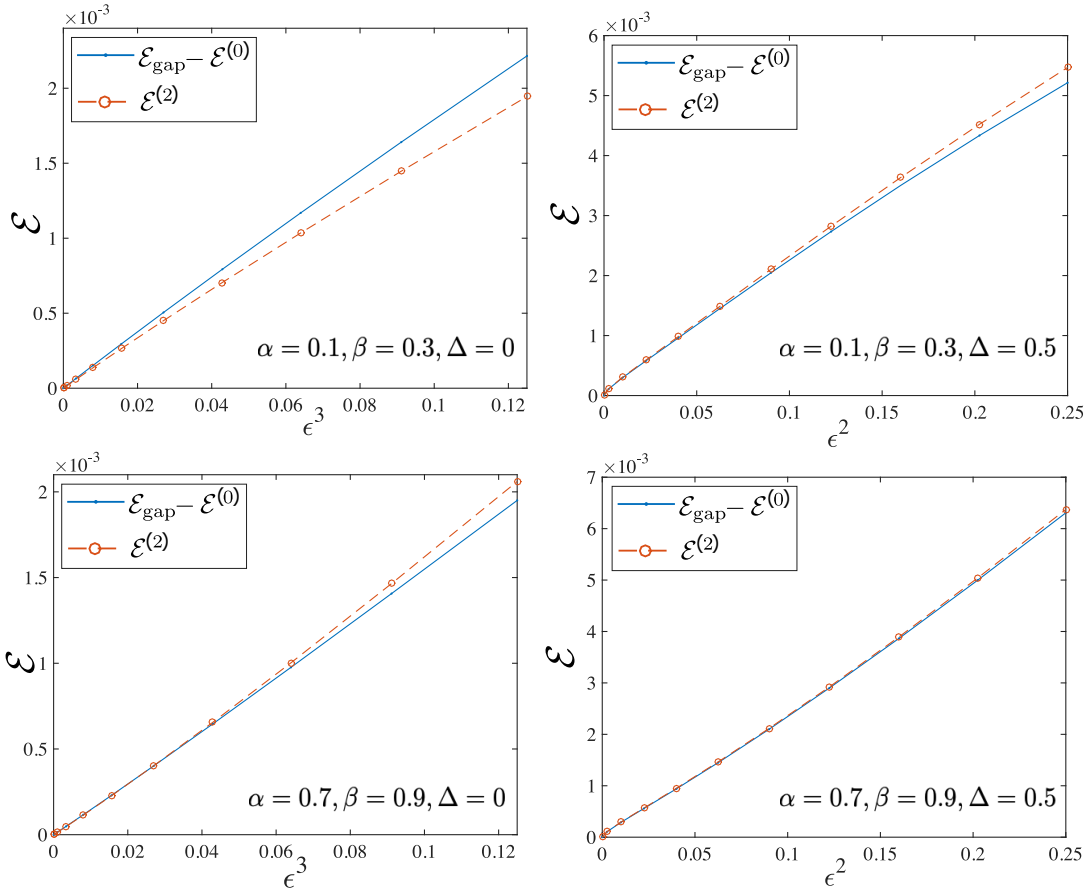

Figure 6.7: The difference between the $\mathcal{E}_{\text{gap}}$ and $\mathcal{E}_1^{(2)}$ along with the second order correction $\mathcal{E}^{(2)\prime\prime}$ for a system size of $N = 7$ with $\Delta = 0$ and 0.5 with boundary driving (α, β) of $(0.1, 0.3)$ and $(0.7, 0.9)$.

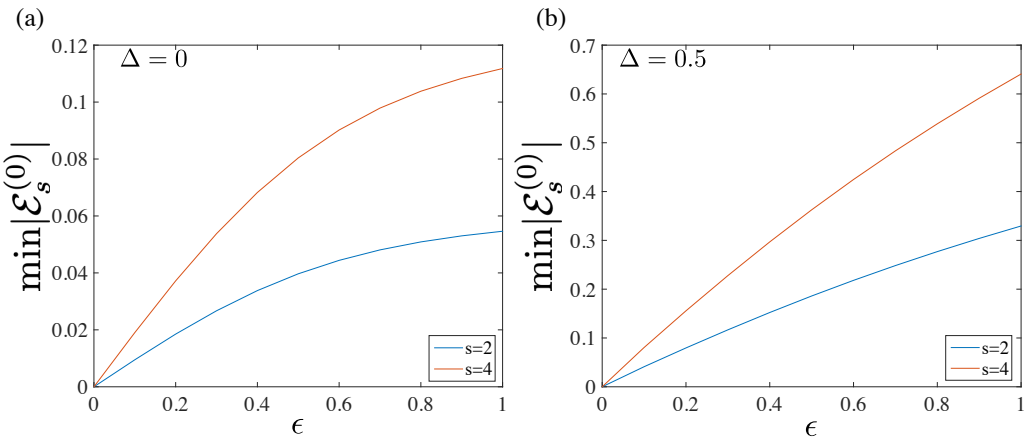

Figure 6.8: The minimum values of $|\mathrm{Re}\mathcal{E}^{(2)}|$ and $|\mathrm{Re}\mathcal{E}^{(4)}|$ for $N = 16$, $\alpha = 0.7$, $\beta = 0.9$, and $\mu = 1$. In the small ϵ limit these eigenvalues are both proportional to ϵ and we have $|\mathcal{E}_1^{(0)}| \approx 2|\mathcal{E}_1^{(2)}|$.

is an overall ϵ^2 factor in each of the $\mathcal{L}$ operators. However, we may also expect some ϵ contributions in both the zeroth order eigenstates and in the real part of the eigenvalues appearing in the denominator.

If the imaginary part of the denominator is small with respect the real part then we see an ϵ^{-1} contribution occurring from these terms. In practice, however, we see that most of the weight of this contribution occurs in the opposite limit where the ϵ^{-1} contribution is negligible. Indeed, we have found that this ϵ^{-1} scaling is compensated for via the ϵ dependence within the eigenstates themselves, leaving a net scaling of ϵ^r with $r \geq 2$. In Fig. 6.7 we compare the $\mathcal{E}_{\mathrm{gap}}$ with the zeroth $\mathcal{E}_2^{(0)}$ estimate along with second order $\mathcal{E}_2^{(2)}$ correction. We see that for $\Delta = 0$ the correction seems to actually scale close to ϵ^3 while for $\Delta = 0.5$ the scaling is closer to ϵ^2 .

One last question remains; how can we be sure that the real gap magnitude of $\mathcal{E}_1^{(0)}$ is smaller than that of $\mathcal{E}_1^{(2)}$? Here we proceed by observation. In Fig. 6.8 we show the behaviour of the absolute value of eigenvalues that are closest to the steady state for a system size of $N = 16$. In this figure and in all other similar calculations we see that the the minimum even gap magnitude comes from the $s = 2$ sector, and that it is approximately half that of the $s = 4$ sector.

6.6 The Meaning of Even and Odd Sector Gaps

Thusfar we have distinguished between the maximum non-zero real eigenvalues from both even and odd parity sectors of the Liouvillian. It is worth discussing briefly what these eigenvalues represent. Firstly, we note that the block-diagonal structure (see Fig. 5.4) can be interpreted as excitation number conservation, which in the representation used here resembles magnetisation on a $2N$-site spin chain. Interactions and/or dissipation can break this symmetry but still allow excitation parity

conservation. Parity then allows us to divide up the full 2^{2N} dimensional space into two 2^{2N-1} dimensional spaces.

The even sector consists of operators that preserve the parity of a state. This includes density operators $\rho = \sum p_\psi |\psi\rangle \langle\psi|$ where $|\psi\rangle$ have well defined parity. For this reason the even-sector gap is what determines the slowest relaxation rate towards the steady state. We have argued that this gap can be largely understood by focusing on the $s = 2$ block of the basis rotated Liouvillian superoperator.

The operator Hilbert space allows for more possibility than density matrices. The odd-sector of the superoperator $\mathcal{L}$, for example, consists of basis states that represent fermionic creation and annihilation operators [Kel15a] and odd numbered products of them. By definition such operators would switch the parity of a state. For excitation number preserving systems suitable combinations of these single-particle operators ($\Gamma^{(1)}$-sector) are the quasi-particle excitations and by combining products of such operators one can generate more complicated n-particle excitation operators in the other excitation number blocks [Kel15a]. Although this meaning is diluted if there is no longer excitation number symmetry, it is important to know where such states occur in order to distinguish them from the even sector gap. We will see again that the extremal sectors ($s = 1$ and $s = 2N - 1$ in this case) allow us to predict the largest odd sector eigenvalue.

6.7 Spectrum of the Odd Sectors

In the canonical basis for the $s = 1$ and $s = 2N - 1$ sub-blocks the elements from the commutator can be read directly from the adjacency-matrix used to define the quadratic Hamiltonian (see e.g. [GC12; Kel15a]). In these sub-blocks the terms from stochastic process occur only on the diagonal:

$$\begin{aligned} \mathcal{L}^{(1)}_{n,n} &= -\epsilon[1/2 + \alpha - (\alpha/2 + 1/4)(\delta_{n,2N-1} + \delta_{n,2N}) \\ &\quad -(\beta/2 + 1/4)(\delta_{n,1} + \delta_{n,2})], \end{aligned} \tag{6.58}$$

$$\begin{aligned} \mathcal{L}^{(2N-1)}_{n,n} &= -\epsilon[1/2 + \beta - (\beta/2 + 1/4)(\delta_{n,2N-1} + \delta_{n,2N}) \\ &\quad -(\alpha/2 + 1/4)(\delta_{n,1} + \delta_{n,2})]. \end{aligned} \tag{6.59}$$

Setting, as throughout, the bulk stochastic hopping amplitude to 1 and neglecting the boundary terms we see that for the $s = 1$ ($s = 2N - 1$) sector the boundary coefficient α (β) acts constantly throughout the bulk of the system and thus the largest real eigenvalues in each sector are effectively linearly dependent on these boundary rates.

On top of this linear dependence, the imaginary components stemming from the Hamiltonian part of the Liouvillian also play a critical role. In the topologically

trivial phase ($|\mu| > 2w$) the bulk imaginary spectrum in the continuum limit behaves approximately as

$$\mathrm{Im}(E) = \pm\sqrt{(\mu + 2w\cos k)^2 + 4\Delta^2 \sin^2 k}. \tag{6.60}$$

In the ferromagnetic/topological phase ($|\mu| < 2w$) the open system develops evanescent edge modes on the $\mathrm{Im}(E) = 0$ line. These modes are the so-called Majorana zero modes that have been studied extensively in recent years [Kit01; FK08; LSD10; ORO10; ST13]. In the limit that these zero-modes have a very long coherence length $\xi \propto |\mu|/\Delta \gg 1$ (i.e. small Δ) we see that the associated real component saturates to the bulk value of $\sim -\epsilon(\gamma/2 + \alpha)$ or $-\epsilon(\gamma/2 + \beta)$ see (6.58) and (6.59). In the ferromagnetic limit ($\Delta = 1$ and $\mu = 0$) the zero-modes are δ-functions at sites $n = 1$ and $n = N$ and thus the real components can be estimated as $-\epsilon(1/2 + \alpha)/2, -\epsilon(1/2 + \beta)/2, -\epsilon(1/4 + \alpha - \beta/2), -\epsilon(1/4 + \beta - \alpha/2)$. When α and β are both small these topological driven states slice through the even-sector gap to become closest to the steady state, see Fig. 6.2 and Fig. 6.7.

Remarks

In the past two chapters we have examined the late-time features of a small number of open quantum systems. Initially, in Chapter 5 we focused on the effects of coherent, that is quantum, processes on the stochastic/classical TASEP model. In particular, we noticed that in constructing the TXY-TASEP model we could analyse an interplay between the quantum and classical phases of the constituent models. This was highlighted by comparing known steady states of the classical model against steady states extracted from the TXY-TASEP. In this process it can be seen that the pairing strength, Δ, plays a crucial role in whether a steady state of TXY-TASEP resembles the corresponding TASEP steady state.

Furthermore, we found that pairing influenced greatly the steady state current that resulted in the low-/high-density phases. This lead to our observations that if pairing was partially present in the system that the current could be driven from being characteristically low-density to high-density and vice-versa. However, on the critical line and in the maximal current phase there is little effect. This is not particularly illuminating as the pairing terms of the Hamiltonian have little effect on the MC steady states.

An interesting aspect to the TXY-TASEP model is the ability to tune between different steady states that derive key properties from the underlying quantum phase. These quantum effects are most profound in the parameter spaces of low magnetic field ($h_z < 1$) where the XY terms opens a Liouvillian gap that is approximately linear in the anisotropy Δ. On the other hand, in the regimes associated with high transverse field ($h_z > 1$) we see that the steady state essentially reverts to the some-

thing like the purely stochastic NESS, mimicking the scenario also found with no XY anisotropy, albeit with a gap now proportional to Δ^2. These are the observations that begin Chapter 6.

Consequently, an understanding of this gap behaviour necessitated access to the Liouvillian gap. Accordingly, we demonstrated a novel technique for estimating the Liouvillian gap in open quantum systems. Moreover, our examination of a particular system with various dissipative processes yields a mixture of exact or close estimates of the Liouvillian gap. The full procedure entails a number of steps. After choosing a particular system one moves to the canonical Majorana basis for the superoperator of the Liouvillian. Next one constructs the 2-excitation sub-block of the Liouvillian in close analogy to a standard block diagonalization of a Hamiltonian with respect to particle number. The non-trivial eigenvalue of this sub-block then determines the first order estimate of the gap and in particular cases the exact Liouvillian gap.

We exemplify this method with the TXY under dissipation modelled by dephasing before repeating the analysis for dissipation modelled by hermitian SSEP and TASEP. The resultant gap is much the same in each case, however, additional considerations are taken in these latter cases as the gap there is a first order estimate albeit an accurate one. These considerations round off our excursion into open quantum systems.

Chapter 7

Conclusion

In this thesis we have explored topological features of one-dimensional many-body quantum models. Our focal point to start our study was the p-wave superconductor model. Building upon this we subsequently took two distinct routes, one regarding closed systems and another focused on open systems.

In the first instance, in Chapter 4, we considered the p-wave superconductor as a topological quantum memory; a quantum memory which relies on the encoding of qubits via Majorana zero modes. This non-local (topological) encoding is essential to the topological protection of the qubit, yet in an interacting system this protection is not automatically guaranteed. In this chapter, we used the topological quantum order (TQO) condition to show how the potential phase error due to bulk energy mismatches in interacting topological systems is suppressed up to times that scale with the system size. This indicates that the TQO condition, while defined in terms of the degenerate ground state manifold, ensures the suppression of errors from local processes that couple to, and evolve for some time in, the bulk. We furthermore discussed how this leads to a high degree of correlation between the bulk spectra of distinct topological sectors. These results are completely general, applying to any material that displays the TQO condition. This is important, given the growing number of novel materials with topological features [Bra+17].

As a direct demonstration of these general results we used a Majorana based topological memory consisting of two interacting p-wave superconducting wires. We exploited a special limit with exact TQO to argue that the fully interacting system satisfied an approximate TQO condition, and we performed extensive numerical analysis to back-up our claims regarding the phase error and bulk spectral correlation.

This bulk spectral correlation could form the starting point for future analysis. For instance, it remains to be seen whether the restrictions on the bulk splittings in [BHM10] can be tightened by the conditions presented here. Furthermore, it is also not clear what the implications of these restricted bulk splittings are on the high temperature properties of topological quantum memories. The bounds here are considerably weaker than those of special cases of strong zero-modes [Gan+11; Jer+14;

Kel15a; Kel15b; Fen16; Kem+17; Mor+17; MKN17; MA18; Pel+20; MA20] (where splittings are exponentially suppressed), and only concern those states that can be reached via local perturbations from the ground states. At the same time, this current work is both non-perturbative and general, requiring no special considerations other than the TQO condition.

A further direction is the question of disorder, its effect on spectral correlations, and if contact can be made with works on constrained thermalisation e.g. [Hus+13; Els+17; KMM18; Nul+20]. In [Con+19] it was shown for a non-interacting system that disorder can be used to suppress the phase-error jump after time T^*. In those simulations disorder did not affect T^* itself, showing that disorder induced localization reduced the amplitudes of excitations reaching the other side, but not the speed at which they got there. The reliability of the TDVP-MPS methodology outlined here suggests that for interacting systems this question could be addressed on a numerical level.

In Chapter 5 we moved to the setting of open systems with a view to consider the effects of combining stochastic (classical) and coherent (quantum) transport models. This entailed combining the p-wave model with dissipation modelled by the totally asymmetric simple exclusion process (TASEP). In this process, we found that each constituent model contributes to features of the total TXY-TASEP model. To an extent many classical features survive in the final NESS and topological features of the superconductor survive in the Liouvillian gap.

We found that the non-equilibrium steady states (NESS) of TXY-TASEP, for a large portion of the parameter space, keep the features of the corresponding TASEP steady states. In particular, coherent hopping and Zeeman magnetic terms have negligible effects. This was previously observed in [TWV12], but we show that when anisotropy is introduced, in the transverse XY model, the situation changes dramatically.

For low- and high-density phases of the TASEP model, the states are manifestly changed. In particular, boundary driving rates corresponding to the low- and high-density phases of TASEP the steady states couple strongly to the Hamiltonian anisotropy terms. As a result, these TASEP states have little resemblance to the TXY-TASEP NESS at the same boundary driving. However, for the TASEP in its maximal current phase the NESS are largely unchanged, even in the limit of an infinite system. The low field deviations from the classical NESS, most pronounced in the TASEP low- and high-density regimes, can be understood by viewing the XY anisotropy Δ as a source of pair creation/annihilation which seeks to drive the system towards half filling, and pin the energy expectation value close to the centre of the many-body spectrum. The high magnetic effect reduces this anisotropic drive toward half filling allowing the particle densities to be largely determined by the classical boundary driving. This coincides with NESS energy expectation values

drifting towards the extremes of the Hamiltonian many-body spectra.

This demarcation of the effect of pairing is reflected also in the effect on the NESS currents. The NESS current in MC phase is unaffected, however, even the partial presence of pairing in the system can drive the current of the LD or HD phase NESS to the expected current of the HD or LD phase respectively. For pairing only in the middle half of the system, this creates a system in which opposite sides of the system exhibit the expected current of each classical phases. Essentially, partial pairing seems to create a smooth transition between low- and high-density currents and vice-versa. It remains to be explored if this observation can be exploited to enhance steady state current in a controlled manner for similar systems.

In our study of the TXY-TASEP NESS we found that the Liouvillian gap, which determines the NESS relaxation rate, has a strong dependence on the phase of the quantum model and further that this gap would remain non-zero in the thermodynamic limit for non-zero pairing strength. As such the Liouvillian gap for TXY-TASEP is topological in nature. In Chapter 6 the connection to the topological phase transition is made concrete. To achieve this we employed two kernel projection methods and analytically verified our numerical observations. Our kernel projection methodology is most clearly exemplified for dissipation modelled by dephasing but we extend our analysis for the cases of hermitian SSEP and TASEP dissipation also.

A future direction of study is to determine precisely for which forms of dissipation the topological properties remain in the form of the Liouvillian gap. At this time, we have verified a topological fingerprint in the Liouvillian gap for the case of local dephasing and nearest neighbour hopping. One would expect that for other forms of dissipation the situation will change. For example, Lindblad jump operators acting on more sites will break the (close to) block diagonal structure of the Liouvillian superoperator. This may result in our projection method failing or the topological feature of the gap disappearing.

A related question is to what extent are these features unique to the p-wave superconductor or transverse XY model. Physically, is the presence of a topological gap due to the appearance (disappearance) of bound states in the closed system? For example, the Su-Schrieffer-Heeger model [SSH79] could be a starting point in this direction. The model can host edge states and has a similar yet distinct topological phase transition. The model itself contains only hopping processes on two alternating sublattices in one dimension. Absent is any superconducting pairing from the Kitaev model yet it can host edge modes at the lattice boundaries and has a similar phase transition. If no corresponding persistent Liouvillian gap could be found in this case then we may be able to conclude it is purely a feature of pairing terms in the Hamiltonian. In this latter case, it yet remains to consider more realistic models such as the s-wave superconductor.

Appendix A

Numerical MPS Methods: A Further Use Case

As a case study of the effectiveness of DMRG we can look at the XXZ Heisenberg spin chain with multiple external fields. We take this model as an example as it is one of the more generic applications of the spin models described in Ch. 2. Primarily the data shown in this chapter is that found by time evolving correlation functions and their Fourier transforms. This formed the basis of the Green's function methods in Chapter 4. By probing these correlation functions we were able, in that case, to understand how robust topological quantum order was in protecting against undesired errors. In particular, we could observe in the time evolved data both the spectral densities between parity sectors and characteristic time before errors occur.

Another application of these methods is the production of dynamical spin structure factors. Dynamical spin structure factors (DSF) are useful tools in describing particle correlations in spin systems that are experimentally accessible. Such DSF can act as probes for quasi-particle excitations e.g. spinon excitation, magnon response or spinon chirality depending on the particular structure factor that is examined. While numerical simulation can only predict features of these structure factors, these predictions can be experimentally verified through inelastic neutron scattering experiments.

The objective of this appendix is to apply time evolved tensor networks to the calculation of DSF. This is not a unique study but nonetheless is a valuable demonstration of the numerical techniques. The algorithm being used here is the time dependent variational principle (TDVP) in a 1-site realisation, these techniques also appear in Sec. 4.5.1 and are a variation upon standard DMRG techniques as explained in Sec. 3.3. This is in the class of tensor network methods employing matrix product states (MPS). The specific model analysed here is a 1-dimensional XXZ spin chain with a combination of additional magnetic fields in either perpendicular and/or parallel directions. We find that our methods allow for access to exotic parameter regimes outside the realm of conventional perturbative or analytic Green's function

methods. Moreover, we are able to introduce generic Dzyaloshinskii-Moriya [Dzy59; Mor60] interaction terms, although they will not be of primary focus.

The structure of the appendix is as follows: Section A.1 begins with a description of the model, the regimes of interest and the particular dynamic structure factors which we analyse. Subsequently, in Section A.2 we describe our approach to calculating these correlations on a lattice by manner of time-evolved tensor networks. We have already summarised the basics of these tensor network techniques in Chapter 3 and so include the additional detail necessary here. In Section A.3 as a check we compare against two structure factors that we computed by a perturbative Green's function method [Eng15]. We see good agreement between these two methods for these perturbatively accessible structure factors. Sections A.4 gives an overview of our numerical simulations for the spin-wave response, extracted from the XX structure factor, to give an understanding of the effect that modifying the magnetic fields has on the response. After this, in Section A.5, we present data for the response of the spinon chirality which can be, in turn, extracted from the (chiral) YZ-ZY dynamic spin structure factor. In particular this chiral spinon response for multiple magnetic fields is inaccessible from perturbative Green's function methods.

A.1 Model

The model we consider is simulated on a finite chain of N sites. The Hamiltonian we use is the Heisenberg XXZ with external magnetic fields, namely,

$$H = \sum_{i=1}^{N-1} \left[J_t(\hat{\sigma}_i^x \hat{\sigma}_{i+1}^x + \hat{\sigma}_i^y \hat{\sigma}_{i+1}^y) + J_z \hat{\sigma}_i^z \hat{\sigma}_{i+1}^z + h_i^x \hat{\sigma}_i^x + h_i^z \hat{\sigma}_i^z \right]. \tag{A.1}$$

Here h^x denotes the magnetic field in the direction perpendicular to the system's polarization and h^z denotes the magnetic field in the parallel direction. The latter is staggered site by site, meaning that: $h_i^z = (-1)^i h$, where h is taken to be constant throughout. The sign and magnitude of h^x is uniform across the system. Furthermore, we have the capability to introduce another interaction term, namely the Dzyaloshinskii-Moriya [Dzy59; Mor60] interaction which has the form,

$$H_{\text{DMI}} = \sum_{i=1}^{N-1} \vec{D} \cdot (\vec{S}_i \times \vec{S}_{i+1}), \tag{A.2}$$

where $\vec{D}$ is a constant times a unit vector, usually $\hat{x}$ or $\hat{z}$, here we will choose $\vec{D} = D\hat{x}$. Such a choice of $\vec{D}$ results in the interaction:

$$H_{\text{DMI}} = D \sum_{i=1}^{N-1} \left(\hat{\sigma}_i^y \hat{\sigma}_{i+1}^z - \hat{\sigma}_i^z \hat{\sigma}_{i+1}^y \right). \tag{A.3}$$

The encoding of this Hamiltonian as an MPO for simulation has been outlined previously in Section 3.3.1. The objects of note in this appendix are the dynamic structure factors (DSF), which are usually defined in the following way

$$S^{\alpha\beta}(q,\omega) \equiv \frac{1}{2\pi}\int dt e^{i\omega t}\frac{1}{N}\sum_{i,j}\langle\hat{\sigma}_i^{\alpha}(t)\hat{\sigma}_j^{\beta}(0)\rangle e^{-iq\cdot(r_i-r_j)}, \tag{A.4}$$

where q denotes momentum (transfer), ω frequency and the expectation is with respect to the ground state of the Hamiltonian, later denoted by $|0\rangle$. The superscripts α, β may take values in $\{x, y, z\}$. As one can readily see this is the double Fourier transform of the two spin correlation function:

$$S^{\alpha\beta}(r_i - r_j, t) = \langle\hat{\sigma}_i^{\alpha}(t)\hat{\sigma}_j^{\beta}(0)\rangle, \tag{A.5}$$

where the $\hat{\sigma}_i^{\alpha}$ operators are Pauli matrices operating on the i^{th} site. Lastly, $\hat{\sigma}_i^{\alpha}(t) = U^{\dagger}(t)\hat{\sigma}_i^{\alpha}U(t)$, where $U(t)$ is the usual time evolution operator under the Hamiltonian above.

In this system the excitations are spinons and the dynamical spin structure factors (DSF) describe properties of these excitations. For example $S^{xx}(q,\omega)$ is known as the spin-wave or magnon response and describes the tendency of the excitation to occur, that is, the tendency for spin flip excitations. $S^{yy}(q,\omega)$, gives similar information so we focus on $S^{xx}(q,\omega)$. The DSF $S^{zz}(q,\omega)$ is referred to as the longitudinal response and describes how the length of the spin varies along the chain. This also gives an indication to the magnetic order fluctuations in the presence of excitations. Finally, the last DSF of interest to us is the combination, $S^{yz}(q,\omega) - S^{zy}(q,\omega)$. Taking our system to be polarized in the $\hat{x}$ direction this is the term of interest that remains from a Dzyaloshinskii-Moriya interaction, which is linked to the chirality of the spinon excitations [Eng15]. As a result the combination above is a probe of the chirality of the spinons in the system.

Usually the regime of large external magnetic field would not be amenable to usual techniques. However, utilising tensor network methods we have been able to determine of results with a high degree of confidence. We set all couplings with respect to J_z which defines our energy scale. Moreover, we can investigate several interesting regimes such as $h^x \gg h^z$ and $h^x \ll h^z$ which are our primary concern in these simulations.

A.2 Lattice Implementation of DSF

The key step in attaining the DSF is to appropriately bring its expression onto a lattice where established TDVP can be applied. However, first, since our goal will be to calculate a variety of structure factors, which are essentially two spin correlation

functions, one needs the ground state of the Hamiltonian, Eq. A.1. In order to obtain the ground state we employ a one-site DMRG algorithm as a first step in our calculations [Whi92; Sch11; Orú14].

While Eq. A.4 is the usual defintion for a lattice, recent work [Pae+19; WL19] presents a modification to improve computational efficiency and accuracy. Firstly rather than time evolving every spin structure factor for all combinations of i and j we fix j at the centre of the chain and sweep through i. This is an important modification to avoid effects from the edge of the system. Next we translate the spin structure factor above to discrete time steps giving:

$$S^{\alpha\beta}(q,\omega) \cong \frac{2\pi}{NT}\delta \sum_{m=0}^{M} e^{i(\omega+i\eta)t_m} \sum_{j=1}^{N} e^{-iq\cdot(j-N/2)} 2\mathrm{Re}\langle \hat{\sigma}_j^{\alpha}(t_m)\hat{\sigma}_{N/2}^{\beta}(0)\rangle. \tag{A.6}$$

Here η is a damping factor to prevent spectral leakage due to a finite time interval and time is discretized as: $t_m = m\delta$ with $M\delta = T$. The damping factor needs only to be approximately 0.01. Moreover at the level of the real space spin correlator, we express this as:

$$\begin{aligned} S^{\alpha\beta}(j,t) &= \langle 0|\, \hat{\sigma}_j^{\alpha}(t_m)\hat{\sigma}_{N/2}^{\beta}(0)\, |0\rangle - \langle 0|\, \hat{\sigma}_j^{\alpha}\hat{\sigma}_{N/2}^{\beta}\, |0\rangle\,, \\ &= e^{iE_0 t_m}\, \langle 0|\, \hat{\sigma}_j^{\alpha}\, |1(t)\rangle_{N/2}^{\beta} - \langle 0|\, \hat{\sigma}_j^{\alpha}\hat{\sigma}_{N/2}^{\beta}\, |0\rangle\,. \end{aligned}$$

We consider the state $|1(t)\rangle_{N/2}^{\beta}$ to be the time evolved state of a β excitation at the central site and the phase in front comes from acting the evolution operator to the left on the ground state. The second term is evaluated once at the beginning of the time evolution. Inserting this real space form of the spin structure factor we perform our evolution using the 1-site TDVP algorithm.

A.3 Comparison against Green's Function Methods

As a further consistency check we include a comparison to an extant semi-analytic approach to the DSF calculation which utilises Green's function methods [Eng15]. It should be noted that the method cited is a first order perturbation theory, capturing the relevant information for 2-spinon excitations on the chain. Firstly, if we examine $S^{xx}(q,\omega)$ without external magnetic fields we can see the agreement between the methods in Fig A.1.

The perturbative method also produced results for the chiral DSF which are compared in Fig. A.2. It is worth noting that figures and results that appear in [Eng15] that involve an external perpendicular field have the field magnitude expressed in units of Tesla, i.e. $B_x = 10\mathrm{T}$. The total coupling which we denote h^x is expressed

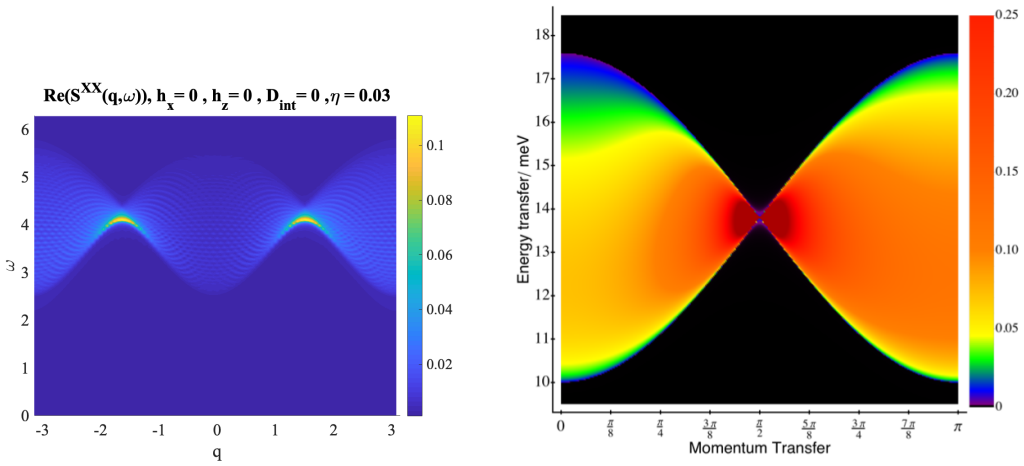

(a) $h^x = h^z = 0$ (b) $B_x = 0$

Figure A.1: XX structure factor without magnetic fields obtained from TN numerics and perturbative methods [Eng15] respectively. Note, smaller values of η give closer agreement with the magnitude of the intensities. In addition the axes and scales do not coincide since the right figure only contains the upper right quadrant of the left figure.

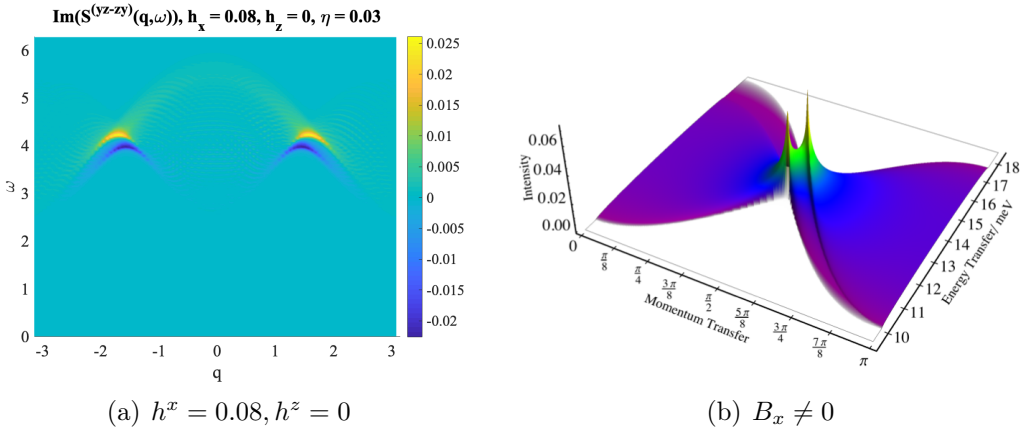

(a) $h^x = 0.08, h^z = 0$ (b) $B_x \neq 0$

Figure A.2: (a) Chiral DSF with perpendicular magnetic field obtained from our numerics. (b) The same object found by perturbative methods. Note that here the intensity is plotted meaning a positive z-axis. In (a) we see that the two peaks correspond to a sharp switch between a negative and positive peak.

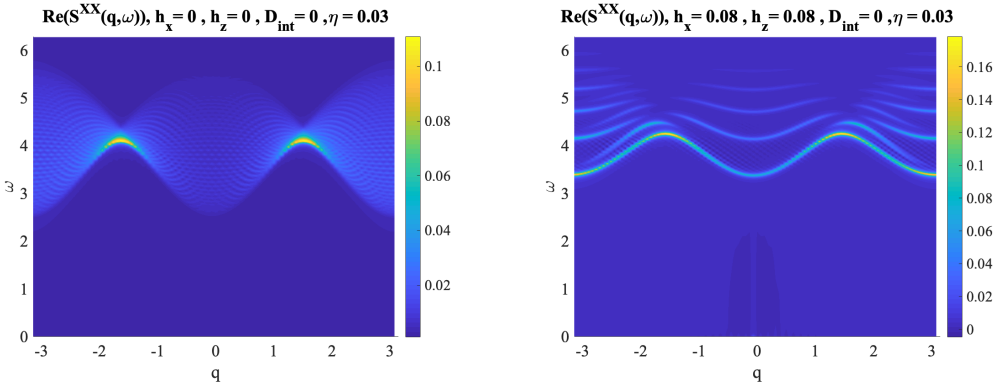

(a) $h^x = h^z = 0$ (b) $h^x = h^z = 0.08 J_z$

Figure A.3: XX structure factor (a) without and (b) with external magnetic fields. In (a) we recover the regular dispersion for the system. In (b) we notice a tighter band that falls off with increasing frequency.

in terms of this magnetic field strength in the manner,

$$h^x = g\mu_B B_x, \tag{A.7}$$

where $g = 2.002319$ is the electron spin g-factor, $\mu_B = 0.05788\text{meV T}^{-1}$ is the Bohr magneton and B_x is the magnitude of the magnetic field. Combined then what we refer to as the magnitude of our magnetic field is in fact:

$$h^x = 0.1159 B_x J_z, \tag{A.8}$$

if we take $J_z = 1\text{meV}$. To give a sense of the values a few conversions would be, $B_x = \{0, \ldots 10\}T \rightarrow h^x = \{0, 0.1159, \ldots 1.159\}\text{meV}$.

A.4 XX Dynamical Structure Factor

Beginning with no fields in Fig. A.3(a) we obtain the DSF for the XXZ model. Additional magnetic fields break this continuum into more discrete energy levels, Fig. A.3(b). The splitting into discrete levels is strongly linked to the parallel field, h^z, rather than the perpendicular field, h^x; to see this compare Fig. A.4(a) and Fig. A.4(b).

A.5 Chiral Dynamical Structure Factor

Importantly, one can see that between Fig. A.5(a) and Fig. A.5(b) that the chiral spin structure factor does not appear until both external fields are present. If no fields are present the response of the chiral DSF is essentially zero up to an accuracy that we could in principle improve. In practice, while we could increase the bond

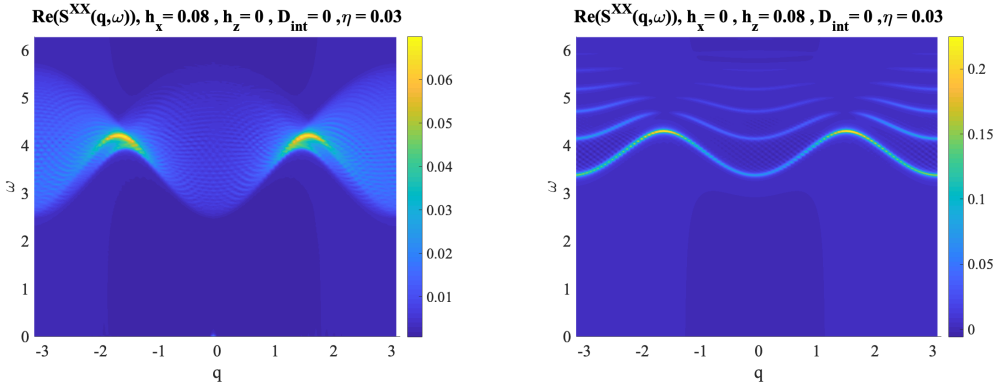

(a) $h^x = 0.08J_z, h^z = 0$ (b) $h^x = 0, h^z = 0.08J_z$

Figure A.4: A comparison between the XX structure factor with only one external field, (a) h^x and (b) h^z respectively. From these two figures we can deduce that the splitting of the peak (Fig. A.2(a)) is due to the field h_x while the tightening of the frequency band (Fig. A.3(b)) is due to h_z.

dimension of the states involved and push the precision of the TVDP algorithm it is not necessary to demonstrate the structure factor's response to external fields. It is worth noting that the non-zero noise seems to correspond to the XX structure factor without fields though clearly smaller by several orders of magnitude.

Crucially, the observation we make here is that the response from the chiral structure factor necessarily requires both magnetic fields to be non-zero. If this is the case we see similarities in its response to increasing field strength. For example, comparing Fig. A.5(b) and Fig. A.4(a) we can see the same effect of increased h_x in producing two close peaks. In addition, the effect of h_z can be seen in Fig. A.6 similarly as found in the response of the XX structure factor seen in Fig. A.4(b). In both cases we see the largest response sharpen and many more diminishing responses appear at higher frequencies. In the case of the chiral spin factor the effect seems to be more pronounced as these higher frequency responses do not diminish quite as rapidly as in the XX case. For much larger h_x, orders of magnitude larger than h_z that is, the result is an initial response at an almost flat ω profile with few higher frequency signals. Any high frequency responses are strongly suppressed.

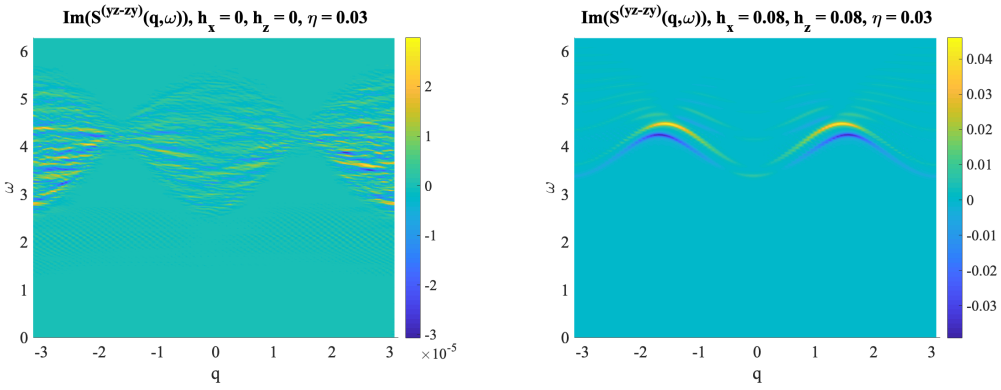

(a) $h^x = h^z = 0$ (b) $h^x = h^z = 0.08J_z$

Figure A.5: Chiral structure (a) without and (b) with external magnetic fields. In (a) we see only a noisy signal of the XX structure factor pattern. Strictly, this should be zero but merely indicates a (small) level of error in our numerical simulations for this system. This could be resolved in a number of ways; for example by using a larger bond dimension for states. In (b) the signal is more clear where we can see two split peaks in a flattened frequency range due to non-zero h_z.

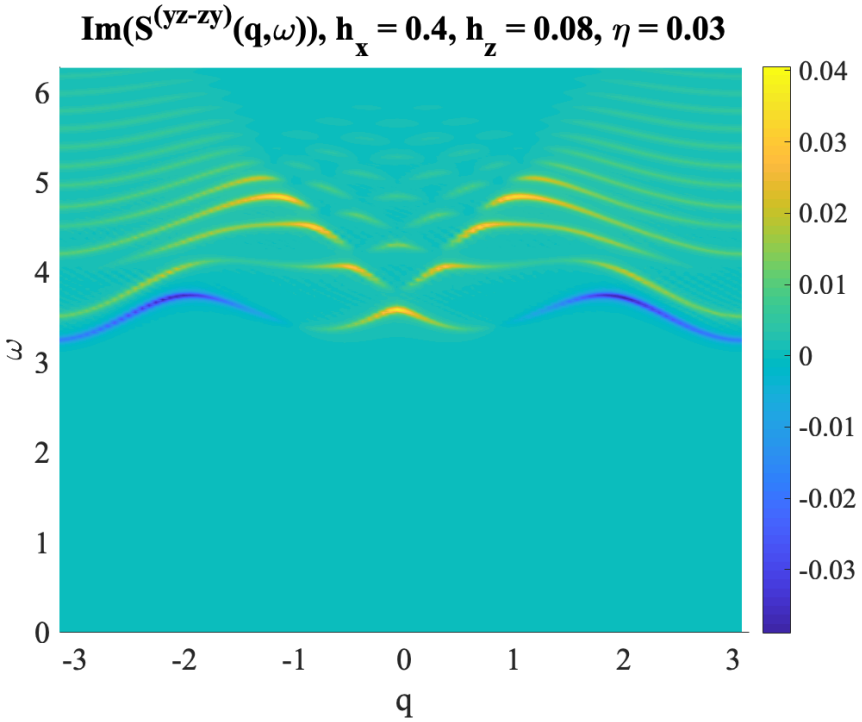

(a) $h^x \gg h^z$

Figure A.6: The chiral spin structure factor at large h_x, $h_x = 5h_z$. Here, we bring together our previous observations. We can see a narrow frequency range beginning at $\omega \sim \pi$ for the initial peaks around $q = \{-2, 0, 2\}$. In addition, the presence of h_z gives rise to diminishing peaks for larger frequency values.

Appendix B

Canonical Basis

Throughout Ch. 5 and Ch. 6 we utilised the operator quantization in the canonical Majorana basis. In operator quantization we must use the Hilbert-Schmidt inner product

$$\langle\langle A|B\rangle\rangle \equiv \mathrm{Tr}\big(A^\dagger B\big)/2^{2N}, \tag{B.1}$$

to define a basis of operators that is orthonormal. However, in the canonical basis this inner product is transformed. We note here the transformation required. First, recall the definition of the canonical basis [GC12; Kel15a]:

$$\begin{aligned}
\Gamma^{(0)}: &\quad I \\
\Gamma^{(1)}: &\quad \gamma_1, \gamma_2, \gamma_3, \ldots, \gamma_{2N}, \\
\Gamma^{(2)}: &\quad i\gamma_1\gamma_2, i\gamma_1\gamma_3, \ldots, i\gamma_{2N-1}\gamma_{2N}, \\
\Gamma^{(3)}: &\quad -i\gamma_1\gamma_2\gamma_3, \ldots, -i\gamma_{2N-2}\gamma_{2N-1}\gamma_{2N}, \\
\vdots &\quad \vdots \\
\Gamma^{(2N)}: &\quad i^{(2N)N}\gamma_1\gamma_2\ldots\gamma_{2N}\ .
\end{aligned} \tag{B.2}$$

where $\gamma_{2n-1} = c_n^\dagger + c_n$ and $\gamma_{2n-} = i(c_n^\dagger - c_n)$. We number each operator by an index a (i.e. Γ_a) , for $a = 1, \ldots, 2^{2N}$. For each a one we use the integer s to be the number of γ's in the product Γ_a. In each of these subsets there are $\binom{2N}{s}$ elements and when we need to refer to a particular element of the subset s we will write $\Gamma_a^{(s)}$. The phases are chosen so that $\Gamma_a^2 = I$ and since the product of two Γ_a's gives a third (up to a phase) and $\mathrm{Tr}\Big(\Gamma_a^{(s)}\Big) = 0$ for $s > 1$ then we have

$$\langle\langle \Gamma_a|\Gamma_b\rangle\rangle \equiv \mathrm{Tr}\big(\Gamma_a^\dagger\Gamma_b\big)/2^{2N} = \delta_{ab}. \tag{B.3}$$

Formally, the transformation to the canonical basis can be made as $\mathcal{L}_{ab} = \langle\langle \Gamma_a|\mathcal{L}|\Gamma_b\rangle\rangle$. This is the object that we regularly work with in the relevant chapters. In practice,

though, we make the rotation $\mathcal{L}' = R^\dagger \mathbb{L} R$ where R is the double transformation

$$R = M \prod_x^N F_x, \tag{B.4}$$

with

$$F_x = \frac{1}{\sqrt{2}} \begin{bmatrix} 1 & 0 & 0 & 1 \\ 0 & 1 & 1 & 0 \\ 0 & -i & i & 0 \\ 1 & 0 & 0 & -1 \end{bmatrix}. \tag{B.5}$$

Further, M is a second basis-reordering that can be defined via alternate single-particle binary identifications

$$\begin{array}{ll} 00000001 & 00000001 \\ 00000010 & 00000010 \\ 00000100 & 00000111 \\ 00001000 \leftarrow & 00001011 \\ 00010000 & 00011111 \\ 00100000 & 00101111 \end{array} \tag{B.6}$$

These binary string label the presence of Majorana operators in the Γ operator strings. Hence, in effect, we have reordered the Majorana operator strings with this transformation. A finite state automata representation of the MPO that achieves the transformation M is

$$M_1 = \frac{1}{2}[I \;\; 0 \;\; 0 \;\; Z], \tag{B.7}$$

$$M_x = \frac{1}{2} \begin{bmatrix} I & X & Y & Z \\ I & X & Y & Z \\ I & -X & -Y & Z \\ I & -X & -Y & Z \end{bmatrix}, \tag{B.8}$$

$$M_N = \begin{bmatrix} I+X \\ I+X \\ I-X \\ I-X \end{bmatrix}, \tag{B.9}$$

where $X = \sigma^x \otimes \sigma^x$, $Y = \sigma^y \otimes \sigma^y$, and $Z = \sigma^z \otimes \sigma^z$. Finally, by utilising this two-fold transformation we are able to attain the correct $\mathcal{L}_{ab}$ expressed in the canonical basis.

Appendix C

TASEP & Its Quantum Embedding

In this appendix, we focus on the totally asymmetric simple exclusion process (TASEP) but nonetheless the quantum embedding can be performed in much the same manner for the symmetric simple exclusion process (SSEP). We first give an overview of the TASEP before presenting the embedding. One of the most useful aspects of TASEP, for our purposes, is the existence of an exact solution [Der+93] for the non-equilibrium steady state (NESS) which we take as a starting point for our (numerical) analysis in Chapter 5 and 6. Since we utilise extensively MPS/DMRG methods in this context there are some convenient similarities to this exact solution and the matrix product states we use. In essence, one can view the exact solution as an MPS and further can encode the NESS for the classical model as an MPS[1]. While we do not find an exact (or ansatz) solution to the full TXY-TASEP NESS; we are able to make concrete comparisons back to the well studied classical model's NESS in various phases/regimes, see Ch. 5. To begin we reproduce the derivation of the NESS ansatz solution that we use in this thesis, in Section C.1. After we describe the quantum embedding of the TASEP in Section C.2.

C.1 Exclusion Process

In a few words, the TASEP is one of the simplest models of a driven diffusive system. In this thesis it is taken with open boundary conditions where the particles all move independently to the right with hard-core repulsion along a 1-dimensional lattice. Particles are fed into the left side of the system and removed from the right. We do not explicitly model the "baths" from which and to which these particles move, see Fig. C.1. Other recursive methods via generating functions were proposed prior [DDM92] to the presentation given here [Der+93]. The basic formulation considers configurations of occupied and unoccupied lattice sites. Each site occupancy is denoted by n_i with a value of 1 or 0 indicating occupied/unoccupied.

[1]Coincidentally, the exact solution of the TASEP model was proposed contemporaneously to the original White formulation of MPS for the 1d AKLT model [Whi92].

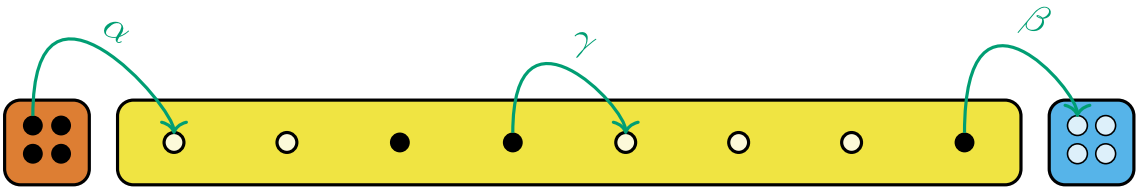

Figure C.1: Here, we schematically describe the totally asymmetric exclusion process. The green arrows show processes that are allowed within the TASEP model (with $\gamma = 1$ usually). Additional processes with matching weights in the left direction recovers the SSEP. The orange and cyan regions on either side of the lattice (coloured yellow) denote infinite baths of particles and holes respectively and are not explicitly modelled.

At each discrete time-step, dt, every site is updated by a few rules determined by the nearest-neighbour occupancies. If the first site, $i = 1$, is empty the probability for the site being injected from outside the system is αdt. Similarly, if the last site, $i = N$, is occupied that particle has a probability to leave the lattice to the right of βdt. In the bulk of the system, provided that site i is occupied and the site $i + 1$ is empty then the particle at site i moves to the right with probability dt^2. The dynamics of the system is then determined by the following relations on the site-wise configurations, n_i:

$$n_1(t+dt) \begin{cases} 1, & \text{with probability } p_1 = n_1 + [\alpha(1-n_1) - n_1(1-n_2)]dt, \\ 0, & \text{with probability } 1 - p_1, \end{cases} \tag{C.1}$$

$$n_i(t+dt) \begin{cases} 1, & \text{with probability } p_i = n_i + [n_{i-1}(1-n_i) - n_i(1-n_{i+1})]dt, \\ 0, & \text{with probability } 1 - p_i, \end{cases} \tag{C.2}$$

$$n_N(t+dt) \begin{cases} 1, & \text{with probability } p_N = n_N + [n_{N-1}(1-n_N) - \beta n_N]dt, \\ 0, & \text{with probability } 1 - p_N. \end{cases} \tag{C.3}$$

In the long-time limit, $T \to \infty$, the system reaches a steady state wherein the probabilities, $\mathcal{P}_N(n_1 \dots n_N)$, of finding the system in configuration $\{n_1 \dots n_N\}$ are stationary such that

$$\frac{d}{dt}\mathcal{P}_N(n_1 \dots n_N) = 0. \tag{C.4}$$

The exact matrix formulation of the steady state allows one to obtain all $\mathcal{P}_N$ for any N. The matrix formulation enters as an unnormalised form of $\mathcal{P}_N$. If we express this as

$$\mathcal{P}_N(n_1 \dots n_N) = \frac{f_N(n_1 \dots n_N)}{\sum_{\{n_i\}} f_N(n_1 \dots n_N)}, \tag{C.5}$$

[2] A particular rate can be given of γ for this bulk hopping but ultimately it can be rescaled out of the equations since in the end it only changes the size of the time-step dt. For this reason we will largely set it to unity thoughtout as in the original formulation.

then the unnormalised weights f_N can be expressed via matrices, D and E, as

$$f_N(n_1 \dots n_N) = \langle W| \prod_{i=1}^{N} (n_i D + (1 - n_i)E) |V\rangle . \tag{C.6}$$

In effect the information on a given configuration only requires two matrices and two vectors to be known. It is here that we can make the connection to an MPS. Taking $A^0 = D$ and $A^1 = E$ one can consider a configuration of say $\{00110101\}$ as being represented by

$$f_N(n_1 \dots n_N) = \langle W| DDEEDEDE |V\rangle = \langle W| A^0 A^0 A^1 A^1 A^0 A^1 A^0 A^1 |V\rangle , \tag{C.7}$$

which is reminiscent of one unpacking a generic MPS as defined in Ch. 3, where we would be extracting the particular entry in the 2^N tensor $\psi^{i_1 \dots i_N}$ for a specific configuration. This gives the weight of a particular state in the superposition of basis states. Then, what are these matrices and vectors D, E, $\langle W|$ and $|V\rangle$? We can obtain relations between these matrices and vectors which are:

$$\begin{aligned} DE &= D + E \equiv C, \\ D |V\rangle &= \frac{1}{\beta} |V\rangle , \\ \langle W| E &= \frac{1}{\alpha} \langle W| , \end{aligned} \tag{C.8}$$

which are obtained shortly from the stationarity of $\mathcal{P}_N$ for a steady state configuration. From these relations one can determine single and two-site expectation values. For example, writing f_N in terms of these matrices gives

$$\mathcal{Z} = \sum_{\{n_i\}} f_N(\{n_i\}) = \langle W| C^N |V\rangle = \langle W| (D + E)^N |V\rangle . \tag{C.9}$$

Then the single site expectation value w.r.t. the steady state is given by

$$\begin{aligned} \langle n_i \rangle &= \sum_{\{n_i\}} \frac{n_i f_N(\{n_i\})}{\mathcal{Z}}, \\ &= \frac{\langle W| C^{i-1} D C^{N-i} |V\rangle}{\langle W| C^N |V\rangle}, \end{aligned} \tag{C.10}$$

where D appears in the i-th position. Similarly the two point expectation value, for $i < j$, is given by

$$\langle n_i n_j \rangle = \frac{\langle W| C^{i-1} D C^{j-i-1} D C^{N-j} |V\rangle}{\mathcal{Z}}. \tag{C.11}$$

This extends onto higher point expectations in the same way. At this point if we can determine "simple" forms of the vectors and matrices in this ansatz we can easily find the density profile of the lattice in steady state or indeed any n-point correlation

functions in a clear, systematic way.

The next step in this direction is to consider the possible transitions between states/configurations that are allowed. For the left-most site we can construct a matrix h_1 representing these transitions in a $\{0,1\}$ basis. We know by the rules governing the model that the only possible transition for this site is

$$\{0, n_2 \dots\} \xrightarrow{\alpha} \{1, n_2 \dots\}, \tag{C.12}$$

which is a particle entering from the left, with rate α. The only remaining "transition" is for the occupied configuration to remain occupied i.e. $\{1, n_2 \dots\}$ to itself with the negation of the previous rate. This produces the matrix

$$h_1 = \begin{pmatrix} -\alpha & 0 \\ \alpha & 0 \end{pmatrix}. \tag{C.13}$$

By a complementary argument the corresponding matrix for the right-most site is given by

$$h_N = \begin{pmatrix} 0 & \beta \\ 0 & -\beta \end{pmatrix}. \tag{C.14}$$

In the bulk of the lattice the allowed transition between neighbouring sites is that of $\{\dots, 1, 0, \dots\} \to \{\dots, 0, 1, \dots\}$ or no change which gives the same h throughout the bulk of the lattice[3]

$$h = \begin{pmatrix} 0 & 0 & 0 & 0 \\ 0 & 0 & 1 & 0 \\ 0 & 0 & -1 & 0 \\ 0 & 0 & 0 & 0 \end{pmatrix}. \tag{C.15}$$

Next we look at the dynamics, using these allowed transitions to expand the expression for the stationarity equation and verify the matrix and vector relations

[3]It is worth noting that for the ASEP model with particles allowed to move to the left with rate γ_L we have a very similar matrix given by

$$h = \begin{pmatrix} 0 & 0 & 0 & 0 \\ 0 & -\gamma_L & \gamma_R & 0 \\ 0 & \gamma_L & -\gamma_R & 0 \\ 0 & 0 & 0 & 0 \end{pmatrix}.$$

The boundary matrices, h_1 and h_N, are generalised in a similar way by adding the appropriate rate to the empty columns such that the columns sum to zero.

(C.8),

$$\begin{aligned}\frac{d\mathcal{P}_N(\{n\})}{dt} &= \sum_{\sigma_1} (h_1)_{n_1\sigma_1}\, \mathcal{P}_N(\sigma_1, n_2, \dots) \\ &\quad + \sum_{i=1}^{N-1} \sum_{\sigma_i\sigma_{i+1}} (h)_{n_i n_{i+1}\sigma_i\sigma_{i+1}}\, \mathcal{P}_N(\dots, \sigma_i, \sigma_{i+1}, \dots) \\ &\quad + \sum_{\sigma_N} (h_N)_{n_N\sigma_N}\, \mathcal{P}_N(\dots, n_{N-1}, \sigma_N).\end{aligned} \tag{C.16}$$

The next step is to assume that there exists some x_0 and x_1 such that the following relations hold for each n_i. These relations consider how the configurations on N sites connect to the configurations on $N-1$ sites. Or rather what the contribution each single site has in the dynamics dependent on which site in particular is removed. The relations are:

$$\begin{aligned}\sum_{\sigma_1} (h_1)_{n_1\sigma_1}\, \mathcal{P}_N(\sigma_1, n_2, \dots) &= x_{n_1} \mathcal{P}_{N-1}(n_2, \dots), \\ \sum_{\sigma_i\sigma_{i+1}} (h)_{n_i n_{i+1}\sigma_i\sigma_{i+1}}\, \mathcal{P}_N(\dots, \sigma_i, \sigma_{i+1}, \dots) &= -x_{n_i} \mathcal{P}_{N-1}(\dots, n_{i-1}, n_{i+1}, \dots) \\ &\quad + x_{n_{i+1}} \mathcal{P}_{N-1}(\dots, n_i, n_{i+2}, \dots), \\ \sum_{\sigma_N} (h_N)_{n_N\sigma_N}\, \mathcal{P}_N(\dots, n_{N-1}, \sigma_N) &= -x_{n_N} \mathcal{P}_{N-1}(\dots, n_{N-1}).\end{aligned} \tag{C.17}$$

Taking the assumption that x_0 and x_1 exist, the stationarity equation (C.16) is satisfied by the relations (C.17). These relations combine together as a telescoping sum of terms so that there are many cancellations reducing the right hand side expressions immensely. Let us illuminate this statement with an example to see how this leads to the relations (C.8). Taking the configuration in its matrix form

$$\mathcal{P}_N(\{n\}) = \frac{1}{\mathcal{Z}} \langle W| \prod_{i=1}^{N} (n_i D + (1 - n_{i+1})E) |V\rangle\,, \tag{C.18}$$

we require that:

$$\begin{aligned}\frac{(h_1)_{00}}{\mathcal{Z}} \langle W|E \prod_{i=2}^{N} (n_i D + (1 - n_{i+1})E) |V\rangle + (h_1)_{01} \langle W| \dots |V\rangle \\ = \frac{x_0}{\mathcal{Z}} \langle W| \prod_{i=2}^{N} (n_i D + (1 - n_{i+1})E) |V\rangle\,, \\ \frac{(h_1)_{10}}{\mathcal{Z}} \langle W|E \prod_{i=2}^{N} (n_i D + (1 - n_{i+1})E) |V\rangle + (h_1)_{11} \langle W| \dots |V\rangle \\ = \frac{x_1}{\mathcal{Z}} \langle W| \prod_{i=2}^{N} (n_i D + (1 - n_{i+1})E) |V\rangle\,.\end{aligned} \tag{C.19}$$

By inspecting these two equalities we can conclude that

$$\begin{aligned} x_0 = -1, \quad x_1 = 1, \\ \langle W| E = \langle W| \frac{1}{\alpha}, \end{aligned} \tag{C.20}$$

noting the values of the elements of h_1. By similar consideration of the bulk and right end cases we find that

$$\begin{aligned} DE = -x_0 D + x_1 E, \\ \beta D |V\rangle = -x_0 |V\rangle = x_1 |V\rangle . \end{aligned} \tag{C.21}$$

Combining all of these leads us to the relations provided in Eq. C.8. The question remains of how to construct the matrices explicitly to satisfy these relations. To find D and E we first consider if they are commuting matrices, in which case

$$\begin{aligned} \langle W| DE |V\rangle = \langle W| ED |V\rangle = \frac{1}{\alpha\beta} \langle W|V\rangle , \\ = \langle W| (D+E) |V\rangle = \left(\frac{1}{\alpha} + \frac{1}{\beta} \right) \langle W|V\rangle . \end{aligned} \tag{C.22}$$

This brings about the conclusion that $\alpha + \beta = 1$ once $\langle W|V\rangle \neq 0$. In this case the two matrices collapse into single numbers: $E = 1/\alpha$, $D = 1/\beta$. In this case all correlations are trivial, so that all n-point expectation values of n_i's become α^n. As such the system is uncorrelated [DDM92]. Instead, we can consider non-commuting matrices. This leads to the result that each are infinite-dimensional matrices. This can be shown by contradiction. Assume that D and E are finite-dimensional. Then if $DE = D + E$ this implies that $D(E - \mathbb{I}) = E$. So by extension if $(E - \mathbb{I})$ is invertible then $D = E(E - \mathbb{I})^{-1}$ and in fact $[D, E] = 0$. This is contradictory, but we can consider still that $E - \mathbb{I}$ is non-invertible. As such it has a zero vector in its kernel and $(E - \mathbb{I}) |v\rangle = 0$ for $|v\rangle \neq 0$. This further leads to

$$D |v\rangle = D (E |v\rangle) = (D + E) |v\rangle = D |v\rangle + |v\rangle \Rightarrow |v\rangle = 0. \tag{C.23}$$

This provides a further contradiction as we have found $|v\rangle = 0$ after the understanding that $|v\rangle \neq 0$. As a result we have the final conclusion that the matrices are infinite-dimensional for $\alpha + \beta \neq 1$. There are a number of choices [Der+93] that satisfy the relations and are infinite-dimensional but we will include only one here

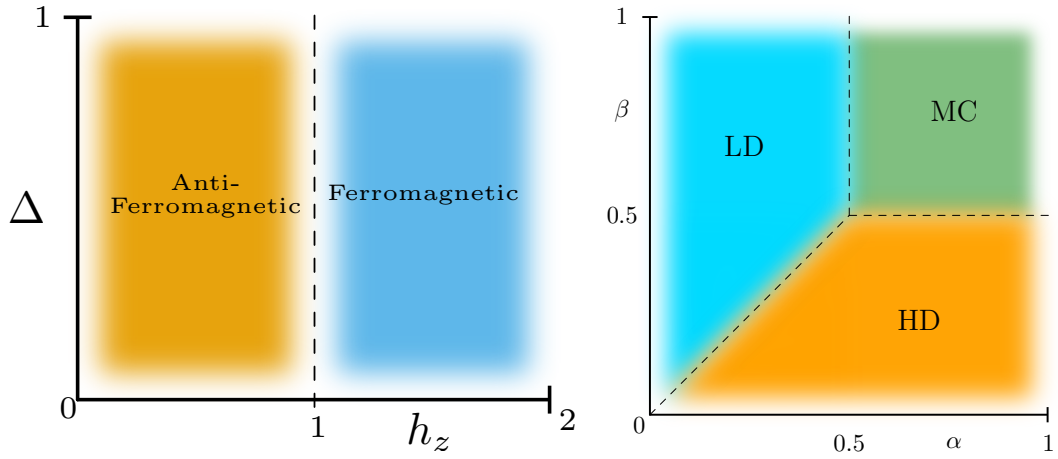

(a) TXY Phases (b) TASEP Phases

Figure C.2: The phase diagrams for the ground state of the TXY Hamiltonian (for $w = 1$) (a), and for non-equilibrium steady state of the TASEP (b) where: LD = Low Density, HD = High Density, MC = Maximal Current.

that we ourselves used. The matrices are:

$$D = \begin{pmatrix} 1/\beta & a & 0 & 0 & \dots \\ 0 & 1 & 1 & 0 & \\ 0 & 0 & 1 & 1 & \\ 0 & 0 & 0 & 1 & \\ \vdots & & & & \ddots \end{pmatrix}, \; E = \begin{pmatrix} 1/\alpha & 0 & 0 & 0 & \dots \\ a & 1 & 0 & 0 & \\ 0 & 1 & 1 & 0 & \\ 0 & 0 & 1 & 1 & \\ \vdots & & & & \ddots \end{pmatrix}, \tag{C.24}$$

with vectors:

$$\langle W| = (1, 0, \dots), \; |V\rangle = (1, 0, \dots)^T, \tag{C.25}$$

where $a^2 = (\alpha + \beta - 1)/\alpha\beta$. Now we have expressions for the matrices from which we can express the steady state for any given boundary rates (α, β). To actually use this matrix product ansatz in our simulations we of course cannot use an infinite bond-dimension matrix product state. Nonetheless for the purpose of choosing an initial state, from which we begin our DMRG calculation, a finite-dimensional form is more than sufficient using truncated forms of the above infinite objects. Moreover, we can trust that using a truncated form of the infinite-dimensional MPA will be sufficient since the matrices are sparse objects and the vectors are non-zero in only one entry. Primarily we use these truncated forms to make comparisons between numerically obtained NESS and the MPA form of the classical steady states.

As a final point we mention the broad properties of the classical steady state for particular boundary rates. For our purposes the phase diagram of the classical model is split into 3 distinct phases, see Fig. C.2(b)[4]. These are descriptively called

[4]There is more sub-structure within these phases than we show here but for us these are the relevant elements of the phase diagram. For example, there is a critical line along $\alpha = \beta$ where the steady state is more akin to the MC phase than the adjacent phases at lower values.

the low-density (LD), high-density (HD) and maximal current (MC) phases. These can be identified directly from the expressions found in this section applied to the current. In steady state the current through a bond i is the expectation value of $n_i(1-n_{i+1})$. Expressed in terms of the MPA this is

$$\begin{aligned}\mathcal{J} &= \frac{1}{\mathcal{Z}} \langle W| C^{i-1} DEC^{N-i-1} |V\rangle , \\ &= \frac{1}{\mathcal{Z}} \langle W| C^{i-1} (D+E) C^{N-i-1} |V\rangle , \\ &= \frac{1}{\mathcal{Z}} \langle W| C^{N-1} |V\rangle .\end{aligned} \tag{C.26}$$

Asymptotic expressions are known for the current and correlations [Der+93] which are readily evaluated in the limit ($N \to \infty$) to yield:

$$\mathcal{J} = \begin{cases} \frac{1}{4}, & \text{for } \alpha \geq \frac{1}{2} \;\&\; \beta \geq \frac{1}{2}, \text{ (MC)} \\ \alpha(1-\alpha), & \text{for } \alpha < \frac{1}{2} \;\&\; \beta > \alpha, \text{ (LD)} \\ \beta(1-\beta), & \text{for } \alpha > \beta \;\&\; \beta < \frac{1}{2}. \text{ (HD)} \end{cases} \tag{C.27}$$

A few comments on these values. In the MC phase we see a current of 1/4 which would indicate an average occupancy across the lattice of 1/2. This is what we see when computing the steady state in this phase, the state is half filled. One such state is that which has sites alternately filled and empty, immediately confirming the current found from the asymptotic expressions. In all phases, by definition the current is flat, only dependent on the particular boundary rates. When we examine the numerically obtained currents for the states of the TXY-TASEP model in later sections we will see that it is not completely flat, there are some variations near the boundaries but for the bulk and for large lattice sizes this will be the case for the classical model. Now that the elements are in place to compare against we describe the dynamics of the TASEP in a manner amenable to combine with the TXY spin model.

C.2 TASEP Embedded in a Quantum Spin Chain

The objective of this section is to embed the TASEP model described in C.1 as a continuous time process in order to join it with the time evolution of the TXY model. In the end we will find that by embedding TASEP in a quantum channel using Kraus operators [NC00] we can achieve this outcome. By this approach we can now model the combination of coherent and stochastic dynamics coming from the TXY and TASEP models respectively.

Notationally, we drop $\mathcal{P}_N$ denoting configurations for a bra-ket computational basis. In particular, we exchange the set of n_i for the vector $|n_i\rangle$. This is later

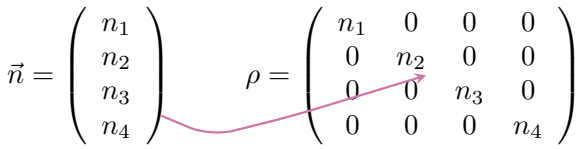

Figure C.3: The classical configuration is embedded directly onto the diagonal of a density matrix. Here for 4 sites, where n_i are valued as zero or one depending on the occupation of the corresponding site.

embedded into a density matrix. This is conceptually not difficult, essentially the classical state written as the vector, $|n_i\rangle$, is embedded onto the diagonal elements of a density matrix (Fig. C.3).

Next the update rules must be translated into an operation on such a diagonal density matrix that preserves the classical nature of the state, i.e., takes a diagonal density matrix to another diagonal density matrix. To update the configuration $|n\rangle_t$ to the configuration $|n\rangle_{t+dt}$ a time-step later, we randomly choose an integer from the set $\{0, 1, ..., N\}$ with a uniform distribution, i.e., each integer has a probability $1/(N+1)$ of being selected. The classical state is then updated by the rules:

1. If the outcome is $i \in \{1, ..., N-1\}$, and if $n_i = 1$ and $n_{i+1} = 0$, we hop the particle from site i to site $i+1$ with the probability γdt.

2. If the outcome is $i = 0$, and if $n_1 = 0$, then we should introduce a particle at site $i = 1$ with the probability αdt.

3. If the outcome is $i = N$, and if $n_N = 1$, then we should remove the particle at site $i = N$ with the probability βdt.

To encode this, consider the operation on a density matrix that performs step 1 above, i.e., the hopping of a particle from site i to site $i+1$. This can be implemented with the operation $\hat{\rho} \to \Lambda_i^{\text{hop}}[\hat{\rho}]$, where

$$\Lambda_i^{\text{hop}}[\hat{\rho}] = \sum_{j=0}^{1} \hat{K}_i^{(j)} \hat{\rho} \hat{K}_i^{(j)\dagger}, \quad i \in \{1, 2, \ldots, N-1\}, \tag{C.28}$$

for the Kraus operators:

$$\begin{aligned} \hat{K}_i^{(0)} \equiv & |0_i 0_{i+1}\rangle \langle 0_i 0_{i+1}| + |0_i 1_{i+1}\rangle \langle 0_i 1_{i+1}| \\ & + \sqrt{1-\gamma dt}\, |1_i 0_{i+1}\rangle \langle 1_i 0_{i+1}| + |1_i 1_{i+1}\rangle \langle 1_i 1_{i+1}|, \\ \hat{K}_i^{(1)} \equiv & \sqrt{\gamma dt}\, |0_i 1_{i+1}\rangle \langle 1_i 0_{i+1}|. \end{aligned} \tag{C.29}$$

Intuitively, the Kraus operator $\hat{K}_i^{(1)}$ hops a particle from site i to site $i+1$, with probability $\gamma \Delta t$, only if site i is occupied and site $i+1$ is unoccupied, i.e., it implements step 1. The Kraus operator $\hat{K}_i^{(0)}$ leaves the system unaffected in all other cases. It is easily checked that $\hat{K}_i^{(0)\dagger} \hat{K}_i^{(0)} + \hat{K}_i^{(1)\dagger} \hat{K}_i^{(1)} = \hat{\mathbb{1}}$, making this is a well-defined, probability preserving quantum operation. It is also easily checked that

this operation preserves the classical nature of a state, since it takes any diagonal density matrix $\hat{\rho}$ to another diagonal density matrix $\hat{\rho}$.

Similarly, the quantum operations that represents steps 2 and 3 above are $\hat{\rho} \to \Lambda^{\text{on}}[\hat{\rho}]$ and $\hat{\rho} \to \Lambda^{\text{off}}[\hat{\rho}]$, respectively, where:

$$\Lambda^{\text{on}}[\hat{\rho}] = \sum_{j=0}^{1} \hat{K}_{\text{on}}^{(j)} \hat{\rho} \hat{K}_{\text{on}}^{(j)\dagger}, \quad \Lambda^{\text{off}}[\hat{\rho}] = \sum_{j=0}^{1} \hat{K}_{\text{off}}^{(j)} \hat{\rho} \hat{K}_{\text{off}}^{(j)\dagger}, \tag{C.30}$$

for the Kraus operators:

$$\begin{aligned}
\hat{K}_{\text{on}}^{(0)} &\equiv \sqrt{1-\alpha dt}\, |0_1\rangle \langle 0_1| + |1_1\rangle \langle 1_1|, \\
\hat{K}_{\text{on}}^{(1)} &\equiv \sqrt{\alpha dt}\, |1_1\rangle \langle 0_1|, \\
\hat{K}_{\text{off}}^{(0)} &\equiv |0_N\rangle \langle 0_N| + \sqrt{1-\beta dt}\, |1_N\rangle \langle 1_N|, \\
\hat{K}_{\text{off}}^{(1)} &\equiv \sqrt{\beta dt}\, |0_N\rangle \langle 1_N|.
\end{aligned} \tag{C.31}$$

Again, it is straightforward to check that $\hat{K}_{\text{on}}^{(0)\dagger}\hat{K}_{\text{on}}^{(0)} + \hat{K}_{\text{on}}^{(1)\dagger}\hat{K}_{\text{on}}^{(1)} = \hat{\mathbb{1}}$ and $\hat{K}_{\text{off}}^{(0)\dagger}\hat{K}_{\text{off}}^{(0)} + \hat{K}_{\text{off}}^{(1)\dagger}\hat{K}_{\text{off}}^{(1)} = \hat{\mathbb{1}}$, and also that these operations preserve the classical (i.e. diagonal) nature of a state $\hat{\rho}$.

Implementing each of these possibilities with the uniform probability $1/(N+1)$ gives the full quantum operation representing the discrete-time state update

$$\begin{aligned}
\hat{\rho}(t+dt) = \Lambda[\hat{\rho}(t)] = \frac{1}{N+1}\Lambda^{\text{on}}[\hat{\rho}(t)] \\
+ \frac{1}{N+1}\Lambda^{\text{off}}[\hat{\rho}(t)] + \frac{1}{N+1}\sum_{i=1}^{N-1}\Lambda_i^{\text{hop}}[\hat{\rho}(t)].
\end{aligned} \tag{C.32}$$

We can find the classical continuous-time master equation in the $dt \to 0$ limit of the discrete dynamics above. First, we focus on the hopping operation Λ_i^{hop}. For this operation alone, the master equation is found as

$$\lim_{dt\to 0} \frac{\Lambda_i^{\text{hop}}(\hat{\rho}(t)) - \hat{\rho}(t)}{dt} = \gamma \mathcal{D}[\hat{\sigma}_i^- \hat{\sigma}_{i+1}^+](\hat{\rho}(t)), \tag{C.33}$$

where $\mathcal{D}[\hat{\ell}](\hat{\rho}) \equiv \hat{\ell}\hat{\rho}\hat{\ell}^\dagger - \frac{1}{2}\hat{\ell}^\dagger\hat{\ell}\hat{\rho} - \frac{1}{2}\hat{\rho}\hat{\ell}^\dagger\hat{\ell}$. Similarly, for the Λ^{on} and Λ^{off} processes, we have

$$\begin{aligned}
\lim_{dt\to 0} \frac{\Lambda^{\text{on}}(\hat{\rho}(t)) - \hat{\rho}(t)}{dt} &= \alpha \mathcal{D}[\hat{\sigma}_1^+](\hat{\rho}(t)), \\
\lim_{dt\to 0} \frac{\Lambda_i^{\text{off}}(\hat{\rho}(t)) - \hat{\rho}(t)}{dt} &= \beta \mathcal{D}[\hat{\sigma}_N^-](\hat{\rho}(t)),
\end{aligned} \tag{C.34}$$

respectively. Combining each of these gives the TASEP continuous-time master

equation

$$\frac{d}{dt}\hat{\rho}(t) = \frac{1}{N+1}\left(\alpha\mathcal{L}(\hat{\sigma}_1^+) + \beta\mathcal{L}(\hat{\sigma}_N^-)\right) + \frac{1}{N+1}\left(\gamma\sum_{i=1}^{N-1}\mathcal{L}(\hat{\sigma}_i^- \otimes \hat{\sigma}_{i+1}^+)\right)[\hat{\rho}(t)]. \tag{C.35}$$

Finally, rescaling the rates α, β, γ by a factor of $N+1$ gives Eq. 5.5, which is the form we use in the main text chapters. Generally, we set the bulk hopping $\gamma = 1$ unless otherwise stated.

Appendix D

Performing the Gap Integral

Herein we present two approaches to tackle the computation of the gap integral (Eq. 6.38). We write it explicitly as it has appeared thusfar, with minor modifications,

$$\mathcal{E}_{gap} = -2\epsilon\gamma \int_0^{\pi} dk \frac{|2\Delta \sin(k)|^2}{(\mu + 2w\cos(k))^2 + |2\Delta \sin(k)|^2}. \tag{D.1}$$

We note that the integral is even in the integration variable (k) so will continue with two times the integral from 0 to π in the remainder of this appendix as above and drop the minus signs in the squared term involving $\cos(k)$. We will take two possible approaches and see what they yield, firstly in Sec. D.1 we use a change of variables and continue to calculate the expression as a real integral. Following this we will convert the original integral to a contour integral about the unit circle in Sec. D.2 and determine if we can gain further insights into the integral from that approach.

We find that both approaches yield the same result which provides a verification of the methods. While the real integration method of Sec. D.1 may be rather straightforward it does require us to use the prior knowledge that the gap is a real valued quantity by definition to evaluate the limits of integration correctly. However, by performing the evaluation via a contour integral in Sec. D.2 we need not have prior knowledge of the quantity to be calculated.

Moreover, the contour integral has the added feature that the poles relevant to the gap are "lifted" off the real axis of the complex plane when the parameters are chosen in the topological region of the Hamiltonian. Outside of the topological region of the parameter space these poles are pinned to the real axis, an example of this feature is seen in Fig. D.1.

D.1 Change of Variables

The change of variables we propose for this section is:

$$x = 2\cos(k),\ dx = -2\sin(k)dk,\ x(\pi) = -2, x(0) = 2. \tag{D.2}$$

Inserting all of this information into (D.1), and expanding the denominator, yields

$$I_x(w,\mu,\Delta) = -2\Delta^2\epsilon\gamma \int_2^{-2} dx \frac{-2\sin\left(\arccos(x/2)\right)}{\mu^2 + 2w\mu x + w^2x^2 + \Delta^2(4-x^2)}. \tag{D.3}$$

Note now that we can use the identity

$$\sin(\arccos(x/2)) = \frac{1}{2}\sqrt{4-x^2}, \tag{D.4}$$

in the denominator and tidy up to obtain

$$I_x(w,\mu,\Delta) = -4\Delta^2\epsilon\gamma \int_{-2}^{2} dx \frac{\sqrt{4-x^2}}{(w^2-\Delta^2)x^2 + 2w\mu x + 4\Delta^2 + \mu^2}. \tag{D.5}$$

Defining the following coefficients:

$$\begin{aligned} a &\equiv w^2 - \Delta^2, \\ b &\equiv 2w\mu, \\ c &\equiv \mu^2 + 4\Delta^2, \end{aligned} \tag{D.6}$$

produces

$$I_x(w,\mu,\Delta) = -4\Delta^2\epsilon\gamma \int_{-2}^{2} dx \frac{\sqrt{4-x^2}}{ax^2 + bx + c}. \tag{D.7}$$

This yields the expression, before evaluating at the integration limits,

$$\begin{aligned} \frac{-1}{4\Delta^2\epsilon\gamma} I_x(w,\mu,\Delta) = &-\frac{1}{a}\arcsin\left(\frac{x}{2}\right) \\ &- \frac{\sqrt{8a^2 + 2ac - b^2 + b\sqrt{b^2-4ac}}}{\sqrt{2}a\sqrt{b^2-4ac}} \\ &\times \operatorname{arctanh}\left(\frac{8a + \left(b - \sqrt{b^2-4ac}\right)x}{\sqrt{8-2x^2}\sqrt{8a^2 + 2ac - b^2 + b\sqrt{b^2-4ac}}}\right) \\ &+ \frac{\sqrt{8a^2 + 2ac - b^2 - b\sqrt{b^2-4ac}}}{\sqrt{2}a\sqrt{b^2-4ac}} \\ &\times \operatorname{arctanh}\left(\frac{8a + \left(b + \sqrt{b^2-4ac}\right)x}{\sqrt{8-2x^2}\sqrt{8a^2 + 2ac - b^2 - b\sqrt{b^2-4ac}}}\right). \end{aligned} \tag{D.8}$$

Some care must be taken when evaluating this expression at the limits $x = \pm 2$ to keep account of the correct sign appearing from the arctanh. Either arctanh provides a limit of $\pm i\pi/2$, so to keep everything, correctly, real we take a minus sign out of the square root in front. The reason we enforce reality here is because the gap is defined as the real component of the $\mathcal{E}_1$ Liouvillian eigenvalue and as such must be real valued. The arcsin directly evaluates to π. This leaves us with the following form

$$\begin{aligned}\frac{1}{4\Delta^2\epsilon\gamma}I_x(w,\mu,\Delta) =& \frac{\pi}{a} - \frac{\pi}{a\sqrt{2}\sqrt{b^2-4ac}}\sqrt{b^2-8a^2-2ac+b\sqrt{b^2-4ac}} \\ &+ \frac{\pi}{a\sqrt{2}\sqrt{b^2-4ac}}\sqrt{b^2-8a^2-2ac-b\sqrt{b^2-4ac}}.\end{aligned} \tag{D.9}$$

Peeling back the a, b, c notation (D.6) gives us

$$\begin{aligned}\frac{1}{4\pi\Delta^2\epsilon\gamma}I_x(w,\mu,\Delta) =& \frac{1}{w^2-\Delta^2} \\ &- \frac{\sqrt{w^2(\mu^2-4w^2+4\Delta^2)+\mu^2\Delta^2+2|\Delta|\mu w\sqrt{\mu^2-4w^2+4\Delta^2}}}{2|\Delta|(w^2-\Delta^2)\sqrt{\mu^2-4w^2+4\Delta^2}} \\ &+ \frac{\sqrt{w^2(\mu^2-4w^2+4\Delta^2)+\mu^2\Delta^2-2|\Delta|\mu w\sqrt{\mu^2-4w^2+4\Delta^2}}}{2|\Delta|(w^2-\Delta^2)\sqrt{\mu^2-4w^2+4\Delta^2}}\end{aligned} \tag{D.10}$$

This is not yet the final, most useful form of the integral. Firstly, in chapter 5 we only take $\Delta > 0$ so we drop the absolute value here. Moreover, we define the square root in the denominator as its own variable ζ

$$\zeta = \sqrt{\mu^2-4w^2+4\Delta^2}. \tag{D.11}$$

This now allows a new more compact form

$$\begin{aligned}\frac{1}{\pi\epsilon\gamma}I_x(w,\mu,\Delta) &= \frac{4\Delta^2}{w^2-\Delta^2}\left(-1+\frac{1}{2\Delta\zeta}\left(\sqrt{(w\zeta+\Delta\mu)^2}-\sqrt{(w\zeta-\Delta\mu)^2}\right)\right), \\ &= \frac{4\Delta^2}{w^2-\Delta^2}\left(-1+\frac{1}{2\Delta\zeta}\left(|w\zeta+\Delta\mu|-|w\zeta-\Delta\mu|\right)\right).\end{aligned} \tag{D.12}$$

We can make a brief analysis of this expression to understand further how this simplifies for the two phases of the quantum model i.e. $|\mu| < 2w$ or $|\mu| > 2w$. First assume that $\zeta \in \mathbb{R}$. Then we have four cases:

1. If $|w\zeta \pm \Delta\mu| > 0$

$$|w\zeta+\Delta\mu| - |w\zeta-\Delta\mu| = 2\mu\Delta$$

2. If $|w\zeta \pm \Delta\mu| < 0$

$$|w\zeta + \Delta\mu| - |w\zeta - \Delta\mu| = -2\mu\Delta$$

3. If $|w\zeta + \Delta\mu| > 0$ & $|w\zeta - \Delta\mu| < 0$

$$|w\zeta + \Delta\mu| - |w\zeta - \Delta\mu| = 2w\zeta$$

4. If $|w\zeta + \Delta\mu| < 0$ & $|w\zeta - \Delta\mu| > 0$

$$|w\zeta + \Delta\mu| - |w\zeta - \Delta\mu| = -2w\zeta$$

which lead to the four corresponding cases for the gap integral:

$$\frac{1}{\pi\epsilon\gamma} I_x(w,\mu,\Delta) = \begin{cases} \frac{4\Delta^2}{w^2-\Delta^2}\left(\frac{\mu}{\zeta} - 1\right), & \text{for case } (i) \\ \frac{4\Delta^2}{w^2-\Delta^2}\left(-\frac{\mu}{\zeta} - 1\right), & \text{for case } (ii) \\ \frac{4\Delta^2}{w^2-\Delta^2}\left(-1 + \frac{w}{\Delta}\right) = \frac{4\Delta}{w+\Delta}, & \text{for case } (iii) \\ \frac{4\Delta^2}{w^2-\Delta^2}\left(-1 - \frac{w}{\Delta}\right) = \frac{-4\Delta}{w-\Delta}, & \text{for case } (iv). \end{cases} \tag{D.13}$$

Finally, how do these cases correspond to the actual phase transition ($|\mu| = 2w$)? Consider how we have split the case by the quantity $w\zeta \pm \mu\Delta$. This quantity changes sign when it crosses zero i.e. when

$$\begin{aligned} w\zeta \pm \mu\Delta &= 0, \\ w^2(\mu^2 - 4w^2 + 4\Delta^2) &= \mu^2\Delta^2, \\ \mu^2(w^2 - \Delta^2) &= 4w^2(w^2 - \Delta^2), \\ \Rightarrow |\mu| &= 2w. \end{aligned} \tag{D.14}$$

D.2 Gap Integral as a Contour Integral

Similarly to the previous subsection we begin with a change of variables, trading k for z in the following way:

$$z = \exp(ik),\ dz = ie^{ik}dk,\ dk = -iz^*dz. \tag{D.15}$$

Note that where we inserted x in the integrand earlier we can insert $z + z^*$. This then gives the new z dependent integrand

$$z^* \frac{1 - (z^2 + (z^*)^2 + 2)/4}{(\mu^2 + 4\Delta^2) + 2w\mu(z + z^*) + w^2(z^*)^2 + 2) + 4\Delta^2(1 - (z^2 + (z^*)^2 + 2)/4)}. \tag{D.16}$$

Rearranging and using a, b, c as defined in the previous section gives us

$$\frac{1}{\Delta^2\epsilon\gamma} I_z(w,\mu,\Delta) = -i \oint dz z^* \frac{2 - z^2 - (z^*)^2}{c + b(z + z^*) + a(z^2 + (z^*)^2 + 2)}. \tag{D.17}$$

Since the integral is over z our next step is to remove any z^* which in this instance is equivalent to $\bar{z}$ or $1/z$ which yields

$$\frac{1}{\Delta^2\epsilon\gamma} I_z(w,\mu,\Delta) = i \oint dz \frac{(z^2-1)^2}{az^5 + bz^4 + (2a+c)z^3 + bz^2 + az}. \tag{D.18}$$

At this point the integrand is in a suitable form to discuss which values of z are poles. In particular one can see that the all come from the denominator which we find from solving the equation

$$az^5 + bz^4 + (2a+c)z^3 + bz^2 + az = 0. \tag{D.19}$$

Normally an arbitrary quintic polynomial would be exceedingly difficult to solve in closed form but luckily this one can be solved symbolically since there is no constant term. This means the actual solution to be found is of a quartic rather than an overly difficult quintic. Solving this quartic gives, in addition to the obvious pole at zero, four others which come in two pairs. Then in total the roots of the full polynomial and hence the potential poles are:

$$z_0 = 0, \tag{D.20}$$

$$z_1^{\pm} = -\frac{1}{4a}(b + \sqrt{b^2 - 4ac}) \pm \frac{1}{a\sqrt{8}} \sqrt{b^2 - 8a^2 - 2ac + b\sqrt{b^2 - 4ac}}, \tag{D.21}$$

$$z_2^{\pm} = -\frac{1}{4a}(b - \sqrt{b^2 - 4ac}) \pm \frac{1}{a\sqrt{8}} \sqrt{b^2 - 8a^2 - 2ac - b\sqrt{b^2 - 4ac}}. \tag{D.22}$$

Having obtained the poles explicitly we can next compute the residue of the integral at each of these values of z. The residues are then, in a, b, c variables:

$$\begin{aligned}
\mathrm{Res}(z_0) &= \frac{1}{a}, \\
\mathrm{Res}(z_1^{\pm}) &= \frac{\mp 1}{a\sqrt{2}\sqrt{b^2 - 4ac}} \sqrt{b^2 - 8a^2 - 2ac + b\sqrt{b^2 - 4ac}}, \\
\mathrm{Res}(z_2^{\pm}) &= \frac{\pm 1}{a\sqrt{2}\sqrt{b^2 - 4ac}} \sqrt{b^2 - 8a^2 - 2ac - b\sqrt{b^2 - 4ac}}.
\end{aligned} \tag{D.23}$$

Now as before we revert to the w, μ, Δ variables by inserting the definitions of a, b, c and doing some minor rearrangement to produce:

$$\begin{aligned}
\mathrm{Res}(z_0) &= \frac{1}{w^2-\Delta^2}, \\
\mathrm{Res}(z_1^{\pm}) &= \frac{\mp 1}{2\Delta(w^2-\Delta^2)\sqrt{\mu^2-4w^2+4\Delta^2}} \\
&\quad \times \sqrt{\mu^2(w^2+\Delta^2)-4w^2(w^2-\Delta^2)+2\mu w\Delta\sqrt{\mu^2-4w^2+4\Delta^2}}, \\
\mathrm{Res}(z_2^{\pm}) &= \frac{\pm 1}{2\Delta(w^2-\Delta^2)\sqrt{\mu^2-4w^2+4\Delta^2}} \\
&\quad \times \sqrt{\mu^2(w^2+\Delta^2)-4w^2(w^2-\Delta^2)-2\mu w\Delta\sqrt{\mu^2-4w^2+4\Delta^2}}.
\end{aligned} \tag{D.24}$$

Recalling the definition of ζ we can write the two pairs compactly as:

$$\begin{aligned}
\mathrm{Res}(z_1^{\pm}) &= \frac{\mp 1}{2\Delta(w^2-\Delta^2)\zeta}\sqrt{w^2\zeta^2+\mu^2\Delta^2+2\mu w\Delta\zeta}, \\
\mathrm{Res}(z_2^{\pm}) &= \frac{\pm 1}{2\Delta(w^2-\Delta^2)\zeta}\sqrt{w^2\zeta^2+\mu^2\Delta^2-2\mu w\Delta\zeta},
\end{aligned} \tag{D.25}$$

which leads to the final form for the residues:

$$\begin{aligned}
\mathrm{Res}(z_0) &= \frac{1}{w^2-\Delta^2}, \\
\mathrm{Res}(z_1^{\pm}) &= \mp\frac{|w\zeta+\mu\Delta|}{2\Delta(w^2-\Delta^2)\zeta}, \\
\mathrm{Res}(z_2^{\pm}) &= \pm\frac{|w\zeta-\mu\Delta|}{2\Delta(w^2-\Delta^2)\zeta}.
\end{aligned} \tag{D.26}$$

Finally, recall the residue theorem

$$\oint_c f(z)dz = 2\pi i\sum_k \mathrm{Res}(f, a_k), \tag{D.27}$$

for c a positively oriented simple closed curve (here the unit circle at the origin) and a_k a pole in the interior of the curve. These points enclosed by the contour are z_0, z_1^+ and z_2^+, see Fig. D.1, which yield

$$\begin{aligned}
\frac{1}{\epsilon\gamma}I_z(w,\mu,\Delta) &= -\frac{2\pi\Delta^2}{w^2-\Delta^2} - \frac{\Delta\pi|w\zeta+\mu\Delta|}{(w^2-\Delta^2)\zeta} + \frac{\Delta\pi|w\zeta-\mu\Delta|}{(w^2-\Delta^2)\zeta}, \\
&= \frac{2\pi\Delta^2}{w^2-\Delta^2}\left(-1+\frac{1}{2\Delta\zeta}\left(|w\zeta+\mu\Delta|-|w\zeta-\mu\Delta|\right)\right)
\end{aligned} \tag{D.28}$$

From this point we can reproduce the same cases as found for the real form of the integral.

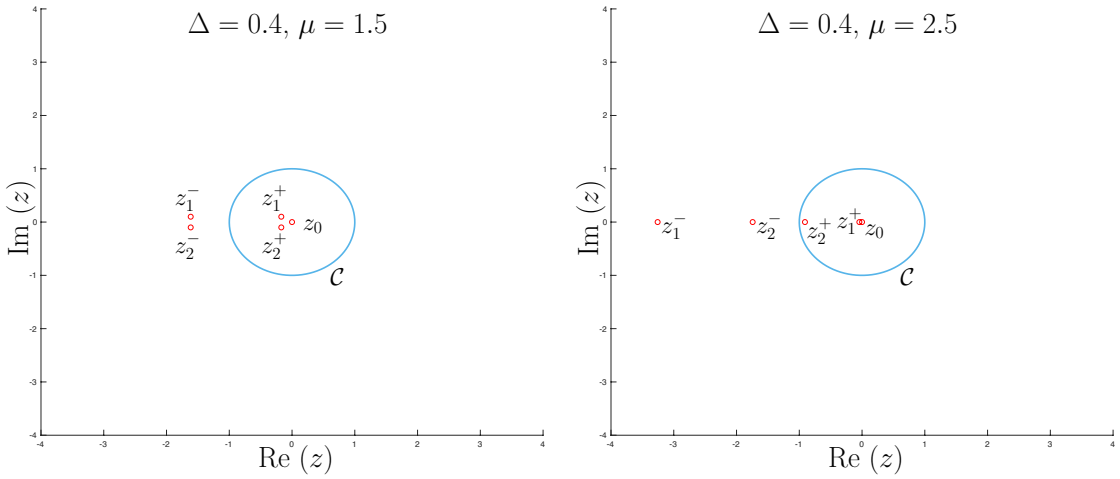

(a) Poles in Topological Phase

(b) Poles in Trivial Phase

Figure D.1: The locations of the poles of the contour integral. The contour itself is the unit circle as defined from our change of variables. (a) We show the poles in the topological phase, $\mu < 2$. (b) We show the poles in the trivial phase, $\mu > 2$. Notice that while the poles move around the complex plane, the poles that are enclosed by the contour are those poles we have labelled, z_0, z_1^+ and z_2^+. Hence, they are the one whose residues we include to obtain our result. Interestingly the topological phase can be seen by the poles "lifting" off the real line.

Bibliography

[AFD21] A. Altland, M. Fleischhauer, and S. Diehl. "Symmetry Classes of Open Fermionic Quantum Matter". *Phys. Rev. X* 11 (2 2021), 021037. DOI: 10.1103/PhysRevX.11.021037.

[AJ14] V. V. Albert and L. Jiang. "Symmetries and conserved quantities in Lindblad master equations". *Phys. Rev. A* 89 (2 2014), 022118. DOI: 10.1103/PhysRevA.89.022118.

[AKL18] P. P. Aseev, J. Klinovaja, and D. Loss. "Lifetime of Majorana qubits in Rashba nanowires with nonuniform chemical potential". *Phys. Rev. B* 98 (15 2018), 155414. DOI: 10.1103/PhysRevB.98.155414.

[Alb+16] S. M. Albrecht et al. "Exponential protection of zero modes in Majorana islands". *Nature* 531.7593 (2016), 206–209. DOI: 10.1038/nature17162.

[Ali+11] J. Alicea et al. "Non-Abelian statistics and topological quantum information processing in 1D wire networks". *Nature Physics* 7 (2011), 412–417. DOI: 10.1038/nphys1915.

[Bao+15] N. Bao et al. "Consistency conditions for an AdS multiscale entanglement renormalization ansatz correspondence". *Phys. Rev. D* 91 (12 2015), 125036. DOI: 10.1103/PhysRevD.91.125036.

[Bar+13] C.-E. Bardyn et al. "Topology by dissipation". *New J. Phys.* 15.8 (2013), 085001. DOI: 10.1088/1367-2630/15/8/085001.

[Bar+20] S. Barbarino et al. "Preparing Atomic Topological Quantum Matter by Adiabatic Nonunitary Dynamics". *Phys. Rev. Lett.* 124 (1 2020), 010401. DOI: 10.1103/PhysRevLett.124.010401.

[BBK21] E. J. Bergholtz, J. C. Budich, and F. K. Kunst. "Exceptional topology of non-Hermitian systems". *Rev. Mod. Phys.* 93 (1 2021), 015005. DOI: 10.1103/RevModPhys.93.015005.

[BC17] J. C. Bridgeman and C. T. Chubb. "Hand-waving and interpretive dance: an introductory course on tensor networks". *Journal of Physics A: Mathematical and Theoretical* 50.22 (2017), 223001. DOI: 10.1088/1751-8121/aa6dc3.

[BDS15] E. Brattain, N. Do, and A. Saenz. *The completeness of the Bethe ansatz for the periodic ASEP*. 2015. DOI: 10.48550/arXiv.1511.03762.

[BdV83] O. Babelon, H.J. de Vega, and C.M. Viallet. "Analysis of the Bethe ansatz equations of the XXZ model". *Nuclear Physics B* 220.1 (1983), 13–34. ISSN: 0550-3213. DOI: https://doi.org/10.1016/0550-3213(83)90131-1.

[Ber+22] D. Bernard et al. "Dynamics of fluctuations in quantum simple exclusion processes". *SciPost Phys.* 12 (2022), 042. DOI: 10.21468/SciPostPhys.12.1.042.

[BH11] S. Bravyi and M. B. Hastings. "A Short Proof of Stability of Topological Order under Local Perturbations". *Communications in Mathematical Physics* 307.3 (2011), 609–627. DOI: 10.1007/s00220-011-1346-2.

[BH13] B. A. Bernevig and T. L. Hughes. *Topological Insulators and Topological Superconductors*. 1st. Princeton University Press, 2013. ISBN: 9780691151755.

[BHM10] S. Bravyi, M. B. Hastings, and S. Michalakis. "Topological quantum order: Stability under local perturbations". *Journal of Mathematical Physics* 51 (2010), 093512. ISSN: 1089-7658. DOI: 10.1063/1.3490195.

[Bİ12] C.-E. Bardyn and A. İmamoğlu. "Majorana-like Modes of Light in a One-Dimensional Array of Nonlinear Cavities". *Phys. Rev. Lett.* 109 (25 2012), 253606. DOI: 10.1103/PhysRevLett.109.253606.

[BJ19] D. Bernard and T. Jin. "Open Quantum Symmetric Simple Exclusion Process". *Phys. Rev. Lett.* 123 (8 2019), 080601. DOI: 10.1103/PhysRevLett.123.080601.

[BP02] H.P. Breuer and F. Petruccione. *The Theory of Open Quantum Systems*. Oxford University Press, 2002. ISBN: 978-0-19-852063-4. DOI: doi.org/10.1093/acprof:oso/9780199213900.001.0001.

[BP21] D. Bernard and L. Piroli. "Entanglement distribution in the quantum symmetric simple exclusion process". *Phys. Rev. E* 104 (1 2021), 014146. DOI: 10.1103/PhysRevE.104.014146.

[Bra+17] B. Bradlyn et al. "Topological quantum chemistry". *Nature* 547 (2017), 298–305. DOI: 10.1038/nature23268.

[Bro+16] B. J. Brown et al. "Quantum memories at finite temperature". *Rev. Mod. Phys.* 88 (4 2016), 045005. DOI: 10.1103/RevModPhys.88.045005.

[Bul+17] N. Bultinck et al. "Fermionic matrix product states and one-dimensional topological phases". *Phys. Rev. B* 95 (7 2017), 075108. DOI: 10.1103/PhysRevB.95.075108.

[BWT12] J. C. Budich, S. Walter, and B. Trauzettel. "Failure of protection of Majorana based qubits against decoherence". *Phys. Rev. B* 85 (12 2012), 121405. DOI: 10.1103/PhysRevB.85.121405.

[BZD15] J. C. Budich, P. Zoller, and S. Diehl. "Dissipative preparation of Chern insulators". *Phys. Rev. A* 91 (4 2015), 042117. DOI: 10.1103/PhysRevA.91.042117.

[CB08] G. M. Crosswhite and D. Bacon. "Finite automata for caching in matrix product algorithms". *Phys. Rev. A* 78 (1 2008), 012356. DOI: 10.1103/PhysRevA.78.012356.

[CGD11] M. Cheng, V. Galitski, and S. Das Sarma. "Nonadiabatic effects in the braiding of non-Abelian anyons in topological superconductors". *Phys. Rev. B* 84 (10 2011), 104529. DOI: 10.1103/PhysRevB.84.104529.

[Cho75] M-D. Choi. "Completely positive linear maps on complex matrices". *Linear Algebra and its Applications* 10.3 (1975), 285–290. ISSN: 0024-3795. DOI: https://doi.org/10.1016/0024-3795(75)90075-0.

[Chu+13] H. O. H. Churchill et al. "Superconductor-nanowire devices from tunneling to the multichannel regime: Zero-bias oscillations and magnetoconductance crossover". *Phys. Rev. B* 87 (24 2013), 241401. DOI: 10.1103/PhysRevB.87.241401.

[Cir+17] J. I. Cirac et al. "Matrix product unitaries: structure, symmetries, and topological invariants". *J. Stat. Mech.* (2017), 083105. DOI: 10.1088/1742-5468/aa7e55.

[Con+19] A. Conlon et al. "Error generation and propagation in Majorana-based topological qubits". *Phys. Rev. B* 100 (13 2019), 134307. DOI: 10.1103/PhysRevB.100.134307.

[Coo+21a] L. Coopmans et al. "Dynamical phase error in interacting topological quantum memories". *Phys. Rev. Research* 3 (3 2021), 033105. DOI: 10.1103/PhysRevResearch.3.033105.

[Coo+21b] L. Coopmans et al. "Protocol Discovery for the Quantum Control of Majoranas by Differentiable Programming and Natural Evolution Strategies". *PRX Quantum* 2 (2 2021), 020332. DOI: 10.1103/PRXQuantum.2.020332.

[CR12] N. Crampé and E. Ragoucy. "Generalized coordinate Bethe ansatz for non-diagonal boundaries". *Nuclear Physics B* 858.3 (2012), 502–512. ISSN: 0550-3213. DOI: https://doi.org/10.1016/j.nuclphysb.2012.01.020.

[CRS10] N. Crampé, E. Ragoucy, and D. Simon. "Eigenvectors of open XXZ and ASEP models for a class of non-diagonal boundary conditions". *Journal of Statistical Mechanics: Theory and Experiment* 2010.11 (2010), P11038. DOI: 10.1088/1742-5468/2010/11/p11038.

[CST11] D. J. Clarke, J. D. Sau, and S. Tewari. "Majorana fermion exchange in quasi-one-dimensional networks". *Phys. Rev. B* 84 (3 2011), 035120. DOI: 10.1103/PhysRevB.84.035120.

[Cub+15] T. S. Cubitt et al. "Stability of Local Quantum Dissipative Systems". *Communications in Mathematical Physics* 337.3 (2015), 1275–1315. DOI: 10.1007/s00220-015-2355-3.

[Cze+16] B. Czech et al. "Tensor networks from kinematic space". *Journal of High Energy Physics* (2016), 100. ISSN: 1029-8479. DOI: 10.1007/JHEP07(2016)100.

[Das+12] A. Das et al. "Zero-bias peaks and splitting in an Al–InAs nanowire topological superconductor as a signature of Majorana fermions". *Nature Physics* 8.12 (2012), 887–895. DOI: 10.1038/nphys2479.

[DDM92] B. Derrida, E. Domany, and D. Mukamel. "An exact solution of a one-dimensional asymmetric exclusion model with open boundaries". *Journal of Statistical Physics* 69.3 (1992), 667–687. ISSN: 1572-9613. DOI: 10.1007/BF01050430.

[Den+02] E. Dennis et al. "Topological quantum memory". *Journal of Mathematical Physics* 43.9 (2002), 4452–4505. DOI: 10.1063/1.1499754.

[Den+12] M. T. Deng et al. "Anomalous Zero-Bias Conductance Peak in a Nb–InSb Nanowire–Nb Hybrid Device". *Nano Letters* 12.12 (2012), 6414–6419. DOI: 10.1021/nl303758w.

[Den+16] M. T. Deng et al. "Majorana bound state in a coupled quantum-dot hybrid-nanowire system". *Science* 354.6319 (2016), 1557–1562. ISSN: 0036-8075. DOI: 10.1126/science.aaf3961.

[Der+93] B. Derrida et al. "Exact solution of a 1D asymmetric exclusion model using a matrix formulation". *Journal of Physics A: Mathematical and General* 26.7 (1993), 1493–1517. DOI: 10.1088/0305-4470/26/7/011.

[DFN05] S. Das Sarma, M. Freedman, and C. Nayak. "Topologically Protected Qubits from a Possible Non-Abelian Fractional Quantum Hall State". *Phys. Rev. Lett.* 94 (16 2005), 166802. DOI: 10.1103/PhysRevLett.94.166802.

[DS00] M. Dudzinski and G. Schuetz. "Relaxation spectrum of the asymmetric exclusion process with open boundaries". *Journal of Physics A: Mathematical and General* 33 (2000), 8351. DOI: 10.1088/0305-4470/33/47/302.

[Dzy59] I. E. Dzyaloshinskii. "On the Magneto-Electrical Effect in Antiferromagnets". *J. Exp. Theor. Phys. (USSR)* 37 (881 1959).

[Eis11] V. Eisler. "Crossover between ballistic and diffusive transport: the quantum exclusion process". *Journal of Statistical Mechanics: Theory and Experiment* 2011.06 (2011), P06007. DOI: 10.1088/1742-5468/2011/06/p06007.

[EKB19] E. Edvardsson, F. K. Kunst, and E. J. Bergholtz. "Non-Hermitian extensions of higher-order topological phases and their biorthogonal bulk-boundary correspondence". *Phys. Rev. B* 99 (8 2019), 081302. DOI: 10.1103/PhysRevB.99.081302.

[Els+17] D. V. Else et al. "Prethermal Strong Zero Modes and Topological Qubits". *Phys. Rev. X* 7 (4 2017), 041062. DOI: 10.1103/PhysRevX.7.041062.

[Eng15] L. P. English. "Anisotropic Heisenberg quantum spin chains: excitations and neutron-scattering cross sections". PhD thesis. University College Dublin, 2015.

[EP20] F. H. L. Essler and L. Piroli. "Integrability of one-dimensional Lindbladians from operator-space fragmentation". *Phys. Rev. E* 102 (6 2020), 062210. DOI: 10.1103/PhysRevE.102.062210.

[ERS99] M. R. Evans, N. Rajewsky, and E. R. Speer. "Exact Solution of a Cellular Automaton for Traffic". *Journal of Statistical Physics* 95.1 (1999), 45–96. ISSN: 1572-9613. DOI: 10.1023/A:1004521326456.

[EV11] G. Evenbly and G. Vidal. "Tensor Network States and Geometry". *Journal of Statistical Physics* 145.4 (2011), 891–918. ISSN: 1572-9613. DOI: 10.1007/s10955-011-0237-4.

[EV14] G. Evenbly and G. Vidal. "Algorithms for Entanglement Renormalization: Boundaries, Impurities and Interfaces". *Journal of Statistical Physics* 157.4 (2014), 931–978. ISSN: 1572-9613. DOI: 10.1007/s10955-014-0983-1.

[EV15] G. Evenbly and G. Vidal. "Tensor Network Renormalization". *Phys. Rev. Lett.* 115 (18 2015), 180405. DOI: 10.1103/PhysRevLett.115.180405.

[Eve11] G. Evenbly. "Foundations and Applications of Entanglement Renormalization". PhD thesis. University of Queensland, 2011. DOI: 10.48550/ARXIV.1109.5424.

[Eve17] G. Evenbly. "Algorithms for tensor network renormalization". *Phys. Rev. B* 95 (4 2017), 045117. DOI: 10.1103/PhysRevB.95.045117.

[Fen16] P. Fendley. "Strong zero modes and eigenstate phase transitions in the XYZ/interacting Majorana chain". *Journal of Physics A: Mathematical and Theoretical* 49.30 (2016), 30LT01. DOI: 10.1088/1751-8113/49/30/30lt01.

[Fin+13] A. D. K. Finck et al. "Anomalous Modulation of a Zero-Bias Peak in a Hybrid Nanowire-Superconductor Device". *Phys. Rev. Lett.* 110 (12 2013), 126406. DOI: 10.1103/PhysRevLett.110.126406.

[FK08] L. Fu and C. L. Kane. "Superconducting Proximity Effect and Majorana Fermions at the Surface of a Topological Insulator". *Phys. Rev. Lett.* 100 (9 2008), 096407. DOI: 10.1103/PhysRevLett.100.096407.

[For+19] A. Fornieri et al. "Evidence of topological superconductivity in planar Josephson junctions". *Nature* 569.7754 (2019), 89–92. DOI: 10.1038/s41586-019-1068-8.

[Ful+19] I. C. Fulga et al. "Topology and localization of a periodically driven Kitaev model". *Phys. Rev. B* 99 (23 2019), 235408. DOI: 10.1103/PhysRevB.99.235408.

[FV17] A. Franco-Rubio and G. Vidal. "Entanglement and correlations in the continuous multi-scale entanglement renormalization ansatz". *Journal of High Energy Physics* 2017.12 (2017), 129. ISSN: 1029-8479. DOI: 10.1007/JHEP12(2017)129.

[Gan+11] S. Gangadharaiah et al. "Majorana Edge States in Interacting One-Dimensional Systems". *Phys. Rev. Lett.* 107 (3 2011), 036801. DOI: 10.1103/PhysRevLett.107.036801.

[GBZ16] N. Goldman, J. C. Budich, and P. Zoller. "Topological quantum matter with ultracold gases in optical lattices". *Nature Physics* 12.7 (2016), 639–645. ISSN: 1745-2481. DOI: 10.1038/nphys3803.

[GC12] G. Goldstein and C. Chamon. "Exact zero modes in closed systems of interacting fermions". *Phys. Rev. B* 86 (11 2012), 115122. DOI: 10.1103/PhysRevB.86.115122.

[GE05] J. de Gier and F. H. L. Essler. "Bethe Ansatz Solution of the Asymmetric Exclusion Process with Open Boundaries". *Phys. Rev. Lett.* 95 (24 2005), 240601. DOI: 10.1103/PhysRevLett.95.240601.

[GE06] J. de Gier and F. H. L. Essler. "Exact spectral gaps of the asymmetric exclusion process with open boundaries". *Journal of Statistical Mechanics: Theory and Experiment* 2006.12 (2006), P12011. DOI: 10.1088/1742-5468/2006/12/p12011.

[Geb+20] V. Gebhart et al. "Topological transition in measurement-induced geometric phases". *Proceedings of the National Academy of Sciences* 117.11 (2020), 5706–5713. ISSN: 0027-8424. DOI: 10.1073/pnas.1911620117.

[GKS76] V. Gorini, A. Kossakowski, and E. C. G. Sudarshan. "Completely positive dynamical semigroups of N-level systems". *Journal of Mathematical Physics* 17.5 (1976), 821–825. DOI: 10.1063/1.522979.

[GS92] L.-H. Gwa and H. Spohn. "Bethe solution for the dynamical-scaling exponent of the noisy Burgers equation". *Phys. Rev. A* 46 (2 1992), 844–854. DOI: 10.1103/PhysRevA.46.844.

[GST14] M. Greiter, V. Schnells, and R. Thomale. "The 1D Ising model and the topological phase of the Kitaev chain". *Annals of Physics* 351 (2014), 1026–1033. ISSN: 0003-4916. DOI: https://doi.org/10.1016/j.aop.2014.08.013.

[Hae+11] J. Haegeman et al. "Time-Dependent Variational Principle for Quantum Lattices". *Phys. Rev. Lett.* 107 (7 2011), 070601. DOI: 10.1103/PhysRevLett.107.070601.

[Has04] M. B. Hastings. "Locality in Quantum and Markov Dynamics on Lattices and Networks". *Phys. Rev. Lett.* 93 (14 2004), 140402. DOI: 10.1103/PhysRevLett.93.140402.

[Has07] M. B. Hastings. "Entropy and entanglement in quantum ground states". *Phys. Rev. B* 76 (3 2007), 035114. DOI: 10.1103/PhysRevB.76.035114.

[He+17] Q. Lin He et al. "Chiral Majorana fermion modes in a quantum anomalous Hall insulator–superconductor structure". *Science* 357.6348 (2017), 294–299. ISSN: 0036-8075. DOI: 10.1126/science.aag2792.

[HK06] M. B. Hastings and T. Koma. "Spectral gap and exponential decay of correlations". *Commun. Math. Phys.* 265 (2006), 781–804. DOI: 10.1007/s00220-006-0030-4.

[HKV21] D. Hartmann, K. Kavanagh, and S. Vandoren. "Entanglement entropy with Lifshitz fermions". *SciPost Phys.* 11 (2021), 031. DOI: 10.21468/SciPostPhys.11.2.031.

[HSD22] Z.-M. Huang, X.-Q. Sun, and S. Diehl. *Topological gauge theory for mixed Dirac stationary states in all dimensions*. 2022. DOI: 10.1103/PhysRevB.106.245204.

[Hu+15] Y. Hu et al. “Majorana fermions in noisy Kitaev wires”. *Phys. Rev. B* 92 (16 2015), 165118. DOI: 10.1103/PhysRevB.92.165118.

[Hus+13] D. A. Huse et al. “Localization-protected quantum order”. *Phys. Rev. B* 88 (1 2013), 014206. DOI: 10.1103/PhysRevB.88.014206.

[HW05] M. B. Hastings and X. G. Wen. “Quasiadiabatic continuation of quantum states: The stability of topological ground-state degeneracy and emergent gauge invariance”. *Phys. Rev. B* 72 (4 2005), 045141. DOI: 10.1103/PhysRevB.72.045141.

[Iem+16] F. Iemini et al. “Dissipative topological superconductors in number-conserving systems”. *Phys. Rev. B* 93 (11 2016), 115113. DOI: 10.1103/PhysRevB.93.115113.

[Ipp+16] M. Ippoliti et al. “Quantum memories with zero-energy Majorana modes and experimental constraints”. *Phys. Rev. A* 93 (6 2016), 062325. DOI: 10.1103/PhysRevA.93.062325.

[Isi25] E. Ising. “Beitrag zur Theorie des Ferromagnetismus”. *Zeitschrift für Physik* 31.1 (1925), 253–258. ISSN: 0044-3328. DOI: 10.1007/BF02980577.

[ISN21] Y. Ishiguro, J. Sato, and K. Nishinari. *Bundled string solutions of the Bethe ansatz equations in the non-Hermitian spin chain*. 2021. arXiv: 2101.10647 [cond-mat.stat-mech].

[Jam72] A. Jamiołkowski. “Linear transformations which preserve trace and positive semidefiniteness of operators”. *Reports on Mathematical Physics* 3.4 (1972), 275–278. ISSN: 0034-4877. DOI: https://doi.org/10.1016/0034-4877(72)90011-0.

[Jer+14] A. S. Jermyn et al. “Stability of zero modes in parafermion chains”. *Phys. Rev. B* 90 (16 2014), 165106. DOI: 10.1103/PhysRevB.90.165106.

[JNK13] C. Joshi, F. Nissen, and J. Keeling. “Quantum correlations in the one-dimensional driven dissipative XY model”. *Phys. Rev. A* 88 (6 2013), 063835. DOI: 10.1103/PhysRevA.88.063835.

[Jon+21] N. G. Jones et al. “Skeleton of matrix-product-state-solvable models connecting topological phases of matter”. *Phys. Rev. Research* 3 (3 2021), 033265. DOI: 10.1103/PhysRevResearch.3.033265.

[JW28] P. Jordan and E. Wigner. “Über das Paulische Äquivalenzverbot”. *Zeitschrift für Physik* 47.9 (1928), 631–651. ISSN: 0044-3328. DOI: 10.1007/BF01331938.

[Kav+22a] K. Kavanagh et al. "Effects of quantum pair creation and annihilation on a classical exclusion process: the transverse XY model with TASEP". *New Journal of Physics* 24.2 (2022), 023024. DOI: 10.1088/1367-2630/ac4ee1.

[Kav+22b] K. Kavanagh et al. "Topological fingerprints in Pairing-induced Liouvillian gaps". In Preparation. 2022.

[KE13] M. J. Kastoryano and J. Eisert. "Rapid mixing implies exponential decay of correlations". *Journal of Mathematical Physics* 54.10 (2013), 102201. DOI: 10.1063/1.4822481.

[Kel15a] G. Kells. "Many-body Majorana operators and the equivalence of parity sectors". *Phys. Rev. B* 92 (8 2015), 081401. DOI: 10.1103/PhysRevB.92.081401.

[Kel15b] G. Kells. "Multiparticle content of Majorana zero modes in the interacting p-wave wire". *Phys. Rev. B* 92 (15 2015), 155434. DOI: 10.1103/PhysRevB.92.155434.

[Kem+17] J. Kemp et al. "Long coherence times for edge spins". *Journal of Statistical Mechanics: Theory and Experiment* (2017), 063105. DOI: 10.1088/1742-5468/aa73f0.

[Kes+12] E. M. Kessler et al. "Dissipative phase transition in a central spin system". *Phys. Rev. A* 86 (1 2012), 012116. DOI: 10.1103/PhysRevA.86.012116.

[KH13] F. Konschelle and F. Hassler. "Effects of nonequilibrium noise on a quantum memory encoded in Majorana zero modes". *Phys. Rev. B* 88 (7 2013), 075431. DOI: 10.1103/PhysRevB.88.075431.

[Kim95] D. Kim. "Bethe ansatz solution for crossover scaling functions of the asymmetric XXZ chain and the Kardar-Parisi-Zhang-type growth model". *Phys. Rev. E* 52 (4 1995). DOI: 10.1103/PhysRevE.52.3512.

[Kit01] A. Y. Kitaev. "Unpaired Majorana fermions in quantum wires". *Physics-Uspekhi* 44.10S (2001), 131. DOI: 10.1070/1063-7869/44/10S/S29.

[Kit03] A. Y. Kitaev. "Fault-tolerant quantum computation by anyons". *Annals of Physics* 303.1 (2003), 2–30. ISSN: 0003-4916. DOI: https://doi.org/10.1016/S0003-4916(02)00018-0.

[Kit06] A. Y. Kitaev. "Anyons in an exactly solved model and beyond". *Annals of Physics* 321.1 (2006), 2–111. ISSN: 0003-4916. DOI: https://doi.org/10.1016/j.aop.2005.10.005.

[KK12] A. Kitaev and L. Kong. "Models for Gapped Boundaries and Domain Walls". *Communications in Mathematical Physics* 313.2 (2012), 351–373. ISSN: 1432-0916. DOI: 10.1007/s00220-012-1500-5.

[KMM18] G. Kells, N. Moran, and D. Meidan. "Localization enhanced and degraded topological order in interacting p-wave wires". *Phys. Rev. B* 97 (8 2018), 085425. DOI: 10.1103/PhysRevB.97.085425.

[Kna+18] C. Knapp et al. "Dephasing of Majorana-based qubits". *Phys. Rev. B* 97 (12 2018), 125404. DOI: 10.1103/PhysRevB.97.125404.

[KPS13] D. Karevski, V. Popkov, and G. M. Schütz. "Exact Matrix Product Solution for the Boundary-Driven Lindblad XXZ Chain". *Phys. Rev. Lett.* 110 (4 2013), 047201. DOI: 10.1103/PhysRevLett.110.047201.

[KRO13] T. Karzig, G. Refael, and F. von Oppen. "Boosting Majorana Zero Modes". *Phys. Rev. X* 3 (4 2013), 041017. DOI: 10.1103/PhysRevX.3.041017.

[Kun+18] F. K. Kunst et al. "Biorthogonal Bulk-Boundary Correspondence in non-Hermitian Systems". *Phys. Rev. Lett.* 121 (2 2018), 026808. DOI: 10.1103/PhysRevLett.121.026808.

[LAB21] A. Lavasani, Y. Alavirad, and M. Barkeshli. "Measurement-induced topological entanglement transitions in symmetric random quantum circuits". *Nature Physics* 17.3 (2021), 342–347. ISSN: 1745-2481. DOI: 10.1038/s41567-020-01112-z.

[Lee16] T. E. Lee. "Anomalous Edge State in a non-Hermitian Lattice". *Phys. Rev. Lett.* 116 (13 2016), 133903. DOI: 10.1103/PhysRevLett.116.133903.

[Lin76] G. Lindblad. "On the generators of quantum dynamical semigroups". *Communications in Mathematical Physics* 48.2 (1976), 119–130. ISSN: 1432-0916. DOI: 10.1007/BF01608499.

[LP14] A. Lazarescu and V. Pasquier. "Bethe Ansatz and Q-operator for the open ASEP". *Journal of Physics A: Mathematical and Theoretical* 47.29 (2014), 295202. DOI: 10.1088/1751-8113/47/29/295202.

[LPK14] A. C. Y. Li, F. Petruccione, and J. Koch. "Perturbative approach to Markovian open quantum systems". *Scientific Reports* 4.1 (2014), 4887. ISSN: 2045-2322. DOI: 10.1038/srep04887.

[LPK16] A. C. Y. Li, F. Petruccione, and J. Koch. "Resummation for Nonequilibrium Perturbation Theory and Application to Open Quantum Lattices". *Phys. Rev. X* 6 (2 2016), 021037. DOI: 10.1103/PhysRevX.6.021037.

[LPP21] M. de Leeuw, C. Paletta, and B. Pozsgay. "Constructing Integrable Lindblad Superoperators". *Phys. Rev. Lett.* 126 (24 2021), 240403. DOI: 10.1103/PhysRevLett.126.240403.

[LR72] E. H. Lieb and D. W. Robinson. "The finite group velocity of quantum spin systems". *Commun. Math. Phys.* 28 (1972), 251–257. DOI: 10.1007/BF01645779.

[LSD10] R. M. Lutchyn, J. D. Sau, and S. Das Sarma. "Majorana Fermions and a Topological Phase Transition in Semiconductor-Superconductor Heterostructures". *Phys. Rev. Lett.* 105 (7 2010), 077001. DOI: 10.1103/PhysRevLett.105.077001.

[Luc+15] A. Lucia et al. "Rapid mixing and stability of quantum dissipative systems". *Phys. Rev. A* 91 (4 2015), 040302. DOI: 10.1103/PhysRevA.91.040302.

[LW06] M. Levin and X.-G. Wen. "Detecting Topological Order in a Ground State Wave Function". *Phys. Rev. Lett.* 96 (11 2006), 110405. DOI: 10.1103/PhysRevLett.96.110405.

[MA18] I. Mahyaeh and E. Ardonne. "Exact results for a $\mathbb{Z}_3$-clock-type model and some close relatives". *Phys. Rev. B* 98 (24 2018), 245104. DOI: 10.1103/PhysRevB.98.245104.

[MA20] I. Mahyaeh and E. Ardonne. "Study of the phase diagram of the Kitaev-Hubbard chain". *Phys. Rev. B* 101 (8 2020), 085125. DOI: 10.1103/PhysRevB.101.085125.

[Maj08] E. Majorana. "Teoria simmetrica dell'elettrone e del positrone". *Il Nuovo Cimento (1924-1942)* 14.4 (2008), 171. ISSN: 1827-6121. DOI: 10.1007/BF02961314.

[McC07] I. P. McCulloch. "From density-matrix renormalization group to matrix product states". *Journal of Statistical Mechanics: Theory and Experiment* (2007), P10014–P10014. DOI: 10.1088/1742-5468/2007/10/p10014.

[MD20] S. Mathey and S. Diehl. "Dynamic renormalization group theory for open Floquet systems". *Phys. Rev. B* 102 (13 2020), 134307. DOI: 10.1103/PhysRevB.102.134307.

[MKN17] M. McGinley, J. Knolle, and A. Nunnenkamp. "Robustness of Majorana edge modes and topological order: Exact results for the symmetric interacting Kitaev chain with disorder". *Phys. Rev. B* 96 (24 2017), 241113. DOI: 10.1103/PhysRevB.96.241113.

[MN18] A. Moon and B. Nachtergaele. "Stability of gapped ground state phases of spins and fermions in one dimension". *Journal of Mathematical Physics* 59.9 (2018), 091415. DOI: 10.1063/1.5036751.

[Mor+17] N. Moran et al. "Parafermionic clock models and quantum resonance". *Phys. Rev. B* 95 (23 2017), 235127. DOI: 10.1103/PhysRevB.95.235127.

[Mor60] T. Moriya. "Anisotropic Superexchange Interaction and Weak Ferromagnetism". *Phys. Rev.* 120 (1 1960), 91–98. DOI: 10.1103/PhysRev.120.91.

[Mou+12] V. Mourik et al. "Signatures of Majorana Fermions in Hybrid Superconductor-Semiconductor Nanowire Devices". *Science* 336.6084 (2012), 1003–1007. ISSN: 0036-8075. DOI: 10.1126/science.1222360.

[MR91] G. Moore and N. Read. "Nonabelions in the fractional quantum Hall effect". *Nuclear Physics B* 360.2 (1991), 362–396. ISSN: 0550-3213. DOI: https://doi.org/10.1016/0550-3213(91)90407-O.

[Nad+14] S. Nadj-Perge et al. "Observation of Majorana fermions in ferromagnetic atomic chains on a superconductor". *Science* 346.6209 (2014), 602–607. ISSN: 0036-8075. DOI: 10.1126/science.1259327.

[Nay+08] C. Nayak et al. "Non-Abelian anyons and topological quantum computation". *Rev. Mod. Phys.* 80 (3 2008), 1083–1159. DOI: 10.1103/RevModPhys.80.1083.

[NC00] M. A. Nielsen and I. L. Chuang. *Quantum Computation and Quantum Information*. Cambridge Series on Information and the Natural Sciences. Cambridge University Press, 2000. ISBN: 978-0-521-63503-5.

[NCS02] Z. Nagy, Appert C., and L. Santen. "Relaxation times in the ASEP model using a DMRG method". *Journal of Statistical Physics* 109 (2002). DOI: 10.1023/A:1020462531383.

[Ng15] H. T. Ng. "Decoherence of interacting Majorana modes". *Scientific Reports* 5.1 (2015), 12530. DOI: 10.1038/srep12530.

[Nis] T. Nishino. *unofficial DMRG + MPS, TPS, MERA, Tensor Network Home Page*. URL: http://quattro.phys.sci.kobe-u.ac.jp/dmrg.html.

[NSY18] B. Nachtergaele, R. Sims, and A. Young. "Lieb-Robinson bounds, the spectral flow, and stability of the spectral gap for lattice fermion systems". *Contemporary Mathematics* (2018). ISSN: 1098-3627. DOI: 10.1090/conm/717.

[Nul+20] S. Nulty et al. "Constrained thermalization and topological superconductivity". *Phys. Rev. B* 102 (5 2020), 054508. DOI: 10.1103/PhysRevB.102.054508.

[NVZ11] B. Nachtergaele, A. Vershynina, and V. A. Zagrebnov. "Lieb-Robinson Bounds and Existence of the Thermodynamic Limit for a Class of Irreversible Quantum Dynamics". *Contemporary Mathematics* (2011). DOI: 10.1090/conm/552.

[ORO10] Y. Oreg, G. Refael, and F. von Oppen. "Helical Liquids and Majorana Bound States in Quantum Wires". *Phys. Rev. Lett.* 105 (17 2010), 177002. DOI: 10.1103/PhysRevLett.105.177002.

[Orú14] R. Orús. "A practical introduction to tensor networks: Matrix product states and projected entangled pair states". *Annals of Physics* 349 (2014), 117–158. ISSN: 0003-4916. DOI: 10.1016/j.aop.2014.06.013.

[Orú19] R. Orús. "Tensor networks for complex quantum systems". *Nature Reviews Physics* 1.9 (2019), 538–550. ISSN: 2522-5820. DOI: 10.1038/s42254-019-0086-7.

[OV08] R. Orús and G. Vidal. "Infinite time-evolving block decimation algorithm beyond unitary evolution". *Phys. Rev. B* 78 (15 2008), 155117. DOI: 10.1103/PhysRevB.78.155117.

[Pac12] J. K. Pachos. *Introduction to Topological Quantum Computation*. Cambridge University Press, 2012. ISBN: 978-1-107-00504-4.

[Pae+19] S. Paeckel et al. "Time-evolution methods for matrix-product states". *Annals of Physics* 411 (2019), 167998. ISSN: 0003-4916. DOI: 10.1016/j.aop.2019.167998.

[Paw+16] R. Pawlak et al. "Probing atomic structure and Majorana wavefunctions in mono-atomic Fe chains on superconducting Pb surface". *npj Quantum Information* 2.1 (2016), 16035. DOI: 10.1038/npjqi.2016.35.

[PD15] F. L. Pedrocchi and D. P. DiVincenzo. "Majorana Braiding with Thermal Noise". *Phys. Rev. Lett.* 115 (12 2015), 120402. DOI: 10.1103/PhysRevLett.115.120402.

[Pel+20] D. Pellegrino et al. "Constructing edge zero modes through domain wall angle conservation". *Journal of Physics A: Mathematical and Theoretical* 53.9 (2020), 095006. DOI: 10.1088/1751-8121/ab6fc7.

[Per+07] D. Perez-Garcia et al. "Matrix Product State Representations". *Quantum Info. Comput.* 7.5 (2007), 401–430. ISSN: 1533-7146.

[Pou10] D. Poulin. "Lieb-Robinson Bound and Locality for General Markovian Quantum Dynamics". *Phys. Rev. Lett.* 104 (19 2010), 190401. DOI: 10.1103/PhysRevLett.104.190401.

[PP08] T. Prosen and I. Pižorn. "Quantum Phase Transition in a Far-from-Equilibrium Steady State of an XY Spin Chain". *Phys. Rev. Lett.* 101 (10 2008), 105701. DOI: 10.1103/PhysRevLett.101.105701.

[Pro08] T. Prosen. "Third quantization: a general method to solve master equations for quadratic open Fermi systems". *New Journal of Physics* 10.4 (2008), 043026. DOI: 10.1088/1367-2630/10/4/043026.

[Pro11] T. Prosen. "Exact Nonequilibrium Steady State of a Strongly Driven Open XXZ Chain". *Phys. Rev. Lett.* 107 (13 2011), 137201. DOI: 10.1103/PhysRevLett.107.137201.

[Pro15] T. Prosen. "Matrix product solutions of boundary driven quantum chains". *Journal of Physics A: Mathematical and Theoretical* 48.37 (2015), 373001. DOI: 10.1088/1751-8113/48/37/373001.

[Pro16] S. Prolhac. "Extrapolation methods and Bethe ansatz for the asymmetric exclusion process". *Journal of Physics A: Mathematical and Theoretical* 49.45 (2016), 454002. DOI: 10.1088/1751-8113/49/45/454002.

[PŽ09] T. Prosen and M. Žnidarič. "Matrix product simulations of non-equilibrium steady states of quantum spin chains". *Journal of Statistical Mechanics: Theory and Experiment* (2009), P02035. DOI: 10.1088/1742-5468/2009/02/p02035.

[QZ10] X.-L. Qi and S.-C. Zhang. "The quantum spin Hall effect and topological insulators". *Physics Today* 63 (2010), 33–38. DOI: 10.1063/1.3293411.

[Raj+97] N. Rajewsky et al. "The asymmetric exclusion process: Comparison of update procedures". 1997. DOI: 10.48550/ARXIV.COND-MAT/9710316.

[RBS12] D. Roy, C. J. Bolech, and N. Shah. "Majorana fermions in a topological superconducting wire out of equilibrium: Exact microscopic transport analysis of a p-wave open chain coupled to normal leads". *Phys. Rev. B* 86 (9 2012), 094503. DOI: 10.1103/PhysRevB.86.094503.

[RE21] J. Robertson and F. H. L. Essler. "Exact solution of a quantum asymmetric exclusion process with particle creation and annihilation". *Journal of Statistical Mechanics: Theory and Experiment* 2021.10 (2021), 103102. DOI: 10.1088/1742-5468/ac22f8.

[Ren+19] H. Ren et al. "Topological superconductivity in a phase-controlled Josephson junction". *Nature* 569.7754 (2019), 93–98. DOI: 10.1038/s41586-019-1148-9.

[Rie+18] M.-T. Rieder et al. "Localization Counteracts Decoherence in Noisy Floquet Topological Chains". *Phys. Rev. Lett.* 120 (21 2018), 216801. DOI: 10.1103/PhysRevLett.120.216801.

[RL12] D. Rainis and D. Loss. "Majorana qubit decoherence by quasiparticle poisoning". *Phys. Rev. B* 85 (17 2012), 174533. DOI: 10.1103/PhysRevB.85.174533.

[RL20] M. S. Rudner and N. H. Lindner. "Band structure engineering and non-equilibrium dynamics in Floquet topological insulators". *Nature Reviews Physics* 2.5 (2020), 229–244. ISSN: 2522-5820. DOI: 10.1038/s42254-020-0170-z.

[Rub+15] M. Ruby et al. "End States and Subgap Structure in Proximity-Coupled Chains of Magnetic Adatoms". *Phys. Rev. Lett.* 115 (19 2015), 197204. DOI: 10.1103/PhysRevLett.115.197204.

[Sac11] S. Sachdev. *Quantum Phase Transitions*. Cambridge University Press, 2011. ISBN: 978-0-52-151468-2.

[Šaf18] D. Šafránek. "Simple expression for the quantum Fisher information matrix". *Phys. Rev. A* 97 (4 2018), 042322. DOI: 10.1103/PhysRevA.97.042322.

[SBD16] L. M. Sieberer, M. Buchhold, and S. Diehl. "Keldysh field theory for driven open quantum systems". *Rep. Prog. Phys.* 79.9 (2016), 096001. DOI: 10.1088/0034-4885/79/9/096001.

[Sch05] U. Schollwöck. "The density-matrix renormalization group". *Rev. Mod. Phys.* 77 (1 2005), 259–315. DOI: 10.1103/RevModPhys.77.259.

[Sch07] M. Schlosshauer. *Decoherence and the Quantum to Classical Transition*. Springer-Verlag Berlin Heidelberg, 2007. ISBN: 978-3-540-35775-9.

[Sch11] U. Schollwöck. "The density-matrix renormalization group in the age of matrix product states". *Annals of Physics* 326.1 (2011), 96–192. ISSN: 0003-4916. DOI: https://doi.org/10.1016/j.aop.2010.09.012.

[Sch26] E. Schrödinger. "An Undulatory Theory of the Mechanics of Atoms and Molecules". *Phys. Rev.* 28 (6 1926), 1049–1070. DOI: 10.1103/PhysRev.28.1049.

[SD12] J. D. Sau and S. Das Sarma. "Realizing a robust practical Majorana chain in a quantum-dot-superconductor linear array". *Nature Communications* 3.1 (2012), 964. DOI: 10.1038/ncomms1966.

[SDV08] K. P. Schmidt, S. Dusuel, and J. Vidal. "Emergent Fermions and Anyons in the Kitaev Model". *Phys. Rev. Lett.* 100 (5 2008), 057208. DOI: 10.1103/PhysRevLett.100.057208.

[SL13] A. Stern and N. H. Lindner. "Topological Quantum Computation: From Basic Concepts to First Experiments". *Science* (2013), 1179–1184. DOI: 10.1126/science.1231473.

[SRM21] T. Simons, A. Romito, and D. Meidan. "Relation between scattering matrix topological invariants and conductance in Floquet Majorana systems". *Phys. Rev. B* 104 (15 2021), 155422. DOI: 10.1103/PhysRevB.104.155422.

[SS13] M. S. Scheurer and A. Shnirman. "Nonadiabatic processes in Majorana qubit systems". *Phys. Rev. B* 88 (6 2013), 064515. DOI: 10.1103/PhysRevB.88.064515.

[SSH79] W. P. Su, J. R. Schrieffer, and A. J. Heeger. "Solitons in Polyacetylene". *Phys. Rev. Lett.* 42 (25 1979), 1698–1701. DOI: 10.1103/PhysRevLett.42.1698.

[ST13] T. D. Stanescu and S. Tewari. "Majorana fermions in semiconductor nanowires: fundamentals, modeling, and experiment". *Journal of Physics: Condensed Matter* 25.23 (2013), 233201. DOI: 10.1088/0953-8984/25/23/233201.

[Sta16] T. D. Stanescu. *Introduction to Topological Quantum Matter & Quantum Computation*. CRC Press, 2016. ISBN: 978-1-31-518150-9. DOI: 10.1201/9781315181509.

[Sti01] R. Stinchcombe. "Stochastic non-equilibrium systems". *Advances in Physics* 50.5 (2001), 431–496. DOI: 10.1080/00018730110099650.

[SW72] M. M. Sternheim and J. F. Walker. "Non-Hermitian Hamiltonians, Decaying States, and Perturbation Theory". *Phys. Rev. C* 6 (1 1972), 114–121. DOI: 10.1103/PhysRevC.6.114.

[Swi12a] B. Swingle. *Constructing holographic spacetimes using entanglement renormalization*. 2012. DOI: 10.48550/ARXIV.1209.3304.

[Swi12b] B. Swingle. "Entanglement renormalization and holography". *Phys. Rev. D* 86 (6 2012), 065007. DOI: 10.1103/PhysRevD.86.065007.

[Ton+20] F. Tonielli et al. "Topological Field Theory Far from Equilibrium". *Phys. Rev. Lett.* 124 (24 2020), 240404. DOI: 10.1103/PhysRevLett.124.240404.

[TWV12] K. Temme, M. M. Wolf, and F. Verstraete. "Stochastic exclusion processes versus coherent transport". *New Journal of Physics* 14.7 (2012), 075004. DOI: 10.1088/1367-2630/14/7/075004.

[Vid04] G. Vidal. "Efficient Simulation of One-Dimensional Quantum Many-Body Systems". *Phys. Rev. Lett.* 93 (4 2004), 040502. DOI: 10.1103/PhysRevLett.93.040502.

[Vid08] G. Vidal. "Class of Quantum Many-Body States That Can Be Efficiently Simulated". *Phys. Rev. Lett.* 101 (11 2008), 110501. DOI: 10.1103/PhysRevLett.101.110501.

[Vid09] G. Vidal. *Entanglement Renormalization: an introduction*. 2009. DOI: 10.48550/ARXIV.0912.1651.

[VMC08] F. Verstraete, V. Murg, and J. I. Cirac. "Matrix product states, projected entangled pair states, and variational renormalization group methods for quantum spin systems". *Advances in Physics* 57.2 (2008), 143–224. DOI: 10.1080/14789940801912366.

[Wan+22] Y. Wang et al. "Observing a topological transition in weak-measurement-induced geometric phases". *Phys. Rev. Research* 4 (2 2022), 023179. DOI: 10.1103/PhysRevResearch.4.023179.

[Wen+16] X. Wen et al. "Holographic entanglement renormalization of topological insulators". *Phys. Rev. B* 94 (7 2016), 075124. DOI: 10.1103/PhysRevB.94.075124.

[Wen90] X. G. Wen. "Topological Order in Rigid States". *Int. J. Mod. Phys. B* 4 (1990), 239. DOI: 10.1142/S0217979290000139.

[Whi92] S. R. White. "Density matrix formulation for quantum renormalization groups". *Phys. Rev. Lett.* 69 (19 1992), 2863–2866. DOI: 10.1103/PhysRevLett.69.2863.

[WL19] L. Wang and H.-Q. Lin. *Dynamic structure factor from real time evolution and exact correction vectors with matrix product states*. 2019. DOI: 10.48550/ARXIV.1901.07751.

[WN90] X. G. Wen and Q. Niu. "Ground-state degeneracy of the fractional quantum Hall states in the presence of a random potential and on high-genus Riemann surfaces". *Phys. Rev. B* 41 (13 1990), 9377–9396. DOI: 10.1103/PhysRevB.41.9377.

[Wol+20] S. Wolff et al. "Nonequilibrium metastable state in a chain of interacting spinless fermions with localized loss". *Phys. Rev. B* 101 (7 2020), 075139. DOI: 10.1103/PhysRevB.101.075139.

[YF14] G. Yang and D. E. Feldman. "Exact zero modes and decoherence in systems of interacting Majorana fermions". *Phys. Rev. B* 89 (3 2014), 035136. DOI: 10.1103/PhysRevB.89.035136.

[ZE20] A. A. Ziołkowska and F. H.L. Essler. "Yang-Baxter integrable Lindblad equations". *SciPost Phys.* 8 (3 2020), 44. DOI: 10.21468/SciPostPhys.8.3.044.

[Zen+19] B. Zeng et al. *Quantum Information Meets Quantum Matter: From Quantum Entanglement to Topological Phases of Many-Body Systems*. Springer New York, 2019. ISBN: 9781493990849. DOI: 10.1007/978-1-4939-9084-9.

[Zha+19] Z.-T. Zhang et al. “Effects of decoherence on diabatic errors in Majorana braiding”. *Phys. Rev. A* 100 (1 2019), 012324. DOI: 10.1103/PhysRevA.100.012324.

[Žni10] M. Žnidarič. “A matrix product solution for a nonequilibrium steady state of an XX chain”. *Journal of Physics A: Mathematical and Theoretical* 43.41 (2010), 415004. DOI: 10.1088/1751-8113/43/41/415004.

[Žni11] M. Žnidarič. “Solvable quantum nonequilibrium model exhibiting a phase transition and a matrix product representation”. *Phys. Rev. E* 83 (1 2011), 011108. DOI: 10.1103/PhysRevE.83.011108.

[Žni15] M. Žnidarič. “Relaxation times of dissipative many-body quantum systems”. *Phys. Rev. E* 92 (4 2015), 042143. DOI: 10.1103/PhysRevE.92.042143.

[ŽP10] B. Žunkovič and T. Prosen. “Explicit solution of the Lindblad equation for nearly isotropic boundary driven XY spin 1/2 chain”. *Journal of Statistical Mechanics: Theory and Experiment* 2010.08 (2010), P08016. DOI: 10.1088/1742-5468/2010/08/p08016.

[Žun14] B. Žunkovič. “Closed hierarchy of correlations in Markovian open quantum systems”. *New Journal of Physics* 16.1 (2014), 013042. DOI: 10.1088/1367-2630/16/1/013042.